Maksim Klinkov

Identification of Unknown Structural Loads from Dynamic Measurements Using Robust Observers

IDENTIFICATION OF UNKNOWN STRUCTURAL LOADS FROM DYNAMIC MEASUREMENTS USING ROBUST OBSERVERS

DISSERTATION

zur Erlangung des akademischen Grades

DOKTOR-INGENIEUR

vorgelegt von

M.Sc. MAKSIM KLINKOV

aus Almalyk (Usbekistan)

eingereicht dem

DEPARTMENT MASCHINENBAU

der UNIVERSITÄT SIEGEN

Referent: Prof. Dr.-Ing. C.-P. Fritzen

Korreferent: Prof. Dr.-Ing. G. De Roeck (K.U.Leuven)

Tag der mündlichen Prüfung

04. November 2011

Preface

To myself I am only a child playing on the beach,
while vast oceans of truth lie undiscovered before me
- Sir Isaac Newton

The following are the products of my efforts as a research assistant at the Institute of Mechanics and Control – Mechatronics of the University of Siegen.

My very special thanks and respect go to my supervisor Prof. Dr.-Ing. C.-P. Fritzen, who has inspired me for the theme of this work and has always created, during my time as an assistant in his group, both very pleasant human as well as very technically conductive climate. "Research makes fun!"

I would also like to thank Prof. Dr.-Ing. G. De Roeck for taking over the second examiner responsibility and the related effort as well as Prof. Dr.-Ing. T. Carouls and Prof. Dr.-Ing. O. Nelles for the contributions to the implementation of the doctorate.

I would also like to express my gratitude to my former and present colleagues at the institute, Dr.-Ing. Boris Künkler, Dr.-Ing. Gregor Mengelkamp, Dr.-Ing Rolf Schulte, Dipl.-Ing Martin Kübbeler, Dipl.-Ing Philip Köster, MSc. Keja Xing, MSc. Yan Niu, MSc. Miguel Torres, MSc. Cheng Yang and especially my long-term roommates Dipl.-Ing Peter Kraemer and Dipl.-Ing Jochen Moll for fruitful work and their tolerance. Moreover, my special thanks go to Mr. Gerhard Dietrich, Dipl.-Ing. Wolfgang Richter and Frau Gisela Thomas for all their help throughout this time. I strongly appreciate the work of Mr. W. John Keyes, Dipl.-Ing Peter Kraemer, MSc. Yan Niu and MSc. Rannam Chaaban for their review of this manuscript and many constructive comments.

A significant share of the success of this work belongs to my wife Anna – who was always supportive and encouraging all through this long journey. Anna, I thank you very sincerely for taking care of our family in such a masterful and peaceful way. In addition, I would like to thank warmly my parents for always being there for me.

Siegen, June 2011   Maksim Klinkov

To my family: Anna, Dana Maria and Michail

Content

Nomenclature

Each equation in the book

would halve the sales.

-Stephen Hawking

Abbreviations

AE	Acoustic Emission
AIC	Akaike Information Criterion
CWT	Continuous Wavelet Transformation
DP	Dynamic Programming
ERA	Eigenvalue Realization Algorithm
EC	Energy Criterion
FRF	Frequency Response Function
FFT	Fast Fourier Transform
FEM	Finite Element Model
GA	Genetic Algorithm
GCV	Generalized Cross Validation
ISF	Inverse Structural Filter
KF	Kalman Filter
KF-UI	Kalman Filter with Unknown Inputs
LMI	Linear Matrix Inequality
LS	Least Square
LSE	Least Square Estimation
LQTP	Linear Quadratic Tracing Problem
LTR	Loop Transfer Recovery
LTI's	Linear Time Invariant system
MIMO	Multi-Input-Multi-Output
MA	Modal Analysis
MPIO	Modified Proportional Integral Observer
NES	Normalized Error Square
NME	Normalized Mean Error
NN	Neural Networks
ODE	Ordinary Differential Equation

PIO	Proportional Integral Observer
RLSE	Recursive Least Square Estimation
SI	System Identification
SHM	Structural Health Monitoring
SWAT	Sum of Weighted Accelerations Technique
SS&IE	Simultaneous State and Input Estimator
SSI	Stochastic Subspace Identification
SV	Singular Value
SVD	Singular Value Decomposition
TF	Transfer Function
T-TLC	Truncated Total Least Square
TSVD	Truncated Singular Value Decomposition
TOA	Time of Arrival
VAR	Vector-Autoregressive
WT	Wavelet Transformation
WEP	Wind Energy Plant

Latin letters

A_D, A	Transition matrices of discrete-time and continuous-time system
$(\hat{A}_D, \hat{B}_D, \hat{C}_D \ \hat{D}_D)$	Estimated discrete sate-space system matrices
B_D, B	Input matrices of discrete-time and continuous-time system
B_o	Input placement matrix
B_m	Normalized modal input matrix
C_D, C	Output matrices of discrete-time and continuous-time system
C_{oq}, C_{ov}, C_{oa}	Nodal displacement, velocity and acceleration output matrices
C_{mq}, C_{mv}, C_{ma}	Modal displacement, velocity and acceleration output matrices
C_k	Controllability matrix in discrete-time domain

$\hat{\boldsymbol{C}}_{AR}$	AR covariance matrix
$c_p(\theta_i)$	Directional phase velocity
c_g	Wave group velocity
$\boldsymbol{D}_D, \boldsymbol{D}$	Direct feed-though matrices of discrete-time and continuous-time system
$\boldsymbol{D}_n, \boldsymbol{D}_m$	Nodal and modal damping matrices
$D_{\theta\theta}$	Composite bending stiffness in direction θ
d	Distance
$\mathrm{E}_{(x,y)}, \mathrm{E}_{(si)}$	Estimated impact location and actual location of the ith sensor
$\boldsymbol{e}(t)$	Error vector
$\boldsymbol{F}(t)$	Load function
$\boldsymbol{F}(\omega), \hat{\boldsymbol{F}}(\omega)$	Real and estimated load spectra
$f_i, \hat{f}_i$	i^{th} real and estimated natural frequency
$\boldsymbol{f}_L(\cdot)$	Known Lipschitz nonlinear function
$\boldsymbol{f}_U(\cdot)$	Unknown nonlinear function
f_s	Sampling rate
$\boldsymbol{H}(s)$	System transfer function
$\boldsymbol{H}_{Markov}$	Markov matrix
H_h	Hamiltonian function
$\bar{\boldsymbol{H}}_i$	Hankel matrix
$\boldsymbol{H}_S$	Matrix of basis functions
$\boldsymbol{H}_i$	Markov parameter
$\boldsymbol{H}(t)$	Impulse response function
$\boldsymbol{H}(\omega)$	Frequency response function
h	Material thickness
$\boldsymbol{I}$	Identity matrix
$\boldsymbol{J}$	Cost function
$\boldsymbol{K}_n, \boldsymbol{K}_m$	Nodal and modal stiffness matrices

$\boldsymbol{K}_{obs}$	Observer gain matrix
$\boldsymbol{K}_k$	Kalman gain matrix
$\left(\boldsymbol{L}(t),\boldsymbol{E}(t),\boldsymbol{G}(t),\boldsymbol{P}(t),\boldsymbol{V}(t)\right)$	Minimal order observer system matrices
$\boldsymbol{L}_{PIO}$	PI observer gain matrix
$\boldsymbol{M}_n,\boldsymbol{M}_m$	Nodal and modal mass matrices
$(\boldsymbol{N},\boldsymbol{L},\boldsymbol{T},\boldsymbol{Q})$	Simultaneous state and input estimator matrices
$\boldsymbol{O}_k$	Observability matrix in discrete-time domain
$\boldsymbol{O}$	Observability matrix in continuous-time domain
$\boldsymbol{P}_i$	Covariance matrix
$\boldsymbol{Q}_k$	Measurement noise covariance matrix
$\boldsymbol{q}(t),\dot{\boldsymbol{q}}(t),\ddot{\boldsymbol{q}}(t)$	Nodal displacement, velocity and acceleration vectors
$\boldsymbol{q}_m(t),\dot{\boldsymbol{q}}_m(t),\ddot{\boldsymbol{q}}_m(t)$	Modal displacement, velocity and acceleration vectors
$\boldsymbol{R}_k$	Process noise covariance matrix
$\boldsymbol{R}_{yu},\boldsymbol{R}_{uu}$	Correlation and autocorrelation matrices between input/output and input/input
$S_i^{'}$	Energy criterion onset function
t^{tof}	Time of flight
t_i^{toa}	Time of arrival for i^{th} sensor
$\boldsymbol{U}(s)$	Input vector in frequency domain
U	Input matrix in discrete-time domain
$\boldsymbol{u}_k,\boldsymbol{u}(t)$	Discrete-time and continuous-time input vectors
$V(\circ)$	Lyapunov function
v	Measurement noise vector
$\boldsymbol{W}_w,\boldsymbol{W}_r$	Weighting and regularization matrices
$\boldsymbol{W}_o$	Observability Gramian
w	Process noise vector
$\boldsymbol{x}_k,\boldsymbol{x}(t)$	Discrete-time and continuous-time state vectors
$\hat{\boldsymbol{x}}_k,\hat{\boldsymbol{x}}(t)$	Estimated discrete-time and continuous-time state vectors

$\hat{\boldsymbol{x}}_k^-, \hat{\boldsymbol{x}}_k^+$	*a priori* and *a posteriori* state estimate
$\boldsymbol{Y}(s)$	Output matrix in frequency domain
$\boldsymbol{Y}$	Output matrix in discrete-time domain
$\boldsymbol{y}_k, \boldsymbol{y}(t)$	Discrete-time and continuous-time output vectors
$\hat{\boldsymbol{y}}_k, \hat{\boldsymbol{y}}(t)$	Estimated discrete-time and continuous-time output vectors
$\boldsymbol{y}(\omega)$	Output spectrum
$\tilde{\boldsymbol{y}}$	Vector of noisy measurements
$\boldsymbol{Z}$	Normalized modal damping matrix

Greek letters

Δt	Time increment
$\delta(t)$	Dirac-Impulse function
δ_i	Complex eigenvalue in discrete-time domain
$\varepsilon(t)$	Observer reconstruction error
λ	Vector of Lagrange multipliers
$\lambda_i, \hat{\lambda}_i$	i^{th} real and estimated eigenvalue
$\xi_i, \hat{\xi}_i$	Real and estimated damping ratio of the ith mode
ρ	Material density
Σ	Matrix of singular values
σ_i	i^{th} singular value
$\boldsymbol{\Phi}$	Modal matrix
$\boldsymbol{\Phi}_T(t)$	Transition matrix
$\boldsymbol{\varphi}_i$	i^{th} eigenvector
$\boldsymbol{\Psi}$	Discrete-time modal matrix
ψ_i	Discrete-time eigenvector
$\boldsymbol{\Psi}_{(a,b)}^m$	Mother wave let function
$\boldsymbol{\Psi}_g^m$	Gabor mother wavelet function
$\boldsymbol{\Omega}$	Matrix of circular frequencies

$$\omega_i, \hat{\omega}_i \qquad\qquad i^{\text{th}} \text{ real and estimated circular natural frequency}$$

Characters

T	Transpose
$+$	Pseudo inverse
$-$	Generalized inverse
$*$	Complex conjugate

Operators

$$\nabla_{\boldsymbol{k}}(\circ) = \begin{bmatrix} \dfrac{\partial(\circ)}{\partial k_1} \\ \vdots \\ \dfrac{\partial(\circ)}{\partial k_n} \end{bmatrix} \qquad\qquad \text{Jacobian operator}$$

$$\nabla_{\boldsymbol{k}}^2(\circ) = \frac{\partial^2(\circ)}{\partial \boldsymbol{k} \partial \boldsymbol{k}} \qquad\qquad \text{Hessian operator}$$

$$\boldsymbol{E}\{\circ\} \qquad\qquad \text{Expectation operator}$$

$$C(\cdot) \qquad\qquad \text{Condition number of a matrix}$$

$$O \qquad\qquad \text{Landau order operator}$$

Abstract

The global trends in the construction of complex structures *e.g.* high buildings, wind turbines or airplanes' tend to make the structures more intelligent by integrating sensing units together with evaluation algorithms which allow the check of structure integrity permanently. This process of structural integrity characterization strategy referred to as Structural Health Monitoring (SHM). Special SHM parameters like material properties and load characteristics are essential when assessment of fatigue life of a structure and its components is done. Therefore, the time history of an external load is an important quantity in the forecast of the remaining lifetime. Furthermore, the load localization problem becomes an important issue, especially in the case of impacts, since the aircraft industry started to use new composite materials more extensively where the impacts cause delaminations which are not detectable by visual inspections. In many practical applications, however, the measurement of external loads is limited or not possible due to sensor limitations or the unknown nature of the external forces. Therefore, indirect load history estimation is a subject of extensive studies in the last two decades. The estimation procedure leads to a so called inverse problem which is 'ill-posed' in the mathematical sense so that the existence, uniqueness or stability of solution is violated.

First of all, this work provides a closer investigation to a variety of existing algorithms of force history reconstruction and location estimation which have been established by mechanical engineers. Secondly, research is carried out for possible candidate methods among the other engineering disciplines. The main focus of the thesis is concentrated on comprehensive design analysis and further development of the qualified algorithms. In particular, model based robust observers are considered as candidates for the online loads and states reconstruction. The aspects of proper model building that allow releasing the sensor placement procedure (from collocated to non-collocated), while simultaneously reducing the model complexity are introduced for the observer design. An innovative model free passive technique for automatic impact location detection is elaborated and extended by incorporation of a fast robust load estimation method. In addition, a novel approach of rank deficiency compensation is proposed for the direct time deconvolution procedure in the non-collocated case.

Selected algorithms are grouped according to their ability to fulfill the load reconstruction requirements and tested either in simulation environment or on laboratory structures. The results are systemized in a form of strong and weak sides for every particular algorithm which might serve for the on-field application and future research in this area.

1 INTRODUCTION

Although this may seem a paradox,
all exact science is dominated by the idea of approximation.
-Bertrand Russell

1.1   LITERATURE REVIEW AND MOTIVATION

Buildings, wind turbines, airplanes or stadiums (during concerts or football matches) are some of the examples where the dynamics of a structure should be taken into consideration for reliable construction. In particular, both, material properties and load characteristics, are essential parameters when assessing the fatigue life of a structure or its components. Therefore, the time history of external forces is an important quantity in the forecast of the remaining lifetime [JOHANNESSON 1999]. In many practical applications, however, the measurement of external loads is limited or not possible due to sensor limitations or the unknown nature of the external load, see Figure 1.1(a). Even when load measurement transducers are available, they may still alter the properties of the system (electronic circuits), intrude in the load path (contacts and joint).
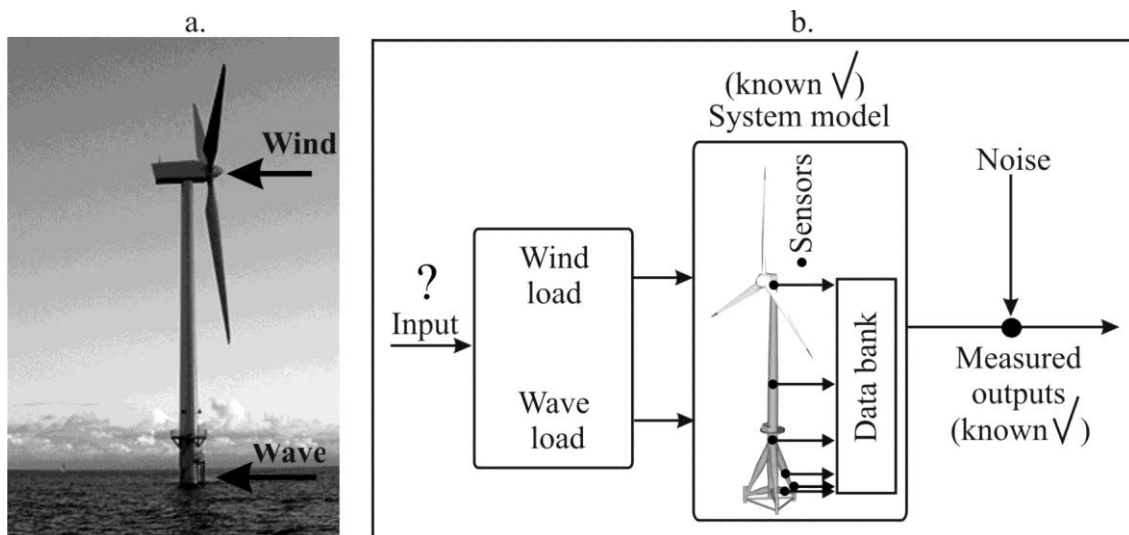
Figure 1.1: Offshore wind energy plant (a) and block diagram of the load reconstruction problem (b)

Furthermore, the load localization problem becomes an important issue, especially in the case of impacts, since the aircraft industry started to use new composite materials more extensively. Impacts cause delaminations in composite materials which might not be found by visual

inspection, thereby leading to structural failure. Accordingly, the process of estimating loads can be partitioned into the following subparts: 1) reconstructing load time history assuming that the location of a load is known *a priori*; and 2) determining the locations of applied forces.

Load history identification has been the subject of extensive studies in the course of the last two decades. Generally, all force reconstruction methods that have been put forth by engineers can be summarized in three main groups [UHL 2007]:

1. Deterministic methods (based on the structural model and measured signals)
2. Stochastic methods (statistical models)
3. Artificial intelligence-based methods (neural networks)

Deterministic approaches are based on the system model, and therefore yield results which are strongly dependent upon the accuracy of identified or analytically developed models. A further classification within this group can be carried out on the basis of the signal analysis procedure applied for load estimation; such procedures include frequency-domain methods [ADAMS and DOYLE 2002] and [HILLARY and EWINS 1984] or time-domain methods [GENARO and RADE 1998] and [JANKOWSKI 2009].

Time-domain approaches are mainly based on the deconvolution of the (Duhamel-Integral)

$$y(t) = \int_0^t H(t-\tau)F(\tau)d\tau \, , \tag{1.1}$$

where $F(t)$ represents external excitation forces, $y(t)$ are the system responses and $H(t)$ represents the structure impulse response function. Accordingly, the force reconstruction problem is posed as follows: given some measurements $y(t)$ and known system response functions $H(t)$, determine the loads $F(t)$. It should be noted that either $y(t)$, $H(t)$ or both may not be known with perfect precision.

In the frequency domain, information regarding the Frequency Response Function (FRF) $H(\omega)$ of the investigated structure and the spectrum of measured responses $Y(\omega)$ are both required. On the basis of this information, the deconvolution of Equation (1.1) is carried out by means of a simpler algebraic equation

$$\hat{F}(\omega) = H^{-1}(\omega)Y(\omega) \, , \tag{1.2}$$

where $\hat{F}(\omega)$ is estimated force spectra. Finally, force histories in the time domain are obtained by the inverse Fourier transformation.

Stochastic methods are attempts at establishing statistical correlations between the output and input. In order to establish such correlations, it is necessary to conduct measurements of the inputs and outputs while the structure is being operated. The most useful statistical model for load identification is the regression model. Remarks regarding the applicability of the regression model to load identification can be found in [Trujillo and Busby 1997]. A dedicated procedure for regression model inversion is presented in [UHL 2007].

Techniques based on artificial intelligence can be realized using Neural Networks (NN) algorithms [UHL and PETKO 2006] and [UHL 2002], fuzzy algorithms [GÓRAL *et al.* 2002] or evolutionary algorithms [UHL and PIECZARA 2003]. These methods require a learning process in order to find the relation between the inputs and outputs. It is necessary for the learning process to conduct direct measurements of loads and system responses. In some cases this might be impossible, but numerical simulations of the system behavior can be applied for the learning process of intelligent system [UHL 2002].

The force reconstruction problem is mainly solved by using indirect measurement techniques, which include the transformations of related measured quantities such as acceleration, velocity, position or strain, see Figure 1.1(b). These transformations generally lead to a so-called inverse problem or deconvolution problem, where the system properties $H(t)$ and responses $y(t)$ are known while the excitations $F(t)$ are unknown, see Equation (1.1). It is well known that inverse problems are 'ill-posed' in the mathematical sense, that is one of 1) the existence, 2) the uniqueness, or 3) the stability of solution is violated [HANSEN *et al.* 1999; JACQUELIN *et al.* 2003]. If this inversion can be done, the system itself becomes its own force sensor, *i.e.* a "**virtual force sensor**" which would solve the problem of the load history estimation. A variety of methods were elaborated to overcome the above mentioned difficulties. Stevens [STEVENS 1987] gave an excellent overview of this topic, which includes some earlier studies on inverse analysis of external forces, and Inoue et al. [INOUE *et al.* 2001] made a good summary for impact force estimation techniques. Some of these methods are based on the frequency or impulse response functions or use regularization and dynamic programming in the time domain, as proposed by Trujillo and Busby [TRUJILLO and BUSBY 1997] and applied by Doyle [DOYLE 1989; ADAMS and DOYLE 2002] and Nordtröm [NORDSTRÖM 2005]. Others use an integration of measured acceleration signals [ELLIOTT *et al.* 2005] and [CARNE *et al.* 1992] or can only determine the sum of all forces and moments applied to the centre of mass (Sum of Weighted Acceleration Technique SWAT) [GENARO and RADE 1998]. Most of the authors assume the prior knowledge of the force location and require first to record the system responses and then do the force history reconstruction. The regularization

techniques or a time shift of the collected measurement data in non-collocated case [STELTZNER and KAMMER March 1999] and [KAMMER and STELTZNER 2001] (sensors and loads positions are not collocated) are used to overcome the ill-posedness of the inverse problem. Other researchers have treated the same problem from the control engineering point of view [SÖFFKER and KRAJCIN 2003], [CORLESS and TU 1998] by using observer properties that are able to estimate the states and unknown inputs or external disturbances.

Applicable to the Structural Health Monitoring (SHM) algorithms which are able to estimate the external forces and their locations online or quasi-online, and also capable to do it for nonlinear or time variant mechanical systems, are of special interest. Among them are [DOYLE and KANNAL 1997; DOYLE 1999], [GOPALAKRISHNAN and DOYLE 1994], [DOYLE and MARTIN 1996] who have treated the two following problems: 1) the impact force history reconstruction and 2) the impact force location estimation primarily from the point of wave propagation theory. For the former, several model based approaches which perform deconvolution of the Equation (1.1) in a frequency/wavelet domain, where it is equivalent to division as in Equation (1.2), were applied. In order to achieve this, the knowledge of the wave propagation and the model (spectral element model or finite element model) was always required. Doyle has shown that for the finite beam type of structures, such as that in Figure 1.2, the measured signals (accelerations, strains or displacements) must undergo a preprocessing procedure where all effects of wave reflections (which always occur in finite structures and, in the case of impact load types, represent the redundant information) and signal trend (especially for accelerometers) must be removed from the acquired data and only then transformed into a frequency domain.
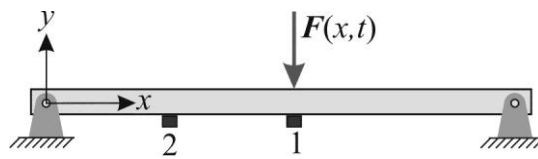
Figure 1.2: Schematic beam excited by unit force with sensors placed on positions 1 and 2

Additional difficulties which Doyle had to deal with were 1) loss of information (zeros or no information available at some frequencies) and 2) inherited oversensitivity (sharp spectral peaks) in the $H(\omega)$ function, see Figure 1.3. These either make division in Equation (1.2) problematic or make $\hat{F}(\omega)$ (at these frequencies) diverge from real force $F(\omega)$ due to mismatch between $Y(\omega)$ and $H(\omega)$. To overcome the above problems, Doyle used more than

one sensor simultaneously together with the addition of small noise which has a regularization property, so that the Equation (1.2) was modified in the following form:

$$\hat{\boldsymbol{F}}(\omega) = \left[\frac{\boldsymbol{H}_1^*(\omega)\boldsymbol{Y}_1(\omega) + \boldsymbol{H}_2^*(\omega)\boldsymbol{Y}_2(\omega)}{\boldsymbol{H}_1^2(\omega) + \boldsymbol{H}_2^2(\omega) + \boldsymbol{R}(\omega)} \right], \qquad (1.3)$$

where an asterisk indicates a complex conjugate and $\boldsymbol{R}(\omega)$ is a small amount of random noise.

Addition of noise to the denominator does not replace the loss of information but rather removes potential singularity at those frequencies where $\boldsymbol{H}(\omega)$ tend to be zero.
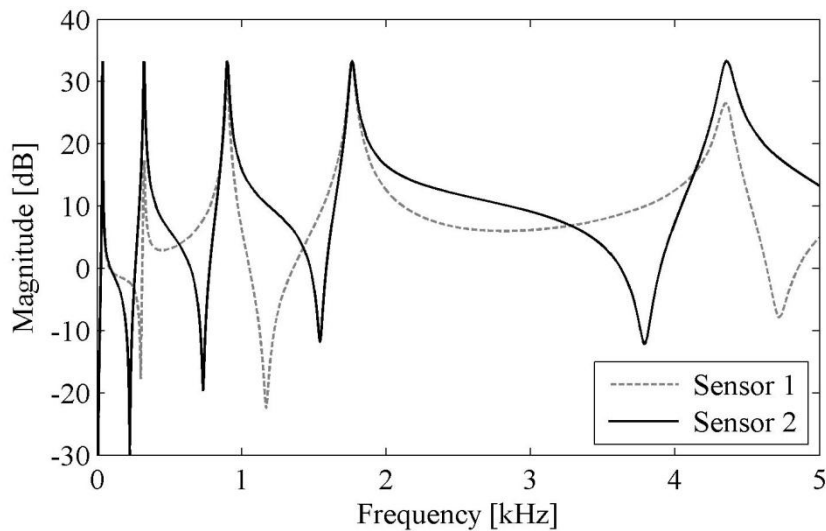
Figure 1.3: Frequency response functions for the modeled hinged beam

Calculated force spectra were then mapped into the time domain by inverse Fourier transform. For the problem of force localization [DOYLE and KANNAL 1997] the advantages of the techniques proposed by [WHISTON 1984] were extended by applying a Genetic Algorithm (GA) for global search in complex frame structure. Here again the model (spectral element model or finite element model) and at least two sensors have been used to estimate the force location. The essence of this approach is the usage of estimated forces from recorded measurements and modeled frequency response function $\boldsymbol{H}(\omega)$ for different positions of applied impact. When the guessed position in $\boldsymbol{H}(\omega)$ is nearly correct then the force reconstructions from both sensors is very similar. As a consequence Doyle used a correlation or difference of these forces as an objective function for GA.

[SEYDEL and CHANG 1994; SEYDEL and CHIU 2001] considered the identification of the impact location and impact load history for a stiffened composite plate by using a smart

sensor layer (a distributed array of sensors glued to the plate) as illustrated in Figure 1.4. For the force history reconstruction, first the position on the plate where the force is applied was found. This information is very important because the authors used a mathematical model (bending equations for an orthotropic plate) for impact history reconstruction which is built with the assumptions that the force location is known in advance. In contrast to [DOYLE and KANNAL 1997], Seydel and Chang worked in time domain and used the information acquired from the area of search (only 4 sensors in the vicinity of impact were used, as shown by the red square of the nearest sensors in Figure 1.4) for impact location identification. As the impact time was not exactly known, the authors utilized only differences between calculated Times Of Arrival (TOA) for these sensors and then tried to minimize the cost function of the following form:

$$\min_{(x,y)}(J) = \sum_{i=2}^{4} \left(\underbrace{(t_i^{toa} - t_1^{toa})}_{\substack{\text{measured} \\ \text{differencies}}} - \left[\underbrace{\frac{E_{(x,y)} - E_{(si)}}{c_p(\theta_i)} - \frac{E_{(x,y)} - E_{(s1)}}{c_p(\theta_1)}}_{\text{estimated differencies}} \right] \right)^2 , \tag{1.4}$$

where t_i^{toa} is the calculated time of arrival for the ith sensor. Estimation of t_i^{toa} from the recorded time signals was done with the help of the double peak technique which is a selection of the minimum before a global maximum. $E_{(x,y)}$ is the estimated impact location on the plate, $E_{(si)}$ is the actual location of the ith sensor. Sensor 1 was always defined as the sensor with the smallest t_1^{toa}. The phase velocity $c_p(\theta_i)$ for the orthotropic plate and given direction θ is found analytically as in [DOYLE 1997]:

$$c_p(\theta_i) = \sqrt[4]{\omega^2 \frac{D_{\theta\theta}}{\rho h}} , \tag{1.5}$$

here $D_{\theta\theta}$ is a composite bending stiffness in direction θ for a specific material and ω is the wave frequency (the frequency that has the maximum response) which in its turn was obtained for each sensor individually with the help of Fast Fourier Transform (FFT), ρ and h are the plate density and thickness respectively. After the impact location was found iteratively by minimization of the cost function in Equation (1.4), the model based optimization technique was applied for final time history estimation. Figure 1.4 shows the principle block diagram of force location estimation and force history reconstruction. The optimization

problem was solved by a smoother filter algorithm developed by [TRACY and CHANG 1998a; TRACY and CHANG 1998b].
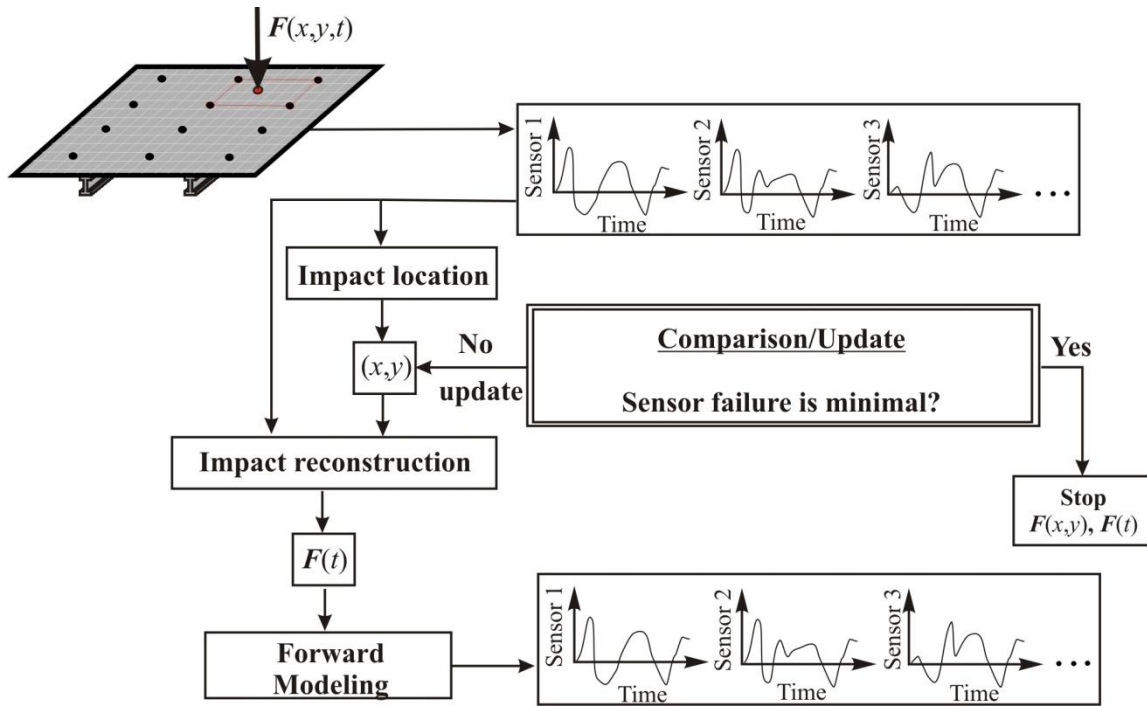
Figure 1.4: Overview of the model-based impact identification scheme [SEYDEL and CHANG 1994]

[STELTZNER and KAMMER 1999; KAMMER and STELTZNER 2001] have proposed a non-causal Inverse Structural Filter (ISF) which takes the structural response data y_k as an input and returns the estimate of the input forces u_k as an output. They considered a discrete-time invariant system in state space domain

$$\begin{aligned} x_{k+1} &= A_D x_k + B_D u_k \\ y_k &= C_D x_k + D_D u_k \end{aligned}, \tag{1.6}$$

where the subscript "D" is used for discrete time system and k represents the time instant. Thus, based on homogenous initial conditions, Equation (1.6) was stepped forward and the output/input relationship was established as:

$$y_k = \sum_{i=0}^{k} H_i u_{k-i}, \tag{1.7}$$

where the Markov parameters H_i (*i.e.* $H_0 = D_D$, $H_i = C_D (A_D)^{i-1} B_D$) were obtained either analytically or during the standard vibration test. Equation (1.6) was manipulated to interchange the input and output, leading to an inverse structural system

$$x_{k+1} = \hat{A}_D x_k + \hat{B}_D y_k$$
$$u_k = \hat{C}_D x_k + \hat{D}_D y_k$$

<div align="right">(1.8)</div>

with

$$\hat{A}_D = \left[A_D - B_D D_D^+ C_D \right] \qquad\qquad \hat{B}_D = B_D D_D^+$$

<div align="right">(1.9)</div>

$$\hat{D}_D = D_D^+ = (D_D^T D_D)^{-1} D_D^T \qquad\qquad \hat{C}_D = -D_D^+ C_D$$

<div align="right">(1.10)</div>

so that the impulse response sequence was written for Equation (1.8) in analogy to the forward system as in Equation (1.7)

$$u_k = \sum_{i=0}^{k} R_i y_{k-i} \, ,$$

<div align="right">(1.11)</div>

where, $R_0 = \hat{D}_D$, $R_i = \hat{C}_D (\hat{A}_D)^{i-1} \hat{B}_D$ are the inverse Markov parameters which are used for construction of causal ISF. Steltzner and Kammer have faced several difficulties including: (a) the Moore-Penrose pseudo-inverse requires that the number of sensors be greater than the number of reconstructed forces; moreover the matrix D_D (which requires acceleration measurements) should have a full column rank to ensure the existence of D_D^+; (b) the inverse matrix $\hat{A}_D$ can be unstable for structural systems with sensors at different locations than applied forces, that is a "non-collocated" sensors scenario, which can lead to divergence of Equation (1.11). These problems were addressed by considering the complete absence of matrix D (all sensors considered as non-collocated), in such a way that the system in Equation (1.6) was stepped forward before the inversion could take place

$$x_{k+1} = A_D x_k + B_D u_k$$
$$y_{k+1} = C_D A_D x_k + C_D B_D u_k$$

<div align="right">(1.12)</div>

so, that non-causal Equation (1.12) was used as a basis for the construction of ISF with "l-lead":

$$u_k = \sum_{i=0}^{N_{R-1}} R_i y_{k+l-i} \, .$$

<div align="right">(1.13)</div>

The "l step forward" is a non-causal lead integer accounting for the finite wave propagation time, from source to sensor, and the number N_{R-l} specifies the order of the ISF. Calculation of the inverse filter coefficients which are combined in matrix R is done with the help of Markov parameters that were cast into a matrix H and accounting the l-lead

$$R = \begin{bmatrix} 0 & 0 & I & 0 \end{bmatrix} H^{+}. \tag{1.14}$$

Here, the deconvolution of Equation (1.1) is done in discrete time domain and normally requires a pseudo-inverse of the matrix built out of the Markov parameters. The beauty of this method is that the pseudo-inverse needs to be done only once. This approach enables an almost online load reconstruction for time invariant systems as well as load estimation in the case when the sensors and excitation positions are not the same (non-collocated). An individual sensor lead was proposed [NORDSTRÖM 2005] as an extension of this method. Disadvantages associated with the method include difficulties in choosing a proper non-causal lead l and high sensitivity to the measurement noise.

[NORDSTRÖM 2005] has extended the Dynamic Programming (DP) method proposed by [TRUJILLO and BUSBY 1997] for input estimation on linear time-variant systems (generally, the moving load and environmental changes are assumed) with measurements contaminated by noise. The starting point for the input reconstruction was a discrete time variant state space system as in Equation (1.6) with a slight modification in the state vector which combined the states and inputs, as follows:

$$\begin{bmatrix} x_{k+1} \\ u_{k+1} \end{bmatrix} = \begin{bmatrix} A_D & B_D \\ 0 & I \end{bmatrix} \begin{bmatrix} x_k \\ u_k \end{bmatrix} + \begin{bmatrix} 0 \\ \Delta u_k \end{bmatrix}. \tag{1.15}$$

Next, the search of a Δu_k sequence that minimizes the weighted least square error between measured y_k and estimated $\hat{y}_k$ responses with Tikhonov regularization is carried out with the help of DP [NORDSTRÖM 2005]:

$$\min_{\Delta u} (J) = \sum_{k=1}^{N} (y_k - \hat{y}_k)^T W_w (y_k - \hat{y}_k) + \Delta u_k^T W_r \Delta u_k \tag{1.16}$$

here, the matrices W_w and W_r are considered to be symmetric and positive definite, containing weighting and regularization coefficients respectively. The DP is the recurrence algorithm that may be used to solve large least square problems and is appropriate for minimizing quadratic functions, and comprises two main steps: a backward and a forward sweep. The backward sweep heuristically establishes the input/output relationships at each discrete time step, whereas the forward sweep constitutes the calculation of the optimal inputs and states for the given initial conditions and relations that where established during the backward sweep. Recently an extended DP algorithm has been applied for identification of dynamic loads [LOURENS et al. 2008; LOURENS et al. 2009].

[WOJCIECHOWSKI 1978] introduced for the first time the Proportional Integral Observer (PIO) which was an extension of the classical proportional Luenberger observer [LUENBERGER 1971]. In contrast to the Luenberger approach, a second loop with two gain matrices and an integrator is also used. [SÖFFKER *et al.* 1995] have studied the PIO in more detail and applied it to estimate nonlinearities, unmodelled dynamics or unknown inputs/disturbances for control purposes Figure 1.5(a). Initially, the PIO technique suffered from the disadvantage of amplifying measurement noise which was due to the usage of high gains in a manner analogous to a Luenberger observer.
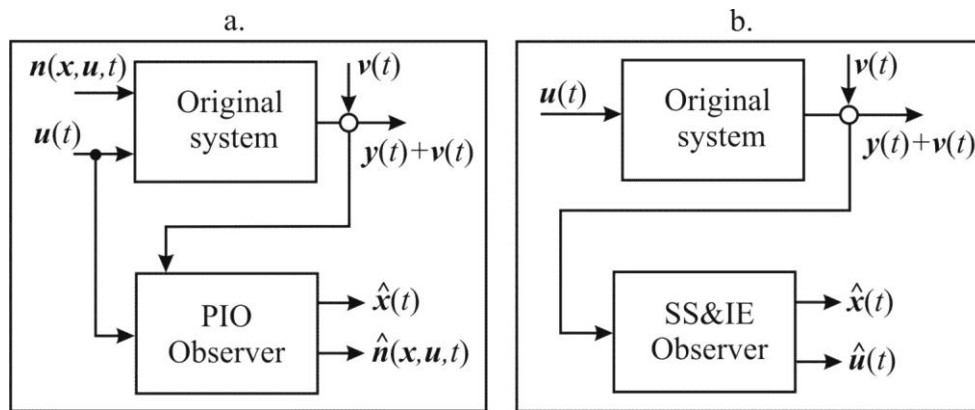
Figure 1.5: Input reconstruction principles with observer techniques (a) proportional integral observer (PIO) and (b) simultaneously state and input estimator (SS&IE)

This problem was solved by [KRISHNA and POUSGA 2001] and the method was then adopted by [SÖFFKER and KRAJCIN 2003] for contact force estimation as well as for crack detection in rotating machines. The modified PIO (MPIO) is equipped with an additional integrator which enables the attenuation of measurement noise. The gain matrices can be found by any conventional pole placement procedure. Nevertheless, the locations of nonlinearities/disturbances should be known prior to the observer design.

[HA *et al.* 2004; HA and TRINH 2004] established a new technique for Simultaneous State and Input Estimation (SS&IE), Figure 1.5(b), for a class of nonlinear systems for control purposes. In their work, the system nonlinearity is assumed to consist of known and unknown parts. To calculate the system observer, a general state space representation of the system is transformed in such way that the states are combined together with inputs. Then, the observer structure which includes only known nonlinearity is designed with the help of a Linear Matrix Inequality (LMI) algorithm. There are still two prerequisite conditions to be fulfilled in order to assure that such an observer exists. Among them is the continuity of the known nonlinear field (the known nonlinear function considered to be Lipschitz in its first argument) and that

the number of sensors should be at least equal to or greater than the number of unknown inputs plus the number of nonlinear terms that do not satisfy the Lipschitz conditions.

Numerous attempts have been made by the researchers to employ the Kalman filter theory for simultaneous input and state estimation. Among them [LIU *et al.* 2000; MA and LIN 2000; MA *et al.* 2003; MA and HO 2004] have adopted the earlier work of [TUAN *et al.* 1996], who used the Kalman filter together with a recursive least squares algorithm, for the load estimation in both linear and nonlinear systems. The Kalman filter has been used initially to generate the residual innovation sequence by observation vector. Then a recursive least-squares algorithm computes the onset time histories of the excitation forces by utilizing the residual innovation sequence. [DENG and HEH 2006] used the same approach for reconstruction of the loads distributed along the beam structure. In the recent work [PAN *et al.* 2010] has proposed to use the Kalman Filter with Unknown Inputs (KF-UI) for the estimation of the joint inputs and states. For this purpose Pan first combined the states and unknown inputs into an extended state vector. Then the weighted least squares problem has been solved for the extended state vector recursively. In comparison to other authors, who used always either displacement or velocity as measurement quantities, Pan's approach utilizes the more general measurement equation, which allows the usage of accelerometer sensors in estimation procedure.

1.2 THESIS OBJECTIVES AND OUTLINE

First of all, this work provides a closer investigation of a variety of existing algorithms of force history reconstruction and location estimation which have been established by mechanical engineers, a determination of their respective advantages and merits in solving the inverse problem by comparing simulated and experimental results. Secondly, research is carried out for possible candidate methods among the other engineering disciplines that could be applied to overcome the ill-posedness of force history estimation and allow online load reconstruction. The main focus of the thesis is concentrated on comprehensive design analysis and further development of the qualified algorithms. In particular, model based robust observers are considered as candidates for the online loads and states reconstruction. The aspects of proper model building that allow releasing the sensor placement procedure (from collocated to non-collocated), while simultaneously reducing the model complexity are introduced for the observer design. An innovative model free passive technique for automatic impact location detection is elaborated and extended by incorporation of a fast robust load estimation method. In addition, a novel approach of rank deficiency compensation is proposed for the direct time deconvolution procedure in the non-collocated case.

In most of the cases the load reconstruction algorithms consider the mechanical system as known beforehand. Therefore, Chapter 2 starts with essential fundamentals of linear time invariant model representations. In particular mechanical systems are shortly presented in nodal and modal coordinates either in continuous or discrete time as well as transfer functions or as state space models. Model construction issues are completed by system identification and modal analysis approaches that are possible alternatives for the model building. Some aspects of nonlinear systems such as stability and linearization are also considered. To cover the knowledge of the observer construction which is used later for the online load reconstruction, the estimation theory is presented. Inverse problems together with associated solving recipes are concluding Chapter 2.

For the sake of clarity the load classification is done in Chapter 3, where the general possible loads are divided into three main categories:

1. impact loads
2. time continuous loads
3. spatially distributed loads.

The estimation of the impact loads is then considered in a very detailed way in Chapter 4. The general estimation procedure is broken down into two parts. The first one deals solely with impact detection and impact location computation based on the wave propagation theory. Automatic picking algorithms which are able to extract the time of signal arrival are revealed together with necessary signal processing tools like continuous wavelet transformation and signal windowing. After the localization procedure, a second step of impact load history reconstruction is presented. Here two possible candidates are taken under closer look. In particular, the direct time deconvolution method and the tracking filter algorithm are presented in a detailed way.

Chapter 5 deals solely with the observer based algorithms, especially the SS&IE is treated in a very comprehensive way. Special aspects of the SS&IE matrices calculation are shown in section 5.1. In addition, gained knowledge from Chapter 2, of system transformation from nodal to modal coordinates which allowed releasing collocation condition is discussed. In sections 5.2 and 5.3 the MPIO and KF-UI are examined for the load history estimation task. Finally, conclusions are drawn with respect to the strong and weak sides of the above algorithms in section 5.4.

Numerical studies and application examples are carried out in Chapter 6. Beginning with the impact load estimation on the aluminum plate in section 6.1, where the direct time deconvolu-

tion method is compared with a tracking algorithm. It continues with a simple two storey test rig in section 6.2. The two storey test rig serves as a basis for the continuous time load estimation performance evaluation of SS&IE, MPIO and KF-UI. In section 6.3 a scrupulous numeric analysis of the SS&IE is done with respect to the system variation and the noise robustness with the help of continuously distributed structures. In addition the non-collocation of the sensor and load position is investigated in a systematic way. Numerical studies are concluded by load estimation on real structures like a simply supported beam, tripod laboratory tower and the wind energy plant M-5000. Afterwards the SS&IE ability of load estimation on nonlinear system is attested in section 6.5.

The thesis results are combined in the summary and discussion in Chapter 7. Here the nuances of every specific load estimation algorithm are signified in a form of their strong and weak sides together with the necessary conditions which should be hold to enable the specific algorithm to fulfill its work. Finally a short outlook gives a potential direction for future researches in the field of load estimation in the SHM and structural design.

2 THEORETICAL FOUNDATIONS

The best model of a cat is another, or

preferably the same, cat.

-Arturo Rosenblueth with Norbert Wiener

2.1 MODELING OF MECHANICAL SYSTEMS

The modeling of real world structures is an essential step towards a better understanding of their physical properties. In most instances, mechanical structures are considered as dynamical systems which can be described with the help of analytical models based on either physical laws, such as Newton's motion law, Lagrange's equations of motion, or D'Alembert's principle [GAWRONSKI 2004]; from Finite-Element Models (FEM); or from test data using System Identification (SI) methods. Such models are represented either in the time domain (differential or difference equations), or in the frequency domain in terms of Transfer Functions (TF). For the purpose of estimating external loads, the existence of an appropriate model is a mandatory condition. Therefore, different model types are considered in the following subsections.

2.1.1 General Linear Time Invariant Systems

NODAL MODELS

A linear system follows the superposition principle, which states that a linear combination of inputs produces an output that is the linear combination of the outputs if the outputs of each input term were applied separately. Linear structural models are represented in time domain, in the form of second-order differential equations or in the form of first-order differential equations (as a state space representation). In the former case, the degrees of freedom of a structure that are usually associated to the discrete masses or nodes are typically used to describe the structural dynamics as follows:

$$M_n \ddot{q}(t) + D_n \dot{q}(t) + K_n q(t) = B_o u(t)$$
$$y(t) = C_{oa} \ddot{q}(t) + C_{ov} \dot{q}(t) + C_{oq} q(t) \quad . \tag{2.1}$$

The above equation represents a nodal structural model (with first dynamic and second output equations) which is derived in nodal coordinates in terms of displacement $q(t)$, velocity $\dot{q}(t)$ and acceleration $\ddot{q}(t)$ vectors in real space R^{n_d} and characterized by the mass matrix M_n,

stiffness matrix $\boldsymbol{K}_n$ and damping matrix $\boldsymbol{D}_n$ of dimensions $n_d \times n_d$; $\boldsymbol{u}(t) \in R^m$ is an input vector together with the input placement matrix $\boldsymbol{B}_o$ of dimensions $(n_d \times m)$; $\boldsymbol{y}(t) \in R^r$ is an output vector and the output displacement $\boldsymbol{C}_{oq}$, velocity $\boldsymbol{C}_{ov}$ and acceleration $\boldsymbol{C}_{oa}$ are matrices of size $r \times n_d$.

MODAL MODELS

The nodal model representation may become impractical for dynamic analysis of complex structures (with many degrees of freedom) which are obtained from FEM or an SI procedure, while the modal representation is a natural outcome of the SI test or Modal Analysis (MA) technique. For these cases the modal models are often used to reduce the order of the system under consideration and to make use of the modes independence properties. The modal models can be obtained from the nodal models by a coordinate transformation as follows [GAWRONSKI 2004]:

$$q(t) = \boldsymbol{\Phi} q_m(t), \tag{2.2}$$

here, $\boldsymbol{\Phi}$ is a transformation matrix with appropriate dimensions. The role of the transformation matrix in this case is a projection from nodal to modal coordinates which is done with the help of the mode shape matrix $\boldsymbol{\Phi}$ and $q_m \in R^{n_m}$, where usually $n_m \leq n_d$. In its turn $\boldsymbol{\Phi}$ is calculated by solving the eigenvalue problem for the first part of Equation (2.1) by assuming free vibration $\boldsymbol{u}(t) = 0$ and setting $\boldsymbol{D}_n = 0$:

$$(\boldsymbol{K}_n - \omega^2 \boldsymbol{M}_n)\varphi = 0 \tag{2.3}$$

this is a set of homogeneous equations with variable ω which have a nontrivial solution if:

$$\det(\boldsymbol{K}_n - \omega^2 \boldsymbol{M}_n) = 0. \tag{2.4}$$

The above equation is satisfied for the number n_d of circular frequencies ω_i with $i = 1, ..., n_d$. By substituting ω_i into Equation (2.3) the corresponding mode vector φ_i is calculated. These results are combined into a matrix of natural circular frequencies $\boldsymbol{\Omega}$ and modal matrix $\boldsymbol{\Phi}$, as follows:

$$\boldsymbol{\Omega} = \begin{bmatrix} \omega_1 & 0 & 0 \\ 0 & \ddots & 0 \\ 0 & 0 & \omega_{n_d} \end{bmatrix}, \qquad \boldsymbol{\Phi} = \begin{bmatrix} \varphi_1 & \cdots & \varphi_{n_d} \end{bmatrix}. \tag{2.5}$$

Inserting the modal coordinates from Equation (2.2) into Equation (2.1) and left-multiplying by $\boldsymbol{\Phi}^T$ leads to a new form:

$$\boldsymbol{\Phi}^T M_n \boldsymbol{\Phi} \ddot{q}_m(t) + \boldsymbol{\Phi}^T D_n \boldsymbol{\Phi} \dot{q}_m(t) + \boldsymbol{\Phi}^T K_n \boldsymbol{\Phi} q_m(t) = \boldsymbol{\Phi}^T B_o u(t)$$
$$y(t) = C_{oa} \boldsymbol{\Phi} \ddot{q}_m(t) + C_{ov} \boldsymbol{\Phi} \dot{q}_m(t) + C_{oq} \boldsymbol{\Phi} q_m(t)$$
$$\tag{2.6}$$

Pre and post multiplication by modal matrix diagonalizes the nodal mass, damping (damping is assumed to be proportional) and stiffness matrices so that the new modal matrices are:

$$M_m = \boldsymbol{\Phi}^T M_n \boldsymbol{\Phi}, \quad D_m = \boldsymbol{\Phi}^T D_n \boldsymbol{\Phi} \text{ and } K_m = \boldsymbol{\Phi}^T K_n \boldsymbol{\Phi}. \tag{2.7}$$

Substituting the modal matrices into Equation (2.6) and dividing by M_m lead to a final *modal* model representation:

$$\ddot{q}_m(t) + 2Z\Omega \dot{q}_m(t) + \Omega^2 q_m(t) = B_m u(t)$$
$$y(t) = C_{ma} \ddot{q}_m(t) + C_{mv} \dot{q}_m(t) + C_{mq} q_m(t)$$
$$\tag{2.8}$$

where, $\Omega^2 = M_m^{-1} K_m$ is a diagonal matrix of circular natural frequencies as before, Z is a diagonal matrix of modal damping ratio $Z = 0.5 M_m^{-1} D_m \Omega^{-1}$ and $B_m = M_m^{-1} \boldsymbol{\Phi}^T B_o$ is the modal input matrix. Output matrices are combined into more compact forms C_{ma}, C_{mv} and C_{mq} that represent modal accelerations, velocities and displacement output matrices, respectively.

The most important result from modal transformation is a complexity reduction of the initial system by proper dimensioning of the modal matrix. In this step only the modes that are of interest are taken for the modal model building.

2.1.2 State Space Representation of Continuous-Time Systems

Beyond the second order differential equations that describe mechanical systems and traditionally used by structural engineers, other representations such as state space or transfer functions are available. State space notation has its origin in the area of control engineering and is extremely useful for several reasons, including the reduction of nth order linear Ordinary Differential Equations (ODEs) to n first-order ODEs. Matrix analysis tools can easily be used and provide a conventional representation for Multi-Input-Multi-Output (MIMO) systems. The state space form represents the mechanical structure as a system of first order differential equations which are combined into special general form:

$$\dot{x}(t) = Ax(t) + Bu(t) + E_n w(t)$$
$$y(t) = Cx(t) + Du(t) + F_n v(t) \quad ,$$

(2.9)

where, $x(t) \in R^n$, $u(t) \in R^m$ and $y(t) \in R^r$ are state, input and output vectors, respectively. Matrices A, B, C, D, E_n and F_n (also known as a *realization* when associated to a particular system) are real, constant, and of appropriate dimensions. Vectors $w(t)$ and $v(t)$ represent process and measurement noise. Equation (2.9) can be obtained directly from Equations (2.1) or (2.8) by letting $x(t) = \begin{bmatrix} q & \dot{q} \end{bmatrix}^T$ and rearranging the matrices as follows:

$$A = \begin{bmatrix} 0 & I \\ -\Omega^2 & -2Z\Omega \end{bmatrix}, \ B = \begin{bmatrix} 0 \\ B_m \end{bmatrix}.$$

(2.10)

The output matrix C and direct feed-through matrix D are constructed to satisfy the output equation in Equation (2.9) according to the measurements that are acquired. An important aspect of the state space realization is that it is not unique to a specific structure and can be changed into a different *realization* by the transformation technique.

2.1.3   Transfer Function Representation of Continuous-Time Systems

The system in Equation (2.9) can also be represented in TF form by taking its Laplace transformation [LePage 1961], assuming the absence of process and measurement noise together with zero initial conditions:

$$sX(s) = AX(s) + BU(s)$$
$$Y(s) = CX(s) + DU(s) \quad ,$$

(2.11)

here s is the Laplace variable. Solving the dynamic equation for $X(s)$ and substituting the resulting expression into the output equation yields the input-output relation in the frequency domain:

$$Y(s) = H(s)U(s) \quad \text{with} \quad H(s) = C(sI - A)^{-1} B + D.$$

(2.12)

The TF $H(s)$ defines the dynamical behavior of the structure and is a very useful representation. It establishes the direct inter-dependencies among the physical properties of mechanical structures when it is obtained directly from the second order system of Equation (2.8) with $s = j\omega$ (where $j^2 = -1$):

$$H(\omega) = \left(C_{mq} + j\omega C_{mv} - \omega^2 C_{ma} \right) \left(\Omega^2 + 2j\omega Z\Omega - \omega^2 I \right)^{-1} B_m.$$

(2.13)

Since the matrices $\boldsymbol{Z}$ and $\boldsymbol{\Omega}$ are diagonal, the above expression can be decoupled for the ith mode:

$$H_{mi}(\omega) = \frac{\left(c_{mqi} + j\omega c_{mvi} - \omega^2 c_{mai}\right)b_{mi}}{\left(\omega_i^2 - \omega^2 + 2j\xi_i\omega_i\omega\right)}, \tag{2.14}$$

where, $H_{mi}(\omega)$ is a mode specific transfer function, ξ_i together with ω_i represents the damping ratio and the circular natural frequency for the ith mode, and c_{mqi}, c_{mvi} and c_{mai} are the ith rows of the position, velocity and acceleration matrices respectively. So that the overall structural TF is established as a sum of individual n modes TF accordingly:

$$H(\omega) = \sum_{i=1}^{n} H_{mi}(\omega) = \sum_{i=1}^{n} \frac{\left(c_{mqi} + j\omega c_{mvi} - \omega^2 c_{mai}\right)b_{mi}}{\left(\omega_i^2 - \omega^2 + 2j\xi_i\omega_i\omega\right)}. \tag{2.15}$$

At the ith resonant frequency the structural TF in Equation (2.15) is approximately equal to the ith modal TF at that frequency:

$$H(\omega_i) \cong H_{mi}(\omega_i) = \frac{\left(-jc_{mqi} + \omega_i c_{mvi} + j\omega_i^2 c_{mai}\right)b_{mi}}{2\xi_i\omega_i^2}. \tag{2.16}$$

The poles of the TF are the roots of the denominator of Equation (2.13) which is referred to as characteristic equation. For each resonant frequency with a small damping which is normally the case for typical mechanical structures, the poles appear as complex conjugate pairs:

$$\lambda_{i(1/2)} = -\xi_i\omega_i \pm j\omega_i\sqrt{1-\xi_i^2}. \tag{2.17}$$

The same results can be obtained by solving the characteristic Equation (2.12). Figure 2.1 represents the relation of the poles locations to natural frequencies and damping ratio.
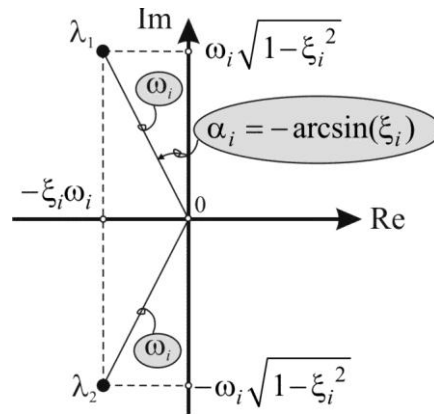
Figure 2.1: Pole location of the ith mode of a lightly damped structure. The radius is equal to the ith natural frequency; the real part is proportional to the ith modal damping and the imaginary part is equal to the damped natural frequency [GAWRONSKI 2004]

2.1.4 Solution for Forced Linear Dynamical Systems

For the calculation of the system responses in the time or frequency domain, a general solution of linear state equations (2.9) or (2.11) is necessary. The general solution of inhomogeneous first order linear vector equations is found by multiplying equations (2.9) with e^{-At} and simultaneously neglecting the process and measurement noise [CRASSIDIS and JUNKINS 2004]:

$$e^{-At}\left(\dot{x}(t) - Ax(t) \right) = \frac{d}{dt}\left(e^{-At}x(t) \right) = e^{-At}Bu(t) \tag{2.18}$$

integrating both sides over the time interval $[t_0, t]$:

$$e^{-At}x(t) - e^{-At_0}x(t_0) = \int_{t_0}^{t} e^{-A\tau}Bu(\tau)d\tau \tag{2.19}$$

and solving it finally for $x(t)$ leads to the final form:

$$x(t) = \underbrace{e^{A(t-t_0)}}_{\Phi_T(t)} x(t_0) + \int_{t_0}^{t} e^{A(t-\tau)}Bu(\tau)d\tau \,. \tag{2.20}$$

The first part of the solution in the Equation (2.20) is the solution of the homogenous part which "maps" the initial states into the current states with the help of the transition matrix $\Phi_T(t) = e^{A(t-t_0)}$, whereas the second part is a particular solution of the inhomogeneous ODE. The solution for the noise free output $y(t)$ in Equation (2.9) is obtained by substitution of

Equation (2.20) and taking into account zero initial conditions $x(t_0)=0$ (making use of the Dirac-Impulse function $\delta(t)$ for integral transformation):

$$y(t) = \int_{t_0}^{t} Ce^{A(t-\tau)} Bu(\tau)\,d\tau + Du(\tau) = \int_{t_0}^{t} \left[Ce^{A(t-\tau)}B + D\delta(t-\tau) \right] u(\tau)\,d\tau . \qquad (2.21)$$

The constant matrices in the Equation (2.21) are combined into impulse response function $H(t-\tau)$:

$$H(t-\tau) = Ce^{A(t-\tau)}B + D\delta(t-\tau), \qquad (2.22)$$

so that Equation (2.21) has a form analog to the convolution integral in Equation (1.1)

$$y(t) = \int_{t_0}^{t} H(t-\tau)u(\tau)\,d\tau . \qquad (2.23)$$

The convolution integral in Equation (2.23) is known as the Volterra integral equation of the first kind which is commonly used for input-output description of dynamical systems.

2.1.5 Discrete-Time Systems

Discrete-time systems became standards in most dynamical applications with the advent of digital computers which are used to process sampled-data systems for estimation and control. The discretization procedure takes place in the analog to digital converter (A/D) where different discretization schemes can be applied. The most common mathematical model for A/D conversion is the "zero-order-hold" model. This model describes the effect of converting a continuous-time signal to a discrete-time one by holding each sample value for one sample interval, see Figure 2.2.
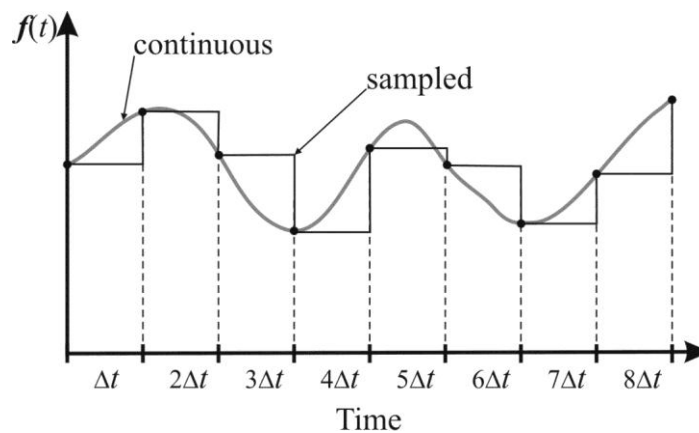
Figure 2.2: Continuous signal and sampled zero-order-hold signal

By using the zero-order-hold model, Equation (2.20) is transformed into a discrete dynamical system for the first sample interval [CRASSIDIS and JUNKINS 2004] as:

$$x(\Delta t) = e^{A\Delta t} x(0) + \left[\int_0^{\Delta t} e^{A(\Delta t - \tau)} d\tau \right] Bu(0) . \tag{2.24}$$

Defining a new variable $\kappa = \Delta t - \tau$ transforms the integral on the right-hand side to:

$$\int_0^{\Delta t} e^{A(\Delta t - \tau)} d\tau = -\int_{\Delta t}^0 e^{A\kappa} d\kappa = \int_0^{\Delta t} e^{A\kappa} d\kappa . \tag{2.25}$$

Therefore, Equation (2.24) becomes:

$$x(\Delta t) = A_D x(0) + B_D u(0) , \tag{2.26}$$

where subscript $(\cdot)_D$ denotes discrete matrices A_D and B_D, which are computed accordingly [CRASSIDIS and JUNKINS 2004]:

$$A_D = e^{A\Delta t} \quad \text{and} \quad B_D = \left[\int_0^{\Delta t} e^{At} dt \right] B . \tag{2.27}$$

Expansion in time for $k+1$ samples yields:

$$x((k+1)\Delta t) = A_D x(k\Delta t) + B_D u(k\Delta t) , \tag{2.28}$$

which is rewritten in a more common way, by dropping the Δt out and joining the discrete output equation:

$$\begin{aligned} x_{k+1} &= A_D x_k + B_D u_k \\ y_k &= C_D x_k + D_D u_k \end{aligned} . \tag{2.29}$$

The matrices $C_D = C$ and $D_D = D$ in the output equation are unaffected by the conversion to discrete-time domain. Analytical computation of the A_D and B_D might be a difficult process for a system of large order. Fortunately a numerical approach which involves series expansion can be used to get these matrices in accurate manner [CRASSIDIS and JUNKINS 2004]:

$$A_D = \sum_{k=0}^{\infty} \frac{A^k \Delta t^k}{k!} \quad \text{and} \quad B_D = \sum_{k=1}^{\infty} \frac{B^{k-1} \Delta t^k}{k!} . \tag{2.30}$$

The main difference in the analysis of a discrete-time versus continuous-time systems rests in the sampling interval. Its influence can also be noticed on the poles locations of the A_D (see Figure 2.3) which are different from the continuous-time system. The sampling interval can affect the system response as well as its stability as can be observed in Figure 2.3.
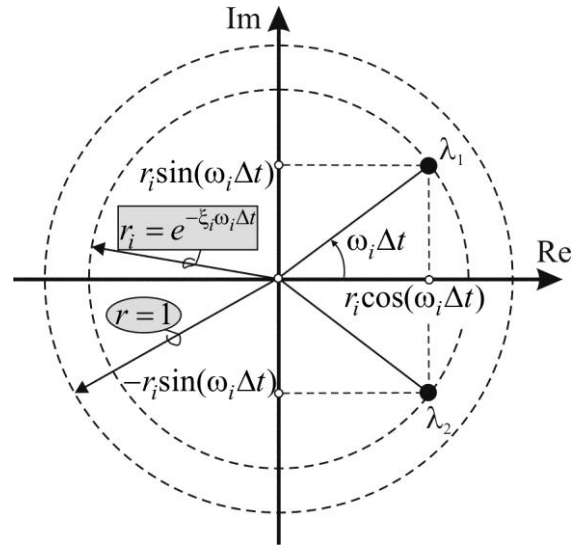
Figure 2.3: Pole location of the ith mode of a lightly damped structure in discrete time [GAWRONSKI 2004]

For a stable system the poles should be inside the unit circle, therefore the Nyquist criterion is often used to ensure proper choice of the sampling time. According to the Nyquist-Shannon sampling theorem the ith natural frequency is recovered if the sampling rate is at least twice the natural frequency in Hz $(f_i = \omega_i / 2\pi)$, *i.e.* if

$$\frac{1}{\Delta t} \geq 2f_i \quad \text{or, if} \quad \Delta t \leq \frac{\pi}{\omega_i} \ . \tag{2.31}$$

Corollary, for all modes considered it should satisfy following condition:

$$\Delta t \leq \frac{\pi}{\max_i(\omega_i)} \ . \tag{2.32}$$

2.1.6 System Identification or Model Construction

System Identification (SI) is the art and science of building mathematical models of dynamic systems from observed input-output or solely output data. Several methodologies and nomenclatures have been developed in different application areas. The SI term originated in the control engineering field, but similar techniques are found in structural engineering, statistics, econometrics, time series analysis, machine learning, data mining, artificial neural networks and fitting of ODE's coefficients [LJUNG 2008]. In general, the SI procedure can be organized into a block diagram as in Figure 2.4.
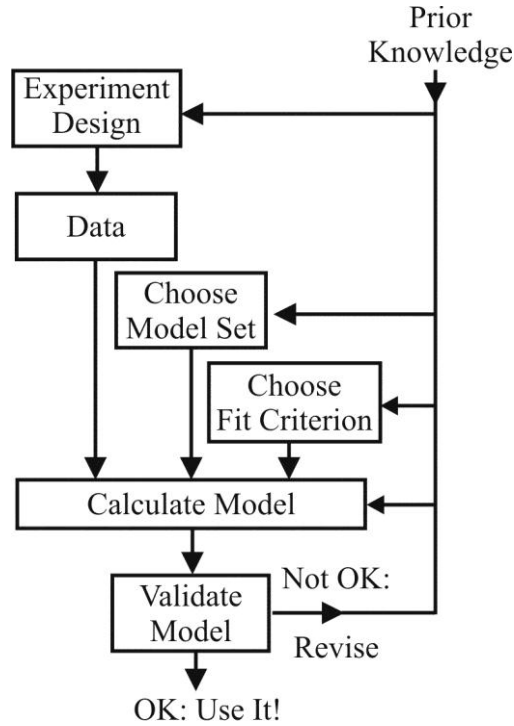
Figure 2.4: The system identification loop[LJUNG 1999]

In structural engineering SI methods that have been tested in practical applications are used. Among them are the Stochastic Subspace Identification (SSI) method [VAN OVERSCHEE and DE MOOR 1996; PEETERS and DE ROECK 1999; PEETERS and DE ROECK 2001]; Eigensystem Realization Algorithm (ERA) [JUANG and PAPPA 1985]; and output only system identification SSI based or with Vector-Autoregressive (VAR) models [KRAEMER and FRITZEN 2010]. All of these techniques attempt to identify the minimum system realization ($\hat{A}_D$, $\hat{B}_D$, $\hat{C}_D$ and $\hat{D}_D$) of discrete systems in Equation (2.29). Both SSI and ERA are based on the construction of the block Hankel matrices $\bar{H}_0$ and $\bar{H}_1$ which, are constructed from the Markov parameters H_i:

$$y_k = \sum_{i=0}^{k} H_i u_{k-i} \quad \text{with} \quad H_0 = D_D, \; H_i = C_D A_D^{\,i-1} B_D \,. \tag{2.33}$$

Thus,

$$\bar{H}_0 = \begin{bmatrix} H_1 & H_2 & \cdots & H_k \\ H_2 & H_3 & \cdots & H_{k+1} \\ \vdots & \vdots & \ddots & \vdots \\ H_k & H_{k+1} & \cdots & H_{2k-1} \end{bmatrix} \quad \text{and} \quad \bar{H}_1 = \begin{bmatrix} H_2 & H_3 & \cdots & H_{k+1} \\ H_3 & H_4 & \cdots & H_{k+2} \\ \vdots & \vdots & \ddots & \vdots \\ H_{k+1} & H_{k+2} & \cdots & H_{2k} \end{bmatrix}. \tag{2.34}$$

Conversely, if the number of samples is greater than the system order *i.e.* $k \gg n$, then the above matrices can be obtained as products of the controllability $\boldsymbol{C}_k$ and observability $\boldsymbol{O}_k$ matrices as follows:

$$\bar{\boldsymbol{H}}_0 = \boldsymbol{O}_k \boldsymbol{C}_k \qquad \text{and} \qquad \bar{\boldsymbol{H}}_1 = \boldsymbol{O}_k \boldsymbol{A}_D \boldsymbol{C}_k, \tag{2.35}$$

where:

$$\boldsymbol{O}_k = \begin{bmatrix} \boldsymbol{C}_D^T & \boldsymbol{A}_D^T \boldsymbol{C}_D^T & \cdots & (\boldsymbol{A}_D^T)^{k-1} \boldsymbol{C}_D^T \end{bmatrix}^T \text{ and } \boldsymbol{C}_k = \begin{bmatrix} \boldsymbol{B}_D & \boldsymbol{A}_D \boldsymbol{B}_D & \cdots & \boldsymbol{A}_D^{k-1} \boldsymbol{B}_D \end{bmatrix}. \tag{2.36}$$

Identification can then be carried out with the help of the decomposition of Hankel matrix $\bar{\boldsymbol{H}}_0$ so that it has an appearance similar to that of Equation (2.35). This is done with the help of Singular Value Decompositions (SVD):

$$\bar{\boldsymbol{H}}_0 = \boldsymbol{V} \boldsymbol{\Gamma}^2 \boldsymbol{U}^T, \tag{2.37}$$

where $\hat{\boldsymbol{O}}_k = \boldsymbol{V} \boldsymbol{\Gamma}$ and $\hat{\boldsymbol{C}}_k = \boldsymbol{\Gamma} \boldsymbol{U}^T$ are the estimated observability and controllability matrices. The matrix $\boldsymbol{\Gamma}$ consists of the Singular Values (SV) and can be used for order determination by the truncation of the small SV's and appropriate dimensioning of matrices $\boldsymbol{V}$ and $\boldsymbol{U}$. Next, a realization ($\hat{\boldsymbol{A}}_D$, $\hat{\boldsymbol{B}}_D$, $\hat{\boldsymbol{C}}_D$) can be calculated from Equation (2.35) and (2.37):

$$\hat{\boldsymbol{A}}_D = \hat{\boldsymbol{O}}_k^+ \bar{\boldsymbol{H}}_1 \hat{\boldsymbol{C}}_k^+ = \boldsymbol{\Gamma}^{-1} \boldsymbol{V}^T \bar{\boldsymbol{H}}_1 \boldsymbol{U} \boldsymbol{\Gamma}^{-1}, \tag{2.38}$$

here '+' represents the pseudo inverse *i.e.*: $\hat{\boldsymbol{O}}_k^+ = (\hat{\boldsymbol{O}}_k^T \hat{\boldsymbol{O}}_k)^{-1} \hat{\boldsymbol{O}}_k^T$ and $\hat{\boldsymbol{C}}_k^+ = \hat{\boldsymbol{C}}_k^T (\hat{\boldsymbol{C}}_k \hat{\boldsymbol{C}}_k^T)^{-1}$. The matrices $\hat{\boldsymbol{B}}_D$ and $\hat{\boldsymbol{C}}_D$ are easily found as the first m columns of $\hat{\boldsymbol{C}}_k$ and the first r rows of $\hat{\boldsymbol{O}}_k$:

$$\begin{aligned} \hat{\boldsymbol{B}}_D &= \hat{\boldsymbol{C}}_k \boldsymbol{E}_m, \qquad \text{where} \qquad \boldsymbol{E}_m = \begin{bmatrix} \boldsymbol{I}_m & 0 \end{bmatrix}^T \\ \hat{\boldsymbol{C}}_D &= \boldsymbol{E}_r^T \hat{\boldsymbol{O}}_k, \qquad \text{where} \qquad \boldsymbol{E}_r = \begin{bmatrix} \boldsymbol{I}_r & 0 \end{bmatrix}^T \end{aligned} \tag{2.39}$$

The main difference between SSI and ERA lays in the construction of the block Hankel matrices. For the ERA algorithm both the input and output data are needed to extract the (k+1) Markov parameters which are collected into a Markov matrix as follows:

$$\boldsymbol{H}_{Markov} = \begin{bmatrix} \boldsymbol{D}_D & \boldsymbol{C}_D \boldsymbol{B}_D & \boldsymbol{C}_D \boldsymbol{A}_D \boldsymbol{B}_D & \cdots & \boldsymbol{C}_D \boldsymbol{A}_D^{k-1} \boldsymbol{B}_D \end{bmatrix}, \tag{2.40}$$

for the construction of the Hankel matrix. The input and output are combined into respective input measurement and output measurement matrices:

$$Y = \begin{bmatrix} y_0 & y_1 & y_2 & \cdots & y_q \end{bmatrix} \text{ and } U = \begin{bmatrix} u_0 & u_1 & u_2 & \cdots & u_k \dots u_q \\ 0 & u_0 & u_1 & \cdots & u_{k-1} \dots u_{q-1} \\ 0 & 0 & u_0 & \cdots & u_{k-2} \dots u_{q-2} \\ \cdots & \cdots & \cdots & \cdots & \cdots \dots \cdots \\ 0 & 0 & 0 & \cdots & u_0 \dots u_{q-k} \end{bmatrix} \qquad (2.41)$$

where, $q \geq k$ so that the input output relationship in Equation (2.33) is represented as $Y = H_{Markov}U$. The Markov parameters are calculated by least squares approximation if the input measurement matrix U has full column rank. For noisy measurements the Markov parameters are determined by using the averaging procedure thus,

$$\hat{H}_{Markov} = R_{yu}R_{uu}^+ \quad \text{with} \quad R_{yu} = \frac{1}{N}\sum_{i=1}^{N} Y_i U_i^T \quad \text{and} \quad R_{uu} = \frac{1}{N}\sum_{i=1}^{N} U_i U_i^T \qquad (2.42)$$

where R_{yu} and R_{uu} are the correlation and autocorrelation matrices between input/output, and input/input which are divided into N segments $i=1,2,\dots N$; the U_i and Y_i are the ith segments of the data records matrices U and Y respectively The estimated matrix $\hat{H}_{Markov}$ contains all the necessary Markov parameters for SI by ERA, Equation (2.34) to (2.39). In addition the ERA allows estimating the direct feed through matrix $\hat{D}_D$ as the first m columns of $\hat{H}_{Markov}$ matrix.

For the SSI method the input is considered to be white noise thus the Hankel matrices are composed from the outputs correlations only:

$$\bar{H}_{i-1,\alpha,\beta} = \begin{bmatrix} \hat{R}_i & \hat{R}_{i+1} & \cdots & \hat{R}_{i+\beta-1} \\ \hat{R}_{i+1} & \hat{R}_{i+2} & \cdots & \hat{R}_{i+\beta} \\ \vdots & \vdots & \ddots & \vdots \\ \hat{R}_{i+\alpha+1} & \cdots & \cdots & \hat{R}_{i+\alpha+\beta-2} \end{bmatrix}, \quad \text{with} \quad \hat{R}_i = \frac{1}{n_t-i-1}\sum_{k=1}^{n_t-i} y_{k+i} y_k^T \qquad (2.43)$$

here, n_t is the number of data points from one sensor that are recorded in one measurement period; and α, β define the number of time shifts in the block Hankel matrix.

The VAR method attempts to build the auto regressive models for the recorded measurements as for r-variate time series [KRAEMER and FRITZEN 2010]:

$$y_k = w + \sum_{l=1}^{p} A_l y_{k-l} + \varepsilon_k . \qquad (2.44)$$

The model error matrix ε consists of r averaged vectors (Gaussian data), with the covariance matrix $\hat{C}_{AR} = E\{\varepsilon \; \varepsilon^T\}$. The matrices $A_1, \ldots, A_p$ are the coefficient matrices of the AR model with order p and the vector w (dimension $r \times 1$) allows consideration of non-zero mean values of the time series. Proper arrangement of the AR coefficients can be used for the construction of ($\hat{A}_D$ and $\hat{C}_D$):

$$\hat{A}_D = \begin{bmatrix} A_1 & A_2 & \cdots & A_{p-1} & A_p \\ I & 0 & \cdots & 0 & 0 \\ \vdots & \vdots & \ddots & \vdots & \vdots \\ 0 & 0 & \cdots & I & 0 \end{bmatrix} \text{ and } \hat{C}_D = \begin{bmatrix} I & 0 & \cdots & 0 & 0 \end{bmatrix}. \tag{2.45}$$

If the dynamic properties of structures under vibrational excitation are needed then the eigensolution is found for the realized state space matrix $\hat{A}_D$:

$$\left(\hat{A}_D - \delta_i I\right)\psi_i = 0, \tag{2.46}$$

with the complex eigenvalues δ_i that are combined into a matrix $\Delta = diag(\delta_1, \delta_2, \ldots, \delta_n)$ and the eigenvectors ψ_i which are combined into matrix $\Psi = [\psi_1, \psi_2, \ldots, \psi_n]$ where n defines the identified system dimensions. The physical frequencies $\hat{\omega}_i$ and damping ratios $\hat{\xi}_i$ are identified by transformation into continuous time domain:

$$\hat{\lambda}_i = -\hat{\xi}_i \hat{\omega}_i \pm j \underbrace{\hat{\omega}_i \sqrt{1 - \hat{\xi}_i^2}}_{\hat{\omega}_{D_i}} = \frac{\ln(\delta_i)}{\Delta t}. \tag{2.47}$$

Thus,

$$\hat{f}_i = \frac{\hat{\omega}_{D_i}}{2\pi} = \frac{\text{Im}(\hat{\lambda}_i)}{2\pi} \text{ and } \hat{\xi}_i = \frac{-\text{Re}(\hat{\lambda}_i)}{|\hat{\lambda}_i|}. \tag{2.48}$$

Similarly, the matrix $\hat{\Phi} = \hat{C}_D \Psi$ is combining the mode shapes for the measurement locations.

2.1.7 Nonlinear Systems, Linearization and Stability

GENERAL NONLINEAR SYSTEM

Many real world structures exhibit a nonlinear behavior that makes their analysis very complicated. Among them are mechanical systems such as [MOON 1998]:

- Buckled structures under vibration

- Gear transition elements with backlash
- Systems with sliding dry friction
- Multilink systems, such as robots
- Fluid-structure or contact dynamics

A general nonlinear first order system has the following form:

$$\begin{aligned} \dot{x} &= f(x, u, t) \\ y &= h(x, u, t) \end{aligned} ,$$

(2.49)

where x, u and y are state, input and output vectors, respectively. Some nonlinear systems can be solved for an exact analytical solution. Unfortunately, there are no standardized methods existing for finding exact solutions and the search for an exact analytical solution requires elaborate mathematics. On the other hand, linearized models of non-linear structures serve well for specific applications especially when the reference motion may be known.

LINEARIZATION

The transformation from non-linear to linear system is done by a linearization procedure either by choosing a proper nominal trajectory or equilibrium point about which the linearization is carried out. The linearization procedure then starts by assuming that the actual quantities x, y and u in Equation (2.49) can be splitted into a reference or nominal x_N, y_N and u_N and small perturbations δx, δy and δu of states, inputs and outputs, respectively, as follows [CRASSIDIS and JUNKINS 2004]:

$$\begin{aligned} x(t) &= x_N(t) + \delta x(t) \\ u(t) &= u_N(t) + \delta u(t) \\ y(t) &= y_N(t) + \delta y(t) \end{aligned} .$$

(2.50)

The linearized dynamical model around a desired trajectory is then obtained by application of a Taylor series which is truncated after the linear part:

$$f(x_N + \delta x, u_N + \delta u, t) = f(x_N, u_N, t) + \nabla_x f(x_N, u_N, t)\delta x + \nabla_u f(x_N, u_N, t)\delta u ,$$ (2.51)

where, ∇ is the Jacobian operator so that the dynamic linear system for perturbations is:

$$\begin{aligned} \delta\dot{x}(t) &= \nabla_x f(x_N, u_N, t)\delta x + \nabla_u f(x_N, u_N, t)\delta u \\ \delta y(t) &= \nabla_x h(x_N, u_N, t)\delta x + \nabla_u h(x_N, u_N, t)\delta u \end{aligned} .$$

(2.52)

It is very essential to choose suitable nominal trajectories or equilibrium points for the linearization procedure and to analyze the effects of errors introduced by the linearization procedure.

Estimating the stability of the reconstruction process is a stringent requirement so that the estimated quantities remain in the bounded interval. Therefore stability analysis is an important matter to both linear and nonlinear systems, and can be commonly checked by Routh-Hurwitz stability criteria that are applicable to Linear Time Invariant systems (LTI's) or by Lyapunov's direct method, which in turn can be applied to both linear and nonlinear systems. Here only Lyapunov's direct or second method is considered due to its generality (it does not require the solution of differential equations, in contrast to Lyapunov's first method) [OGATA 1970]. This method yields a globally sufficient condition for asymptotic stability. Lyapunov's model is closely related to the energy of a system, which is a scalar function; the energy must be in general continuous and should have continuous derivatives with respect to all states. Lyapunov has shown that if the total energy of a system is dissipated, then its state is confined to a volume bounded by a surface of a constant energy, so that the system should eventually settle to an equilibrium point [CRASSIDIS and JUNKINS 2004]. The equilibrium state for the system:

$$\dot{x} = f(x,t) \tag{2.53}$$

is defined as $f(x_e,t)=0$ for all t. Representing the solution for Equation (2.53) as $\phi(t;x_0,t_0)$ where the $x=x_0$ at $t=t_0$ and t is the observed time, one obtains,

$$\phi(t_0;x_0,t) = x_0. \tag{2.54}$$

Then the stability in the sense of Lyapunov is denoted with the help of the spherical regions $S(\delta)$ and $S(\varepsilon)$ about the equilibrium state x_e as represented for the two dimensional case in Figure 2.5. The spherical regions consist of all points within the following distances from the equilibrium point, wherein the distances are expressed in the Euclidean metric:

$$\begin{aligned} \|x_0 - x_e\| &\le \delta, & \forall \delta \in S(\delta) \\ \|\phi(t;x_0,t_0) - x_e\| &\le \varepsilon, & \forall \varepsilon \in S(\varepsilon), \text{ for all } t \ge t_0 \end{aligned} \tag{2.55}$$

The equilibrium state is then said to be *asymptotically stable* if every solution starting at x_0 within the region $S(\delta)$ converges to x_e without leaving $S(\varepsilon)$ as t grows to infinity, where δ and ε are small values.
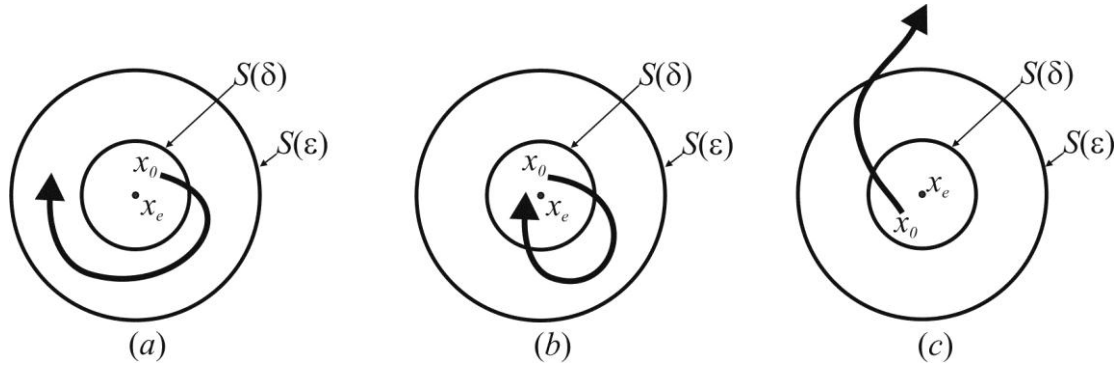
Figure 2.5: (a) Stable equilibrium state and respective trajectory; (b) asymptotically stable equilibrium state and respective trajectory; (c) unstable equilibrium state and respective trajectory [OGATA 1970]

This concept of Lyapunov stability is formulated mathematically for continuous systems as in Equation (2.53) with the help of a scalar *Lyapunov function* $V(x)$ for which the following conditions are held:

$$1.\, V(\boldsymbol{0}) = 0$$
$$2.\, V(\boldsymbol{x}) > 0 \text{ for } \boldsymbol{x} \neq 0 \tag{2.56}$$
$$3.\, \dot{V}(\boldsymbol{x}) < 0.$$

If the conditions in Equation (2.56) are satisfied then the dynamical system under consideration is said to be asymptotically stable. The simplest and most commonly used Lyapunov function is the quadratic form function which is constructed as:

$$V(\boldsymbol{x}) = \boldsymbol{x}^T \boldsymbol{P}_L \boldsymbol{x}, \tag{2.57}$$

where $\boldsymbol{P}_L$ is a positive definite symmetric matrix. Applying the quadratic Lyapunov function to the LTI system of form:

$$\dot{\boldsymbol{x}} = \boldsymbol{A}\boldsymbol{x}, \tag{2.58}$$

leads to the following time derivative of $V(\boldsymbol{x})$:

$$\dot{V}(\boldsymbol{x}) = \dot{\boldsymbol{x}}^T \boldsymbol{P}_L \boldsymbol{x} + \boldsymbol{x}^T \boldsymbol{P}_L \dot{\boldsymbol{x}} = \boldsymbol{x}^T (\boldsymbol{A}^T \boldsymbol{P}_L + \boldsymbol{P}_L \boldsymbol{A}) \boldsymbol{x}. \tag{2.59}$$

The stability of the system can now be found by solving a new equation of the form:

$$\boldsymbol{A}^T \boldsymbol{P}_L + \boldsymbol{P}_L \boldsymbol{A} = -\boldsymbol{Q}_L. \tag{2.60}$$

Hence if matrices Q_L and P_L are positive definite then the system will converge to its equilibrium state. In practice instead of first specifying a positive definite matrix P_L and examining whether or not Q_L is positive definite, it is convenient to specify matrix Q_L initially and then examine if an appropriate P_L can be found to satisfy Equation (2.60) [OGATA 1970]. In the case of a discrete system $x_{k+1} = f(x_k, \Delta t)$ the conditions for $V(x)$ in Equation (2.56) are modified as:

1. $V(0) = 0$
2. $V(x_k) > 0$ for $x_k \neq 0$ $\qquad\qquad\qquad\qquad\qquad$. $\qquad\qquad\qquad\qquad$ (2.61)
3. $\Delta V(x_k) = V(x_{k+1}) - V(x_k) < 0$

Then the matrix Lyapunov Equation (2.60) for a discrete system $x_{k+1} = A_D x_k$ is of the form:

$$A_D^T P_L A_D - P_L = -Q_L .$$

(2.62)

For the analysis of nonlinear systems the modified techniques that are based on Lyapunov's second method are used. Such techniques include Krasovskii's method for testing sufficient conditions for asymptotic stability, Schultz-Gibson's variable gradient method for generating Lyapunov functions [OGATA 1967].

2.2   OBSERVER THEORY

In the beginning of 60th David G. Luenberger initiated the theory of observers for the state reconstruction of linear dynamical systems. Since then, owing to its utility and intimate connection to fundamental system concepts, observer theory continued to be a fruitful area of research and has been substantially developed in many different directions [O'REILLY 1983]. The most important area of application is control engineering where observer theory has had its greatest impact among state-space control methods, such as pole-shifting, deadbeat control, and optimal linear regulator design. The problem of state observation centers on the construction of an auxiliary dynamic system, known as a state reconstructor/estimator or observer, driven by the available system inputs and outputs. A block diagram of the open loop system together with the state reconstruction process is presented in Figure 2.6. The observer is constructed on the basis of a mathematical model which mimics the real system.
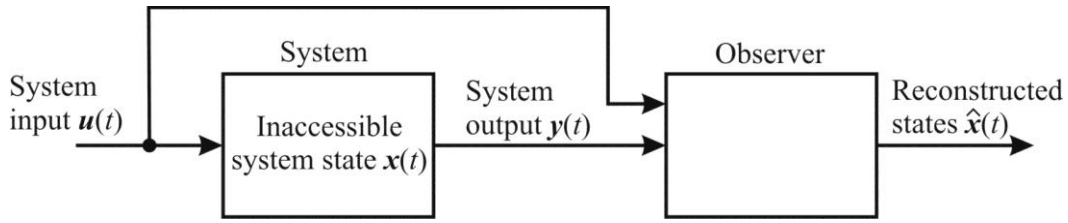
Figure 2.6: Open-loop system state reconstruction

A primary assumption for state reconstruction based on past measurements is the observability of the system otherwise it is not possible to construct an observer for the system.

2.2.1 System Observability

Taking a noise free linear state-space system of Chapter 2.1.2 into consideration:

$$\dot{x}(t) = A(t)x(t) + B(t)u(t), \quad x(t_0) = x_0 \tag{2.63}$$

$$y(t) = C(t)x(t), \tag{2.64}$$

where $x(t) \in R^n$ is the system state, $x(t_0) \in R^n$ is the state at initial time t_0, $u(t) \in R^m$ is the external input, and the output $y(t) \in R^r$ represents linear combinations of the state $x(t)$ available for measurement, the matrices $A(t)$, $B(t)$ and $C(t)$ are assumed to have compatible dimensions and to be continuous and bounded. The above system is said to be observable if the following theorems are valid [O'REILLY 1983]:

Theorem 2.1 *The linear system* (2.63)*,* (2.64) *or the pair* ($A(t), C(t)$) *is uniformly completely observable (uniformly completely state reconstructible) if and only if for some* $\sigma > 0$ *there exist positive constants* $\alpha_i, i = 1,2$ *such that:*

$$0 < \alpha_1 I \leq W_o(\tau, \tau + \sigma) \leq \alpha_2 I, \tag{2.65}$$

holds for all τ. The W_o matrix is the observability Gramian, defined as:

$$W_o(\tau, t) = \int_{\tau}^{t} \Phi_T^T(\sigma, \tau) C^T(\tau) C(\tau) \Phi_T(\sigma, \tau) d\sigma, \tag{2.66}$$

where the $\Phi_T(\sigma, \tau)$ is the transition matrix defined as in Chapter 2.1.4. As a corollary it is implied that the Gramian matrix W_o should be positive definite.

If the dynamical system (2.63), (2.64) is time invariant the observability can be easily checked by the following criteria [O'REILLY 1983]:

Theorem 2.2 *The linear time-invariant system* (2.63), (2.64) *or a pair* (A, C) *is completely observable if and only if:*

$$rank\ (\boldsymbol{O}) = rank\left(\left[\begin{array}{cccccc} \boldsymbol{C}^T & \boldsymbol{A}^T\boldsymbol{C}^T & \left((\boldsymbol{A})^T\right)^2 \boldsymbol{C}^T & \cdots & \left((\boldsymbol{A})^T\right)^{n-1}\boldsymbol{C}^T \end{array}\right]^T\right) = n \qquad (2.67)$$

The system in Equations (2.63), (2.64) does not take into consideration measurement noise and model uncertainty. The usage of observability Gramian is preferable in case when the systems are of higher orders e.g. $n=100$, due to its computational efficiency [GAWRONSKI 2004].

2.2.2 Classical Luenberger Observer

The Luenberger observer is often known as a full-order observer or estimator. It constructs the auxiliary observer system on the basis of a known model, with the assumption that the pair (A, C) of original realization (A, B and C) in Equations (2.63) and (2.64) is observable. The observer is mathematically formulated for the time-invariant original system as:

$$\dot{\hat{\boldsymbol{x}}}(t) = \boldsymbol{A}\hat{\boldsymbol{x}}(t) + \boldsymbol{B}\boldsymbol{u}(t) + \boldsymbol{K}_{obs}\left(\boldsymbol{y}(t) - \boldsymbol{C}\hat{\boldsymbol{x}}(t)\right) \qquad (2.68)$$

and coupled to the original system through the available inputs and outputs. The last term represents the mismatch between estimated and measured outputs. Constructing the state reconstruction error as:

$$\boldsymbol{e}(t) = \hat{\boldsymbol{x}}(t) - \boldsymbol{x}(t), \qquad (2.69)$$

implies that the error will converge asymptotically to zero accordingly

$$\dot{\boldsymbol{e}}(t) = \left(\boldsymbol{A} - \boldsymbol{K}_{obs}\boldsymbol{C}\right)\boldsymbol{e}(t). \qquad (2.70)$$

The matrix $\boldsymbol{K}_{obs}$ stabilizes the error dynamics by shifting the poles of $(\boldsymbol{A} - \boldsymbol{K}_{obs}\boldsymbol{C})$ to the left-hand complex plane.

2.2.3 Minimal Order Observer

It often makes sense to estimate only states that cannot be measured or in other words to design the *minimal-order observer* having a lower order (lower complexity) than the original system. Keeping in mind that the main objective is to reconstruct the system states $\boldsymbol{x}(t) \in R^n$, on the basis of r available outputs $\boldsymbol{y}(t) \in R^r$, which represent r linear combinations of the

states, it is advisable to construct a *minimal-order observer* where the dimension of the observer states is *n-r*.

Thus, given *r* linear state combinations in the outputs $y(t)$, the remaining *n-r* states combinations require to be reconstructed [O'REILLY 1983]:

$$z(t) = T(t)x(t), \quad z(t) \in R^{n-r}. \tag{2.71}$$

Combining equations (2.64) and (2.71):

$$\begin{bmatrix} y(t) \\ z(t) \end{bmatrix} = \begin{bmatrix} C(t) \\ T(t) \end{bmatrix} x(t) \Rightarrow x(t) = \begin{bmatrix} C(t) \\ T(t) \end{bmatrix}^{-1} \begin{bmatrix} y(t) \\ z(t) \end{bmatrix} = \begin{bmatrix} V(t) & P(t) \end{bmatrix} \begin{bmatrix} y(t) \\ z(t) \end{bmatrix} \tag{2.72}$$

where $T(t)$ is chosen so that it is invertible, and $V(t)$ and $P(t)$ are respective inverses of $C(t)$ and $T(t)$. In the case that the $z(t)$ exists, the original states can be directly reconstructed. However, $T(t)x(t)$ cannot be measured directly, so it should be estimated by means of the secondary dynamical system of order $n-r$

$$\dot{z}(t) = L(t)z(t) + E(t)y(t) + G(t)u(t) \tag{2.73}$$

$$\hat{x}(t) = P(t)z(t) + V(t)y(t) \tag{2.74}$$

here, Equation (2.73) represents the auxiliary dynamical system whereas Equation (2.74) is obtained from the Equation (2.72) simply combines the measured and estimated states to form a compete *n* dimensional state vector. The *observer reconstruction error* is

$$\varepsilon(t) = z(t) - T(t)x(t). \tag{2.75}$$

Taking the derivative of Equation (2.75) with respect to time and using Equations (2.63), (2.64) and (2.73) the error dynamics of the observer is

$$\begin{aligned} \dot{\varepsilon}(t) = L(t)\varepsilon(t) + \left(L(t)T(t) - T(t)A(t) + E(t)C(t) - \dot{T}(t) \right) x(t) \\ + \left(G(t) - T(t)B(t) \right) u(t) \end{aligned}, \tag{2.76}$$

which can be reduced to a homogeneous equation

$$\dot{\varepsilon}(t) = L(t)\varepsilon(t). \tag{2.77}$$

Providing that the following conditions are hold

    a. $L(t)T(t) - T(t)A(t) = \dot{T}(t) - E(t)C(t)$ (2.78)

    b. $G(t) = T(t)B(t)$ (2.79)

$$\text{c. } \begin{bmatrix} C(t) \\ T(t) \end{bmatrix}^{-1} = \begin{bmatrix} V(t) & P(t) \end{bmatrix} \text{ or } V(t)C(t) + P(t)T(t) = I_n .\tag{2.80}$$

Conditions (2.78), (2.79) and (2.80) are known as Luenberger observer constraint equations with parameter matrices $T(t)$, $L(t)$, $E(t)$, $T(t)$, $G(t)$ and $V(t)$. If such constraints are held, the observer error dynamics will diminish exponentially if the observer matrix $L(t)$ is chosen to be asymptotically stable. Finally, denoting the actual *state reconstruction error* by

$$e(t) = \hat{x}(t) - x(t) \tag{2.81}$$

and making use of Equations (2.74), (2.64) and (2.75) the state reconstruction error is turned into

$$e(t) = P(t)\varepsilon(t) + \left(P(t)T(t) + V(t)C(t) - I_n \right) x(t) \tag{2.82}$$

by invoking condition constraint Equation (2.80) the above equation is reduced to

$$e(t) = P(t)\varepsilon(t) . \tag{2.83}$$

Thus, the accuracy of the state reconstruction is a linear function of the observer states $z(t)$. In addition, referring to Equation and (2.80), the observer design parameters can be reduced by using

$$\begin{bmatrix} C(t) \\ T(t) \end{bmatrix} \begin{bmatrix} V(t) & P(t) \end{bmatrix} = \begin{bmatrix} C(t)V(t) & C(t)P(t) \\ T(t)V(t) & T(t)P(t) \end{bmatrix} = \begin{bmatrix} I_m & 0 \\ 0 & I_{n\text{-}m} \end{bmatrix} . \tag{2.84}$$

Post multiplying Equation (2.78) by $P(t)$ produces

$$L(t) = T(t)A(t)P(t) + \dot{T}(t)P(t) \tag{2.85}$$

while post multiplication of Equation (2.78) by $V(t)$ yields

$$E(t) = T(t)A(t)V(t) + \dot{T}(t)V(t) . \tag{2.86}$$

Equations (2.79), (2.85), (2.86) and the proper choice of the matrix $T(t)$ conclude the calculation of the observer design (*i.e.*, the calculation of matrices $L(t)$, $E(t)$, $T(t)$, $P(t)$ and $V(t)$) for the given dynamical system $A(t)$, $B(t)$ and $C(t)$.

Both, the full-order and the minimal-order observers suffer from measurement noise, which is incorporated into the measured quantities. It can be easily shown that the noise is present in the error dynamics and amplified by the observer gain matrix (*i.e.* for a full-order observer

and noisy outputs $\boldsymbol{y}(t) = \boldsymbol{C}\boldsymbol{x}(t) + \boldsymbol{v}(t)$ the error dynamics is: $\dot{\boldsymbol{e}}(t) = (\boldsymbol{A} - \boldsymbol{K}_{obs}\boldsymbol{C})\boldsymbol{e}(t) + \boldsymbol{K}_{obs}\boldsymbol{v}(t)$).
This drawback gave an impulse to search for alternatives. An outcome of this search was a new type of estimators: Recursive Least Square Estimator (RLSE) and the Kalman-Bucy filter with the inherited immunity against the noise corrupted signals [KALMAN and BUCY 1961].

2.2.4   Linear Sequential Estimator and Kalman-Bucy Filter

LINEAR SEQUENTIAL ESTIMATOR

The *Linear Sequential Estimator* (LSE) is a modification of Gauss's principle least squares algorithm which solves the traditional problem of parameter estimation $\hat{\boldsymbol{x}} \in R^n$ of the given equation [CRASSIDIS and JUNKINS 2004]:

$$\tilde{\boldsymbol{y}} = \boldsymbol{H}_S\hat{\boldsymbol{x}}, \tag{2.87}$$

where $\tilde{\boldsymbol{y}} \in R^r$ represents the measured values and $\boldsymbol{H}_S \in R^{r \times n}$ is a combination of the *basis functions* or a mathematical model of the process. Gauss proposed a choice of unknown parameters $\hat{\boldsymbol{x}}$ that minimize the weighted sum of the squared residual errors $\boldsymbol{e} = \tilde{\boldsymbol{y}} - \boldsymbol{H}_S\hat{\boldsymbol{x}}$, given by

$$J = \frac{1}{2}\boldsymbol{e}^T\boldsymbol{W}\boldsymbol{e} = \frac{1}{2}(\tilde{\boldsymbol{y}}^T\boldsymbol{W}\tilde{\boldsymbol{y}} - 2\tilde{\boldsymbol{y}}^T\boldsymbol{W}\boldsymbol{H}_S\hat{\boldsymbol{x}} + \hat{\boldsymbol{x}}^T\boldsymbol{H}_S^T\boldsymbol{W}\boldsymbol{H}_S\hat{\boldsymbol{x}}) \tag{2.88}$$

where $\boldsymbol{W}$ is a symmetric positive definite weight matrix. Using matrix calculus the global minimum of the quadratic function $\boldsymbol{J}$ has to fulfill the following conditions:
necessary condition:

$$\nabla_{\hat{\boldsymbol{x}}}\boldsymbol{J} = \boldsymbol{H}^T\boldsymbol{W}\boldsymbol{H}_S\hat{\boldsymbol{x}} - \boldsymbol{H}_S^T\boldsymbol{W}\,\tilde{\boldsymbol{y}} = 0 \tag{2.89}$$

sufficient condition:

$$\nabla_{\hat{\boldsymbol{x}}}^2\boldsymbol{J} = \boldsymbol{H}_S^T\boldsymbol{W}\boldsymbol{H}_S \geq 0 \;\; \text{must be positive definite}\,. \tag{2.90}$$

If the sufficient conditions are satisfied, $\boldsymbol{H}_S$ is required to have full column rank *i.e.* $rank(\boldsymbol{H}_S) = n$, and the explicit solution is obtained from the necessary condition (2.89):

$$\hat{\boldsymbol{x}} = (\boldsymbol{H}_S^T\boldsymbol{W}\boldsymbol{H}_S)^{-1}\boldsymbol{H}_S^T\boldsymbol{W}\,\tilde{\boldsymbol{y}}\,. \tag{2.91}$$

In its turn, the LSE attempts to use the knowledge of the previous estimations $\hat{\boldsymbol{x}}_k$ to estimate the current state $\hat{\boldsymbol{x}}_{k+1}$, which has a close relation to the general observer. If the current state is

estimated according to Equation (2.91) with the addition of the k letter to all involving matrices, then the current state estimated from both data sets is as follows:

$$\hat{x}_{k+1} = \left(\begin{bmatrix} H_{Sk} \\ H_{Sk+1} \end{bmatrix}^{T} \begin{bmatrix} W_k & 0 \\ 0 & W_{k+1} \end{bmatrix} \begin{bmatrix} H_{Sk} \\ H_{Sk+1} \end{bmatrix} \right)^{-1} \begin{bmatrix} H_{Sk} \\ H_{Sk+1} \end{bmatrix}^{T} \begin{bmatrix} W_k & 0 \\ 0 & W_{k+1} \end{bmatrix} \begin{bmatrix} \tilde{y}_k \\ \tilde{y}_{k+1} \end{bmatrix}. \tag{2.92}$$

Since the W is a block diagonal this expression can be represented in the form:

$$\hat{x}_{k+1} = (H_{Sk}^{T} W_k H_{Sk} + H_{Sk+1}^{T} W_{k+1} H_{Sk+1})^{-1}(H_{Sk}^{T} W_k \tilde{y}_k + H_{Sk+1}^{T} W_{k+1} \tilde{y}_{k+1}). \tag{2.93}$$

Defining new variables

$$\begin{aligned} &1.\ P_k = (H_{Sk}^{T} W_k H_{Sk})^{-1} && \Rightarrow && P_k^{-1} = H_{Sk}^{T} W_k H_{Sk} \\ &2.\ P_{k+1} = (H_{Sk}^{T} W_k H_{Sk} + H_{Sk+1}^{T} W_{k+1} H_{Sk+1})^{-1} && \Rightarrow && P_{k+1}^{-1} = P_k^{-1} + H_{Sk+1}^{T} W_{k+1} H_{Sk+1} \end{aligned} \tag{2.94}$$

and incorporating them into the Equations (2.93) and (2.91) the results are

$$1.\ \hat{x}_k = P_k H_{Sk}^{T} W_k \tilde{y}_k \quad \text{and} \quad 2.\ \hat{x}_{k+1} = P_{k+1}(H_{Sk}^{T} W_k \tilde{y}_k + H_{Sk+1}^{T} W_{k+1} \tilde{y}_{k+1}). \tag{2.95}$$

Pre-multiplying the first Equation in (2.95) by P_k^{-1} and using the relation:

$$P_k^{-1} = P_{k+1}^{-1} - H_{Sk+1}^{T} W_{k+1} H_{Sk+1} \tag{2.96}$$

which can be obtained by manipulating the second Equation (2.94), yielding

$$H_{Sk}^{T} W_k \tilde{y}_k = (P_{k+1}^{-1} - H_{Sk+1}^{T} W_{k+1} H_{Sk+1})\hat{x}_k. \tag{2.97}$$

Substituting Equation (2.97) into the second Equation in (2.95) leads to

$$\begin{aligned} \hat{x}_{k+1} &= \hat{x}_k + P_{k+1} H_{Sk+1}^{T} W_{k+1} \tilde{y}_{k+1} - P_{k+1} H_{Sk+1}^{T} W_{k+1} H_{Sk+1} \hat{x}_k \\ &= \hat{x}_k + P_{k+1} H_{Sk+1}^{T} W_{k+1}(\tilde{y}_{k+1} - H_{Sk+1}\hat{x}_k) \\ &= \hat{x}_k + K_{k+1}(\tilde{y}_{k+1} - H_{Sk+1}\hat{x}_k) \end{aligned} \tag{2.98}$$

with:

$$K_{k+1} = P_{k+1} H_{Sk+1}^{T} W_{k+1} \tag{2.99}$$

which is known as a *Kalman gain matrix*. The final form of Equation (2.98) which modifies the previous best correction by an additional correction is known as a *Kalman update equation* [KALMAN and BUCY 1961]. The inverse of P_{k+1}^{-1} which is defined in Equation (2.94) is needed (the specific form of P^{-1} is known as *information matrix recursion*) for the

calculation of the Kalman gain can be done more efficiently using the Sherman-Morrison-Woodbury matrix inversion lemma [GOLUB and VAN LOAN 1996]:

$$F = (A + BCD)^{-1} = A^{-1} - A^{-1}B(DA^{-1}B - C^{-1})^{-1}DA^{-1}. \tag{2.100}$$

so that the information recursion now becomes

$$P_{k+1} = P_k + P_k H_{Sk+1}^T (H_{Sk+1} P_k H_{Sk+1}^T - W_{k+1}^{-1})^{-1} H_{Sk+1} P_k. \tag{2.101}$$

Inserting this into the Kalman gain matrix expression (2.99) and performing necessary mathematical rearrangements a new *covariance recursion form* is obtained:

$$\hat{x}_{k+1} = \hat{x}_k + K_{k+1}(\tilde{y}_{k+1} - H_{Sk+1}\hat{x}_k) \tag{2.102}$$

$$K_{k+1} = P_{k+1} H_{Sk+1}^T (H_{Sk+1} P_k H_{Sk+1}^T + W_{k+1}^{-1})^{-1} \tag{2.103}$$

$$P_{k+1} = (I - K_{k+1} H_{Sk+1}) P_k. \tag{2.104}$$

The covariance form is the most commonly used in practice. The estimation process can be initialized by an *a priori* estimate $\hat{x}_1$ and covariance estimate P_1. If they are unavailable the *a priori* estimate and covariance can be initialized according to following expressions [CRASSIDIS and JUNKINS 2004]:

$$P_1 = \left[\frac{1}{\alpha^2} I + H_{S1}^T W_1 H_{S1} \right]^{-1} \tag{2.105}$$

$$\hat{x}_1 = P_1 \left[\frac{1}{\alpha^2} \beta + H_{S1}^T W_1 \tilde{y}_1 \right], \tag{2.106}$$

where α is a very "large" number and β is a vector of very "small" numbers.

KALMAN-BUCY FILTER

In fact the covariance recursion form of LSE is a *Kalman Filter* (KF) if the weight matrix W is chosen to minimize the variance between the estimated $\hat{x}$ and the real x sates which is defined as:

$$E\left\{ (\hat{x}_i - x_i)^2 \right\} \tag{2.107}$$

in the presence of measurement noise $\tilde{y} = H_S \hat{x} + v$. It has been proven that the optimum can be found with Equations (2.102), (2.103) and (2.104) if $W^{-1} = R = \mathrm{cov}(v) = E\left\{ vv^T \right\}$. The

Kalman filter attempts to estimate the states of the "original" discrete time invariant system (2.29) with $\boldsymbol{D}_D=0$ and extended by process $\boldsymbol{w}_k$ and measurement $\boldsymbol{v}_k$ noise as:

$$\begin{aligned}
\boldsymbol{x}_{k+1} &= \boldsymbol{A}_D\boldsymbol{x}_k + \boldsymbol{B}_D\boldsymbol{u}_k + \boldsymbol{\Upsilon}_k\boldsymbol{w}_k \\
\tilde{\boldsymbol{y}}_k &= \boldsymbol{C}_D\boldsymbol{x}_k + \boldsymbol{v}_k
\end{aligned} \tag{2.108}$$

In addition the $\boldsymbol{w}_k$ and $\boldsymbol{v}_k$ are assumed to be *zero-mean Gaussian white noise processes*, which means that they are not correlated forward and backward in time:

$$E\left\{\boldsymbol{v}_k\boldsymbol{v}_j^T\right\} = \begin{cases} 0 & k \neq j \\ \boldsymbol{R}_k & k = j \end{cases} \quad \text{and} \quad E\left\{\boldsymbol{w}_k\boldsymbol{w}_j^T\right\} = \begin{cases} 0 & k \neq j \\ \boldsymbol{Q}_k & k = j \end{cases}, \tag{2.109}$$

furthermore, the process and measurement noise are assumed to be uncorrelated $E\{\boldsymbol{v}_k\boldsymbol{w}_j^T\} = 0$ for all k. The estimator uses the model realization ($\boldsymbol{A}_D$, $\boldsymbol{B}_D$ and $\boldsymbol{C}_D$) as basis for estimation and the correction term based on the measured $\tilde{\boldsymbol{y}}_k$ and estimated $\hat{\boldsymbol{y}}_k^-$ outputs:

$$\begin{aligned}
\hat{\boldsymbol{x}}_{k+1}^- &= \boldsymbol{A}_D\hat{\boldsymbol{x}}_k^- + \boldsymbol{B}_D\boldsymbol{u}_k + \boldsymbol{K}_k(\tilde{\boldsymbol{y}}_k - \hat{\boldsymbol{y}}_k^-) \\
\hat{\boldsymbol{y}}_k^- &= \boldsymbol{C}_D\hat{\boldsymbol{x}}_k^-
\end{aligned} \tag{2.110}$$

In the literature, the KF in (2.110) can be found in the other form, see for example [CRASSIDIS and JUNKINS 2004]. Since the main interest is the estimation of the state, the KF is represented as:

$$\hat{\boldsymbol{x}}_{k+1}^- = \boldsymbol{A}_D\hat{\boldsymbol{x}}_k^+ + \boldsymbol{B}_D\boldsymbol{u}_k \tag{2.111}$$

$$\hat{\boldsymbol{x}}_k^+ = \hat{\boldsymbol{x}}_k^- + \boldsymbol{K}_k(\tilde{\boldsymbol{y}}_k - \boldsymbol{C}_D\hat{\boldsymbol{x}}_k^-) \tag{2.112}$$

where Equation (2.111) is called a *propagation* equation which propagates into a future with the help of the estimated (*a posteriori*) $\hat{\boldsymbol{x}}_k^+$ states and the dynamical model. Equation (2.112) is an *update* equation which modifies the previous best correlation $\hat{\boldsymbol{x}}_k^-$ (*a priori* estimate from all previous measurements without the current one $\tilde{\boldsymbol{y}}_k$). By using the minimum variance approach of Equation (2.107) it can be shown that the discrete KF can be modified similarly to SLE with the optimal Kalman gain [WELCH and BISHOP 2001]. These equations are summarized below:

1. *Initialization*

   a. $\hat{\boldsymbol{x}}(t_0) = \hat{\boldsymbol{x}}_0$

   b. $\boldsymbol{P}_0 = E\left\{\tilde{\boldsymbol{x}}(t_0)\tilde{\boldsymbol{x}}^T(t_0)\right\}$, with $\quad \tilde{\boldsymbol{x}} = \hat{\boldsymbol{x}} - \boldsymbol{x}$

$$\tag{2.113}$$

2. *Gain*

$$K_k = P_k^- C_D^T (C_D P_k^- C_D^T + R_k)^{-1} \tag{2.114}$$

3. *Update*

    a. $\hat{x}_k^+ = \hat{x}_k^- + K_k(\tilde{y}_k - C_D \hat{x}_k^-)$

    b. $P_k^+ = (I - K_k C_D) P_k^-$ $\tag{2.115}$

4. *Propagation*

    a. $\hat{x}_{k+1}^- = A_D \hat{x}_k^+ + B_D u_k$

    b. $P_{k+1}^- = A_D P_k^+ A_D^T + \Upsilon_k Q_k \Upsilon_k^T$ $\tag{2.116}$

The propagation stage is as follows: if the measurements are available at the initial time then the states and covariance are updated using Equations (2.114) and (2.115) with $\hat{x}_0^- = \hat{x}_0$ and $P_0^- = P_0$, as the covariance and the states are propagated according to Equations (2.116); if the measurements are unavailable at the initial time then the estimate and covariance are propagated first to the next available measurement point with $\hat{x}_0^+ = \hat{x}_0$ and $P_0^+ = P_0$. The process is then repeated sequentially. Many modifications of the KF are created for specific problems which include: nonlinear systems, correlated process and measurement noise and colored noise which leads to biased estimation. Improvements are achieved in computational methods of matrix inversions with the help of matrix factorization, see [WELCH and BISHOP 2001]. As has been stated above, the KF takes into account the measurement and process noise; although the precise knowledge of these quantities is not required, still an accurate knowledge of their respective covariance is necessary. In some applications, the R and Q can be estimated online [CRASSIDIS and JUNKINS 2004]; in this case the KF is called an *adaptive filter*. Lastly, several statistical tests can be applied to check the consistency of the KF from the desired characteristics of the measurement residuals, especially in the KF tuning phase. Among them are: the Normalized Error Square (NES) test, the autocorrelation test and the Normalized Mean Error (NME) test [BAR-SHALOM *et al.* 2001].

2.3   INVERSE PROBLEMS IN MECHANICS

In earlier works, the reconstruction of the external loads was considered a solution of the integral Equation (1.1) which can be written as an integral Fredholm equation of the first kind [HANSEN 1998]:

$$\int_0^1 \boldsymbol{K}(s,t)\boldsymbol{f}(t)dt = \boldsymbol{g}(s), \qquad 0 \le s \le 1, \tag{2.117}$$

where the *right-hand side* $\boldsymbol{g}$ and the *kernel* $\boldsymbol{K}$ are known functions, at least in principle, while $\boldsymbol{f}$ is the unknown, sought solution. This type of problem is known as inverse problem and can be formulated as follows: determining the unknown inputs that give rise to the measured output signals (input reconstruction); or determining the internal structure of a physical system from the system's measured behavior given input (system identification). It is well known that inverse problems are 'ill-posed' in the mathematical sense, that is, one of 1) the existence, 2) the uniqueness, or 3) the stability of solution is violated [HANSEN *et al.* 1999; JACQUELIN *et al.* 2003]. Simply put, one cannot trust the solution unless additional treatment is applied.

2.3.1   Ill-conditioned and Rank Deficient Inverse Problems

The main source for the ill-posedness lies in the kernel operator $\boldsymbol{K}$. The analysis of $\boldsymbol{K}$ combines the extensive treatment of the general Fredholm integral equations of the first kind. Therefore, for the purpose of clarity, the main features such as *ill-conditioning* and *rank deficiency* are shown relative to the force reconstruction problem.

Starting with the convolution integral in Equation (1.1) which can be modified for the structure where the responses $y(M,t)$ are acquired at points M and the loads $\boldsymbol{F}(I,t)$ are exerted at the locations I so that a new direct formulation is

$$y(M,t) = \int_0^t \boldsymbol{H}(I,M,t-\tau)\boldsymbol{F}(I,\tau)d\tau, \tag{2.118}$$

here $\boldsymbol{H}(I,M,t-\tau)$ represents the impulse response function between points M and I. In the discrete time domain Equation (2.118) has the form:

$$y(M,\Delta t) = \boldsymbol{H}(I,M,\Delta t)\boldsymbol{F}(I,\Delta t), \tag{2.119}$$

where the discrete impulse response matrix $\boldsymbol{H}(I,M,\Delta t)$ for n–samples, is constructed as:

$$\boldsymbol{H}(I,M,\Delta t) = \begin{bmatrix} \boldsymbol{H}_1(I,M,\Delta t) & \boldsymbol{0} & \cdots & \boldsymbol{0} \\ \boldsymbol{H}_2(I,M,\Delta t) & \boldsymbol{H}_1(I,M,\Delta t) & \cdots & \boldsymbol{0} \\ \vdots & \vdots & \ddots & \vdots \\ \boldsymbol{H}_n(I,M,\Delta t) & \boldsymbol{H}_{n-1}(I,M,\Delta t) & \cdots & \boldsymbol{H}_1(I,M,\Delta t) \end{bmatrix}. \tag{2.120}$$

The inversion of $H(I,M,\Delta t)$ is required for the solution of $F(I,\Delta t)$ from the Equation (2.119). Practice has shown that in most of the cases the direct inversion is not possible due to the bad conditioning of the impulse response matrix. Ill-conditioning is a property of a coefficient matrix $H(I,M,\Delta t)$ that can be qualified with the help of the condition number $C(H)$ which is defined as product of the matrix norm $\| H \|$ and the norm of the inverse matrix $\| H^{-1} \|$ [HENSEL 1991]:

$$C(H) = \| H^{-1} \| \cdot \| H \|. \tag{2.121}$$

If the condition number is less than or equal one, then the matrix is said to be well conditioned, otherwise it is ill-conditioned. Another interpretation of condition number $C(\cdot)$ is as a measure of the error amplification in the solution vector $F(I,\Delta t)$ of Equation (2.119) if the error (noise) is present in $y(M,\Delta t)$, which is always the case if real measurements are taken. The size of the matrix H has a direct connection to its condition number $C(\cdot)$, with the corollary that inversion can be done only for short signals. Moreover, the matrix H can be *rank-deficient* which implies that some of the equations are numerically dependent or filled with zeros. Physically, this means that a time delay occurs between the applied load and the captured measurements, which is natural for complex/distributed structures.

A useful tool in the analysis of *ill-conditioned* and *rank-deficient* matrices is SVD. The SVD of $(m \times n)$, $m \gg n$ real matrix H is defined as:

$$H = U\Sigma V^T = \sum_{i=1}^{n} u_i \sigma_i v_i^T, \tag{2.122}$$

where U is the unitary matrix of left singular vectors, V is the unitary matrix of right singular vectors and Σ is the diagonal matrix with SV placed in decaying order. Taking the SVD of H into account the solution for the Equation (2.119) is formulated in a new way:

$$\hat{F}(I,\Delta t) = \sum_{i=1}^{n} u_i^T \frac{y(M,\Delta t)}{\sigma_i} v_i. \tag{2.123}$$

The ability to solve the above equation depends on the Singular Values SV and vectors of a matrix H. In order that the sum in Equation (2.123) converges, the Picard conditions [ENGL *et al.* 2000] should be satisfied:

$$\sum_{i=1}^{n} \left(\frac{(\boldsymbol{u}_i^T \boldsymbol{y})}{\sigma_i} \right)^2 < \infty . \tag{2.124}$$

The Picard condition of stability states that the absolute value of the coefficients $(\boldsymbol{u}_i^T \boldsymbol{y})$ must decay faster than the corresponding SV σ_i in order that a square integrable solution exists. This requires that $\boldsymbol{y}$ be in the column space of $\boldsymbol{H}$, otherwise the sum is diverging. Unfortunately, in practical situations the measurements $\boldsymbol{y}$ are always contaminated by noise $\boldsymbol{v}(t)$ which leads to violation of the Picard condition regardless of how small the measurement noise is. As a result, a naive approach to solve the Equation (2.123) would fail or lead to the completely wrong solution with an extremely large norm $\| \hat{\boldsymbol{F}} \| \to \infty$ as $n \to \infty$. From that point onwards, the decay rate of the SV can yield important properties which can describe the fundamental behavior of ill-posed problems. In addition, the condition number $C(\boldsymbol{H})$ in terms of σ can be calculated as $C(\boldsymbol{H}) = \sigma_1 / \sigma_{rank(\boldsymbol{H})}$. Hofmann [HOFMANN 1986] gives the following definition for the *degree of ill-posedness*: if there exists a positive number α such that:

$$\begin{aligned} \sigma_i &= O(i^{-\alpha}) \to \text{moderately ill-posed} \\ \sigma_i &= O(e^{-\alpha i}) \to \text{severely ill-posed} \end{aligned}, \tag{2.125}$$

were O is the Landau order operator. Likewise, for the matrix $\boldsymbol{H}$ to be valid

1. The SV steadily decay to zero. The problem is then said to be *solely ill-posed*. The increase in dimensions of $\boldsymbol{H}$ will increase the number of small σ_i.

2. The SV decay gradually to zero and there is a well determined gap between large and small SV. The problem is then said to be *ill-posed and rank deficient*. The occurrence of the gap indicates the *pseudo-rank* of the investigated system.

These two characteristics are illustrated in Figure 2.7 for 19 SV of the ill-conditioned impulse response matrix $\boldsymbol{H}$.
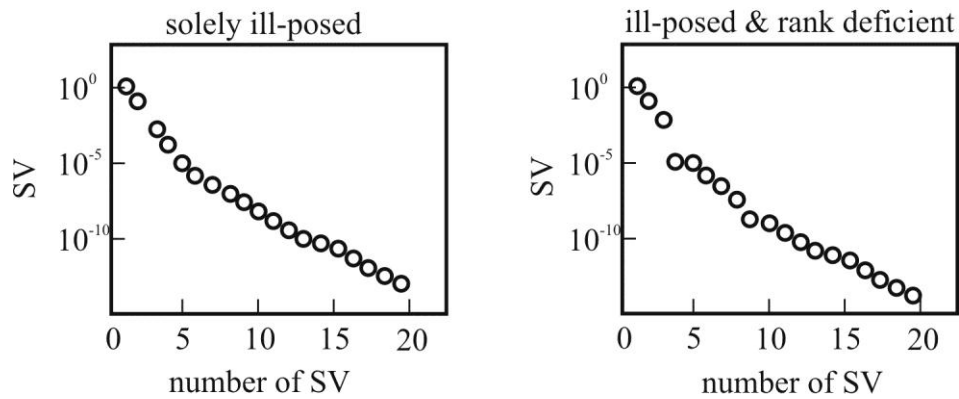
*Figure 2.7: Singular values for ill-posed and rank deficient matrix **H***

Summing up the drawbacks of working with the inverse problems one can conclude that the additional treatment is needed because the direct solution would produce unsatisfactory results.

2.3.2   Conventional Solutions and Regularization Techniques

The literature combines a long list of algorithms that convert ill-posed problems into well-posed ones [HANSEN 1998]. This conversion of ill-posed problems is known as regularization. Among the most used regularization methods the following six direct techniques are to be emphasized [HANSEN 1998]:

1. Tikhonov regularization
2. The Truncated SVD (TSVD)
3. Rutishauser's method
4. The method of O'Brien and Holt
5. Maximum entropy regularization
6. The Truncated Total Least Square T-TLS method

O'Brien's and Rutishauser's algorithms are the derivatives of Tikhonov regularization, whereas T-TLS bears a strong similarity to TSVD. Since Tikhonov regularization and TSVD have found broad application in the field of engineering due to their relative simplicity, only such methods will be illustrated in more details.

TIKHONOV REGULARIZATION

Tikhonov regularization includes the additional information to the initial problem. Such information attempts to compromise the residual norm of the discrete convolution as in Equation (2.119) and a smoothness condition on the solution, *i.e.* the bounded norm of the reconstructed force or its derivatives. Mathematically, Tikhonov regularization for the

deconvolution of Equation (2.119) (by leaving time and location variables) is formulated as follows:

$$\min_{\boldsymbol{F}} \left\{ \| \boldsymbol{HF} - \boldsymbol{y} \| + \alpha^2 \| \boldsymbol{L}\hat{\boldsymbol{F}} \| \right\}, \tag{2.126}$$

where the additional term $\alpha^2 \| \boldsymbol{L}\hat{\boldsymbol{F}} \|$ is a smoothing norm with α as a regularization parameter defining the smoothness and $\boldsymbol{L}$ is a regularization matrix. $\boldsymbol{L}$ is often taken as the identity matrix or as the derivative operator of first or second order, *i.e.* $\boldsymbol{L}^1$ or $\boldsymbol{L}^2$ to enforce smoothness if the underlying vector is believed to be mostly continuous. Setting $\boldsymbol{L}=\boldsymbol{I}$ the estimation of $\boldsymbol{F}$ can be found from Equation (2.126) as:

$$\hat{\boldsymbol{F}} = (\boldsymbol{H}^T \boldsymbol{H} + \alpha \boldsymbol{I})^{-1} \boldsymbol{H}^T \boldsymbol{y}. \tag{2.127}$$

The term $\alpha \boldsymbol{I}$ in Equation (2.127) transforms the initial ill-posed problem into a well-posed one by adding some terms to the singular values of $\boldsymbol{H}$. The regularization can become more obvious if the SVD from Equation (2.122) is used:

$$\hat{\boldsymbol{F}} = \sum_{i=1}^{q} \boldsymbol{u}_i^T \frac{\sigma_i \boldsymbol{y}}{\sigma_i^2 + \alpha^2} \boldsymbol{v}_i. \tag{2.128}$$

The upper limit q of the sum defines the effective rank of matrix $\boldsymbol{H}$.

TRUNCATED SVD

The technique comprises eliminating small singular values that spoil the convergence of Equation (2.123) up to the rank χ. The χ in this case is a regularization parameter and has a similar functionality to α in Tikhonov algorithm. In addition to a "bad" SV it should also "knock out" the oscillating singular vectors. The solution of Equation (2.123) is of a form:

$$\hat{\boldsymbol{F}} = \sum_{i=1}^{\chi} \boldsymbol{u}_i^T \frac{\boldsymbol{y}}{\sigma_i} \boldsymbol{v}_i, \tag{2.129}$$

where only "good" singular values are left. As a result of truncation the norm of $\| \hat{\boldsymbol{F}} \|$ is reduced, which leads to a smother solution, but simultaneously it enlarges the residual norm $\| \boldsymbol{H}\hat{\boldsymbol{F}} - \boldsymbol{y} \|$ which implies a larger distance from the true solution.

In both regularizations the choice of the stabilizing parameter α or χ is an important issue. Unfortunately, there is no universal method for such parameters that produces an optimal result. The most used are the *L*-curve [TIKHONOV and ARSENIN 1977] and the Generalized Cross Validation (GCV) methods [HANSEN and O'LEARY 1993].

The *L*-curve is a graphical tool for the analysis of parameters α and χ, which is obtained as an *L*-shaped plot of discrete smoothing norm of the regularized solution $\| L\hat{F} \|$ versus the corresponding residual norm $log \| H\hat{F} - y \|$ for all valid regularization parameters on the log-log scale, see Figure 2.8(a) for α. The distinct corner of the *L*-curve is taken as an optimal tradeoff between the degree of smoothness and residual error.

The GCV criterion is based on the fact that a good parameter α or χ has to predict the missing data well. Mathematically it is formulated as a minimization of the predictive mean-square error

$$ GCV = \frac{\| H\hat{F} - y \|}{\| I - HH^+ \|}. \tag{2.130} $$

Figure 2.8(b) is the typical graph of the GCV versus the regularization parameter. The optimality is found as the minimum point of this function. Both the *L*-curve and GCV have some ambiguity (the *L*-curve may have more than one corner, the GCV might be flat near the minimum) in real applications. Therefore, it is beneficial to use them both and to compare the results.
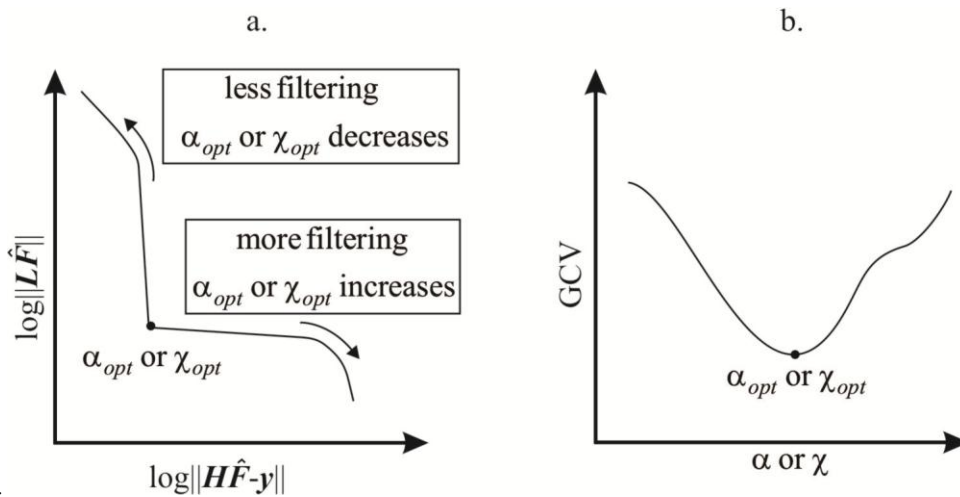
Figure 2.8: The generic form of the Tikhonov L-curve (a) and GCV curve (b)

3 EXTERNAL LOAD CLASSIFICATION

All the effects of nature are only the mathematical consequences
of a small number of immutable laws.
-Pierre-Simon Laplace

Before the actual reconstruction of the external loads is shown, a classification of possible load scenarios is performed in this chapter. Experience in the field of load estimation has proven that load reconstruction algorithms dramatically differ from each other depending on the load type and the structure under consideration. In principle, external loads can be categorized according to: their excitation duration in time (short or long excitation) and their location along the structure (concentrated or spatially distributed).

3.1   CONCENTRATED LOAD

3.1.1   Impact Load

An impact load $f(t,q)$ is characterized by its short duration in time t and concentrated location in space $q(x,y,z)$. As used herein, "short duration" means that the load action is very fast relative to the overall system dynamics. It can ideally be represented in the form of Dirac's delta function as:

$$\delta(t) = \begin{cases} +\infty, & t = 0 \\ 0, & t \neq 0 \end{cases}, \quad \text{but} \quad \int_{-\infty}^{\infty} \delta(t)dt = 1 \tag{3.1}$$

which is in its turn a derivative of the Heaviside function

$$H_\delta(t) = \begin{cases} 0, & t < 0 \\ 1, & t > 0 \end{cases}. \tag{3.2}$$

The ideal Dirac's delta function is shown in Figure 3.1 (a), nevertheless in practice there is no such thing as a load with infinite amplitude. Therefore, an approximation is often used as illustrated in Figure 3.1 (b). The finite impact load $f(t)$ is mathematically formulated as follows:

$$f(t) = \begin{cases} \dfrac{\overline{F}}{\varepsilon}, & 0 \leq t \leq \varepsilon \\ 0, & elsewhere \end{cases}, \quad \text{with} \quad \int_{-\infty}^{\infty} f(t)dt = \overline{F}. \tag{3.3}$$

a.   b.
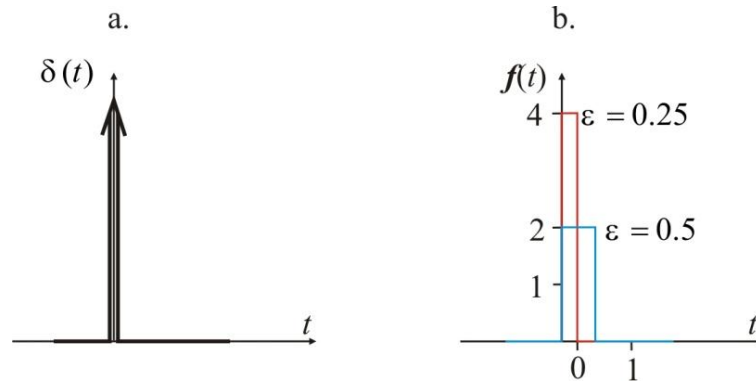
Figure 3.1: Dirac delta function (a), normalized delta function of finite duration (b)

As an assumption, the impact is always considered to be acting in a relatively small area, *i.e.* as a load applied only at one DOF for FEM. In the case of analytical models, the load location is incorporated into the model mathematically. The Dirac function can be used again for the concentrated allocation in space for the analytical models, so that the impact force for the two dimensional space $q(x(t),y(t))$, shown in Figure 3.2 is formulated as:

$$f(x_a(t), y_a(t), t) = \underbrace{\delta(x - x_a(t))\delta(y - y_a(t))}_{\text{space allocation } q} \begin{cases} \bar{F}, & 0 < t < \varepsilon \\ 0, & else \end{cases}, \tag{3.4}$$

where $\bar{F}$ is the amplitude of the impact, ε is the time duration of the impact, and the two δ functions are used to position the applied impact force. It is worth to mention that localization of the impact (identification of $x_a(t)$ and $y_a(t)$) is always required prior to its amplitude estimation.
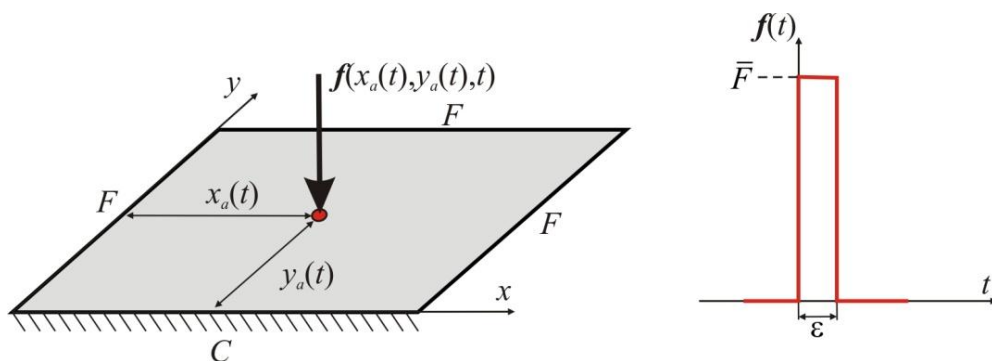
Figure 3.2: Clamped-Free-Free-Free (C-F-F-F) plate under the impact force

This feature renders the concept of impact reconstruction completely unlike the other algorithms. Special requirements are also applied to the measurement equipment. In particular, data sets should be recorded with a high resolution; as a consequence a high sampling rate is mandatory. Moreover, assuming only one impact acting in a given time, a distributed

sensor array is required to fulfill the localization procedure. All these aspects will be treated in more detail in Chapter 4.

3.1.2 Time Continuous Load

In contrast to impacts continuous loads last longer in time. They can be categorized into the following classes: deterministic (harmonic, periodic or non-periodic); stochastic (or random). In most of the cases these loads are generated by external forces/moments or appear as the interaction between machine parts (*i.e.* contact problems). The location of the load is assumed to be known and fixed in time, so establishing the load history is the only objective of the reconstruction procedure, see Figure 3.3. In addition, the dynamic characteristic of the load is assumed to be known in advance (*e.g.* the wind load would be expected to bear a correlation to the wind speed) in order that suitable data acquisition equipment can be chosen for the specific task at hand.
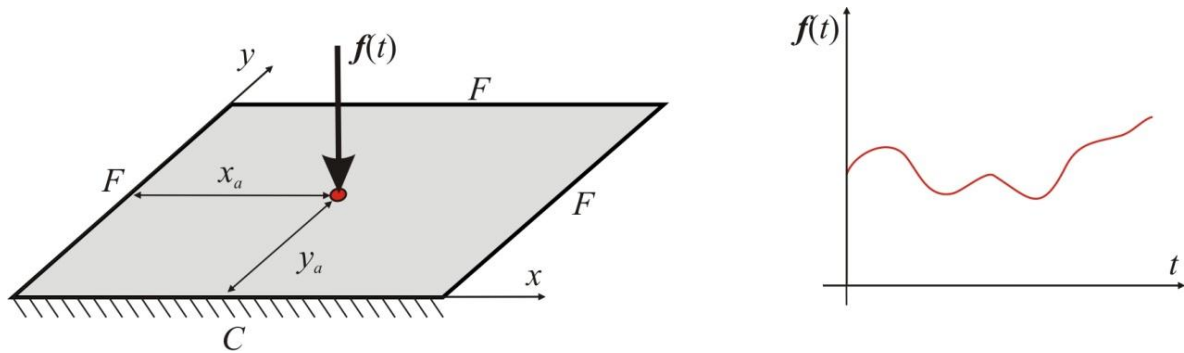
Figure 3.3: Clamped-Free-Free-Free (C-F-F-F) plate under continuous force

3.2   DISTRIBUTED LOAD

Distributed loads, which are shown in Figure 3.4, may be the most difficult case in all possible scenarios for the load reconstruction routine. They can last longer in time or exhibit an impact type behavior (*e.g.* wind gusts). The main characteristic of distributed loads is their spatiality; as a result, complex modeling as well as elaborated equipment is required. In some cases, they can be represented with the help of Fourier coefficients which are defined at the specific locations, if a prior knowledge about spatial distribution is at hand (*e.g.* the wind load along the Wind Energy Plant (WEP) can be assumed to increase gradually with the altitude of the WEP). Then, the estimation problem is reduced to the time history reconstruction of these coefficients. This type of loads will not be considered in this contribution, nevertheless some preliminary work can be found in [NIU *et al.* 2010].
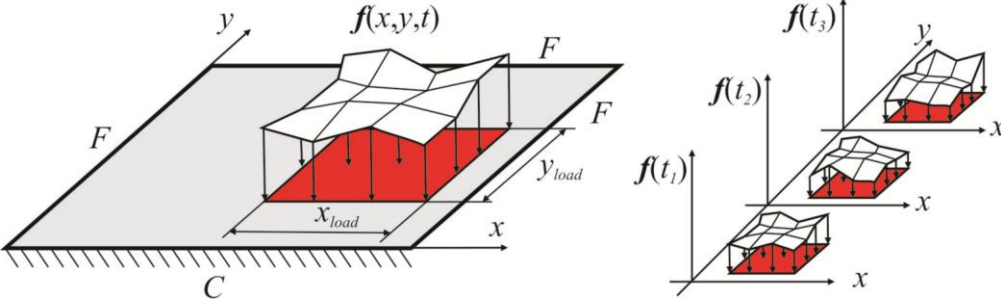
Figure 3.4: Clamped-Free-Free-Free (C-F-F-F) plate under distributed load

4 IMPACT RECONSTRUCTION

It is the theory which decides
what we can observe
-Albert Einstein

The reconstruction of an impact consists of two phases, as detailed in Chapter 3.1.1. The first phase includes the localization of the impact, which adopts many well established techniques from the Acoustic Emission (AE) testing. The key procedure at this step is the analysis of the acquired signals which allows extraction of the essential information from the excitation waves in terms of contained frequencies and their times of arrival. The extracted frequencies in their turn serve as basis for the estimation of the wave propagation velocities which are usually frequency dependent (in dispersive media). Based on the extracted time and estimated velocity information, the optimization procedure attempts to localize the impact position [DZHAFEROV 2009]. In the second phase the identified location is used for the model construction and the estimation of the impact history. Both tasks are fulfilled by analysis of the acquired data in cooperation with the model of the dynamical system. Therefore, signal preprocessing is an important issue and should be presented prior to the actual algorithms for the localization and history estimation phases.

4.1   SIGNAL PROCESSING

Signal processing contributes major aspects to the accuracy of the localization phase and together with the fidelity of the model implicitly influences the time history estimation phase. In general, the purpose of signal processing is the extraction of information from a signal, especially when it is difficult to obtain from direct observation. The methodology of extracting information from a signal has three key stages:

- acquisition (signal acquisition is concerned with instrumentation)
- processing
- interpretation

The signal acquisition is assumed to be well designed to properly resolve the high velocity impact in time. The acquisition scheme for the impact load is represented in Figure 4.1 with one input and multiple outputs which are contaminated by noise. The responses are recorded in volts and then normally transformed into physical quantities (strains, accelerations).
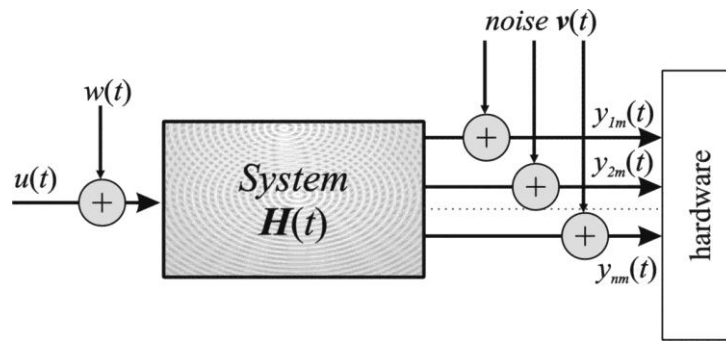
Figure 4.1: Data acquisition scheme

Recorded time histories of signals can be classified as: deterministic or non-deterministic signals. The analysis algorithms are considerably different depending on the „type" of signal. Generally, signals are mixed, so the classification which is given in [SHIN and HAMMOND 2008] may not be easily applicable, and thus the choice of analysis methods may not be apparent. A typical response to the impact load is represented in Figure 4.2, which can be categorized accordingly as a deterministic non-stationary signal [SHIN and HAMMOND 2008]. The recorded response includes an initial wave package in the very initial phase and the multiples of reflections together with the wave's interferences in the later time history. Among a vast set of techniques, Wavelet Transformation can be used to modify the acquired non-stationary raw signals, such as those in Figure 4.2 and to transform them into a new form of information that is more useful for the interpretation procedure [SHIN and HAMMOND 2008].
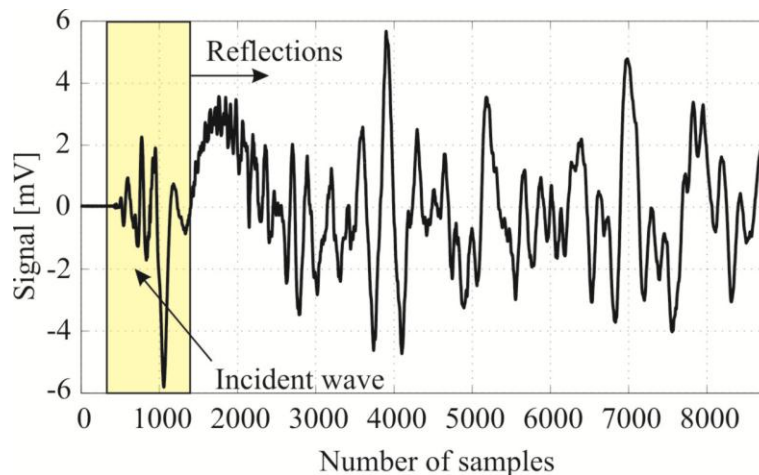
Figure 4.2: Typical impact response signal recorded by PZT sensor after impact excitation on aluminum plate

4.1.1   Wavelet Transformations

The Wavelet Transformation WT is a good alternative to fast Fourier transformation with a definitive advantage in terms of variable resolution in time and frequency. The Continuous

Wavelet Transform (CWT) of an arbitrary function $f(t)$ is defined [STRANG and NGUYEN 1996] as:

$$F_\Psi(a,b) = \frac{1}{\sqrt{a}} \int_{-\infty}^{\infty} f(t) \Psi_{(a,b)}^m \left(\frac{t-b}{a} \right) dt, \qquad (4.1)$$

where

$$\Psi_{(a,b)}^m(t) = \frac{1}{\sqrt{a}} \Psi^m \left(\frac{t-b}{a} \right) \qquad (4.2)$$

is the wavelet function, with a and b being scaling and translation parameters, respectively. The scaling parameter a is the primary characteristic of the WT which bears a direct relation to the frequency $\omega = \omega_0 / a$ with ω_0 being a positive number. The mother wavelet function $\Psi^m(t)$ may be considered as a window function both in the time and frequency domain. The size of the time window is controlled by the translation parameter b, while the length of the frequency band is controlled by the scaling parameter a [GAUL and HURLEBAUS 1998]. It is possible to change the window size either in the time or in the frequency domain by controlling the dilation and translation. This property of the WT is called multi-resolution [WU and DU 1996]. The class of the mother wavelets functions is very broad, nevertheless the most appropriated function for the analysis of the impact responses, as reported by [KISHIMOTO *et al.* 1995], is the Gabor function, which provides a small window in the time and in the frequency domain. The Gabor function is defined by:

$$\Psi_g^m(t) = \frac{1}{\sqrt[4]{\pi}} \sqrt{\frac{\omega_0}{\gamma}} \exp \left[-\frac{(\omega_0 / \gamma)^2}{2} t^2 + i\omega_0 t \right], \qquad (4.3)$$

where γ and ω_0 are positive constants and set according to [KISHIMOTO *et al.* 1995] to be $\gamma = \pi \sqrt{2 / \ln 2}$ and $\omega_0 = 2\pi$. The Gabor function can be physically considered as a complex sinusoidal function with a Gaussian window, as shown Figure 4.3 (a). Whereas in frequency domain the Gabor function $\hat{\Psi}_g^m(\omega)$ is real, see Figure 4.3 (b), centered at $\omega_0 = 2\pi$ and expressed as:

$$\hat{\Psi}_g^m(\omega) = \frac{\sqrt{2\pi}}{\sqrt[4]{\pi}} \sqrt{\frac{\gamma}{\omega_0}} \exp \left[-\frac{(\gamma / \omega_0)^2}{2} (\omega - \omega_0)^2 \right]. \qquad (4.4)$$

The CWT in Equation (4.1) carries out a transformation of the one dimensional signal $f(t)$ into two dimensional time-scale plane (*a-b*). Moreover, the reciprocal of scale parameter a is related to frequency and the translation parameter b is associated with time, as mentioned above.
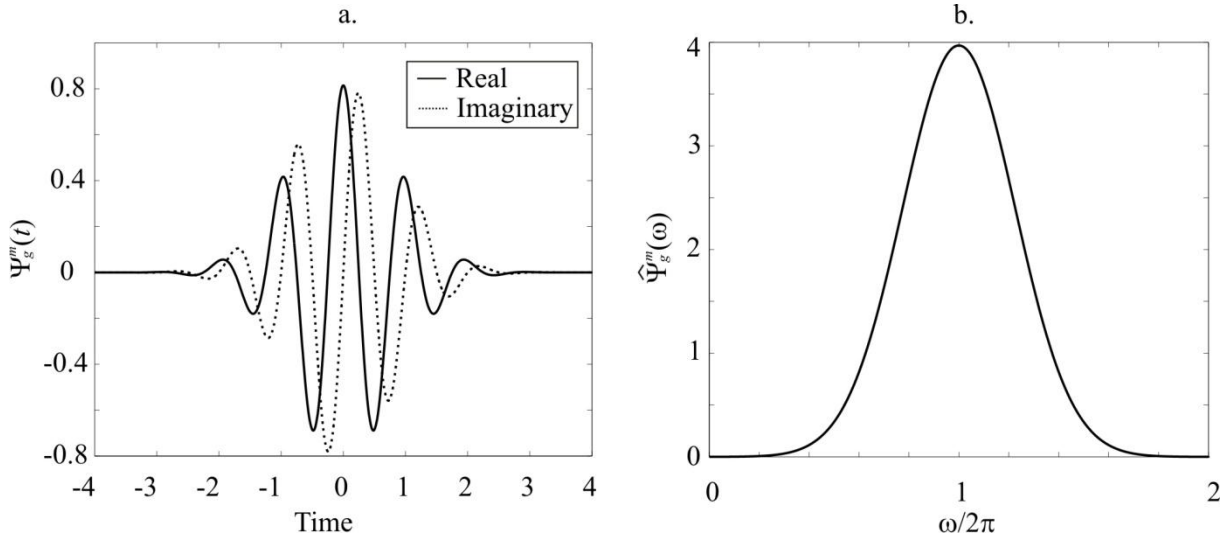
Figure 4.3: Gabor function in time (a) and frequency (b) domains

In order to obtain the physical frequency and time information from the coefficients of CWT, the quantitative relations from time-scale (*a-b* domain) to time-frequency ($t - \hat{f}$ domain) has to be established. This can be done by following equalities [WANG 2004]:

$$\hat{f} = \frac{f_s}{a} \qquad \text{and} \qquad t = b, \tag{4.5}$$

where f_s is the sampling rate of the $f(t)$. In addition, it is important to have knowledge of the relationship between the wave propagation and the wavelet analysis in order to determine the arrival times of the flexural waves. A wave propagating in a plane can be specified by the wavelength λ and the angle between the x_1 axis and the propagation direction θ. Hence, one can obtain the apparent wavelengths in the x_1 and x_2 directions as defined by $\lambda_1 = \lambda / \cos(\theta)$ and $\lambda_2 = \lambda / \cos(\theta)$, respectively, see Figure 4.4. By considering two waves traveling in a plane with the same amplitude and the frequencies ω_1 and ω_2 which are formulated mathematically [GAUL and HURLEBAUS 1998]:

$$f(x_1, x_2, t) = \exp\left[i(\omega_1 t - k_{11}x_1 - k_{12}x_2)\right] + \exp\left[i(\omega_2 t - k_{21}x_1 - k_{22}x_2)\right], \tag{4.6}$$

where k_{ij} are the wave numbers corresponding to the ith frequency ω_i and to the coordinate x_i. The wave number is defined as $k = 2\pi / \lambda$ so that $k_{j1} = k_j \cos\theta$ and $k_{j2} = k_j \sin\theta$ and therefore Equation (4.6) can be reformulated as:

$$\begin{aligned}
f(x_1, x_2, t) = {} & \exp\left[i(\omega_1 t - k_1 \cos\theta x_1 - k_1 \sin\theta x_2)\right] \\
& + \exp\left[i(\omega_2 t - k_2 \cos\theta x_1 - k_2 \sin\theta x_2)\right].
\end{aligned} \tag{4.7}$$
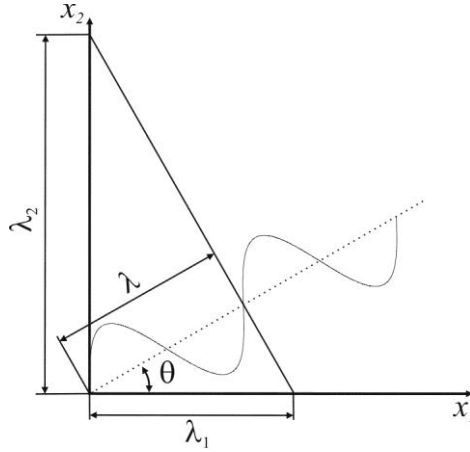
Figure 4.4: Wave propagation in plane

Using Parseval's theorem [STRANG and NGUYEN 1996] which states that the WT of $f(t)$ can be obtained as:

$$F_\Psi(a,b) = \frac{\sqrt{a}}{2\pi} \int_{-\infty}^{\infty} f(\omega) e^{ib\omega} \overline{\hat{\Psi}_g^m(a,\omega)}\, d\omega \,, \tag{4.8}$$

where $\overline{\hat{\Psi}_g^m}$ represents the complex conjugate of the Gabor function in frequency domain and $f(\omega)$ is the Fourier transform of the $f(t)$. The wave propagation in (4.7) can be transformed into the time-scale plane by WT [GAUL and HURLEBAUS 1998]:

$$\begin{aligned}
F_\Psi(x_1,x_2,a,b) = \sqrt{a}\, \Big\{ &\exp\big[i(\omega_1 b - k_1 \cos\theta x_1 - k_1 \sin\theta x_2)\big] \overline{\hat{\Psi}_g^m(a\omega_1)} \\
+ &\exp\big[i(\omega_2 b - k_2 \cos\theta x_1 - k_2 \sin\theta x_2)\big] \overline{\hat{\Psi}_g^m(a\omega_2)} \Big\}.
\end{aligned} \tag{4.9}$$

Multiplying Equation (4.9) by its complex conjugate it is possible to obtain the magnitude of the WT under the assumption that $\hat{\Psi}_g^m$ is real:

$$\begin{aligned}
\big|F_\Psi(x_1,x_2,a,b)\big| = \sqrt{a}\, \Big\{ &\left(\hat{\Psi}_g^m(a\omega_1)\right)^2 + \left(\hat{\Psi}_g^m(a\omega_2)\right)^2 \\
&+ 2\left(\hat{\Psi}_g^m(a\omega_1)\right)^2 \left(\hat{\Psi}_g^m(a\omega_2)\right)^2 \cos(2\Delta\omega b - 2\Delta k \cos\theta x_1 - 2\Delta k \sin\theta x_2) \Big\}^{\frac{1}{2}},
\end{aligned} \tag{4.10}$$

with $\Delta\omega = (\omega_1 - \omega_2)/2$ and $\Delta k = (k_1 - k_2)/2$ respectively. If two waves traveling in the plane are only slightly different so that Δk is small, then $\omega_1 \approx \omega_2$ and $k_1 \approx k_2$ and $\hat{\Psi}_g^m(a\omega_1) \approx \hat{\Psi}_g^m(a\omega_2) \approx \hat{\Psi}_g^m(a\omega)$, the magnitude of the WT will be [GAUL and HURLEBAUS 1998]:

$$\left|F_{\Psi}(x_1,x_2,a,b)\right| = \sqrt{a}\left|\hat{\Psi}_g^m(a\omega)\right|\left[1+2\cos(2\Delta\omega b-2\Delta k\cos\theta x_1-2\Delta k\sin\theta x_2)\right]^{\frac{1}{2}}, \quad (4.11)$$

which reaches its maximum if the cosine function is equal to one and $a = \omega_0/\omega$. This is the case when:

$$b = \frac{\Delta k}{\Delta\omega}(\cos\theta x_1 + \sin\theta x_2) = \frac{1}{c_g}(\cos\theta x_1 + \sin\theta x_2). \quad (4.12)$$

Equation(4.11) implies that the peak of the WT represents the arrival time of the flexural wave with group velocity c_g. The peak frequency can be used for the extraction of the wave velocity of the incoming signal with the help of dispersion diagrams, which are obtained for the specimen either analytically or experimentally. In most of the cases the lateral impact causes only the asymmetric waves spreading in media. As a consequence, only the zero asymmetric mode curve might be sufficient for the extraction of c_g. An example of CWT for the impact response in Figure 4.2 is shown in Figure 4.5 which combines both the raw signal and its CWT.
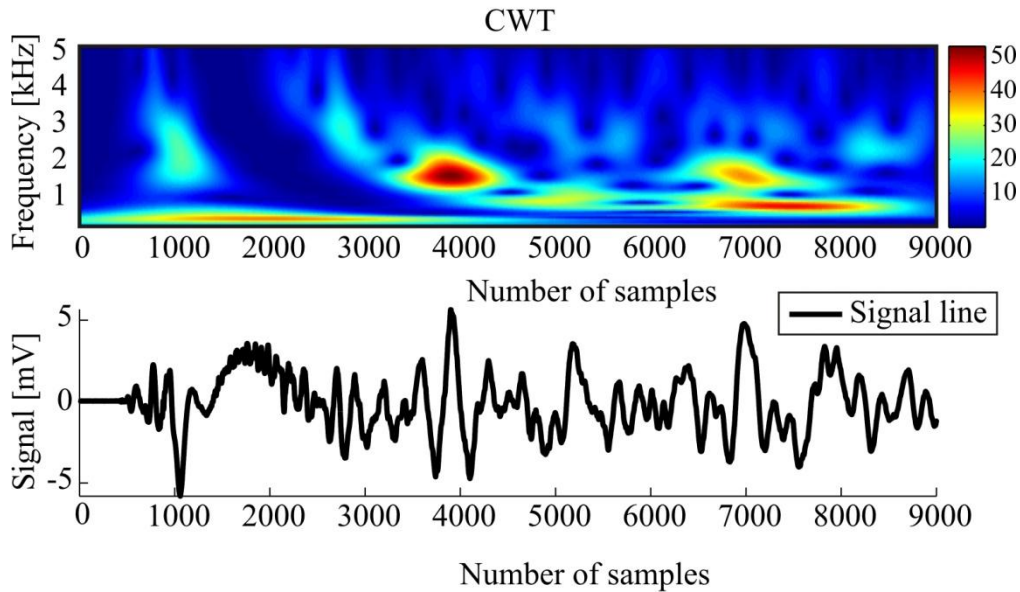
Figure 4.5: CWT off the impact response

The observation can be made from Figure 4.5 that the maximum of CWT lies in the reflection region, which is separated from the incident wave. This contradicts with the statements above with respect to the maximum of WT. Nevertheless, in the interferences and reflection region the assumption of two close waves is not valid anymore. As a result, only the first part of the acquired signal (up to 2000 samples) should be used for the frequency content estimation of the incoming wave. This could be achieved by either proper truncation or windowing.

4.1.2 Windowing and Filtering

The truncation mentioned above leads to leakage during the WT, which in turn can lead to the wrong frequency estimation. Windowing is thus more preferable. This difference is exemplified in Figure 4.6(a) and (b) where the impulse response is shown.
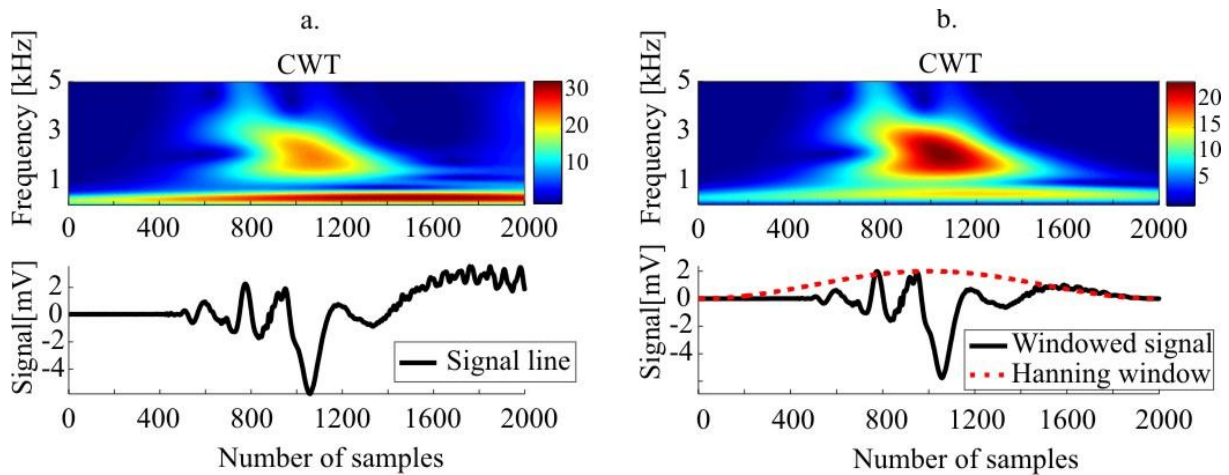
Figure 4.6: CWT of the (a) truncated impact response; (b) truncated and windowed impact response

Plain truncation in Figure 4.6(a) leads to a wrongly identified frequency having a maximum approximately at 1600 sample (mostly in the low frequency region which takes reflections into account), whereas, as illustrated in Figure 4.6(b), the incident wave frequency is determined properly at 1000 sample and the reflection part is suppressed by the application of the Hanning window. The same result can also be achieved by straight truncation but this would require permanent signal monitoring which would be impractical for an automated impact detection algorithm. In this example the Hanning window is well aligned in time to emphasize only the incoming wave package and its size is set to obtain the best estimation results. For optimized alignment an extracted time of arrival for the wave package is required. This is a task on its own and is discussed in the following chapter.

4.2 IMPACT DETECTION AND LOCALIZATION

Firstly, it should be mentioned that impact reconstruction is based on passive sensor technology. This implies that all the data recording equipment is in the listening state. After the impact event has taken place, a procedure should be started that is able to extract only the data that belong to the impact. This procedure is called impact detection and involves *trigger setting* for starting the data acquisition process, analysis of the recorded data and extraction of the Time Of Arrival (TOA). The TOA (also referred to in certain references as *onset time*)

represents an initial time for every sensor and a very important quantity in the impact localization step which is based on calculated distances. For clarity, the responses in Figure 4.7 which are recorded after the impact event has taken place on the rectangular plate are shown, with four sensors distributed along the structure. The recording is started after the threshold is exceeded by one of the sensor signals see Figure 4.7 and is continuous for a pre-defined amount of time. One can directly see that a pre-trigger window is required to catch the dynamic response completely. Especially in the case of noisy measurements, the threshold is set to avoid false triggers, thereby naturally leading to a delayed start of the recording. Usually, the statistical algorithms are taken to set the threshold, for example, at three times the standard deviation of the noise which assures that 99.73% of the noise will be within the confidence interval bounded by the threshold lines.
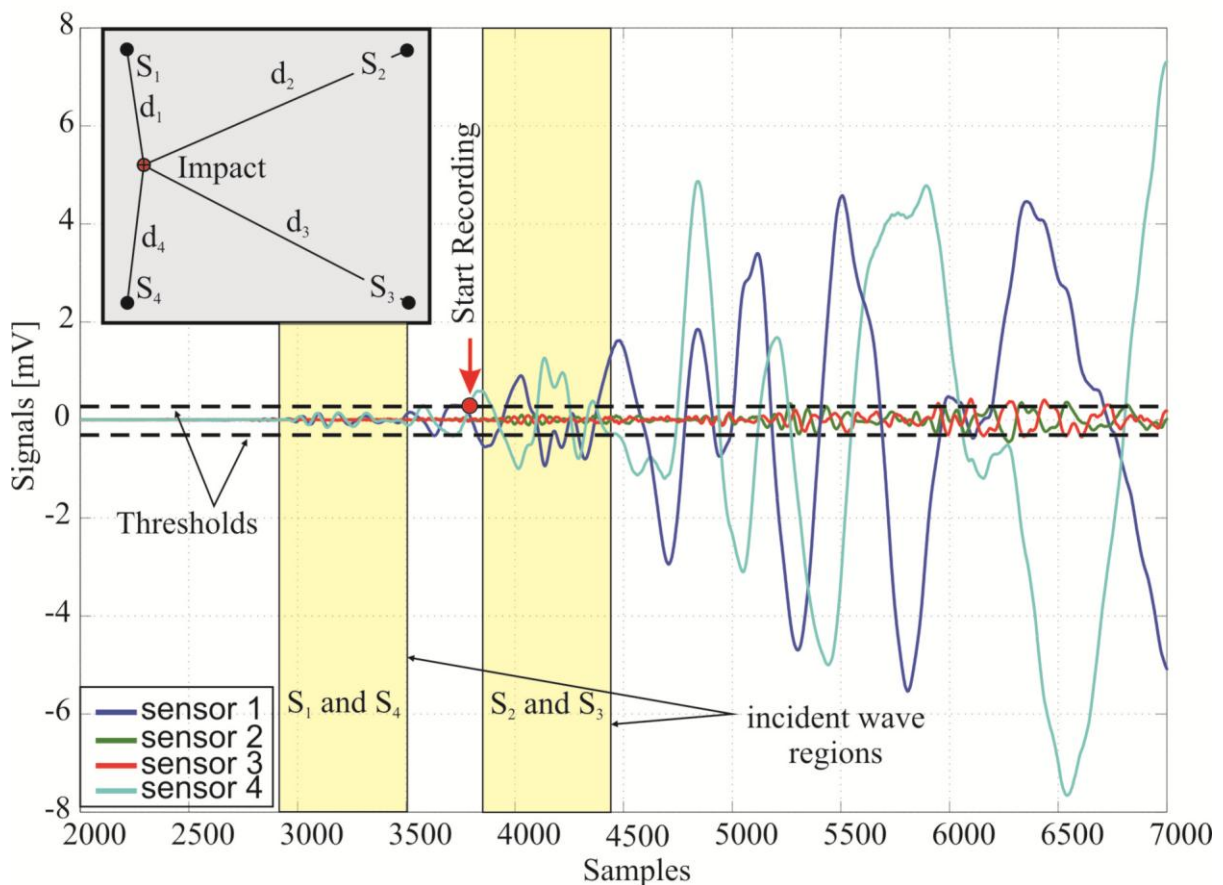
Figure 4.7: Typical responses after the impact load

4.2.1   Time of Arrival Extraction

After the signals are recorded the procedure of determination of the TOA is started. In Figure 4.7 (marked by yellow areas) obvious differences are to be noticed between signals from sensors (1 and 4) and (2 and 3), which are due to the time delay for the last sensors that are

positioned further from the impact location. Moreover, there is no clear starting point for each sensor. Therefore, an automatic picking algorithm to extract the TOA would be beneficial. Many such techniques are already available from AE testing (automatic onset time picking) [GROSSE and OHTSU 2008] or [HEROLD *et al.* 2007]. The most reliable among them are the Energy Criterion (EC) and Akaike Information Criterion (AIC).

ENERGY CRITERION PICKER

The EC algorithm is based on the assumption that the arrival of a wavelet corresponds to a change in energy function S' with negative trend which is defined as:

$$S'_i = \sum_{k=0}^{i}\left(y_k^2 - i\frac{S_N}{\alpha N}\right) \quad \text{with, } i=[0...N],\tag{4.13}$$

where y_k is the measured signal at the kth time instant and the second part of the equation represents the negative trend with respect to the total energy S_N for the whole signal length N. Parameter α is used to reduce the delaying effect of negative trend. This is a tuning parameter which should be set properly to avoid incorrect TOA estimation. Its influence is shown in Figure 4.8 in a more evident manner for the impact response signal.
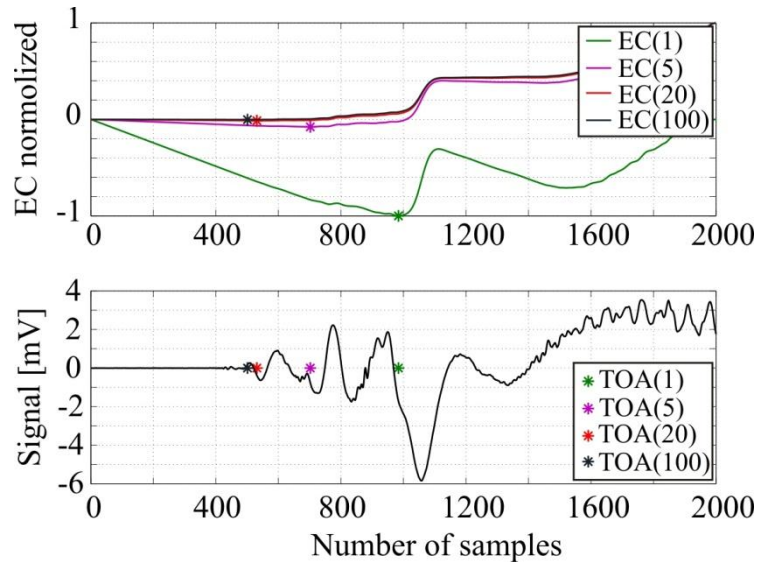
Figure 4.8: Energy Criterion (EC) for different α parameters (α=1, 5, 20, 100) and respective time of arrivals

The tuning is certainly a disadvantage associated with this picking method. For the signal shown in Figure 4.8, an increase of α higher than 100 does not affect the TOA estimation anymore.

AKAIKE INFORMATION CRITERION PICKER

The AIC is an autoregressive (AR) time picking algorithm capable of detecting arrival times of signals developed by [KURZ *et al.* 2005]. Also used in partial discharge location and seismology [HEROLD *et al.* 2007], AIC divides the sampled data into two stationary parts which are each modeled by an AR process. Changes in the value or order of the AR coefficients before and after a pulse occurrence indicate the onset by a global minimum. The AIC is calculated according [GROSSE and OHTSU 2008]:

$$\boldsymbol{AIC}(k) = t_k \log_{10} E\left\{\left(\boldsymbol{y}_1^k\right)^2\right\} + \left(t_N - t_k - 1\right)\log_{10} E\left\{\left(\boldsymbol{y}_{k+1}^N\right)^2\right\}, \text{ with } 1 \le k \le N \qquad (4.14)$$

where $E\left\{\boldsymbol{y}^2\right\}$ is the expectation operator which represents a variance of the signal $\boldsymbol{y}$. The interpretation of Equation (4.14) is fairly straightforward for every time t_k, the signal $\boldsymbol{y}_k$ is broken into two parts; that leading up to t_k, $\boldsymbol{y}_1^k$ and after t_k, $\boldsymbol{y}_{k+1}^N$. The AIC describes the similarity in information-entropy (which measures the amount of *uncertainty*) between the two parts of the signal when t_k becomes aligned with the onset of the signal, the portion of the record before t_k is composed of high-entropy uncorrelated noise, while the portion after t_k contains the low-entropy waveform showing marked correlation [HENSMAN *et al.* 2010]. The global minimum from all values of this criterion corresponds to a point of the arrival time, see Figure 4.9.
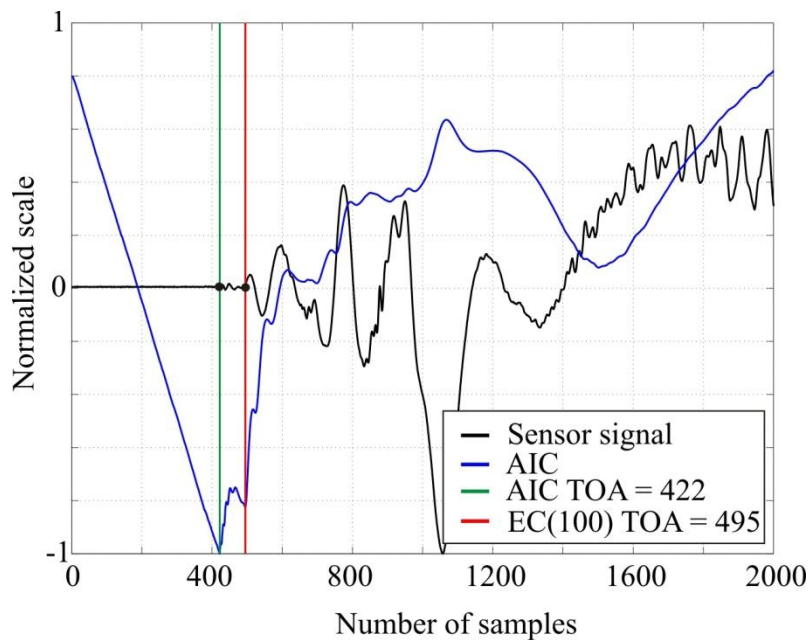
Figure 4.9: Akaike Information Criterion (AIC) together with Energy Criterion (EC) for automatic picker technique

The AIC picker showed better performance in TOA estimation and is really independent from any tuning parameters which renders it a more preferable choice for future applications. At this stage the TOA for every sensor together with its frequency content is known. As a next, step these quantities are utilized for the impact localization procedure.

4.2.2   Location Searching Strategies

The impact location procedure is based on the technique which utilizes a relation between the wave propagation group velocity c_g, the time of flight information t^{tof}, and the travelling distance d inside the isotropic medium (*i.e.* a medium wherein waves travel at the same speed in all directions):

$$d = t^{tof} c_g .$$

(4.15)

In case of an anisotropic medium the fact that velocity is direction-dependent should be taken into account. For an isotropic material the simple relation in Equation (4.15) can be used for the distributed sensors array as illustrated in Figure 4.10.
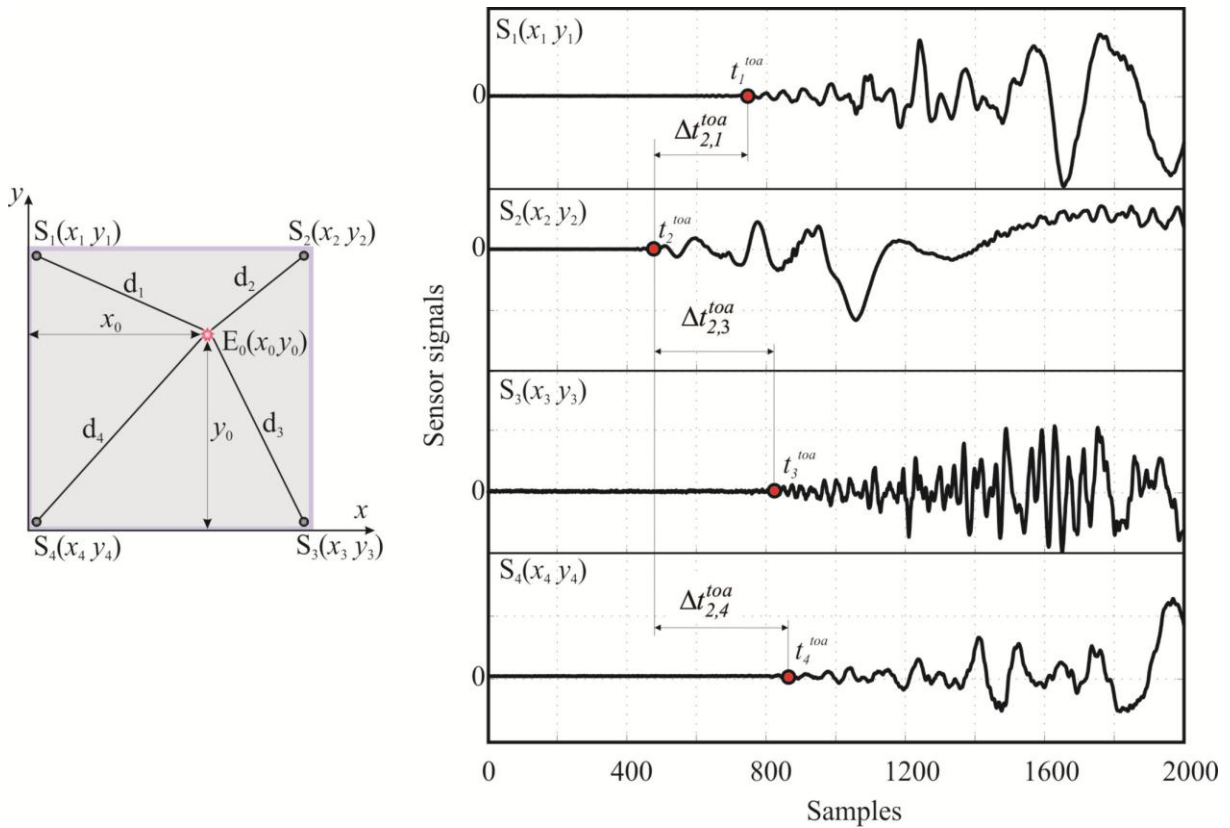
Figure 4.10: Principle: Isotropic plate with the distributed sensor array and their responses to the impact load

The time of flight information is calculated as a difference between impact time t^{impact} and the TOA t_i^{toa} at the ith sensor:

$$t_i^{tof} = t_i^{toa} - t^{impact}.$$
(4.16)

In the case of passive sensor technology, however, the initial impact time is not known, therefore the differences in TOA's are employed together with the distance differences. The localization of the impact is forged to the minimization of the objective function J in Equation (4.17) with respect to E to find the impact position:

$$\min_{E(x,y)}(J) = \sum_{i,j} \Delta t_{i,j}^{toa} - \frac{\overbrace{\| E - S_i \|}^{d_i} - \overbrace{\| E - S_j \|}^{d_j}}{c_g}$$
(4.17)

where the c_g is a group wave velocity. The global minimum of the scalar function of the Equation (4.17) can be found numerically by means of available optimization algorithms, *e.g.* the conjugate gradient method or the simplex method.

4.3   IMPACT HISTORY ESTIMATION

After the impact location is identified the impact time history can be reconstructed with the help of a dynamic model, which incorporates the identified impact location within itself. The model of the structure can be of any of the types described in Chapter 2.1 and can be adapted into a specific form for every force reconstruction algorithm by means of simple algebraic transformations.

4.3.1   Direct Deconvolution in Time Domain

For impact-type loading it is possible to use a direct deconvolution in a continuous time domain or an inversion in a discrete time domain. The problem of load reconstruction is addressed with the Inverse Structural Filter (ISF) as modified by [NORDSTRÖM 2005]. The algorithm is constructed on the basis of the ISF which takes into account the MIMO discrete state-space representation of the structure with zero initial conditions x_0=0 at k=0, as in Chapter 2.1.5, in the form of Markov parameters H_i:

$$y_k = \sum_{i=1}^{k} H_i u_{k-i}, \quad \text{with: } H_0 = D, \ H_i = C(A_D)^{i-1} B_D \ \text{and} \ H_i \in R^r \times R^m,$$
(4.18)

where r and m are the number of sensors and of input forces, respectively, as set forth in the previous chapters. Formulating the relationship of (4.18) for each discrete time $k=0, \ldots, N$ yields a block matrix form:

$$\underbrace{\begin{bmatrix} H_0 & H_1 & \cdots & H_N \\ 0 & H_0 & \cdots & H_{N-1} \\ \vdots & \vdots & \ddots & \vdots \\ 0 & 0 & \cdots & H_0 \end{bmatrix}}_{H} \begin{bmatrix} u_N \\ u_{N-1} \\ \vdots \\ u_0 \end{bmatrix} = \begin{bmatrix} y_N \\ y_{N-1} \\ \vdots \\ y_0 \end{bmatrix}. \qquad (4.19)$$

The unique solution for the impact sequence $\{u_k\}_{k=0}^{N}$ requires the upper triangular block Toeplitz matrix to have a full column rank. This requirement is met if the $r \times m$ block diagonal element matrix H_0 has a full column rank (which is always valid if $r > m$, that is if number of outputs is greater than the number of inputs). In addition, matrix H should be well-conditioned, which occurs if the length of recorded signals is short enough. All the above conditions are met for the impact reconstruction, but there is still one hurdle to overcome. Specifically, the non-collocation of the impact and sensors positions results in a number of zero rows in the H_0 matrix, thereby rendering it rank-deficient. From a physical standpoint, this is due to the fact that the impulse of some of the input components has not yet reached any of the sensors by the end of the measured sequence. To solve this, a sensor-specific l-step time delay, is applied as first taught by [NORDSTRÖM 2005]. Furthermore, the use of previous knowledge regarding the TOA for each sensor in order to overcome the difficulty in choosing an optimal time delay l (a problem also faced by [NORDSTRÖM 2005]), is proposed in this thesis. Taking into account the specific sensor delay $l_1, \ldots, l_r$ the impact estimation (4.18) is reformulated for each individual sensor $s = s_1, \ldots, s_r$:

$$y_{k,s} = \sum_{i=l_s}^{k} h_{i,s} u_{k-i} \qquad k = l_s, \ldots, N \qquad (4.20)$$

where $y_{k,s}$ is the sth component of y_k and $_{i,s}$ is the sth row of H_i. It is clear from Equation (4.20) that only the input sequence $\{u_k\}_{k=0}^{N-\max(l_s)}$ will be obtained since the input with a longest signal transfer time $\max(l_s)$ cannot be determined from the output sequences at hand $\{y_k\}_{k=0}^{N}$. Introducing a new end time $N_l = N - \max(l_s)$ the final form of deconvolution problem in Equation (4.19) can be written as:

$$
\underbrace{\begin{bmatrix} \boldsymbol{H}_0^{TD} & \boldsymbol{H}_1^{TD} & \cdots & \boldsymbol{H}_{N_l}^{TD} \\ 0 & \boldsymbol{H}_0^{TD} & \cdots & \boldsymbol{H}_{N_l-1}^{TD} \\ \vdots & \vdots & \ddots & \vdots \\ 0 & 0 & \cdots & \boldsymbol{H}_0^{TD} \end{bmatrix}}_{\boldsymbol{H}^{TD}} \begin{bmatrix} \boldsymbol{u}_{N_l} \\ \boldsymbol{u}_{N_l-1} \\ \vdots \\ \boldsymbol{u}_0 \end{bmatrix} = \begin{bmatrix} \boldsymbol{y}_{N_l}^{TD} \\ \boldsymbol{y}_{N_l-1}^{TD} \\ \vdots \\ \boldsymbol{y}_0^{TD} \end{bmatrix},
\tag{4.21}
$$

where

$$
\begin{aligned}
\boldsymbol{H}_k^{TD} &= \begin{bmatrix} h_{(k+l_1),1} & h_{(k+l_2),2} & \cdots & h_{(k+l_r),r} \end{bmatrix}^T \\
\boldsymbol{y}_k^{TD} &= \begin{bmatrix} y_{(k+l_1),1} & y_{(k+l_2),2} & \cdots & y_{(k+l_r),r} \end{bmatrix}^T
\end{aligned}.
\tag{4.22}
$$

Thus, both Markov parameters and measurements have been shifted in time. An appropriate automatic individual shift is found with the help of a TOA calculated in the impact localization phase. This is set forth below in the application chapter together with comments on the complexity of models complexity for impact reconstruction.

4.3.2   Linear Quadratic Tracking Problem (LQTP)

This reconstruction method originating in control engineering attempts to solve the optimal tracking problem by finding an optimal control input. This approach is formulated as follows [LEWIS 1986]: "Construct an optimal control scheme that makes the system follow (or track) a desired trajectory over the entire time interval". For the force reconstruction procedure, the desired trajectories are the measured system responses which are used to find an optimal forcing function with the help of a dynamical model. Starting with a linear discrete system as in Chapter 2.1.5:

$$
\begin{aligned}
\boldsymbol{x}_{k+1} &= \boldsymbol{A}_D \boldsymbol{x}_k + \boldsymbol{B}_D \boldsymbol{u}_k = f(\boldsymbol{x}_k, \boldsymbol{u}_k) \\
\boldsymbol{y}_k &= \boldsymbol{C}_D \boldsymbol{x}_k
\end{aligned},
\tag{4.23}
$$

and bringing into focus the main goal of the study, which is: to make a certain linear combination of the states follow a desired known reference signal r_k over a time interval $[0,\ldots,N]$. The cost function (performance index) that should be minimized is of the following form:

$$
J_0 = \underbrace{\frac{1}{2}(\boldsymbol{C}_D \boldsymbol{x}_N - \boldsymbol{r}_N)^T \boldsymbol{P}(\boldsymbol{C}_D \boldsymbol{x}_N - \boldsymbol{r}_N)}_{\phi(N,\boldsymbol{x}_N)} + \underbrace{\frac{1}{2}\sum_{k=i}^{N-1}\left[(\boldsymbol{C}_D \boldsymbol{x}_k - \boldsymbol{r}_k)^T \boldsymbol{Q}(\boldsymbol{C}_D \boldsymbol{x}_k - \boldsymbol{r}_k) + \boldsymbol{u}_k^T \boldsymbol{R} \boldsymbol{u}_k\right]}_{L^k(\boldsymbol{x}_k,\boldsymbol{u}_k)}
\tag{4.24}
$$

where $\boldsymbol{P} \geq 0$, $\boldsymbol{Q} \geq 0$ and $\boldsymbol{R} > 0$ are positive definite and symmetric weighting matrices and the actual value $\boldsymbol{x}_N$ is not constrained; $[i, \dots, N]$ is the time interval over the region of interest; $\phi(N, \boldsymbol{x}_N)$ is the function of the final time N and the states at the final time, and $L^k(\boldsymbol{x}_k, \boldsymbol{u}_k)$ is an in-general time varying function of the states and control input at each intermediate time k in $[i, \dots, N\text{-}1]$. To find the optimal $\boldsymbol{u}_k$ which is related to the value of force at time k the cost function in Equation (4.24) together with the system Equations (4.23) which can also be considered as a constraint equation, are adjoined into the Hamiltonian function:

$$H_h = J_0 + \lambda^T f(\boldsymbol{x}_k, \boldsymbol{u}_k) \tag{4.25}$$

where λ^T are Lagrange multipliers. The minimal point of the performance index J_0 that satisfies the constraint equation $f(\boldsymbol{x}_k, \boldsymbol{u}_k) = 0$ is guaranteed by the necessary conditions:

State equation:

$$\frac{\partial H_h}{\partial \lambda} = f = 0 \qquad\qquad \Rightarrow \boldsymbol{x}_{k+1} = A_D \boldsymbol{x}_k + B_D \boldsymbol{u}_k . \tag{4.26}$$

Costate equation:

$$\frac{\partial H_h}{\partial \boldsymbol{x}} = J_{\boldsymbol{x}} + f_{\boldsymbol{x}}^T \lambda = 0 \qquad \Rightarrow \lambda_k = A_D^T \lambda_{k+1} + C_D^T Q C_D \boldsymbol{x}_k - C_D^T Q \boldsymbol{r}_k . \tag{4.27}$$

Stationary conditions:

$$\frac{\partial H_h}{\partial \boldsymbol{u}} = J_{\boldsymbol{u}} + f_{\boldsymbol{u}}^T \lambda = 0 \qquad \Rightarrow 0 = B_D^T \lambda_{k+1} + R \boldsymbol{u}_k , \tag{4.28}$$

where $(\cdot)_j \equiv \dfrac{\partial(\cdot)}{\partial j}$ is the gradient (column vector) with respect to the jth variable. These three equations allow determining $\boldsymbol{x}$, λ and $\boldsymbol{u}$ in that respective order. State and costate equations can be joined into a nonhomogeneous Hamiltonian system:

$$\begin{bmatrix} \boldsymbol{x}_{k+1} \\ \lambda_k \end{bmatrix} = \begin{bmatrix} A_D & -B_D R^{-1} B_D^T \\ C_D^T Q C_D & A_D^T \end{bmatrix} \begin{bmatrix} \boldsymbol{x}_k \\ \lambda_{k+1} \end{bmatrix} + \begin{bmatrix} \boldsymbol{0} \\ -C_D^T Q \end{bmatrix} \boldsymbol{r}_k , \tag{4.29}$$

where $\boldsymbol{r}_k$ represents the measurement at instance k so that the optimal input is found from the stationary condition

$$\boldsymbol{u}_k = -R^{-1} B_D^T \lambda_{k+1} . \tag{4.30}$$

Equations (1.31) and (1.32) cannot be practically implemented since the development occurs part forward and part backward in time. Nevertheless, by performing some algebraic operations and taking into account boundary conditions the optimal input can be found by the following scheme [LEWIS 1986]:

1. *Initialization*:

$$x_0 = 0$$
$$S_N = C_D^T P C_D \qquad (4.33)$$
$$v_N = C_D^T P r_N$$

2. *Backward sweep*:

$$K_k^{LQTP} = (B_D^T S_{k+1} B_D + R)^{-1} B_D^T S_{k+1} A_D \qquad (4.34)$$

$$S_k = A_D^T S_{k+1} (A_D - B_D K_k^{LQTP}) + C_D^T Q C_D \qquad (4.35)$$

$$v_k = (A_D - B_D K_k^{LQTP})^T v_{k+1} + C_D^T Q r_k \qquad (4.36)$$

$$K_k^v = (B_D^T S_{k+1} B_D + R)^{-1} B_D^T \qquad (4.37)$$

3. *Forward sweep*:

$$u_k = -K_k^{LQTP} x_k + K_k^v v_{k+1} \qquad (4.38)$$

$$x_{k+1} = A_D x_k + B_D u_k. \qquad (4.39)$$

At this point an optimal "control" input is found which would force the system to follow the desired trajectory. It is worth mentioning that the weighting matrices P, Q and R play an important role in the solution quality together with the complexity of the mathematical model. Their influence on the aluminum plate will be shown in the application example section 6.1 of this dissertation.

5 CONTINUOUS TIME LOAD RECONSTRUCTION

Far better an approximate answer to the right question,
which is often vague, than an exact answer to the wrong question,
which can always be made precise.
-John W. Tukey

In contrast to impact force reconstruction, which demands a location estimation followed by an impact history computation that should be done possibly fast, the continuous load case requires a permanent reconstruction at a normally predefined load position. On the one hand, this approach simplifies the estimation strategy as no localization procedure is necessary and implies the usage of a more complex observer theory to guarantee a permanent online estimation on the other. In this section, three possible candidate methods are considered that are capable to ensure a permanent load reconstruction. Their estimation capabilities and limitations will be presented together with the necessary requirements with respect to model quality and measurements quantities.

5.1   SIMULTANEOUS STATE AND INPUT ESTIMATOR

The Simultaneous State and Input Estimation (SS&IE) method is based on the observer principle shown in Figure 5.1, proposed by [HA and TRINH 2004], and has been originally used in the field of control engineering. This approach is robust to noisy measurements and applicable for both linear and nonlinear systems. Generally, it can be categorized among deterministic algorithms, which use a mathematical model as a basis for observer calculation.
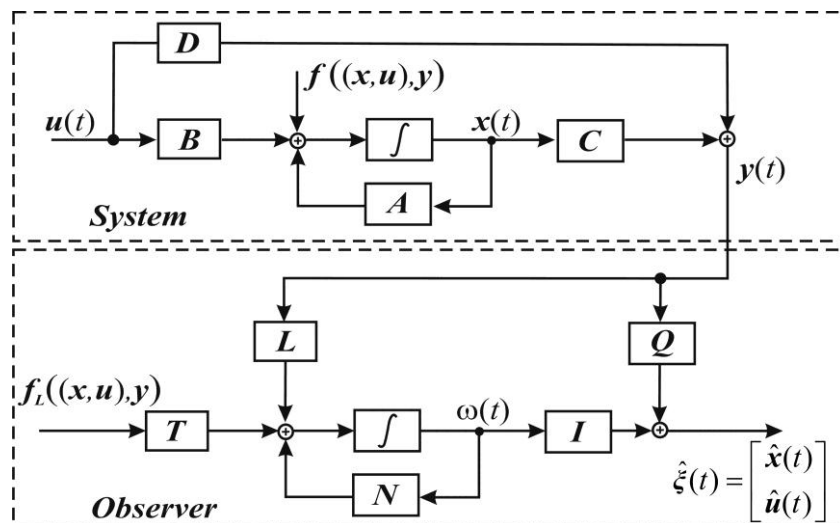
Figure 5.1: Simultaneous State and Input Estimator (SS&IE) for a class of nonlinear systems

5.1.1 Initial Model Definition

The problem of observer construction can be stated as follows. Consider a dynamic system as in Chapter 2.1.1 with n_q degrees of freedom, described by the second order differential equation of motion as:

$$M_n \ddot{q}(t) + D_n \dot{q}(t) + K_n q(t) + g\big(q(t), \dot{q}(t), u(t)\big) = B_o u(t), \tag{5.1}$$

here, $q(t) \in R^{n_q}$, $u(t) \in R^m$ are generalized coordinates (in this case nodal) and inputs accordingly. M_n, D_n, K_n and B_o are the mass, damping, stiffness and force allocation matrices of appropriate dimensions. $g(q(t), \dot{q}(t), u(t))$ is added to take into account nonlinear dependencies of the displacement, velocities and inputs.

Equation (5.1) can be transformed into state space notation with the following structure:

$$\begin{aligned} \dot{x}(t) &= Ax(t) + Bu(t) + f\big((x(t), u(t)), y(t)\big) \\ y(t) &= Cx(t) + Du(t) \end{aligned}, \tag{5.2}$$

where, $x(t) \in R^n$ (with $n = 2n_q$), $u(t) \in R^m$ and $y(t) \in R^r$ are the states, unknown inputs and measured outputs, respectively. $A_{n \times n}$, $B_{n \times m}$, $C_{r \times n}$ and $D_{r \times m}$ are real constants of appropriate dimensions. $f(\cdot)$ is a real nonlinear vector function on R^n (in the case of a nonlinear system) which combines two portions as follows:

$$f\big((x(t), u(t)), y(t)\big) = f_L\big((x(t), u(t)), y(t)\big) + W f_U\big((x(t), u(t)), y(t)\big), \tag{5.3}$$

where $f_L(\cdot) \in R^n$ and $f_U(\cdot) \in R^d$ are known Lipschitz and unknown nonlinear vectors, respectively. The matrix $W_{n \times d}$ is real and assumed to have full column rank d.

The objective is to design an asymptotic observer to estimate the unknown states $x(t)$ and unknown inputs $u(t)$ from the measured output signals $y(t)$. Therefore, a new state variable is introduced:

$$\xi(t) = \begin{bmatrix} x(t) \\ u(t) \end{bmatrix}, \quad \xi(t) \in R^{n+m} \tag{5.4}$$

and matrices E, M and H to combine the previous state space matrices:

$$E_{n \times (n+m)} = \begin{bmatrix} I_n & 0_{n \times m} \end{bmatrix}, \quad M_{n \times (n+m)} = \begin{bmatrix} A & B \end{bmatrix}, \quad H_{r \times (n+m)} = \begin{bmatrix} C & D \end{bmatrix}. \tag{5.5}$$

Using the new state variable, system (5.2) is transformed into algebraic differential equation:

$$E\dot{\xi}(t) = M\xi(t) + f_L\big(\xi(t), y(t)\big) + Wf_U\big(\xi(t), y(t)\big) \tag{5.6}$$

$$y(t) = H\xi(t). \tag{5.7}$$

The problem of the state and input estimator design for system (5.2) is now transformed into designing the observer for the generalized system in Equations (5.6) and (5.7), such that estimates $\hat{\xi}(t)$ converges asymptotically to the true states $\xi(t)$. For this purpose, a general minimal order observer structure, such as that in Chapter 2.2.3, is used with an additional nonlinear term:

$$\dot{\omega}(t) = N\omega(t) + Ly(t) + Tf_L\big(\hat{\xi}(t), y(t)\big) \tag{5.8}$$

$$\hat{\xi}(t) = \omega(t) + Qy(t), \tag{5.9}$$

where $\hat{\xi}(t)$ represents the state estimation of $\xi(t)$, $\omega(t) \in R^{n+m}$ is the observer states vector, and matrices N, L, T and Q are of appropriate dimension. As input the observer uses measured signals from the original system (5.7) and the known nonlinear function in its dynamic equation. In addition, measurements $y(t)$ are incorporated into the output observer Equation (5.9) as a correction term.

OBSERVER DESIGN PROCEDURE

The observer matrices N, L, T and Q need to be determined. To this end, a state estimation error is constructed first:

$$e(t) = \hat{\xi}(t) - \xi(t). \tag{5.10}$$

Using Equations (5.9) and (5.7), the error becomes

$$e(t) = \omega(t) + (QH - I_{n+m})\xi(t), \tag{5.11}$$

introducing the following relation

$$TE + QH = I_{n+m} \tag{5.12}$$

the state error is transformed into

$$e(t) = \omega(t) - TE\xi(t). \tag{5.13}$$

Taking the first derivative with respect to time and substituting expressions from (5.6) and (5.8) for $E\dot{\xi}(t)$ and $\dot{\omega}(t)$ respectively, the error dynamic is obtained as:

$$\dot{e}(t) = N\omega(t) + Ly(t) + Tf_L\left(\hat{\xi}(t), y(t)\right)$$
$$- T\left[M\xi(t) + f_L\left(\xi(t), y(t)\right) + Wf_U\left(\xi(t), y(t)\right)\right].$$

(5.14)

Inserting $y(t) = H\xi(t)$ and $\omega(t) = e(t) + TE\xi(t)$ from Equations (5.7) and (5.13) respectively the error dynamic finally appears as:

$$\dot{e}(t) = Ne(t) + \left[NTE + LH - TM\right]\xi(t) - TWf_U\left(\xi(t), y(t)\right)$$

$$+ T\left[f_L\left(\underbrace{e(t) + \xi(t)}_{\hat{\xi}(t)}, y(t)\right) - f_L\left(\xi(t), y(t)\right)\right]$$

(5.15)

According to Equation (5.15) the time dependant error would converge asymptotically to zero if the following conditions are held:

$$TE + QH = I_{n+m}$$

(5.16)

$$TW = 0$$

(5.17)

$$NTE + LH - TM = 0$$

(5.18)

Thus upon the satisfaction of conditions (5.16)-(5.18) the error dynamic expression (5.15) is reduced to:

$$\dot{e}(t) = Ne(t) + T\left[f_L\left(\hat{\xi}(t), y(t)\right) - f_L\left(\xi(t), y(t)\right)\right],$$

(5.19)

which would be asymptotically stable if the matrix N is Hurwitz (the real part of the eigenvalues must be negative) and the following assumption holds:

Assumption 1. $f_L(\cdot)$ is assumed to satisfy the Lipschitz condition with a Lipschitz constant γ so that:

$$\left\|f_L\left(\xi(t), y(t)\right) - f_L\left(\hat{\xi}(t), y(t)\right)\right\| \leq \gamma\left\|\xi(t) - \hat{\xi}(t)\right\|, \quad \forall y(t),$$

(5.20)

where, $\|\cdot\|$ represents the norm and γ is a positive scalar referred later as Lipschitz constant.

Combining the Equations (5.16) and (5.17) into a general one leads to:

$$Condition\ 1: \begin{cases} TE + QH = I_{n+m} \\ TW = 0 \end{cases}$$

(5.21)

In addition Equation (5.18) can be partitioned into two parts by $TE = I_{n+m} - QH$:

$$N + \left[L - NQ \right] H - TM = 0 .$$ (5.22)

Introducing a new matrix $F = L - NQ$, expression (5.22) can be written in terms of the general condition:

$$Condition\ 2: \begin{cases} N = TM - FH \\ F = L - NQ \end{cases}$$ (5.23)

5.1.2   Computation of the Observer Matrices T and Q

Condition 1 also can be written in a more compact form:

$$\begin{bmatrix} T & Q \end{bmatrix} S = \begin{bmatrix} I_{n+m} & 0 \end{bmatrix}, \text{where}\ S_{(n+r)\times(n+m+d)} = \begin{bmatrix} E_{n\times(n+m)} & W_{n\times d} \\ H_{r\times(n+m)} & 0_{r\times d} \end{bmatrix},$$ (5.24)

which can be directly used for calculation of the observer matrices T and Q. The matrix dimensions are added as subscripts for clarity. It is easy to show that the transpose of Equation (5.24):

$$S^T \begin{bmatrix} T^T \\ Q^T \end{bmatrix} = \begin{bmatrix} I_{n+m} \\ 0 \end{bmatrix}$$ (5.25)

is equivalent to the normal linear system of the form $AX = B$, where X is an unknown variable matrix and A and B are known matrices. The only condition for the solution existence is that the system in Equation (5.25) should be a consistent system[1], *i.e.* $rank(A) = rank(\begin{bmatrix} A & B \end{bmatrix})$ or, equivalently:

$$rank(S^T) = rank\left(\begin{bmatrix} S^T & I_{n+m} \\ & 0 \end{bmatrix} \right).$$ (5.26)

Using the rank property: $rank(A) = rank(A^T)$ equality (5.26) is rewritten as:

$$rank(S) = rank\left(\begin{bmatrix} S \\ I_{n+m} & 0 \end{bmatrix} \right).$$ (5.27)

The rank of the right hand side of Equation (5.27) is easily determined by taking into account the components of S matrix

---

[1] If the system has at least one solution it is called a consistent system

$$rank\left(\begin{bmatrix} \mathbf{S} \\ \mathbf{I}_{n+m} & \mathbf{0} \end{bmatrix}\right) = rank\begin{pmatrix} \mathbf{E} & \mathbf{W} \\ \mathbf{H} & \mathbf{0} \\ \mathbf{I}_{n+m} & \mathbf{0} \end{pmatrix} = n + m + rank(\mathbf{W}) = n + m + d \tag{5.28}$$

if $\mathbf{W}$ has full column matrix. The rank of $\mathbf{S}$ is evaluated as:

$$rank(\mathbf{S}) = rank\left(\begin{bmatrix} \mathbf{E} & \mathbf{W} \\ \mathbf{H} & \mathbf{0} \end{bmatrix}\right) = rank\left(\begin{bmatrix} \mathbf{I}_n & \mathbf{0}_{n\times m} & \mathbf{W}_{n\times d} \\ \mathbf{C}_{r\times n} & \mathbf{D}_{r\times m} & \mathbf{0}_{r\times d} \end{bmatrix}\right) \tag{5.29}$$

performing the simple row operation by multiplying Equation (5.29) from the left

$$\begin{aligned} rank(\mathbf{S}) &= rank\left(\begin{bmatrix} \mathbf{I}_n & \mathbf{0}_{n\times r} \\ -\mathbf{C}_{r\times n} & \mathbf{I}_r \end{bmatrix}\begin{bmatrix} \mathbf{I}_n & \mathbf{0}_{n\times m} & \mathbf{W}_{n\times d} \\ \mathbf{C}_{r\times n} & \mathbf{D}_{r\times m} & \mathbf{0}_{r\times d} \end{bmatrix}\right) \\ &= rank\left(\begin{bmatrix} \mathbf{I}_n & \mathbf{0}_{n\times m} & \mathbf{W}_{n\times d} \\ \mathbf{0}_{r\times n} & \mathbf{D}_{r\times m} & -\mathbf{C}_{r\times n}\mathbf{W}_{n\times d} \end{bmatrix}\right) \end{aligned} \tag{5.30}$$

Expression (5.30) can be finally written as:

$$rank(\mathbf{S}) = n + rank\left(\begin{bmatrix} \mathbf{D}_{r\times m} & -\mathbf{C}_{r\times n}\mathbf{W}_{n\times d} \end{bmatrix}\right). \tag{5.31}$$

Taking into account the definition of consistency (*i.e.* a solution for $\mathbf{T}$ and $\mathbf{Q}$) together with Equations (5.28) requires that the rank of matrix $\mathbf{S}$ be equal to $n+m+d$. This is only true for Equation (5.31) if the following assumption is held:

Assumption 2. Matrix $\begin{bmatrix} \mathbf{D} & \mathbf{CW} \end{bmatrix}$ has full column rank.

$$\text{rank}\left(\begin{bmatrix} \mathbf{D} & \mathbf{CW} \end{bmatrix}_{r\times(m+d)}\right) = m + d \tag{5.32}$$

Corollary, this assumption requires that the number of outputs should be at least equal to the number of unknown inputs plus the size of nonlinear terms $\mathbf{f}_U$ which do not satisfy the Lipschitz condition: $rank(r\times(m+d)) = \min(r, m+d) \Rightarrow r \geq m+d$. In addition, the $\mathbf{D}$ matrix should not be zero or empty to fulfil this condition. That makes the usage of acceleration sensors obligatory in this method.

If the equality in Equation (5.27) is not held then the system is inconsistent (*i.e.* the measurements are not independent). However, it is still possible to find $\mathbf{S}^-$, a generalized inverse of $\mathbf{S}$, and use it for the computation of the *general solution* of matrices $\mathbf{T}$ and $\mathbf{Q}$. The solution for the consistent system is only a part of the overall class of general solutions which can be obtained according to [RAO C. R. and MITRA S. K. 1971] for $\mathbf{AX} = \mathbf{B}$ as:

$$\mathbf{X} = \mathbf{A}^-\mathbf{B} + (\mathbf{I} - \mathbf{A}^-\mathbf{A})\mathbf{Z} \tag{5.33}$$

or, analogically:

$$[T \quad Q] = [I_{n+m} \quad 0] S^- + Z(I_{n+r} - SS^-) , \tag{5.34}$$

where S^- is a generalized inverse of matrix S and Z is an arbitrary symmetric matrix of real numbers. If S is a full column rank square matrix, the second part of the general solution is equal to zero, because $S^-S = SS^- = I$. In the other case the generalized solution attempts to compute the closest solution that is either in the row or column space of matrix S. Therefore the general solution is used as basis for the calculation of matrices T and Q, which are obtained as follows:

$$T = [I_{n+m} \quad 0] S^- \begin{bmatrix} I_n \\ 0 \end{bmatrix} + Z(I_{n+r} - SS^-) \begin{bmatrix} I_n \\ 0 \end{bmatrix} \tag{5.35}$$

$$Q = [I_{n+m} \quad 0] S^- \begin{bmatrix} 0 \\ I_r \end{bmatrix} + Z(I_{n+r} - SS^-) \begin{bmatrix} 0 \\ I_r \end{bmatrix} \tag{5.36}$$

Combining some parts of Equations (5.35) and (5.36) into new matrices:

$$G_{(n+r) \times n} = (I_{n+r} - SS^-) \begin{bmatrix} I_n \\ 0 \end{bmatrix}, \quad J_{(n+m) \times n} = [I_{n+m} \quad 0] S^- \begin{bmatrix} I_n \\ 0 \end{bmatrix} \tag{5.37}$$

$$K_{(n+r) \times r} = (I_{n+r} - SS^-) \begin{bmatrix} 0 \\ I_r \end{bmatrix}, \quad V_{(n+m) \times r} = [I_{n+m} \quad 0] S^- \begin{bmatrix} 0 \\ I_r \end{bmatrix}, \tag{5.38}$$

thus Equations (5.35) and (5.36) are now:

$$T = J + ZG \tag{5.39}$$

$$Q = V + ZK . \tag{5.40}$$

5.1.3 Computation of Observer Matrices N and L

The part of the observer is now calculated and can be used for the computation of the remaining observer matrices N and L, where two methods can be applied. The first one assumes general nonlinear systems and uses an LMI algorithm [BOYD *et al.* 1994] to assure the asymptotic stability of the error dynamic system via a Lyapunov function. The second approach considers solely linear systems and uses the standard pole placement procedure [NIU *et al.* 2010].

Recalling the error dynamic Equation (5.19) and substituting solution (5.39) for matrix $\boldsymbol{T}$ into the first part of condition 2, Equation (5.23) of the error dynamics is:

$$\dot{\boldsymbol{e}}(t) = (\bar{\boldsymbol{\Phi}} + \boldsymbol{Z}\bar{\boldsymbol{\Psi}} - \boldsymbol{F}\boldsymbol{H})\boldsymbol{e}(t) + (\boldsymbol{J} + \boldsymbol{Z}\boldsymbol{G})\left[\boldsymbol{f}_L(\boldsymbol{e}(t) + \xi(t), \boldsymbol{y}(t)) - \boldsymbol{f}_L(\xi(t), \boldsymbol{y}(t))\right] \qquad (5.41)$$

where, $\boldsymbol{N}$ has been substituted by:

$$\boldsymbol{N} = \boldsymbol{T}\boldsymbol{M} - \boldsymbol{F}\boldsymbol{H} = \boldsymbol{J}\boldsymbol{M} + \boldsymbol{Z}\boldsymbol{G}\boldsymbol{M} - \boldsymbol{F}\boldsymbol{H} = \bar{\boldsymbol{\Phi}} + \boldsymbol{Z}\bar{\boldsymbol{\Psi}} - \boldsymbol{F}\boldsymbol{H}. \qquad (5.42)$$

Matrices $\bar{\boldsymbol{\Phi}} = \boldsymbol{J}\boldsymbol{M}$ and $\bar{\boldsymbol{\Psi}} = \boldsymbol{J}\boldsymbol{M}$ are introduced for the sake of simplicity. The error dynamics, Equation (5.41), incorporates the nonlinear terms; therefore, one way to ensure its asymptotic convergence to zero is to use the Lyapunov stability method. To this end a Lyapunov candidate summarizing function is introduced:

$$V(\boldsymbol{e}(t)) = \boldsymbol{e}^T(t)\boldsymbol{P}\boldsymbol{e}(t), \qquad (5.43)$$

where $\boldsymbol{P}$ is a symmetric positive definite matrix. Considering Equations (2.56) to (2.59), if the first derivative of V is smaller than zero for all time, then the nonlinear error function in Equation (5.41) is stable and converges to zero. Taking a derivative of V with respect to time and substituting Equation (5.41) for $\dot{\boldsymbol{e}}(t)$ leads to the following expression:

$$\begin{aligned}
\dot{V}(\boldsymbol{e}) = \boldsymbol{e}^T(t)\Big(\boldsymbol{P}\bar{\boldsymbol{\Phi}} + \boldsymbol{P}\boldsymbol{Z}\bar{\boldsymbol{\Psi}} - \boldsymbol{P}\boldsymbol{F}\boldsymbol{H} + \bar{\boldsymbol{\Phi}}^T\boldsymbol{P} + \bar{\boldsymbol{\Psi}}^T\boldsymbol{Z}^T\boldsymbol{P} - \boldsymbol{H}^T\boldsymbol{F}^T\boldsymbol{P} \Big)\boldsymbol{e}(t) \\
+ \boldsymbol{e}^T(t)\Big(\left(\boldsymbol{P}\boldsymbol{J} + \boldsymbol{P}\boldsymbol{Z}\boldsymbol{G}\right)\tilde{\boldsymbol{f}}_L + \tilde{\boldsymbol{f}}_L^T\left(\boldsymbol{J}^T\boldsymbol{P} + \boldsymbol{G}^T\boldsymbol{Z}^T\boldsymbol{P}\right)\Big)\boldsymbol{e}(t)
\end{aligned} \qquad (5.44)$$

where, $\boldsymbol{f}_L(\boldsymbol{e}(t) + \xi(t), \boldsymbol{y}(t)) - \boldsymbol{f}_L(\xi(t), \boldsymbol{y}(t))$ is referred to as $\tilde{\boldsymbol{f}}_L$ for simplicity. Using the Yong's matrix inequality $\boldsymbol{Z}\boldsymbol{Y}^T + \boldsymbol{Y}\boldsymbol{Z}^T \le \kappa \boldsymbol{Y}\boldsymbol{Y}^T + \dfrac{1}{\kappa}\boldsymbol{Z}\boldsymbol{Z}^T$ [ZHAN 2002], where κ is a positive scalar, the second part of Equation (5.44) is modified as:

$$\begin{aligned}
\boldsymbol{e}^T(t)\Big(\left(\boldsymbol{P}\boldsymbol{J} + \boldsymbol{P}\boldsymbol{Z}\boldsymbol{G}\right)\tilde{\boldsymbol{f}}_L + \tilde{\boldsymbol{f}}_L^T\left(\boldsymbol{J}^T\boldsymbol{P} + \boldsymbol{G}^T\boldsymbol{Z}^T\boldsymbol{P}\right)\Big)\boldsymbol{e}(t) \\
\le \frac{1}{\kappa_1}\boldsymbol{e}^T(t)\boldsymbol{P}\boldsymbol{J}\boldsymbol{J}^T\boldsymbol{P}\boldsymbol{e}(t) + \kappa_1\tilde{\boldsymbol{f}}_L^T\tilde{\boldsymbol{f}}_L + \frac{1}{\kappa_2}\boldsymbol{e}^T(t)\boldsymbol{P}\boldsymbol{Z}\boldsymbol{G}\boldsymbol{G}^T\boldsymbol{Z}^T\boldsymbol{P}\boldsymbol{e}(t) + \kappa_2\tilde{\boldsymbol{f}}_L^T\tilde{\boldsymbol{f}}_L.
\end{aligned} \qquad (5.45)$$

Substitution of Equation (5.45) into (5.44) subject to Assumption 1 gives [HA and TRINH 2004]:

$$\dot{V}(\boldsymbol{e}) = \boldsymbol{e}^T(t)\boldsymbol{R}_{LMI}\boldsymbol{e}(t) + (\kappa_1 + \kappa_2)\tilde{\boldsymbol{f}}_L^T\tilde{\boldsymbol{f}}_L \le \boldsymbol{e}^T(t)\Big(\boldsymbol{R}_{LMI} + \gamma^2(\kappa_1 + \kappa_2)\boldsymbol{I}\Big)\boldsymbol{e}(t) \qquad (5.46)$$

where

$$R_{LMI} = P\bar{\Phi} + \bar{\Phi}^T P + PZ\bar{\Psi} + \bar{\Psi}^T Z^T P - PFH - H^T F^T P$$
$$+ \frac{1}{\kappa_1} PJJ^T P + \frac{1}{\kappa_2} PZGG^T Z^T P \qquad , \qquad (5.47)$$

and γ is a Lipschitz constant from Assumption 1. Therefore, the estimation error $e(t) \to 0$ as the time $t \to \infty$ if the derivative of Lyapunov function $\dot{V}(e) < 0$.

Hence,

$$\left(R_{LMI} + \gamma^2(\kappa_1 + \kappa_2)I \right) < 0 \qquad (5.48)$$

must hold. Equation (5.48) is a Riccati inequality which should be solved in a computationally efficient manner. For the sake of simplicity new variables that combine constant matrices are introduced:

$$X = PF, \qquad Y = PZ . \qquad (5.49)$$

Riccati inequality (5.48) thus becomes:

$$P\bar{\Phi} + \bar{\Phi}^T P + Y\bar{\Psi} + \bar{\Psi}^T Y^T - XH - H^T X^T + \frac{1}{\kappa_1} PJJ^T P + \frac{1}{\kappa_2} YGG^T Y^T + \gamma^2(\kappa_1 + \kappa_2)I < 0. \qquad (5.50)$$

Using the Schur complement [ZHANG 2005] (5.50) can be transformed into a more compact form of LMI:

$$\begin{bmatrix} \bar{\Phi}^T P + \bar{\Psi}^T Y^T - H^T X^T + P\bar{\Phi} + Y\bar{\Psi} - XH + \gamma^2(\kappa_1 + \kappa_2)I & PJ & YG \\ J^T P & -\kappa_1 I & 0 \\ G^T Y^T & 0 & -\kappa_2 I \end{bmatrix} < 0 \qquad (5.51)$$

and solved numerically by the *interior-point polynomial algorithm* [BOYD *et al.* 1994]. The estimation error $e(t) = \hat{\xi}(t) - \xi(t)$ will converge to zero if the matrices $P = P^T > 0$, X, Y and positive scalars κ_1 and κ_2 exist such the LMI (5.51) is satisfied. Finally the observer matrices N and L can be calculated according to the following algorithm:

1. Provide a mathematical model in state space representation (either by analytical modelling or by an identification procedure).

2. Solve the LMI problem (5.51) (*e.g.* using the Matlab LMI toolbox) [NESTEROV and NEMIROVSKI 1994].

3. If P, X, Y, κ_1 and κ_2 satisfying the LMI (5.51) are found then go to step 4, otherwise choose a smaller value of γ.

4. Obtain the matrices $Z = P^{-1}Y$ and $F = P^{-1}X$. The observer matrices N and L are then given as in Equations (5.42) and (5.23):

$$N = \Phi + Z\Psi - FH \tag{5.52}$$

$$L = F + NQ \tag{5.53}$$

If the matrix S in Equation (5.37) and (5.38) is square of a full rank, the matrices G and K which represent the error after generalized inverse are equal to zero. Hence $\bar{\Psi} = 0$ and one can choose Z and Y equal to zero. In this case the LMI (5.51) is reduced to:

$$\begin{bmatrix} \bar{\Phi}^T P - H^T X^T + P\bar{\Phi} - XH + \gamma^2 \kappa_1 I & PJ \\ J^T P & -\kappa_1 I \end{bmatrix} < 0 \,. \tag{5.54}$$

The procedure of N and L computation stays the same as before except for minor modifications in Equation (5.52) where $Z\bar{\Psi}$ is equal to zero.

N AND L COMPUTATION VIA POLE PLACEMENT

To ensure the stable dynamics of the error function in (5.19) subject to Assumption 1 (5.20) the matrix N should be Hurwitz or in other words, have all eigenvalues in the negative region of the phase plane. On closer observation, Equation (5.42) can be reformulated as:

$$\underset{p}{N^T} = \bar{\Phi}^T - \underbrace{\begin{bmatrix} -\bar{\Psi}^T & H^T \end{bmatrix}}_{B} \underbrace{\begin{bmatrix} Z^T \\ F^T \end{bmatrix}}_{K} = \bar{\Phi}^T - \Lambda^T \begin{bmatrix} Z^T \\ F^T \end{bmatrix} \tag{5.55}$$

where, matrices $\bar{\Phi}$, H and $\bar{\Psi}$ are known matrices and $\Lambda^T = \begin{bmatrix} -\bar{\Psi}^T & H^T \end{bmatrix}$, opening the similarity to a general closed loop state space system with a state feedback input as:

$$\dot{x}(t) = Ax(t) + Bu(t), \quad \text{with: } u(t) = -Kx(t) \Rightarrow \dot{x}(t) = (A - BK)x(t) \tag{5.56}$$

with a desired closed loop dynamics $(A - BK)$ characterized by predefined closed loop poles p which can be achieved by proper choice of a feedback gain matrix K (*e.g.* by means of Ackermann's formula [KAILATH 1980]). Therefore, another possible way to compute observer matrices N and L is to use the standard pole placement procedure [NIU *et al.* 2010], in particular by assigning predefined negative eigenvalues to matrix N and successive calculation of matrices Z and F by means of a pole placement procedure [KAUTSKY *et al.* 1985] if

the matrix pair $(\bar{\boldsymbol{\Phi}}^{T}, \boldsymbol{\Lambda}^{T})$ is controllable (*e.g.* the matrix pair $(\boldsymbol{\Lambda}, \bar{\boldsymbol{\Phi}})$ is observable). The observer matrix $\boldsymbol{L}$ is then computed as before with the help of Equation (5.53).

5.1.4   Effect of the Process and Measurement Noise

It is valid to mention that in the observer design the absence of measurement and process noise has been assumed. Nevertheless, the measurement and model uncertainties are always present in real world applications. Adding both process noise $\boldsymbol{w}(t)$ and measurement errors $\boldsymbol{v}(t)$ to the system in Equations (5.6) and (5.7) leads to:

$$\boldsymbol{E}\dot{\boldsymbol{\xi}}(t) = \boldsymbol{M}\boldsymbol{\xi}(t) + \boldsymbol{f}_{L}\big(\boldsymbol{\xi}(t), \boldsymbol{y}(t)\big) + \boldsymbol{W}\boldsymbol{f}_{U}\big(\boldsymbol{\xi}(t), \boldsymbol{y}(t)\big) + \boldsymbol{w}(t) \tag{5.57}$$

$$\boldsymbol{y}(t) = \boldsymbol{H}\boldsymbol{\xi}(t) + \boldsymbol{v}(t). \tag{5.58}$$

Employing the previously defined observer model as in Equations (5.8) and (5.9), the error dynamic Equation (5.19) under satisfaction of conditions 1 and 2 is of the following form:

$$\begin{aligned}
\dot{\boldsymbol{e}}(t) = \boldsymbol{N}\boldsymbol{e}(t) &+ \boldsymbol{T}\big[\boldsymbol{f}_{L}(\boldsymbol{e}(t) + \boldsymbol{\xi}(t), \boldsymbol{y}(t)) - \boldsymbol{f}_{L}(\boldsymbol{\xi}(t), \boldsymbol{y}(t))\big] \\
&+ \big(\boldsymbol{L} - \boldsymbol{N}\boldsymbol{Q}\big)\boldsymbol{v}(t) + \boldsymbol{Q}\dot{\boldsymbol{v}}(t) - \boldsymbol{T}\boldsymbol{w}(t)
\end{aligned} \tag{5.59}$$

Examination of the error dynamic equation shows that both inaccuracies are amplified by the observer matrices. Consequently, they will appear as a reconstruction error in the estimated variables or even lead to complete observer failure if the model and measurement noise are prevailing. This effect will be apparent when shown in the examples section.

5.2   PROPORTIONAL INTEGRAL OBSERVER

5.2.1   Initial Formulation

The Proportional Integral Observer (PIO) originally appeared in the work of [WOJCIECHOWSKI 1978], as an extension of the classical proportional Luenberger observer [LUENBERGER 1971]. The PIO scheme, shown in Figure 5.2(a), was utilized by [SÖFFKER *et al.* 1995; KRAJCIN and SÖFFKER 2005], and has been used for reconstruction and compensation of the unknown disturbances/nonlinearities which were assumed to be piecewise constant functions. The original system in Figure 5.2(a) is written in a general state space form:

$$\begin{aligned}
\dot{\boldsymbol{x}}(t) &= \boldsymbol{A}\boldsymbol{x}(t) + \boldsymbol{B}\boldsymbol{u}(t) + \boldsymbol{N}\boldsymbol{n}(\boldsymbol{x}(t), \boldsymbol{u}(t), t) \\
\boldsymbol{y}(t) &= \boldsymbol{C}\boldsymbol{x}(t) + \boldsymbol{v}(t)
\end{aligned} \tag{5.60}$$

where $x(t) \in R^n$, $u(t) \in R^m$ and $y(t) \in R^r$ are similar to Equation (5.2), $n(x,u,t) \in R^{n_2}$ is a vector function which describes nonlinearities, unknown inputs and unmodelled dynamics of the plant, and $v(t) \in R^r$ represents the measurement noise.
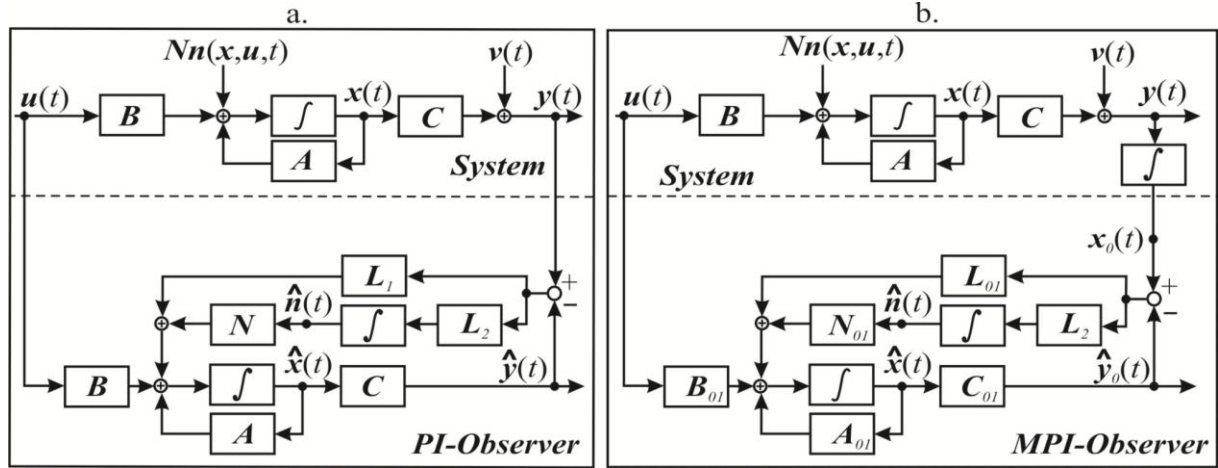
Figure 5.2: The original system and (a) – proportional integral observer (PIO); (b) – modified proportional integral observer (MPIO)

Matrix N is a corresponding nonlinearity distribution matrix which is assumed to be known. The PIO in Figure 5.2(a) is of the following form:

$$\dot{\hat{x}}(t) = A\hat{x}(t) + N\hat{n}(t) + Bu(t) + L_1(y(t) - \hat{y}(t)), \quad \hat{y}(t) = C\hat{x}(t)$$
$$\dot{\hat{n}}(t) = L_2(y(t) - \hat{y}(t))$$

(5.61)

or, in extended form:

$$\begin{bmatrix} \dot{\hat{x}}(t) \\ \dot{\hat{n}}(t) \end{bmatrix} = \begin{bmatrix} A - L_1C & N \\ -L_2C & 0 \end{bmatrix} \begin{bmatrix} \hat{x}(t) \\ \hat{n}(t) \end{bmatrix} + \begin{bmatrix} B \\ 0 \end{bmatrix} u(t) + \begin{bmatrix} L_1 \\ L_2 \end{bmatrix} y(t)$$

(5.62)

where $\hat{x}(t)$ and $\hat{n}(t)$ are the estimates of $x(t)$ and $n(t)$ respectively, and matrices L_1 and L_2 are to-be-designed PIO gain matrices. Defining the state estimation error $e(t) = \hat{x}(t) - x(t)$ and input estimation error $\tilde{n}(t) = \hat{n}(t) - n(t)$, then the error dynamic equation of PIO becomes:

$$\begin{bmatrix} \dot{e}(t) \\ \dot{\tilde{n}}(t) \end{bmatrix} = \begin{bmatrix} A_e - L_{PIO}C_e \end{bmatrix} \begin{bmatrix} e(t) \\ \tilde{n}(t) \end{bmatrix} - F_e\dot{n}(t) + L_{PIO}v(t),$$

(5.63)

where $A_e = \begin{bmatrix} A & N \\ 0 & 0 \end{bmatrix}$, $L_{PIO} = \begin{bmatrix} L_1 \\ L_2 \end{bmatrix}$, $C_e = \begin{bmatrix} C & 0 \end{bmatrix}$ and $F_e = \begin{bmatrix} 0 \\ I \end{bmatrix}$ are the matrices of the extended system. Apparently, the error Equation (5.63) is strongly influenced by the dynamics of the unknown and measurement disturbances $\dot{n}(t)$ and $v(t)$ respectively. If the disturb-

ance $n(t)$ is slowly-changing ($\dot{n}(t) \approx 0$) and the measurement noise $v(t)$ is bounded by small scalar σ, *i.e.* $\|v\| \leq \sigma << 1$, then it is possible to force the error in Equation (5.63) to be asymptotically stable as the time evolves, by shifting the poles in Equation (5.63) at the arbitrary negative locations with the help of the observer gain matrix L_{PIO} if the matrix pair (A_e, C_e) is observable. The observability condition implies that the number of independent measurements should be equal to or greater than the number of states and unknown disturbances *i.e.* $r \geq n + n_2$. Computation of the PIO gain matrix can be done either by an eigenstructure assignment strategy [DUAN *et al.* 2001] or by using a Loop Transfer Recovery (LTR) design method [SHAFAI *et al.* 1996]. By using the second algorithm the gain matrix L_{PIO} can be obtained by solving the following algebraic Riccati equation:

$$A_e P + P A_e^T + Q_{LTR} - P C_e^T R_{LTR}^{-1} C_e P = 0 \quad \Rightarrow L_{PIO} = P C_e^T R^{-1}, \tag{5.64}$$

where, Q_{PIO} is a weighting matrix of an extended system and R_{PIO} is a weighting matrix of measurement, constructed as:

$$\begin{aligned} Q_{LTR} &= I_{(n+n_2)\times(n+n_2)} + q_{LTR} F_e I_{(n+n_2)\times(n+n_2)} F_e^T \\ R_{LTR} &= I_{r\times r} \end{aligned} \tag{5.65}$$

and P is a positive definite symmetric matrix. The q_{LTR} is an LTR design parameter which has to be chosen very large to achieve satisfactory results [DOYLE and STEIN 1979]. This choice leads to large values in L_{PIO} gain, and as a result the PIO observer is also known as a high gain observer. The high observer gains do not only serve for the fast observer convergence but simultaneously magnify measurement noise $v(t)$ which leads to inacceptable performance. To attenuate the influence of the measurement noise, a modified formulation of the PIO (MPIO), as in Figure 5.2(b), has been proposed by [KRISHNA and POUSGA 2001], where additional integration of the measured output has been added:

$$x_0(t) = \int_0^t y(\tau)d\tau, \quad \Rightarrow y(t) = \dot{x}_0(t), \tag{5.66}$$

so that the original system is of the following form:

$$\begin{aligned} \dot{z}(t) &= A_0 z(t) + B_0 u(t) + N_0 n(x(t), u(t), t) + C_{01}^T v(t) \\ y_0(t) &= C_{01} z(t) \end{aligned} \tag{5.67}$$

where, $z(t) = \begin{bmatrix} x_0(t) & x(t) \end{bmatrix}^T$ is the augmented state variable $z(t) \in R^{n+r}$, and

$A_0 = \begin{bmatrix} 0 & C \\ 0 & A \end{bmatrix}$, $B_0 = \begin{bmatrix} 0 \\ B \end{bmatrix}$, $N_0 = \begin{bmatrix} 0 \\ N \end{bmatrix}$ and $C_{01} = \begin{bmatrix} I & 0 \end{bmatrix}$ are   the   augmented   matrices   of

appropriate dimensions. The PIO structure in Equation (5.62) is modified accordingly:

$$\begin{bmatrix} \dot{\hat{z}}(t) \\ \dot{\hat{n}}(t) \end{bmatrix} = \begin{bmatrix} A_0 - L_{01}C_{01} & N_0 \\ -L_2 C_{01} & 0 \end{bmatrix} \begin{bmatrix} \hat{z}(t) \\ \hat{n}(t) \end{bmatrix} + \begin{bmatrix} B_0 \\ 0 \end{bmatrix} u(t) + \begin{bmatrix} L_{01} \\ L_2 \end{bmatrix} y_0(t) \qquad (5.68)$$

Letting the state estimation error $e(t) = \hat{z}(t) - z(t)$ and input estimation error $\tilde{n}(t) = \hat{n}(t) - n(t)$

be as before, the error dynamic equation of the MPIO appears to be:

$$\begin{bmatrix} \dot{e}(t) \\ \dot{\tilde{n}}(t) \end{bmatrix} = \begin{bmatrix} A_{me} - L_{MPIO} C_{me} \end{bmatrix} \begin{bmatrix} e(t) \\ \tilde{n}(t) \end{bmatrix} - F_{me}\dot{n}(t) + C_{me}^T v(t) \qquad (5.69)$$

where, $A_{me} = \begin{bmatrix} A_0 & N_0 \\ 0 & 0 \end{bmatrix}$, $L_{MPIO} = \begin{bmatrix} L_{01} \\ L_2 \end{bmatrix}$, $C_{me} = \begin{bmatrix} C_{01} & 0 \end{bmatrix}$ and $F_{me} = \begin{bmatrix} 0 \\ I \end{bmatrix}$ are   the   matrices   of

extended system. From Equation (5.69) one can clearly see that the disturbance $v(t)$ is not any

more affected by the high observer gains. Therefore if the matrix pair (A_{me}, C_{me}) is observable

then it is possible to compute the MPIO gain L_{MPIO} such that stabilizing terms prevail over the

perturbation term $C_{me}^T v(t)$, for the slowly changing disturbance/nonlinearity ($\dot{n}(t) \approx 0$). The

computation can be done in a similar manner as for classical PIO structure.

5.2.2   Load Reconstruction Formulation

In the case when the MPIO is used for the reconstruction of external loads, the original block

diagram in Figure 5.2(b) needs to be customized. The modification is done by leaving out the

input line and by assigning $n(t) = u(t)$ simultaneously setting the placement matrix $N = B$.

This is schematically shown in Figure 5.3.

A new mathematical model of the extended system is similar to Equation (5.67):

$$\begin{aligned} \dot{z}(t) &= A_0 z(t) + B_0 u(t) + C_{01}^T v(t) \\ y_0(t) &= C_{01} z(t) \end{aligned}, \qquad (5.70)$$

as well as a customized MPIO model analogous to Equation (5.68):

$$\begin{bmatrix} \dot{\hat{z}}(t) \\ \dot{\hat{u}}(t) \end{bmatrix} = \begin{bmatrix} A_0 - L_{01}C_{01} & B_0 \\ -L_2 C_{01} & 0 \end{bmatrix} \begin{bmatrix} \hat{z}(t) \\ \hat{u}(t) \end{bmatrix} + \begin{bmatrix} L_{01} \\ L_2 \end{bmatrix} y_0(t). \qquad (5.71)$$
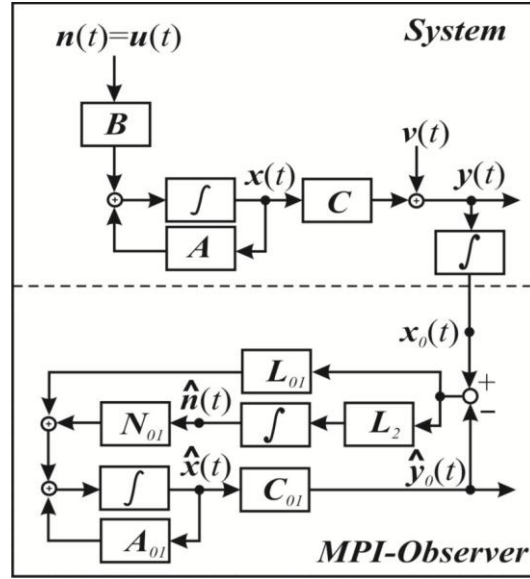
Figure 5.3: Customized MPIO for load reconstruction

The error dynamic Equation (5.69) has not been changed by the above manipulations. In the error dynamic equation, either for PIO (5.63) or MPIO (5.69), a major assumption has been made with respect to the rate of change of the unknown input/disturbance $\dot{n}(t) \approx 0$ which would guarantee the required observer performance. As a result, the rapidly changing unknown inputs will cause a high level of divergence between estimated and real inputs, which would be exemplified in Chapter 6.

5.3   KALMAN FILTER WITH UNKNOWN INPUTS

Numerous attempts have been made to employ the Kalman filter theory for simultaneous input and state estimation. In recent work, [PAN *et al.* 2010] has proposed to use the Kalman filter with unknown inputs (KF-UI) for the jointed estimation of the inputs and states. For this purpose Pan first combined the states and unknown inputs into an extended state vector. The weighted least square problem similar to Equation (2.88) was then solved for the extended state vector recursively as in Equations (2.91) - (2.104). This led to the KF-UI which is designed for the original invariant discrete-time system as in Equation (2.108) with added direct feed through matrix $\boldsymbol{D}_D$ to the output equation:

$$
\begin{aligned}
\boldsymbol{x}_{k+1} &= \boldsymbol{A}_D \boldsymbol{x}_k + \boldsymbol{B}_D \boldsymbol{u}_k + \boldsymbol{w}_k \\
\tilde{\boldsymbol{y}}_k &= \boldsymbol{C}_D \boldsymbol{x}_k + \boldsymbol{D}_D \boldsymbol{u}_k + \boldsymbol{v}_k
\end{aligned}
\tag{5.72}
$$

where $\boldsymbol{x}_k \in R^n, \boldsymbol{y}_k \in R^r$ and $\boldsymbol{u}_k \in R^m$. The process $\boldsymbol{w}_k$ noise and measurement noise $\boldsymbol{v}_k$ respectively, are assumed to be mutually uncorrelated zero-mean Gaussian signals with

known covariance matrices $Q_k = E\{w_k w_k^T\}$ and $R_k = E\{v_k v_k^T\}$. If for the system in Equation (5.72) the following conditions are satisfied:

1. the number of outputs is greater than the number of unknown inputs: $r > m$
2. matrix pair (A_D, C_D) is observable,

   i.e. $\left[C_{D,0}^T, \quad A_{D,0}^T C_{D,1}^T, \quad \ldots \quad , A_{D,0}^T A_{D,1}^T \cdots A_{D,k-1}^T C_{D,k}^T \right]^T$ has full column rank ($k \geq 1$)

3. the matrix $(D_D - C_D A_D^{-1} B_D)$ has full column rank, i.e.

   $rank(D_{D,i} - C_{D,i} A_{D,i}^{-1} B_{D,i}) = m$ with ($i = 0,1,2,\cdots,k-1$ and $k \geq 1$)

4. matrix D_D has full column rank i.e. $rank(D_D) = m$

then a minimum variance unbiased (MVU) Kalman estimator exists [PAN et al. 2010]. The KF-UI is computed in the following recursive steps:

1. *Initialization*

   a. $\hat{x}(t_0) = \hat{x}_0 \qquad \hat{u}(t_0) = \hat{u}_0$

   b. $P_0 = E\left\{\tilde{x}(t_0)\tilde{x}^T(t_0)\right\}$, with $\quad \tilde{x} = \hat{x} - x$ $\qquad\qquad$ (5.73)

   c. $S_0 = E\left\{\tilde{u}(t_0)\tilde{u}^T(t_0)\right\}$, with $\quad \tilde{u} = \hat{u} - u$

2. *Gains*

   $$K_k = P_k^- C_D^T (C_D P_k^- C_D^T + R_k)^{-1}$$
   $$S_k = \left(D_D^T R_k^{-1} (I_r - C_D K_k) D_D \right)^{-1}$$

   (5.74)

3. *Update*

   a. $\hat{u}_k = S_k D_D^T R_k^{-1} (I_r - C_D K_k)(\tilde{y}_k - C_D \hat{x}_k^-)$

   b. $\hat{x}_k^+ = \hat{x}_k^- + K_k(\tilde{y}_k - C_D \hat{x}_k^- - D_D \hat{u}_k)$ $\qquad\qquad$ (5.75)

   c. $P_k^+ = (I_n - K_k D_D S_k D_D^T R_k^{-1} C_D)(I_n - K_k C_D)P_k^-$

4. *Propagation*

   a. $\hat{x}_{k+1}^- = A_D \hat{x}_k^+ + B_D \hat{u}_k$ $\qquad\qquad$ (5.76)

   b. $P_{k+1}^- = A_D P_k^+ A_D^T + B_D D_D^T R_k^{-1} C_D A_D^T + A_D C_D^T R_k^{-1} D_D B_D^T + B_D S_k B_D^T + Q_k$

The evolution of the algorithm is as follows: if the measurements are available at the initial time then the states x, the inputs u and covariance P are updated using Equations (5.74) and (5.75) with $\hat{x}_0^- = \hat{x}_0$ and $P_0^- = P_0$, as the covariance and the states are propagated according to Equations (5.76); If the measurements are unavailable at the initial time then the estimate

and covariance are propagated first to the next available measurement point with $\hat{\boldsymbol{x}}_0^+ = \hat{\boldsymbol{x}}_0$ and

$\boldsymbol{P}_0^+ = \boldsymbol{P}_0$. The process is then repeated sequentially (steps 2 to 4). This estimation process will be used in the example section, where all the candidate algorithms will be tested on the same structure.

5.4   ALGORITHMS SUMMARY

All the algorithms mentioned in sections 5.1, 5.2 and 5.3 have their strong and weak sides which are explicit outcomes of the method assumptions or generalizations. To reveal them all they are summarized in a more compact form below.

5.4.1   Necessary Conditions and Assumptions

NUMBER AND TYPE OF MEASUREMENTS REQUIRED

All of three algorithms (MPIO, SS&IE and KF-UI) require that the system under consideration possesses the observability, *i.e.* observability matrix $\boldsymbol{O}$ in Equation (2.67) has full column rank. As a result the number of sensors should be equal to or greater than the number of unknown functions (inputs/nonlinearities). In addition, the SS&IE and KF-UI require the full column rank of the direct feed through matrix $\boldsymbol{D}$, thus the sensors that would generate this matrix into output equation are necessary*, e.g.* accelerometers. On the other hand the MPIO algorithm deals with a simplified output equation that considers solely the linear combination of the states in the acquired measurements, see Equation (5.67); as a consequence, displacement, velocity or strain gauges need to be utilized.

ALGORITHMS SENSITIVITY

Both MPIO and KF-UI work for linear systems and are tolerant to measurement noise, whereas the SS&IE can handle both linear and nonlinear systems but is more sensitive to measurement disturbances, see Equation (5.59). Therefore, if the SS&IE method is utilized special prerequisites should be taken for the noise attenuation. Moreover, the KF-UI has certain inherent advantages over the others due to its capability to minimize the error caused by the model uncertainties and also due to its potential to handle time variant systems (*i.e.* the realization $\boldsymbol{A}_D$, $\boldsymbol{B}_D$, $\boldsymbol{C}_D$, and $\boldsymbol{D}_D$ in Equations (5.72)-(5.76) can be replaced with time varying matrices respectively). In addition, the usage of the MPIO algorithm will lead to a higher error if the unknown input function is of a fast dynamical nature (*e.g.* impact load), see Equation (5.69).

5.4.2   Sensors Allocation and Model Type

In the light of the above observations, and in particular of the conditions applied to matrix D for SS&IE and KF-UI algorithms, it is important to mention that the full column rank holds only for the case when the unknown inputs are collocated with specific sensors, *e.g.* accelerometers. Nevertheless, this requirement can be released if the system realization (A, B, C, D) is obtained from the model in modal coordinates, see for details Chapter 2.1.1. In this case the full column rank condition of the matrix D holds if the sensor is placed in the vicinity of the original input location.

All the above issues are exemplified in section 6.2, where all three candidates are tested on the similar test rig.

6 NUMERICAL STUDIES AND APPLICATION EXAMPLES

In theory, there is no difference between theory and practice;

In practice, there is.

-Chuck Reid

In this section, the load estimation approaches which are mentioned in Chapters 4 and 5 are applied to different test structures. This Chapter provides an overview of the strong and weak sides of every particular algorithm, starting with an impact type load reconstruction on an aluminum plate in section 6.1. It then covers the continuous time online load estimation for lamped mass in section 6.2 and spatial distributed structures in sections 6.3 and 6.4. Lastly, a force estimation procedure for a nonlinear test rig is considered in section 6.5.

6.1 IMPACT LOAD RECONSTRUCTION ON ALUMINUM PLATE

An aluminum plate, shown in Figure 6.1, was used for the impact type load reconstruction. It is 3mm thick (x=0.5m, y=0.4m) and simply supported from all sides, see Figure 6.1(right), instrumented with 8 "HBM" strain gauges (4 for each direction: x and y). All relevant specifications together with the analytical plate model which has been used for the impact history reconstruction can be found in Appendix C. The impact has been applied by an impulse hammer fitted with a piezo force cell at its tip. The impact load has been exerted in different locations which are marked on the plate as a grid, see Figure 6.1. Measured signals have been recorded simultaneously and evaluated off-line.

6.1.1 Impact Localization

The impact reconstruction was carried out according to the impact estimation strategy described in Chapter 4.2 and 4.3. As a first step, the impact location was estimated.
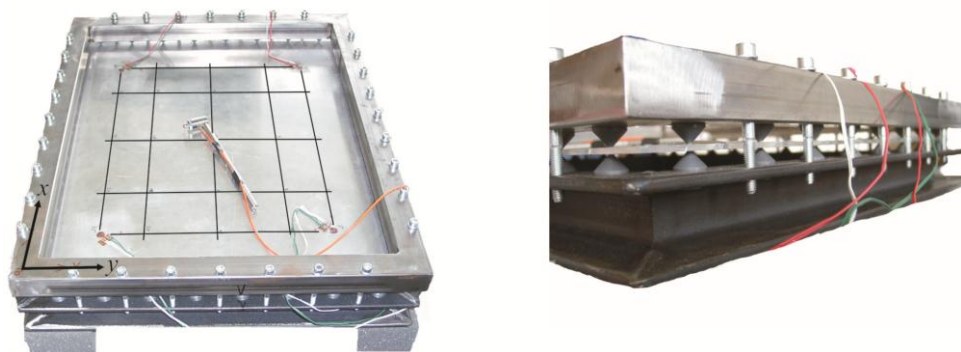
Figure 6.1: A hinged aluminum plate equipped with 8 strain gauges and its side view

For the location detection the entire set of 8 strain measurements were used together with the material properties. First, the TOA's for every specific sensor were determined from the acquired strain signals. Next, a frequency content of the first wave front was extracted with the help of the CWT technique and used together with an analytical dispersion curve to obtain the wave group velocity. Finally, the search procedure was initiated by inserting all related information into Equation (4.17). The results of the location search procedure for four different impact positions are shown in Figure 6.2. The estimation error was bounded in all the instances by 10% in both the *x* and *y* directions relative to the plate dimensions.
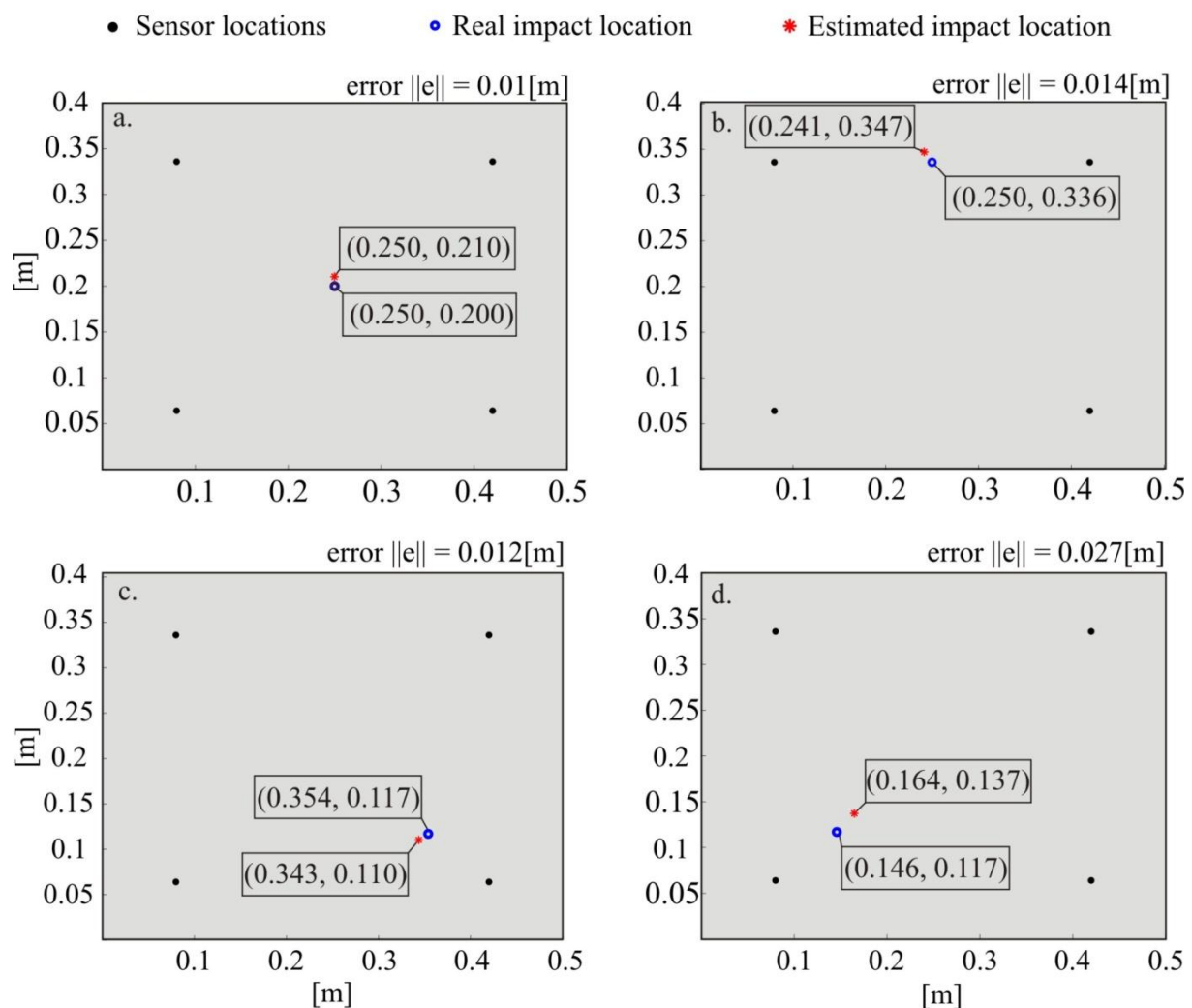
Figure 6.2: Impact location estimation examples

6.1.2 Impact History Reconstruction

After the locations of the impacts were found, the impact history was estimated by means of the LQTP and direct time domain deconvolution algorithms described in Chapter 4.3. Both used an analytical model of a simply supported plate which incorporated estimated impact

location (the detailed model can be found in Appendix C). The estimation results of the LQTP algorithm for the estimated location (a) in Figure 6.2 are shown in Figure 6.3. Several important issues which should be taken into account when following the LQTP approach are emphasized in Figure 6.3(a) through (d).

(a) – It is recommended that the model complexity be kept as low as possible in order to reach satisfactory estimation results, because it severely influences the computational time of the algorithm (*i.e.* a 5, 10, 15 modes model requires 0.14, 3.027 and 30.8 seconds, respectively, on a Pentium 4, 2.8GHz machine), but only yields a slight improvement in the estimation quality. Consequently, the frequency content analysis of acquired signals is needed prior to impact estimation, since its result can be used for the model complexity guess. As a rule, the model should include at least all frequencies exited by the impact load (*i.e.* observed in the sensors responses).

(b) – The data length of the measurement signals which are used for the time history reconstruction should be as short as possible. Ideally, it should cover only the impulse duration, since the LQTP tends to optimize input to the overall measure interval at the cost of neglecting (reducing) the most important part of the initial impact.

(c) – The increase in the values of the residual weighting matrix Q compels the estimated force to approach the magnitude of the real force, but at the same time this can lead to instability (*i.e.* higher oscillations) in the solution, as is apparent by comparing the black line $Q=100I$ to others.

 (d) – It is important that the input weighting matrix R (which is a scalar in the case of a single impact force) be kept as small as possible but larger than zero, since an increase in its values restricts the input variation and simultaneously smoothes the reconstructed impact. The value of matrix P does not influence the quality of the reconstruction of the impact, therefore it has been kept equal to zero for all results.

To gauge the influence of inaccuracies in the estimation of the location on the quality of impact reconstruction, the estimated impact location (a) and (d) in Figure 6.1 has been compared with the impact estimation for the case when the impact position was identified perfectly with similar QLTP parameters ($Q=10I$, $R=1e^{-13}$, $P=0$). This comparison is shown in Figure 6.4, where one can readily notice that the reconstruction error decreases as the estimation of the location approaches the real impact position; see Figure 6.4(a) for comparison. In contrast to Figure 6.4(a), Figure 6.4(b) does not show a significant improvement,

which leads to the conclusion that the QLTP is tolerant to some inaccuracy in the estimation of the location.
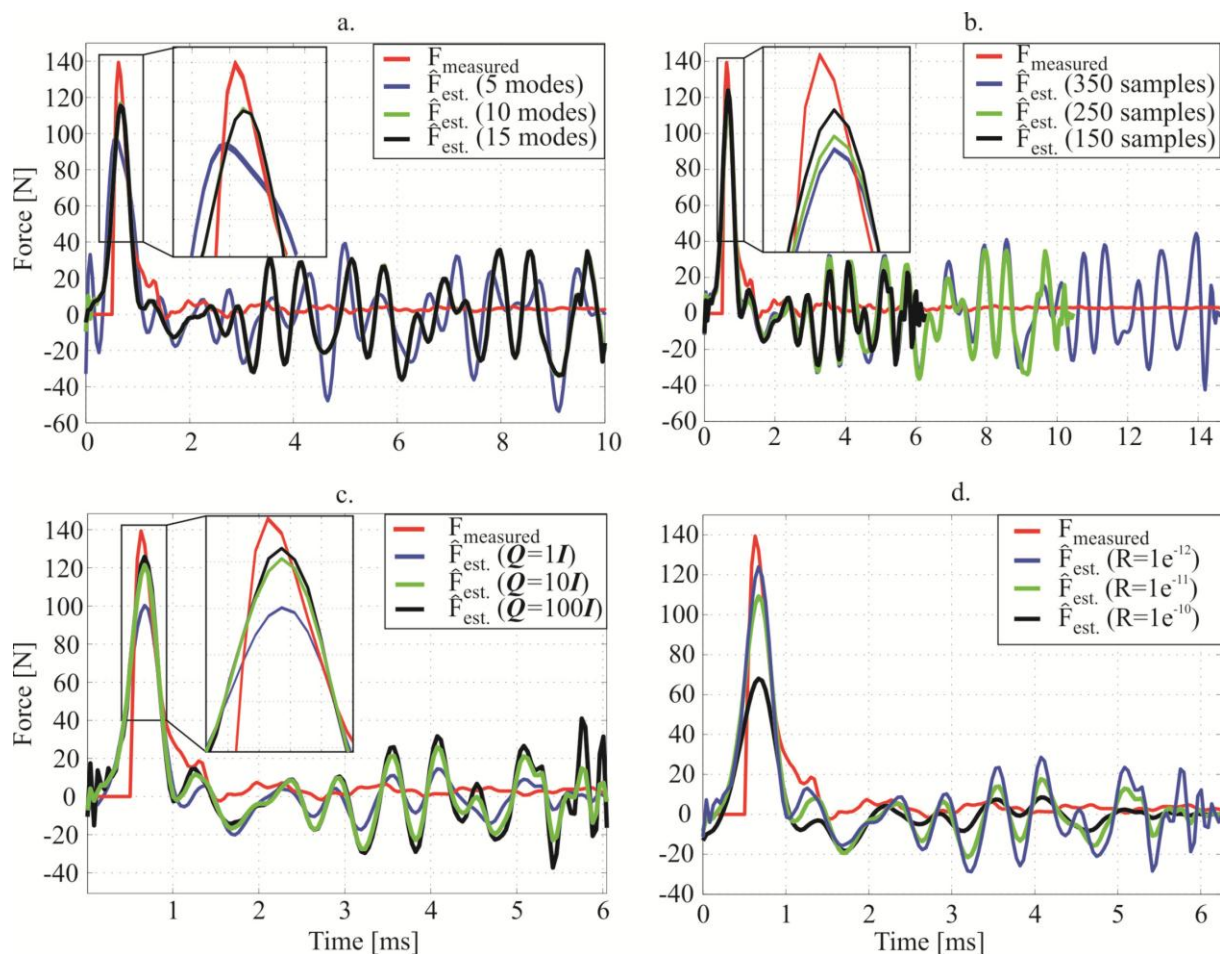
Figure 6.3: Impact load estimation by LQTP algorithm: (a)- model complexity variation with constant $\mathbf{Q}=20\mathbf{I}$, $R=1e^{-12}$, $\mathbf{P}=\mathbf{0}$; (b)-variation of data length with constant $\mathbf{Q}=20\mathbf{I}$, $R=1e^{-12}$, $\mathbf{P}=\mathbf{0}$; (c)- variation of residual weighting matrix $\mathbf{Q}$ with constant $R=1e^{-12}$, $\mathbf{P}=\mathbf{0}$; (d)- variation of input weighting matrix $\mathbf{R}$ with constant $\mathbf{Q}=10\mathbf{I}$, $\mathbf{P}=\mathbf{0}$
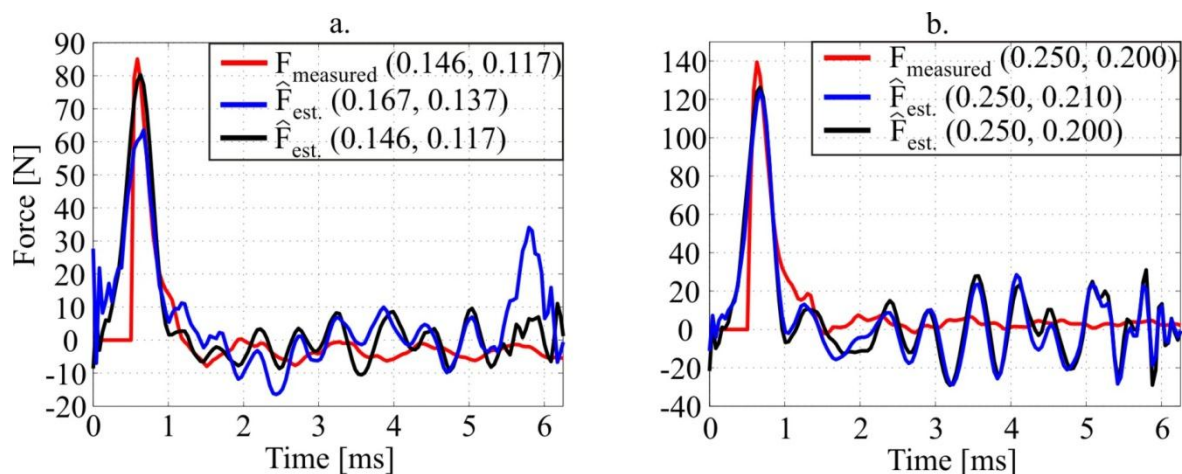
Figure 6.4: Impact load estimation by LQTP algorithm: (a)- for estimated impact location in Figure 6.2(d); (b)- for estimated impact location in Figure 6.2(a)

The same impact locations have been taken for impact history reconstruction by direct time deconvolution algorithm. In addition to the theory described in Chapter 4.3.1, a specific sensor delay is taken from the previously estimated TOA's. The results are set forth in similar form as for the QLTP approach, in Figure 6.5 and Figure 6.6, respectively.

An analysis of Figure 6.5(a) and (b) leads to several outcomes with respect to the model complexity and the length of the data set used for the load estimation:

(a) − The model complexity should be kept sufficiently small, since doing so improves the reconstruction curve (it smoothes the estimation result by reducing the condition number of the Toeplitz matrix, see Chapter 4.3.1) by means of a more complex model on the one hand and simultaneously increases the computational time on the other hand (*i.e.* a 5, 10, 15 modes models require 4.6, 29.5 and 283.8 seconds, respectively, on a Pentium 4, 2.8 GHz machine). As a result, the same strategy as for LQTP algorithm can be used for model order choice.

(b) – The data length influences the solution, as mentioned in Chapter 4.3.1. In the worst case, a wrong choice of the time interval would lead to unstable solution. This trend can be observed in Figure 6.5(b), where the solution diverges at the final sample for each data set. Additionally, longer data sets require longer computational times which can be a knock-out criterion if the quasi online impact estimation is required.
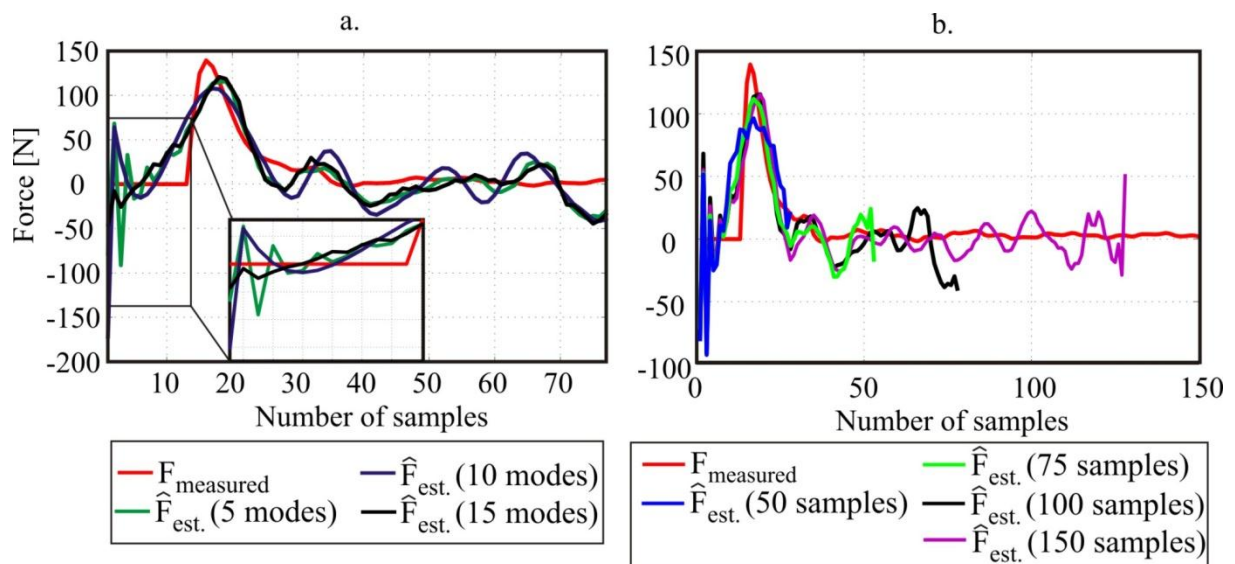
Figure 6.5: Impact load estimation by direct deconvolution in time domain: (a)- model complexity variation for 100 samples and TOA sensor delay; (b)- variation of data set length for 10 modes model and TOA sensor delay

For the reasons stated in Chapter 4.3.1, a solution for the direct deconvolution method does not exist if the time delay is not introduced; therefore, a proper selection of time delay is needed. The TOA of every sensor can be an optimal candidate for this task. The influence on

the impact reconstruction by TOA variation within 20% for every sensor delay is set forth in Figure 6.6. Obviously, if the time delay is smaller or bigger than the actual time of arrival, then the estimation quality decreases, see green and black lines in Figure 6.6, especially in the beginning and end phases.
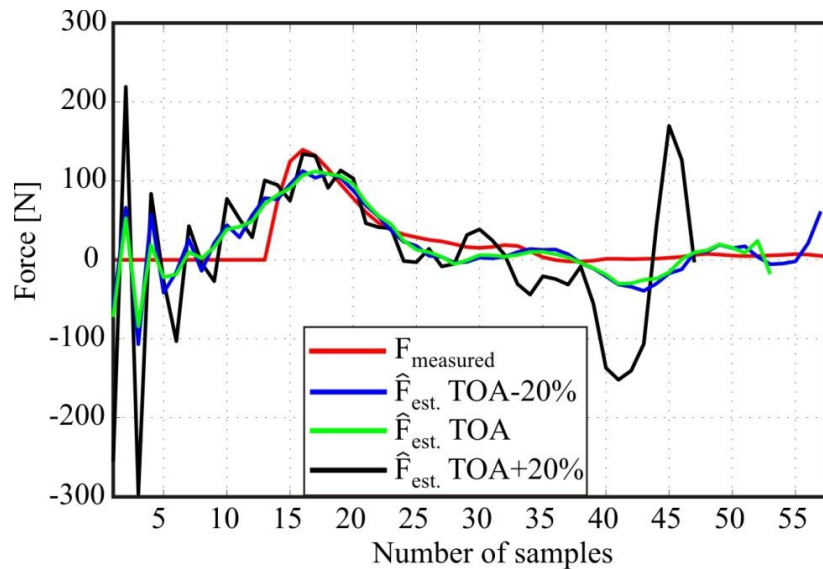
Figure 6.6: Impact load estimation by direct deconvolution in time domain with different sensor specific delays for a 10 modes model and 75 samples data set

For the purpose of assessing the sensitivity of the direct deconvolution algorithm to the error in location estimation, both locations (a) and (d) in Figure 6.2 were compared with the impact estimation for the case when the impact position was identified perfectly. This comparison is shown in Figure 6.7, where TOA reconstruction error decreases as the estimation location approaches the real impact position (black curves in Figure 6.7), see Figure 6.4(b) for comparison.
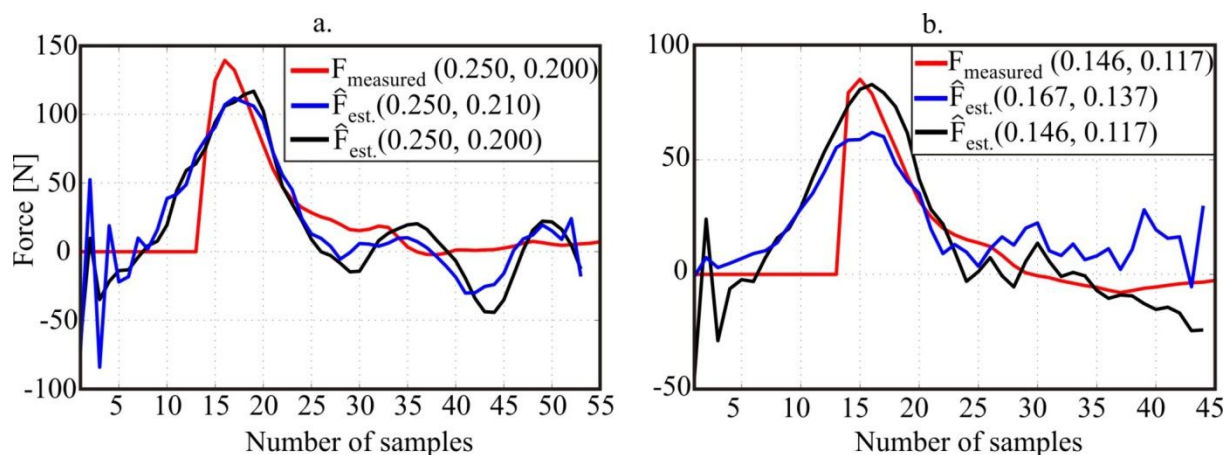
Figure 6.7: Impact load estimation by direct deconvolution in time domain: (a)- for estimated impact location in Figure 6.2(a); (b)- for estimated impact location in Figure 6.2(d)

For Figure 6.4(a) no significant improvement is noticeable in the peak of the impact curve; nevertheless, the initial part of the estimated signal has been smoothed by the correction in impact location. Summarizing all the issues which should be taken into consideration for both the impact reconstruction methods presented in this section, and taking into account the quality of the estimated impact signal, a fair decision can be made by giving more benefits to the LQTP algorithm. However, direct time deconvolution can be used if no elaborated model of the system is at hand and certain precautions are taken in order to keep the solution within stable boundaries.

6.2   TIME CONTINUOUS LOAD RECONSTRUCTION ON LUMPED MASS STRUCTURE

A two storey laboratory structure, shown in Figure 6.8(a) and (b), was used for the experimental validation of SS&IE, MPIO and KF-UI force reconstruction algorithms mentioned in Chapter 5. Each load estimation method has been constructed on the basis of a simplified mathematical model, as illustrated in Figure 6.8(b), with the assumption that the system exhibited only planar motion (in the *z-x* plane). The detailed modeling procedure can be found in Appendix A together with all relevant information (*e.g.* physical/geometrical features and positions of the sensors).
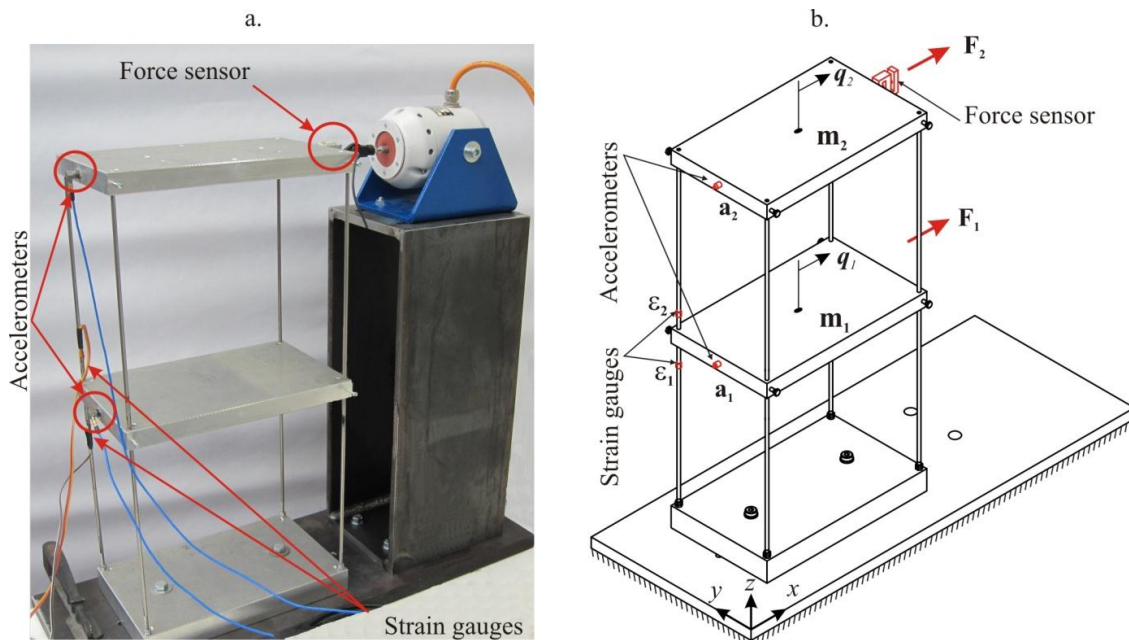
Figure 6.8: A two storey lumped mass linear structure with shaker (a) and its model (b)

The data for the observers has been acquired with the help of two "PCB" accelerometers model M353B15 which operate in the frequency range of $\pm 1\,\text{Hz}$ to $\pm 10\,\text{kHz}$, and two "HBM" strain gauges of type 0.6/120LY11 in the half-bridge configuration in order to

eliminate temperature effects. Recorded sensor signals were first passed to the operational amplifiers: *accelerations* - to a "Kistler" coupler model 5134A (*i.e.* a 4 channel piezoelectric sensor power supply and signal conditioner), where the signals were primarily filtered by means of an integrated low-pass filter with the cut-off frequency set at 10 kHz; *strains* - to the carrier-frequency measuring PICAS amplifier from "PEEKEL Instruments". Finally, the measured data were collected and fed online to the observers with the help of a "dSpace" DS1104 R&D controller board.

For the system excitation two main sources were used. The first one was a Type 9722 "Kistler" quartz impulse hammer which is able to capture the impact force up to 2 kN and excite the structure until 450Hz in frequency range with a grey tip extension. In addition, the impact position (lower or upper mass) was changed during the experiment. A shaker from "TIRA GmbH" type TIRAvib S504, with a rated peak force of 18 N and a frequency range of 2 Hz to 11 kHz was used as a second load source for the test rig, see Figure 6.8(a). To validate the load applied by the shaker, an "ME" load cell of type KD24S with a nominal maximum load of 20 N was installed in the path between the shaker and the upper mass m_2, see Figure 6.8(a).

The mathematical model for the observer computation which was derived with the help of the MA procedure based on ARV method, was obtained for the structure without being connecting to the shaker (the shaker was considered as an external load). Nevertheless, the attachment of the shaker to the structure modified the overall dynamics of the system. Therefore, models with and without the shaker being connected to the structure were validated prior to beginning the actual force reconstruction test. For this purpose, an impact force was applied to the upper mass m_2 of the structure with and without shaker. Then, the acceleration responses were recorded and used for the MA procedure which delivered the essential quantities for the model construction, see Table 6.1.

Table 6.1: Modal analysis results for lumped mass structure

Structure without shaker			
Mode	f_{damped} [Hz]	ξ	φ
1	5.95	0.0029	$[0.5253\ 0.8508]^T$
2	15.94	0.0011	$[0.8365\ \text{-}0.548]^T$
3	278.4	0.0031	$[0.1926\ 0.9757]^T$
Structure with shaker			
1	8.2	0.0707	$[0.6241\ 0.7688]^T$
2	16.4	0.0206	$[0.7881\ \text{-}0.6338]^T$

Typical stabilization diagrams are shown in Figure 6.9 for the structure with (a) and without shaker (b). An obvious difference between identified parameters can be noticed from both Figure 6.9 and Table 6.1. First of all, the system with a disconnected shaker is characterized by apparently three natural frequencies, so that the simplified model in Appendix A, which accounts for only two degrees of freedom structure (first two modes of vibration), will serve as a sufficient basis for the observer construction only if the structure will be excited within the third natural frequency. Consequently, all observers will have higher errors if the external load is able to excite the structure in the vicinity of or higher than 278.4Hz.
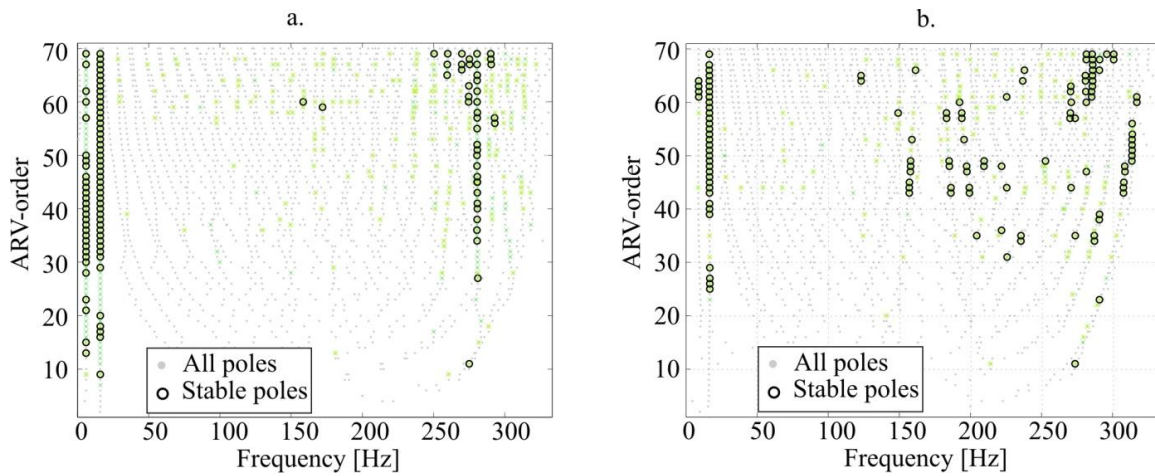
Figure 6.9: Stabilization diagrams for excitation on the upper mass (a)-disconnected shaker; (b)-connected shaker

By the same token, the diversity between the system with and without shaker is very high, especially for the first frequency $\approx 40\%$, as well as the difference in the damping ratios for the first two modes. The magnitude plots of the system transfer functions, for the inputs to the first strain ε_1 and the inputs to first acceleration sensor a_1, as illustrated in Figure 6.10, give a better representation of the difference between the systems with and without shaker in the frequency domain. Both acceleration and strain transfer functions in Figure 6.10 show similarity in the regions before and after natural frequencies, *i.e.* the red and blue lines are coincident. By contrast, in the vicinity of the natural frequencies the difference in both amplitude and shift of transfer function peaks experiences an increase. Therefore, the load reconstruction error is expected to increase for observers that are based on the structure without shaker if the structure is excited by a periodic load in the neighborhood of these peaks. Bearing in mind all expected sources of estimation error (*i.e.* neglected third natural mode and the difference between the structure with and without shaker), the estimation procedure was carried out for the structure that was first excited by the impact load at the

lower and upper mass, respectively. A sinusoidal load with different frequencies was then applied to the upper mass.
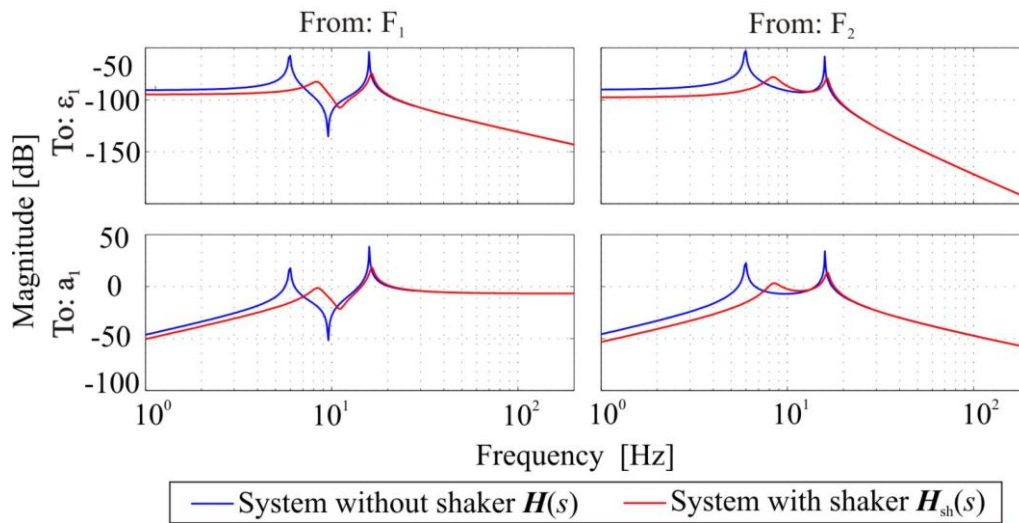
Figure 6.10: Transfer functions magnitudes from both inputs to the lower accelerometer a_1 and lower strain gauge ε_l

6.2.1 Estimation of Impact Forces

The results of the impact estimation by all observers are shown in Figure 6.11 to Figure 6.13 for the impact applied on the lower mass.
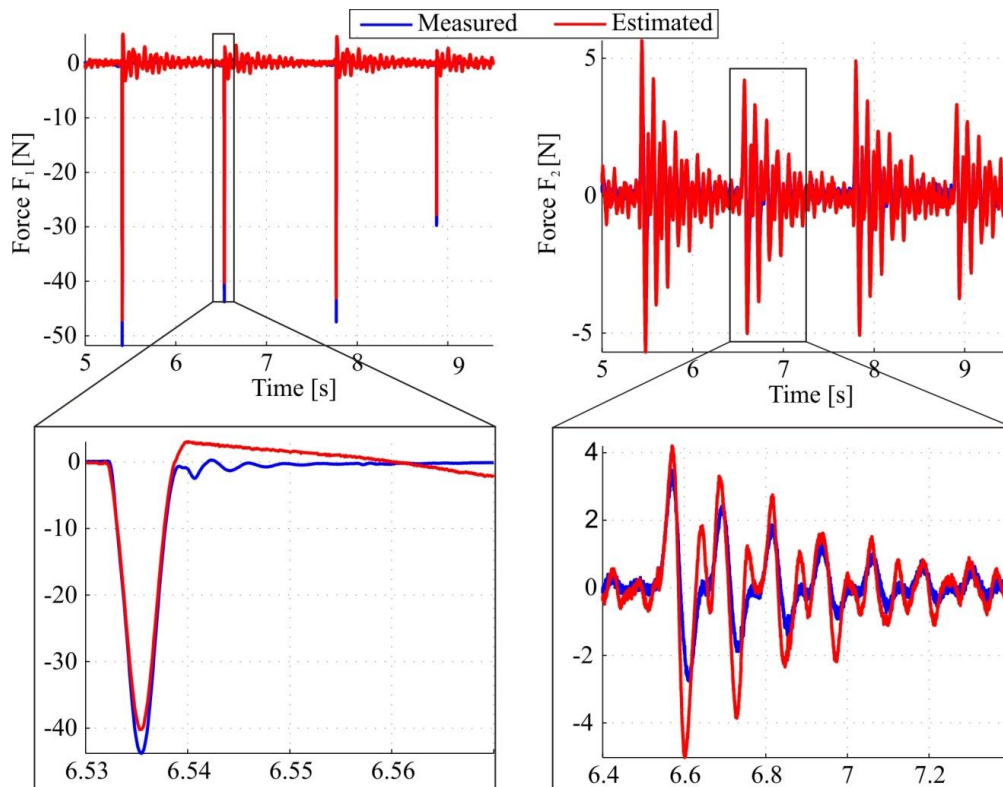
Figure 6.11: Estimated forces using SS&IE, impact on lower mass
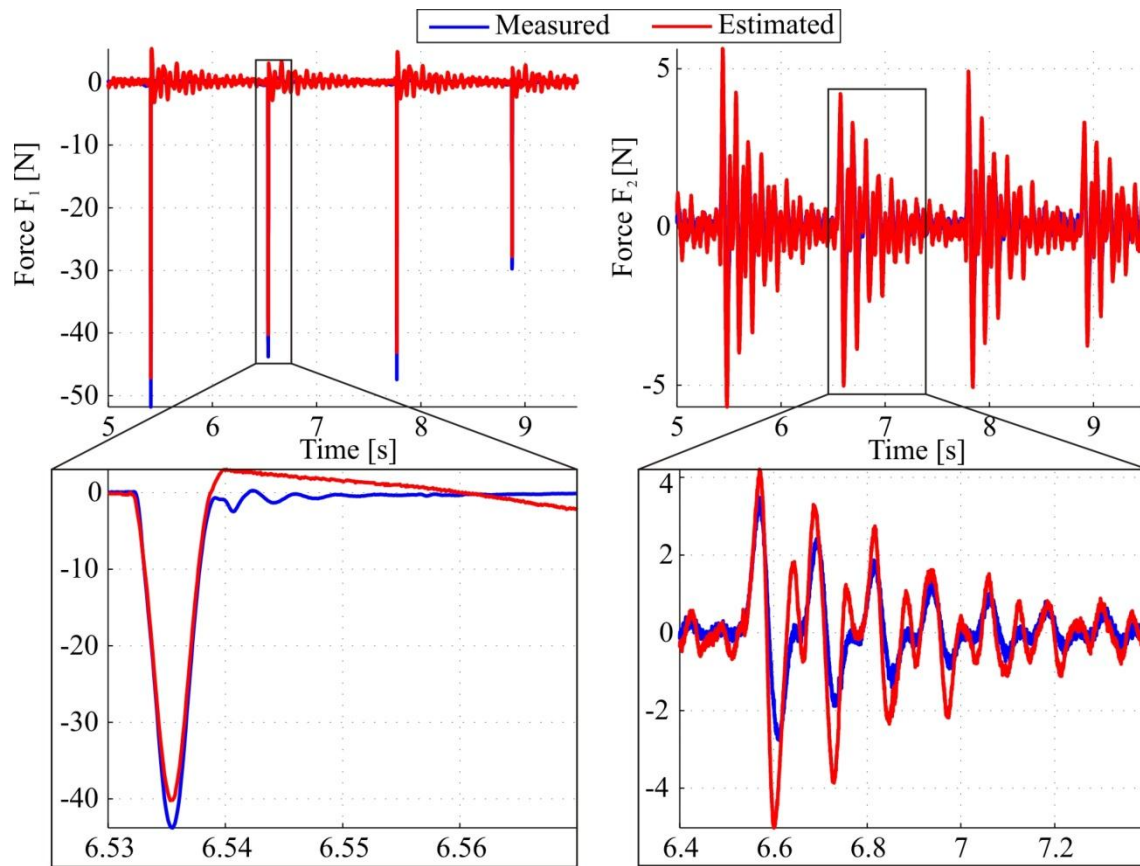
Figure 6.12: Estimated forces using KF-UI, impact on lower mass
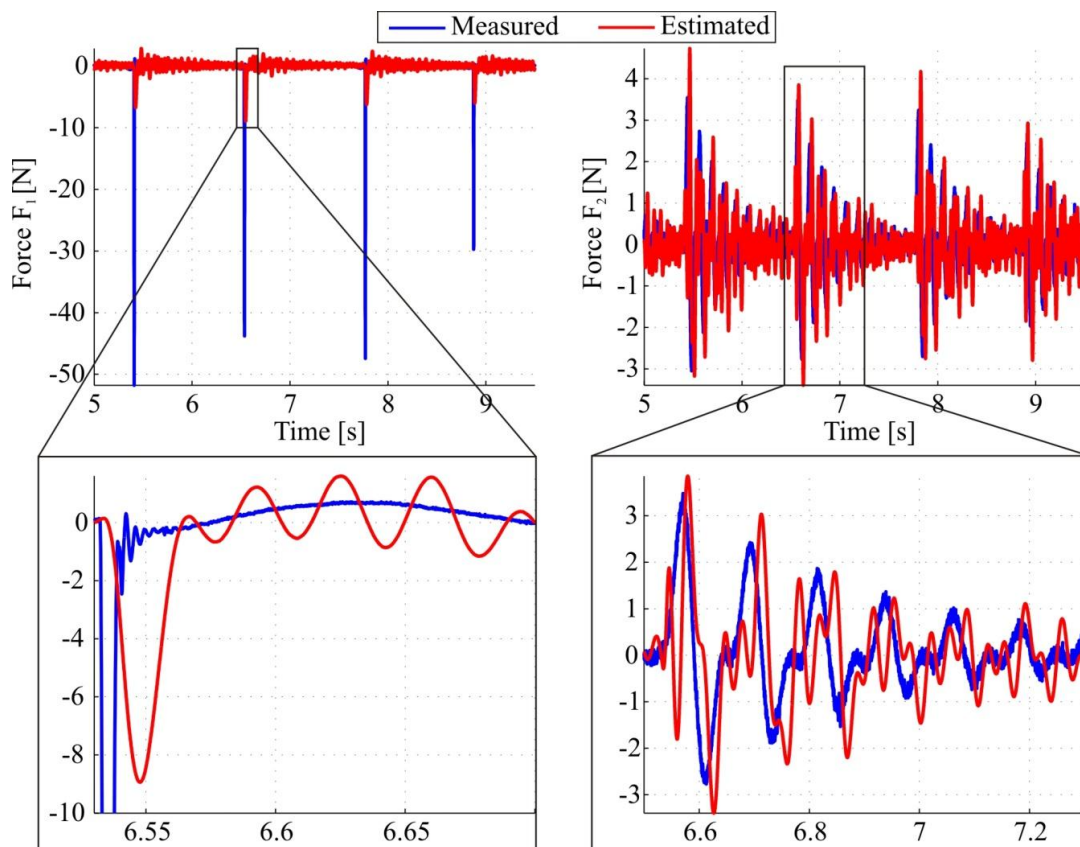
Figure 6.13: Estimated forces using MPIO, impact on lower mass.

An observation of Figure 6.11 and Figure 6.12 reveals that both SS&EI and KF-UI are capable of estimating the impact load as well as the shaker resistance load with minor errors. The main sources of error are the measurement noise and model uncertainties which can be observed before and after impact, respectively. The noise dependant error level can be easily attenuated with the help of a low-pass filter, whereas for the reduction of the model error a model update procedure might be necessary. MPIO in its turn is not able to follow the highly dynamical impact force in amplitude, as shown in Figure 6.13, and as expected from Equation (5.69). Nevertheless, it registers the occurring impact with some phase shift and attempts to reconstruct a slower force applied by the shaker connection. Similar results are obtained if the impact load is applied to the upper mass, see Figure 6.14 to Figure 6.16. Here, the SS&IE together with KF-UI again show a good performance and great similarity in the estimated forces which in this case are a combination of the impact and shaker resistance for the upper mass. Both of them incorrectly estimate the force on the lower mass with the similar range of error. The MPIO once more cannot follow the impact but attempts to follow the load introduced throughout the load cell by the shaker resistance, see Figure 6.16.
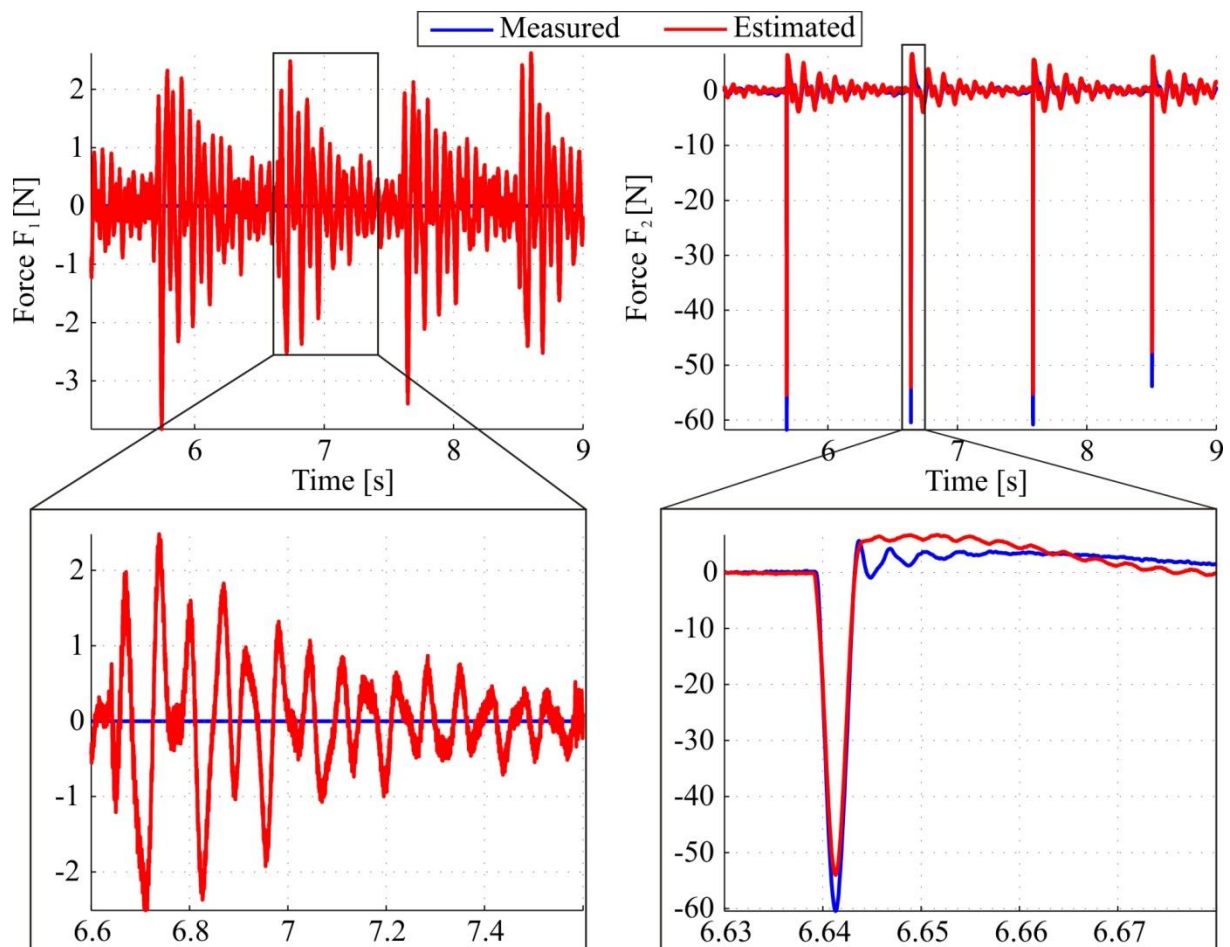
Figure 6.14: Estimated force using SS&IE, impact on the upper mass
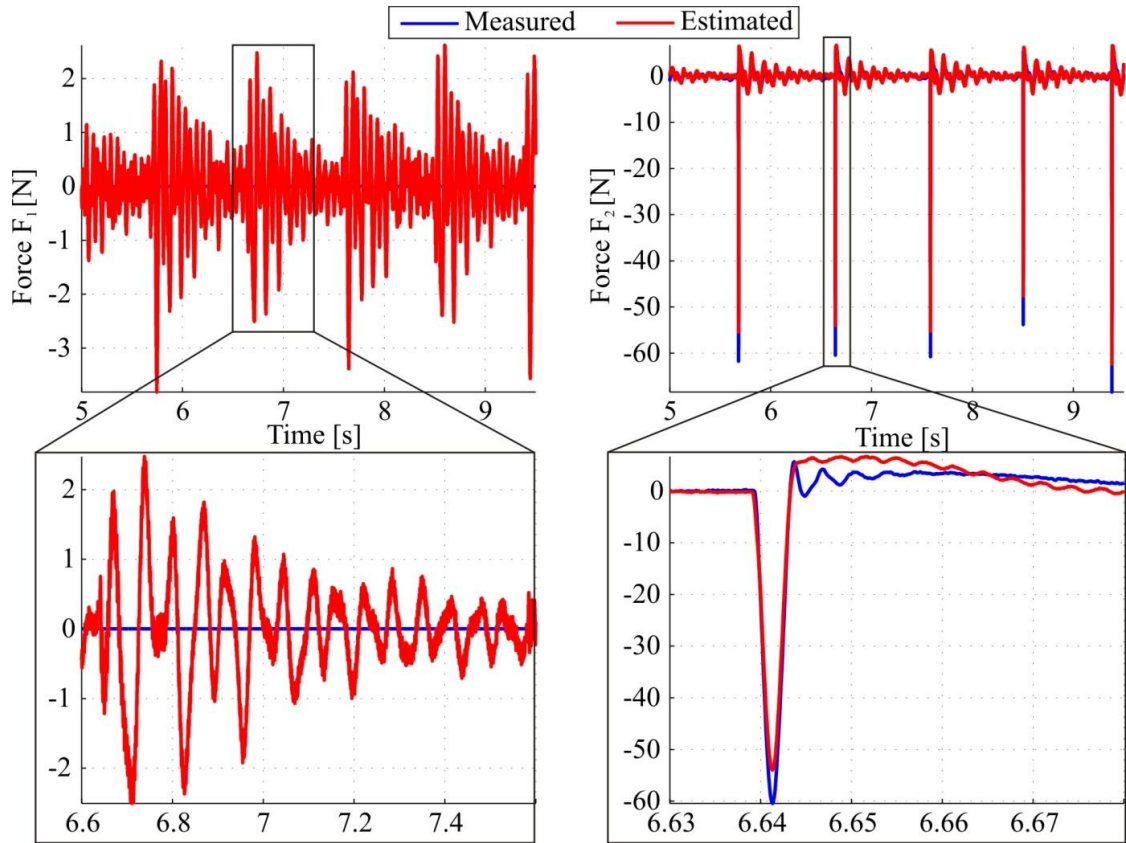
Figure 6.15: Estimated force using KF-UI, impact on the upper mass
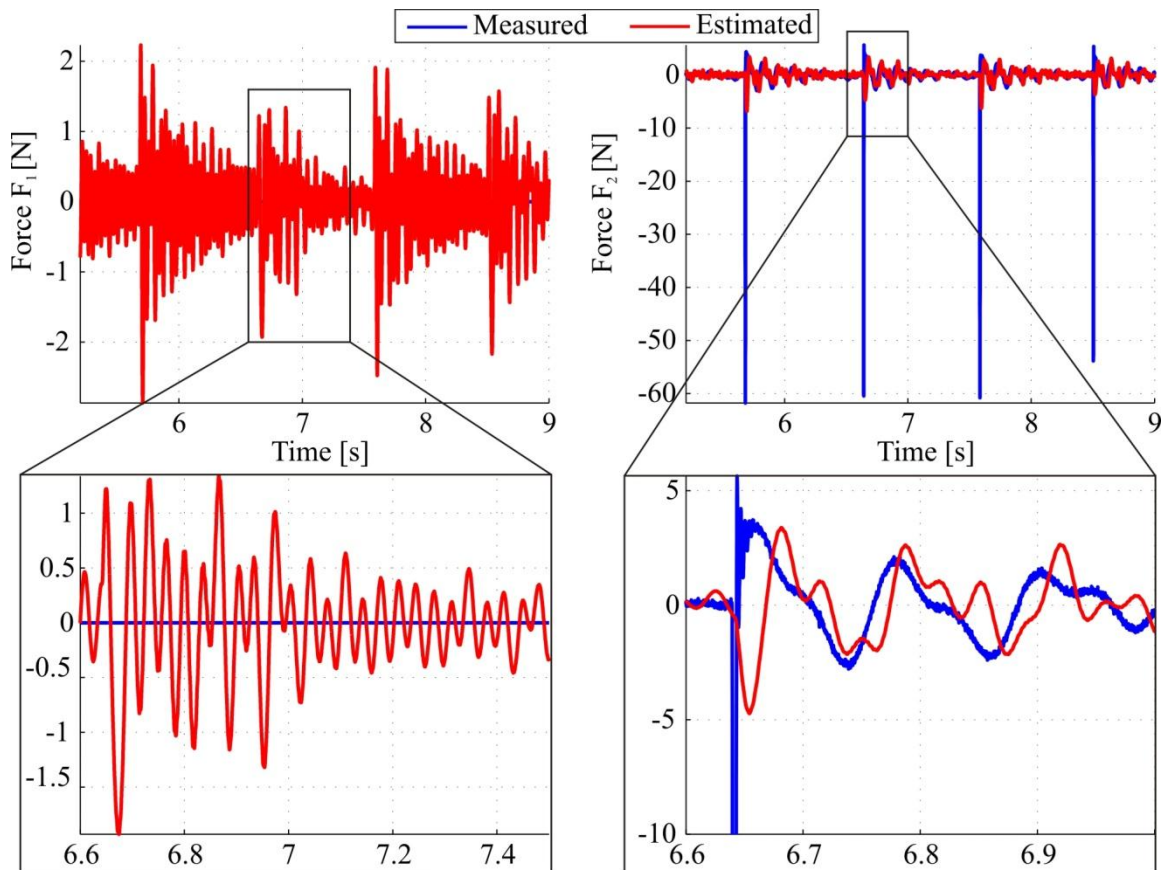
Figure 6.16: Estimated force using MPIO, impact on the upper mass

6.2.2 Estimation of Sinusoidal Forces

To validate the estimation performance at different frequency ranges, a sinusoidal force has been applied to the upper mass. The excitation frequencies were intentionally set as: $f_{ex} = 2\text{Hz}, 7\text{Hz}, 16\text{Hz}, 50\text{Hz}$. Two such frequencies, *i.e.* 7 and 16 Hz are located in the vicinity of the model discrepancy, see Figure 6.10, so that the estimation error was expected to be high for those frequencies. The results for every observer type are presented in Figure 6.17 to Figure 6.19.

A closer reading of these figures validates the above prognostication with respect to frequencies 7Hz and 16Hz. If the periodic excitation is in the other frequency ranges, *i.e.* 2Hz or 50Hz, both SS&IE and KF-UI provide a good estimate of the exerted load which is applied to the upper mass. Simultaneously, the SS&IE together with KF-UI produce a similar false estimate of the load on the lower mass where no force has been applied. The falsely estimated lower load reaches up to 100% of the applied load on the upper mass for frequencies 7Hz and 16Hz and lies within 25% for frequencies 2Hz and 50Hz. In light of these observations, a direct connection of the estimation error to the model quality can be made, in particular by observing the results of load estimation at 2Hz and 50Hz in Figure 6.17 or Figure 6.18 and in parallel to the model quality in Figure 6.10. The transfer function curves in Figure 6.10 are almost identical starting from 20Hz which serves for good load reconstruction (having an error less than 10% at lower mass) at the frequency of 50Hz.

The MPIO was not able to track load with fast dynamics, see Figure 6.19 for 50Hz. However it was quite successful in the 2Hz region, although it was using only the strain signals. For the excitation at 7Hz, the MPIO was able to estimate the load at the upper mass but produced a false estimation at the lower mass, as in the case of the other observers.

On the basis of all the above findings, the following can be concluded:

(a) Both SS&IE and KF-UI are able to estimate a vast range of load types with almost the same reconstruction quality.

(b) Usage of MPIO algorithm would be preferable for slowly changing forces as it requires only the strain sensors, which requires less computational costs than in the case of SS&IE and KF-UI.

(c) All observers strongly depend on the model accuracy. Therefore, an *a priori* verification of the utilized model is needed in order to obtain a good estimation quality, or the frequencies that are excited by the external load should be covered by the simplified (*e.g.* uncertain) model well.
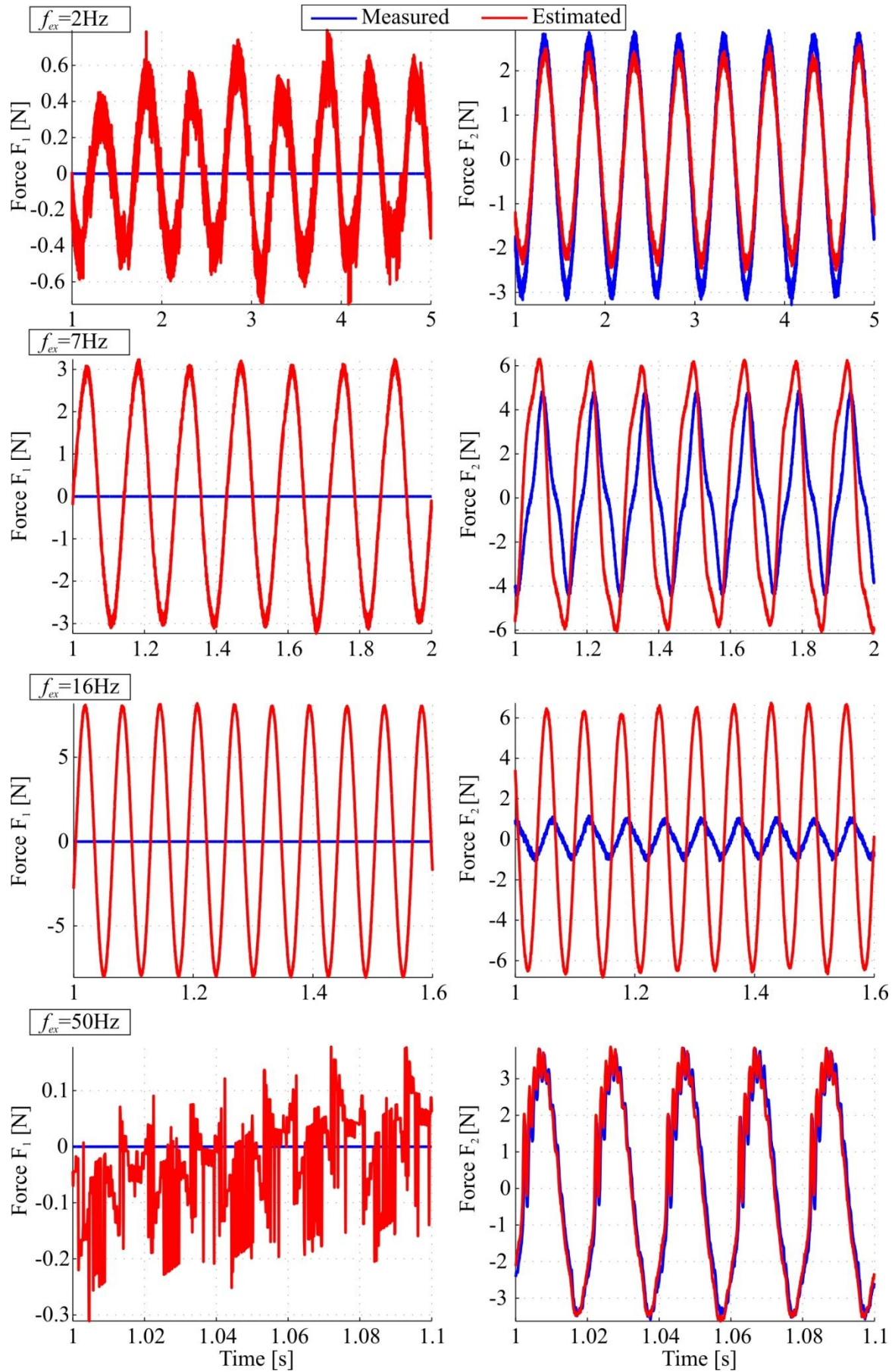
Figure 6.17: Periodic load estimation using SS&IE, $f_{ex} = 2\,\text{Hz}, 7\,\text{Hz}, 16\,\text{Hz}, 50\,\text{Hz}$
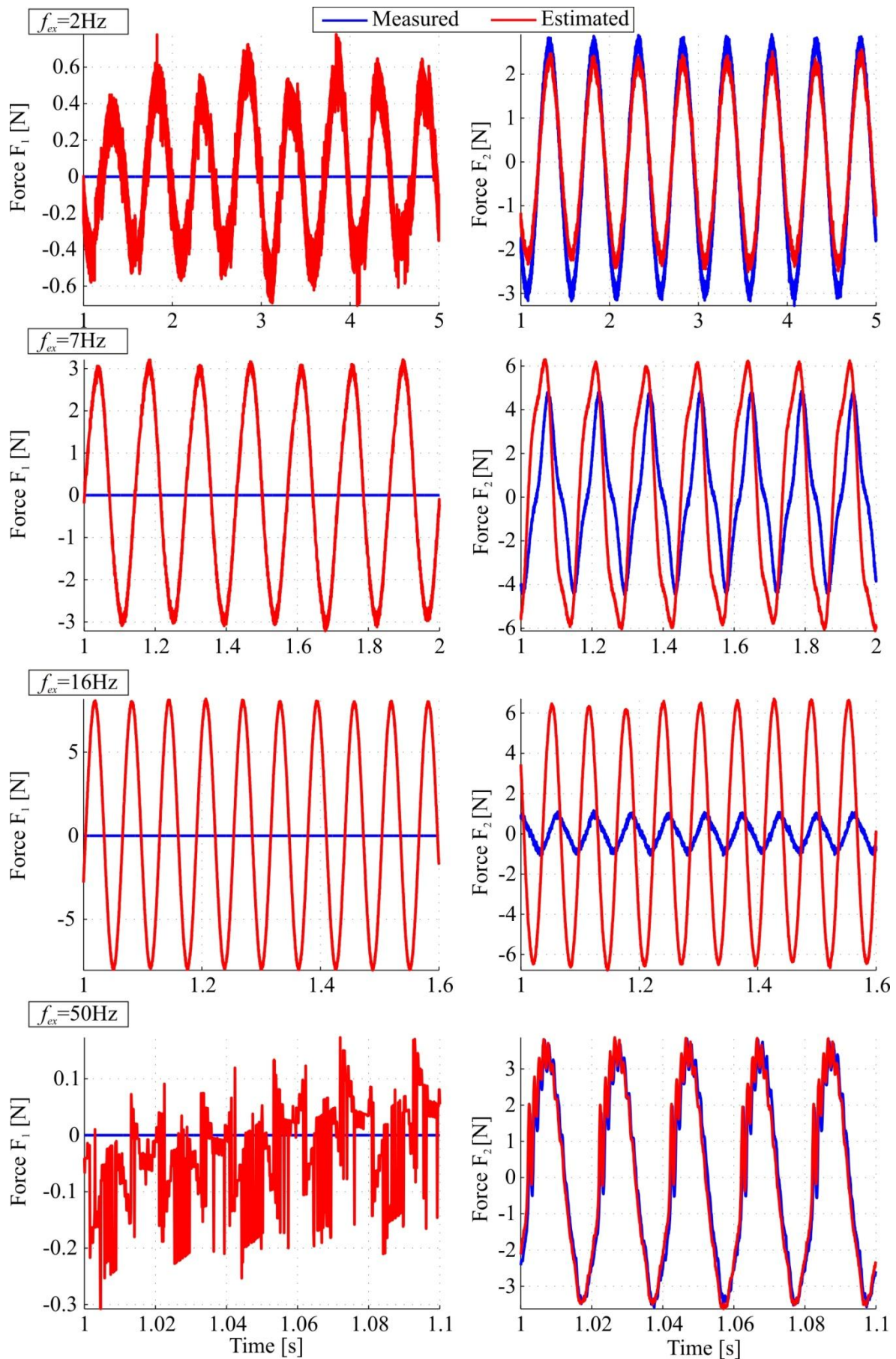
Figure 6.18: *Periodic load estimation using KF-UI,* $f_{ex} = 2\,\mathrm{Hz}, 7\,\mathrm{Hz}, 16\,\mathrm{Hz}, 50\,\mathrm{Hz}$
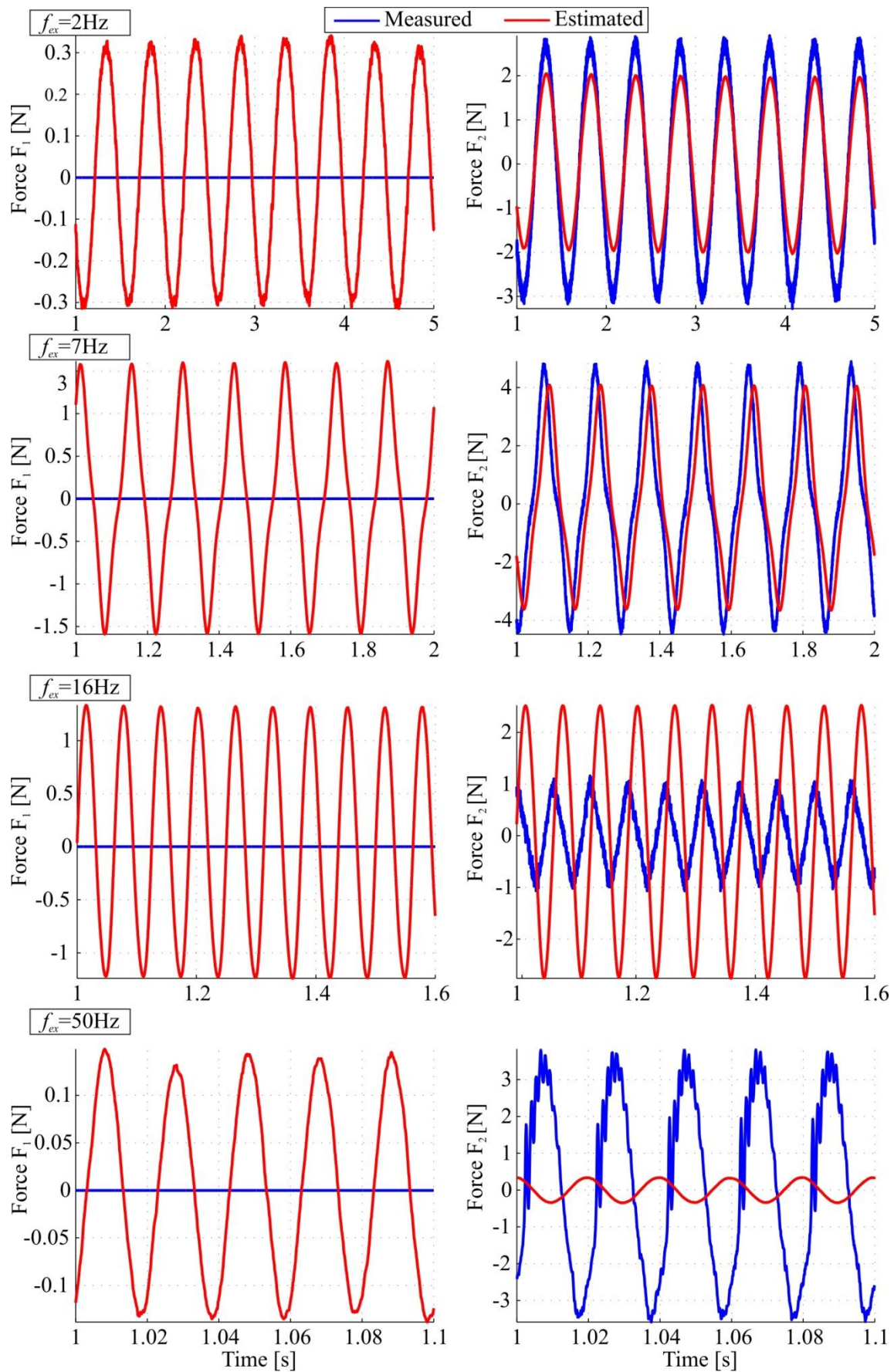
Figure 6.19: Periodic load estimation using MPIO, $f_{ex} = 2\,\mathrm{Hz}, 7\,\mathrm{Hz}, 16\,\mathrm{Hz}, 50\,\mathrm{Hz}$

6.3   TIME CONTINUOUS LOAD RECONSTRUCTION ON CONTINUOUS SYSTEMS

This chapter consists of three subsections where load estimation is validated on continuous structures. In the first section, an analytical model of a simply supported aluminum beam is used, and SS&IE is tested in the case where the load and the acceleration sensor are not collocated. In the second section a FEM of a tripod tower structure is used to validate the observer robustness to measurement and model uncertainties for both collocated and non-collocated scenarios. Finally, the results of completed laboratory tests for a quasi-static load on the beam and a wind load on the tripod structure are presented in the last subsection.

6.3.1   Simply Supported Beam

In this section, the SS&IE observer was attested on a model of simply-supported beam, as shown in Figure 6.20. The SS&IE algorithm was chosen as superior to KF-UI and MPIO due to its similar performance with KF-UI in the case of linear systems and its inherent ability to work with nonlinear systems. The main objective was to test the SS&IE algorithm constructed from the modal model which was able to release a sensors-load collocation condition in Equation (5.32) for the direct feed through matrix D.

To this end, the sensors denoted by s_1, a_2, a_3 and representing strain gauge and two acceleration sensors, respectively, were positioned along the beam, see Figure 6.20.
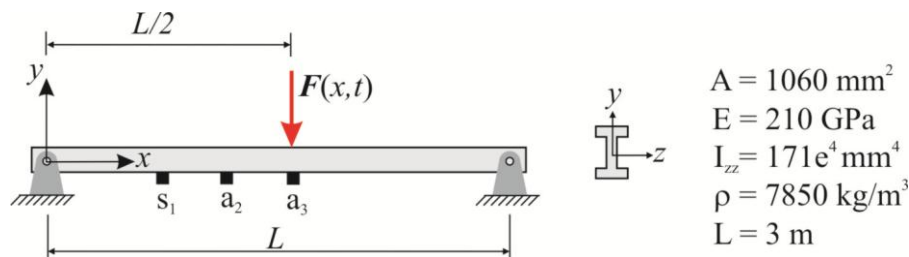
Figure 6.20: Simply supported beam model

The combination of only two sensors (one strain s_1 and one of two accelerometers a_2 or a_3) was used for every simulation run. In both instances, white noise was added to simulated outputs with a similar Signal to Noise Ratio (SNR) defined as the Root Mean Square (RMS) ratio of noise free signal S to noise signal N:

$$SNR = RMS(S) / RMS(N) \tag{6.1}$$

which was set as equal to 10. The simulation was performed with the SIMULINK/MATLAB® software package. The reduced analytical Euler-Bernoulli beam model containing four modes was used for calculating the observer. The number four was chosen arbitrarily; in general, the

complexity of the modal observer (*i.e.* the number of modes included in the model) depends on the application requirements, *e.g.* the frequency band excited by the external load. To keep the error function free from modeling errors the original system was assumed to have the same number of modes in the simulation procedure. The simulation results are plotted in Figure 6.21. Panel (a) in Figure 6.21 shows the force reconstruction with satisfactory accuracy (influenced by the sensor noise only) for the sensor couple s_1 and a_3, which were placed at 0.3L and 0.5L, respectively.
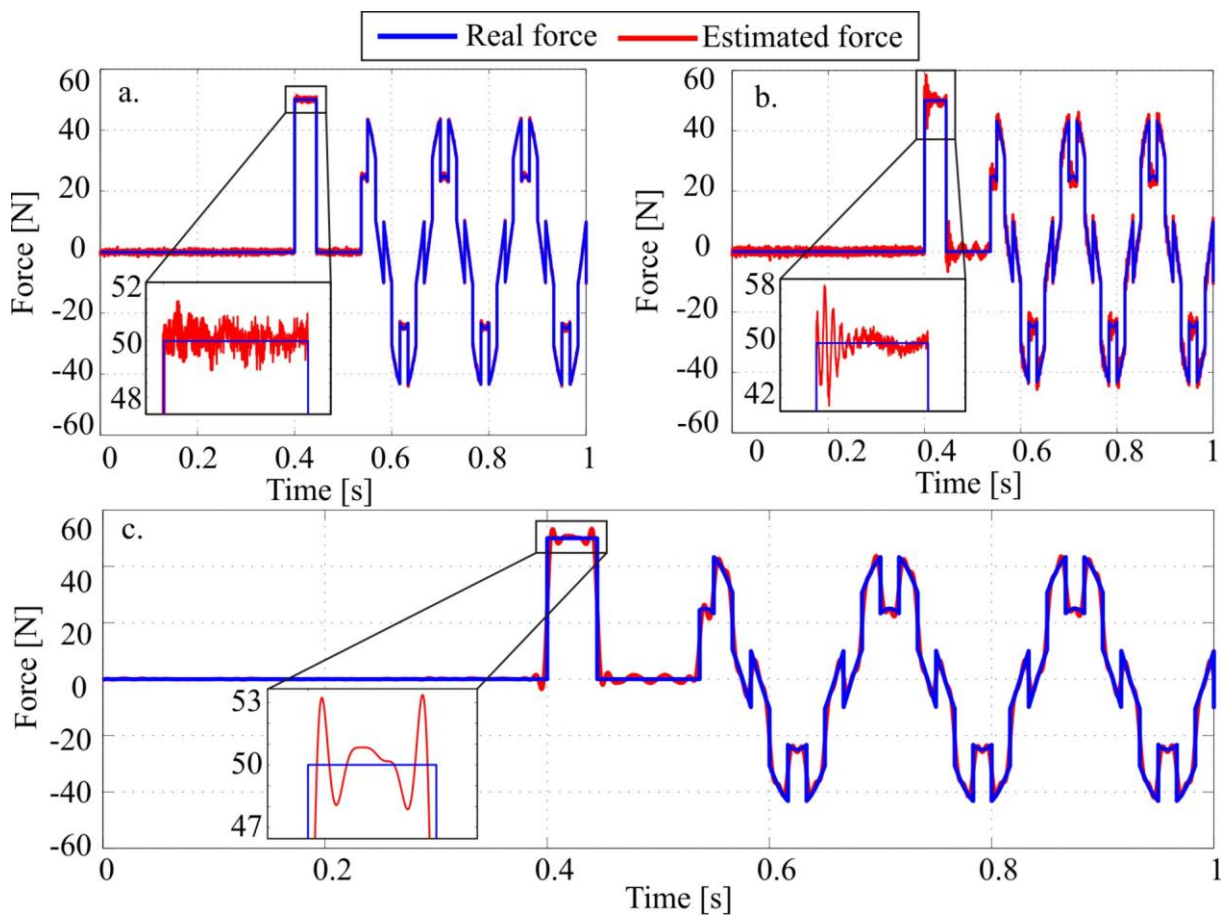
Figure 6.21: Force estimation, simulation results: (a) – sensors combination s_1 and a_3; (b) – sensors combination s_1 and a_2; (c) – filtered estimated signal for sensor combination s_1 and a_2

Panel (b) in Figure 6.21 illustrates load estimation for the s_1 and a_2 sensors combination, where a_2 is positioned at 0.4L along the beam. The calculated observers led to a good result, although the non-collocated case, plot (b) in Figure 6.21, is more sensitive to the noisy data. This drawback of high frequency pollution of the reconstructed force can be minimized by a low pass filtering of the identified force. The filtered reconstructed force signal is illustrated in Figure 6.21, panel (c); here a simple fifth order Butterworth low pass zero phase filter with 100Hz edge frequency was applied. The results of estimation results led to the logical

question as to what was the maximum possible sensor to load location offset determination under which the load estimation was still possible. To answer this question, simulation tests for a similar test configuration with one strain sensor and different accelerometer positions relative to the load position was carried out. For the validation of load estimation quality a relative error was used, which was defined as:

$$error = 100 \times \sqrt{\frac{\sum \left(F_{exact} - F_{estimated}\right)^2}{\sum F_{exact}^2}} \quad [\%] \,. \tag{6.2}$$

The results of the test are shown in Figure 6.22, where the same load was applied at F(x=0.5L).
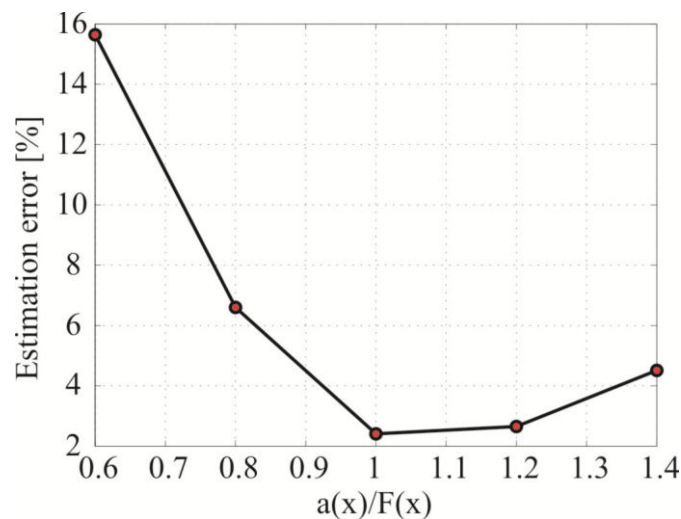
Figure 6.22: The load estimation error for the relative force F(x=0.5L) to accelerometer a_3(x) position

In Figure 6.22 the SS&IE observer was able to deliver the stable estimation results only for a maximum relative to offset of 0.4 in either direction. The minimum estimation error observed was at the collocated position, as expected. In addition, the error function was not symmetric relative the collocation position a(x)/F(x)=1 which was due to the strain and accelerometer sensor coupling (a(x)/F(x)=0.6 is equal to the 0.3L, where the strain sensor was positioned).

6.3.2   Scaled Tripod Tower of the Wind Energy Plant

For the sake of complete study of SS&IE, several numerical tests were performed to validate its robustness to model variation and noise level changes in both instances, *i.e.* collocated and non-collocated accelerometer and load positions. To this end, the SS&IE observer which was based on the FEM of the scaled tripod WEP tower represented in Figure 6.23 was tested in the

SIMULINK/MATLAB® environment under different conditions. The simulations were run to address the following questions:

1. How does the complexity of the calculated observer (*i.e.* the number of modes which are included in the state space model) influence the reconstruction of an external force?

2. To which extent does the noise level of each sensor change the observer performance?

3. Does shifting the acceleration sensor location from the point where the force was applied still preserve the stable load reconstruction if the measurement is corrupted by noise?

4. To which extent does the observer and model divergence influence the estimation quality?
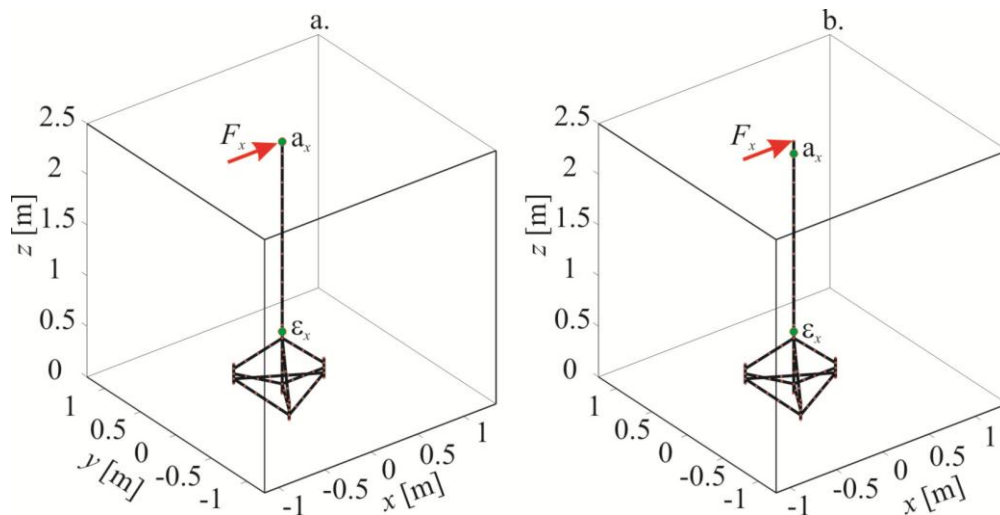
*Figure 6.23: FE model for the numerical study (a) – **collocated** accelerometer and force; (b) – **non-collocated** accelerometer and force*

For the simulations, the original system as in Figure 6.23 was built from the FE model consisting of a first 30 mode shapes. The set of observers with 8, 10, 12 and 14 modes in which only the bending modes were included in both (x and y) directions, were calculated, whereas the force was applied only in the x direction. Each of these observers was then tested for increasing noise levels on one of the sensors, *i.e.* either the strain gauge or the accelerometer, while the noise on the other sensor was kept constant and equal to 2% or SNR=50. In Figure 6.24 the relative error behavior between the 30 modes system (assumed to be an original system) and the reconstructed force from the observers with a different number of modes is shown. Here, the acceleration sensor was collocated with the position of the applied force as in Figure 6.23(a). The relative and the noise level were measured by the relative discrepancy D

$$D_{\text{relative}} \equiv 100 \times \sqrt{\frac{\sum\left(\text{Signal}_{\text{exact}} - \text{Signal}_{\text{noisy}}\right)^2}{\sum \text{Signal}_{\text{exact}}^2}} \ . \tag{6.3}$$

The load for all simulations was a unit force that was applied for three seconds at a single node (see Figure 6.23) in one direction and is described using MATLAB® functions as:

$$F(t) = 200\sin\left(2\pi f_1 t\right) + 20\,\text{square}\left(2\pi f_2 t\right) + 10\,\text{sawtooth}\left(2\pi f_3 t\right) \tag{6.4}$$

here, t is a time interval equal to $(0,\ldots,3)$ seconds and, $f_1 = 2$, $f_2 = 30$ and $f_3 = 220$ represent the excitation frequencies in Hz respectively. The same pattern of excitation as well as the noise variation was applied for the case when the accelerometer was shifted by one node (0.13 meter) down from the force location as in Figure 6.23(b). The observer performance for this case is presented in Figure 6.25.
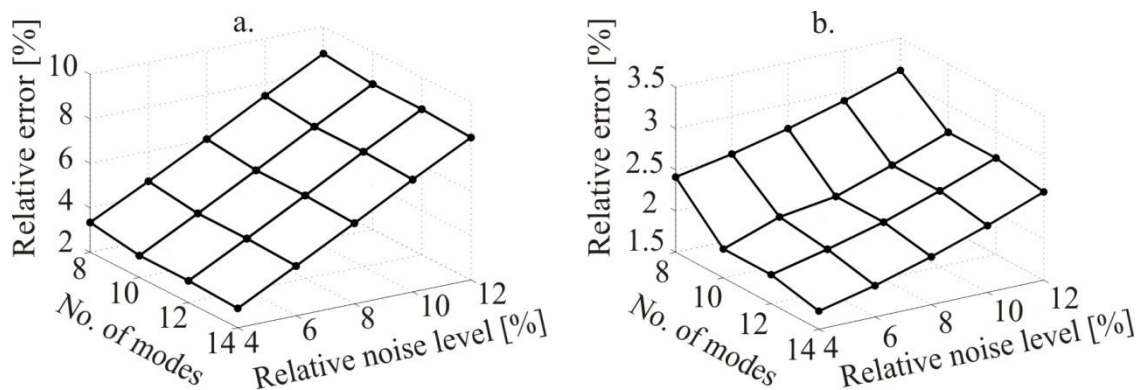
Figure 6.24: Relative simulated error of estimated force for different number of modes and (a) – relative noise level of strain gauge (b) – relative noise level of the **collocated** accelerometer and force
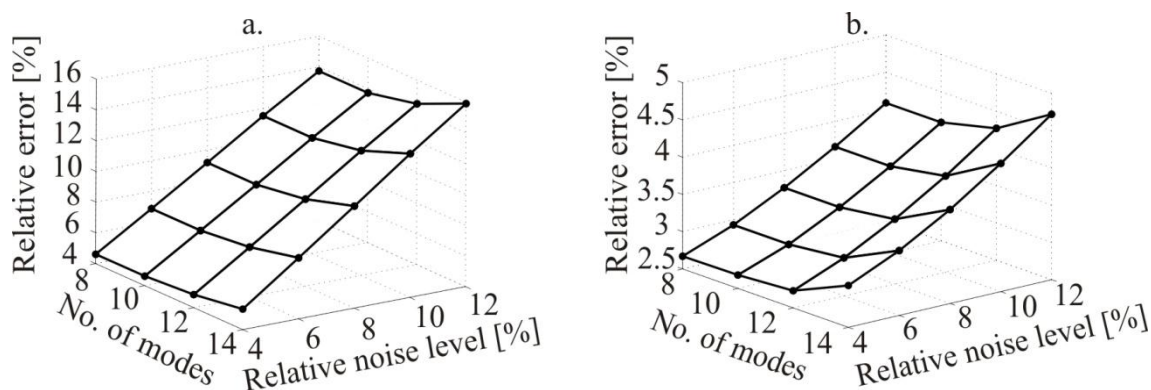
Figure 6.25: Relative simulated error of estimated force for different number of modes and (a) – relative noise level of strain gauge (b) – relative noise level of the **non-collocated** accelerometer and force

Both figures show that the presence of noise and respectively its increase, especially in the strain gauge, leads to a higher deviation between the estimated and real force. On the other hand, the noise contamination of the acceleration signals does not lead to a strong force perturbation. There is an important difference between collocated and non-collocated observer behavior that can be noticed from Figure 6.24 and Figure 6.25. The performance of the collocated observer slightly improves as the observer size increases (higher number of modes included), whereas in the non-collocated case the opposite tendency is seen. This behavior can be due to weaker measured signals (either strain or acceleration) so that the overall noise to signal ratio increases, especially for higher modes of vibration which leads to stronger oscillations of the estimated force.

A change in the original system dynamics (*e.g.* a shift of the eigenfrequencies) due to environmental conditions (*e.g.* temperature variations, marine growth), was considered by another simulation test. Here, the global Young's modulus was changed from the origin by 2.5%, 5% and 7.5%, which led to changes of the natural frequencies that are shown in Table 6.2 for *x* directional bending modes.

Table 6.2: Natural frequencies for different Young's modulus (E) of the tripod structure

	E(100%)	*E*(97.5%)	*E*(95%)	*E*(92.5%)
f_{1x}[Hz]	6.28	6.20	6.12	6.04
f_{2x}[Hz]	47.38	46.79	46.19	45.58
f_{3x}[Hz]	141.89	140.12	138.34	136.53
f_{4x}[Hz]	198.30	195.83	193.33	190.80
f_{5x}[Hz]	203.12	200.58	198	195.39
f_{6x}[Hz]	233.86	230.95	228	225.01
f_{7x}[Hz]	258	255.03	252.01	248.94
f_{8x}[Hz]	288.48	284.88	281.22	277.52

The performance of the observer with SNR=50 for both sensors is presented in Figure 6.26 for both collocated and non-collocated instances. The results clearly show that an increase in observer complexity does not necessarily improve the force estimation. The reason for this is the test load with a highest frequency of 200Hz which was covered by the simplest tipod tower model of 4 modes. Another issue which can be noticed from Figure 6.26 is that the non-collocated observer is less sensitive to changes in original system complexity.

The above numerical studies on both test structures prove that the SS&IE algorithm is able to reconstruct an external input in a robust way under model and measurement uncertainties for both collocated and non-collocated accelerometer and load positions. Furthermore, the

complexity of a model depends only on the frequency range of the excitation. In non-collocated cases the SS&IE can also deliver acceptable load estimation even if the original system is not observable and special signal processing is carried out to attenuate the noise content of the responses.
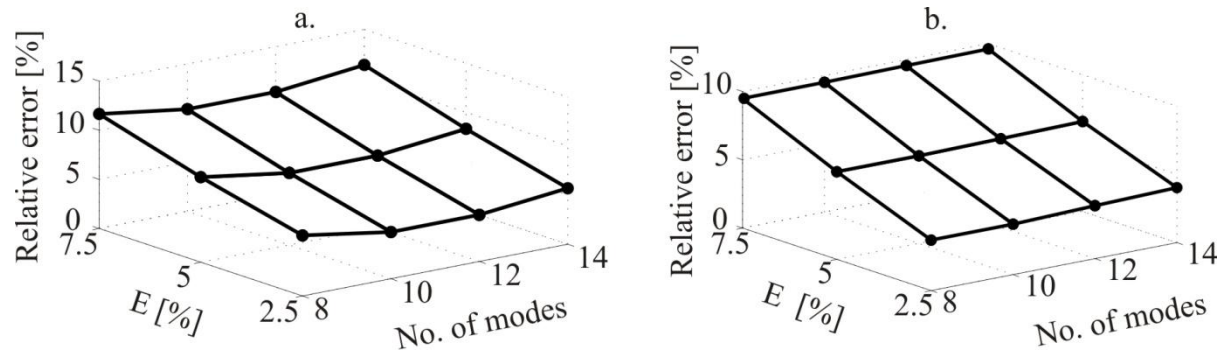
*Figure 6.26: Relative simulated error of the estimated force for different number of modes and relative change of the global Young's modulus E; (a) – **collocated** force and accelerometer (b) – **non-collocated** force and accelerometer*

6.3.3 Laboratory Tests

SIMPLY SUPPORTED BEAM UNDER QUASI STATIC LOAD

The results of the simulations lead to the conclusion that the observer is capable to reconstruct the non-collocated load with acceptable accuracy if additional signal filtering is introduced. To validate this capability on the experimental laboratory structure a simply supported **I** beam with the same physical and geometrical properties as in the model before, as shown in Figure 6.27, was utilized.
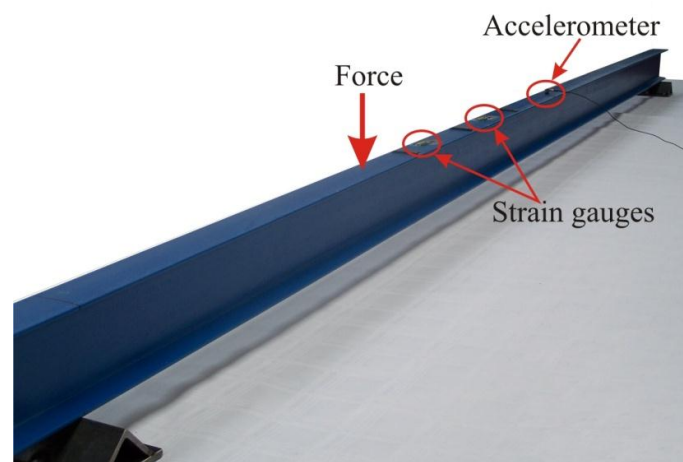
Figure 6.27: Simply supported steel beam (laboratory structure)

The beam was fitted with two "HBM" strain gauges of type 0.6/120LY1 which were fixed along the beam at 0.3L and 0.4L, respectively, and one movable "PCB" accelerometer of type M353B15. A four modes analytical model of the beam with one strain gauge at 0.3L and one accelerometer at 0.4L were used for constructing the observer. It should be borne in mind that the presence of strain gauges is only necessary if static or quasi static loads need to be estimated. In other instances, the SS&IE may rely only on acceleration measurements provided that assumption (5.32) is held. The typical acquired system responses to quasi-static load which was applied by human weight and respective up-down motion are demonstrated in Figure 6.28(a) and (b), where one can see a significant contribution of strain measurements for quasi-static load estimations.
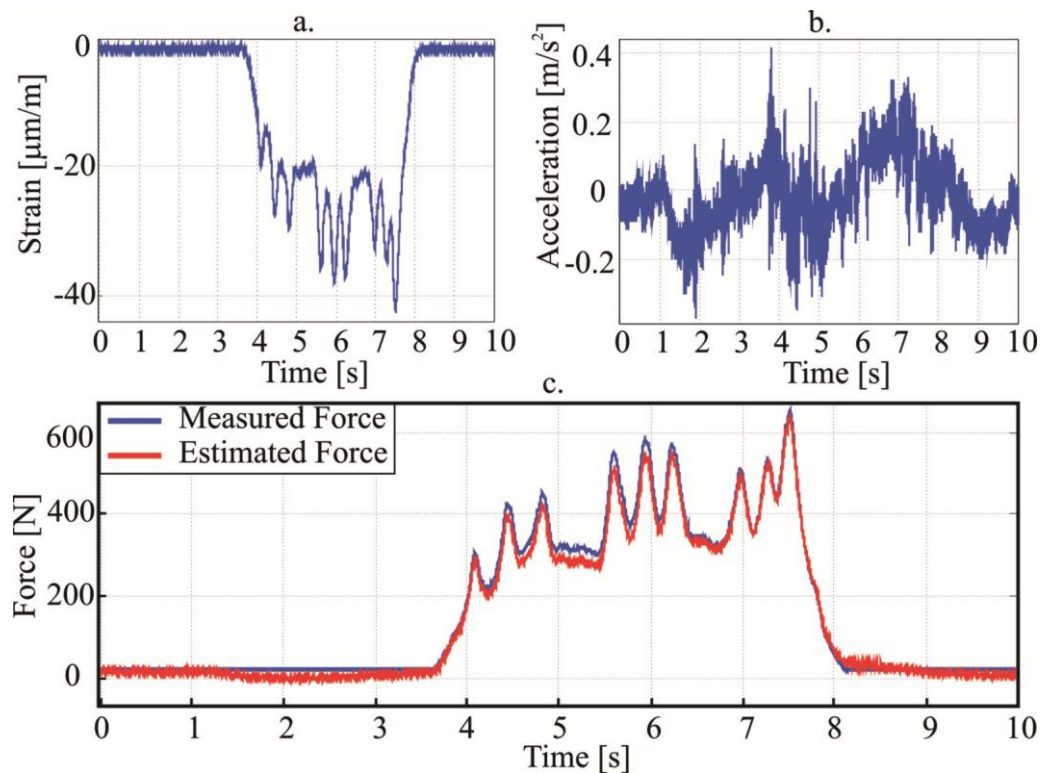
Figure 6.28: Measured strain (a) and acceleration (b) used for the load estimation; (c) quasi-static load reconstruction

The exemplary result of quasi-static load estimation by the SS&IE algorithm applied at 0.5L which was measured by means of a force sensor is represented in Figure 6.28. Based on the quality of estimation in Figure 6.28 one can conclude that a simple beam model which includes only 4 modes is absolutely sufficient for the purpose of constructing SS&IE.

TRIPOD LABORATORY TOWER UNDER WIND LOAD

Finally, a collocated SS&IE observer based on the FE model which combines the first eight modes (4 in *x* and 4 in *y* directions) has been tested on the real laboratory structure shown in

Figure 6.29. The tripod made of steel pipes with the diameters (37.2 mm and 21.3 mm that are welded together) and fixed to the concrete foundation with four bolts at each leg.
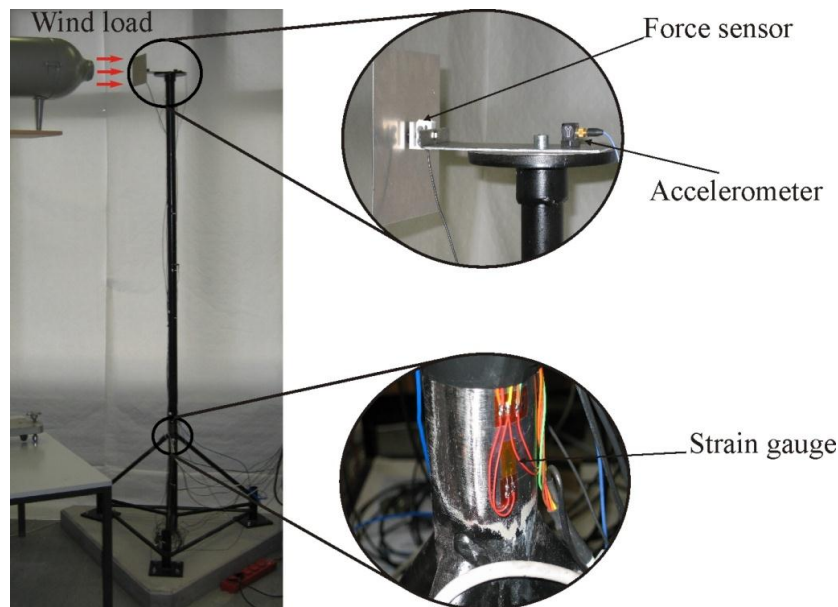
Figure 6.29: Scaled tripod laboratory structure

The load was applied to the tower with the help of a wind fan blowing onto an aluminum plate. Between the plate and the supporting beam, which in turn was rigidly connected to the tower, a "ME" load cell of type KD24S with a nominal maximum load of 20N was located for later validation of the estimated force. Two types of sensors were used for data acquisition, a "PCB" three axis accelerometer of type SN23231 was positioned at the tower top and two "HBM" strain gauges of type 0.6/120LY11 in the half-bridge configuration in order to eliminate the temperature effects which were located near the tripod junction, see Figure 6.29 for details. The acquired measurement data was directly fed into the observer, as shown in Figure 6.30(a) and (b).

One can see that the noise level of the strain gauge is very high. This leads to a strong perturbation of the reconstructed force in the steady state (up to 2.5 seconds) that is over-lapped with the measured force in Figure 6.30(c). Nevertheless the real force was estimated well after the fan was switched on (see Figure 6.30(c) magnification). The relative error between the estimated and measured external force was 11.5%, where the error was calculated according to Equation (6.2). Signal preprocessing was necessary, especially in order to remove the offsets from the acceleration and strain signals which are always present even if the structure is in a steady state.
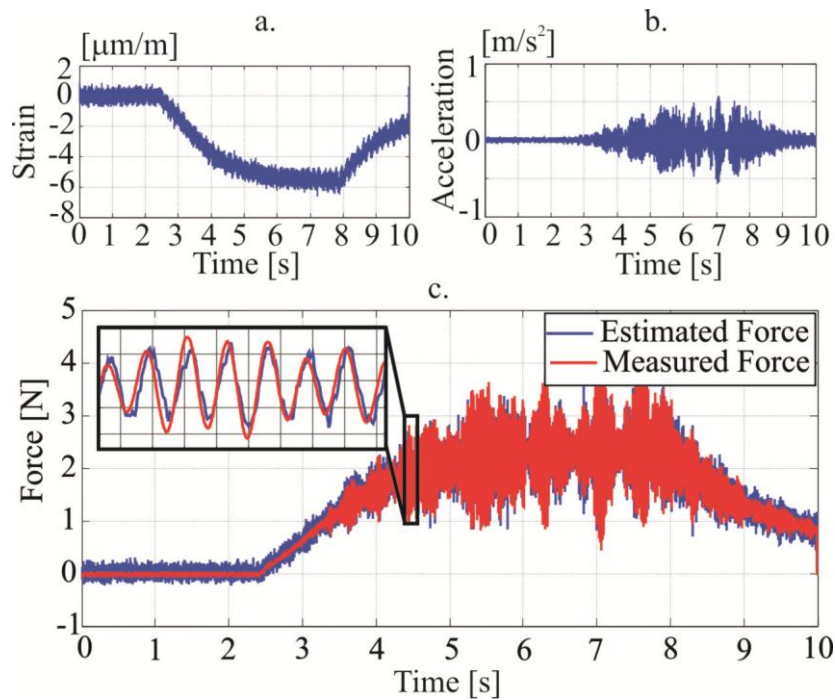
Figure 6.30: Wind load estimation on tripod structure by the SS&IE algorithm

6.4   THE WIND ENERGY PLANT M5000-2

The SS&IE algorithm was tested on the on field structure. For the purpose of the test 167 sensors were installed on the M5000-2 onshore WEP in Bremerhaven. The M5000-2 is a 5 MW wind turbine [AREVA 2010] with a tripod tower structure as shown in Figure 6.31(a). The equipment installation and data collection were carried out by the Federal Institute for Material Research and Testing, Germany.

The external load reconstruction was performed offline as a sub-part of the overall SHM package for future offshore WEPs. For the observer design, an updated FE model was used and two sensor types (two 2-D accelerometers and two strain gauges) were needed. Load estimation was then carried out for the section where the nacelle is connected to the tower. This section was chosen intentionally and included all possible forces that the tower should subtend (external wind forces, static nacelle orientation, blades dynamics, mass unbalance, etc.). In Figure 6.31(c-e), one of the working states of the WEP M5000-2, together with the operational conditions (wind velocity, pitch angle, etc.), is illustrated.

In Figure 6.31(b), the WEP is shown from the top, with the green thick line representing the nacelle with the rotor. Strain sensors are fixed to the tower at 330° and have their own orientation in space which is displayed on the same subplot by the black lines, one line per sensor, respectively. The acceleration sensor is located in the nacelle which is always changing its orientation in space. This causes difficulties for calculation of the observer as it is

based on the modal state space model which has fixed orientation. Therefore, measurements transformation was performed to overcome this problem.
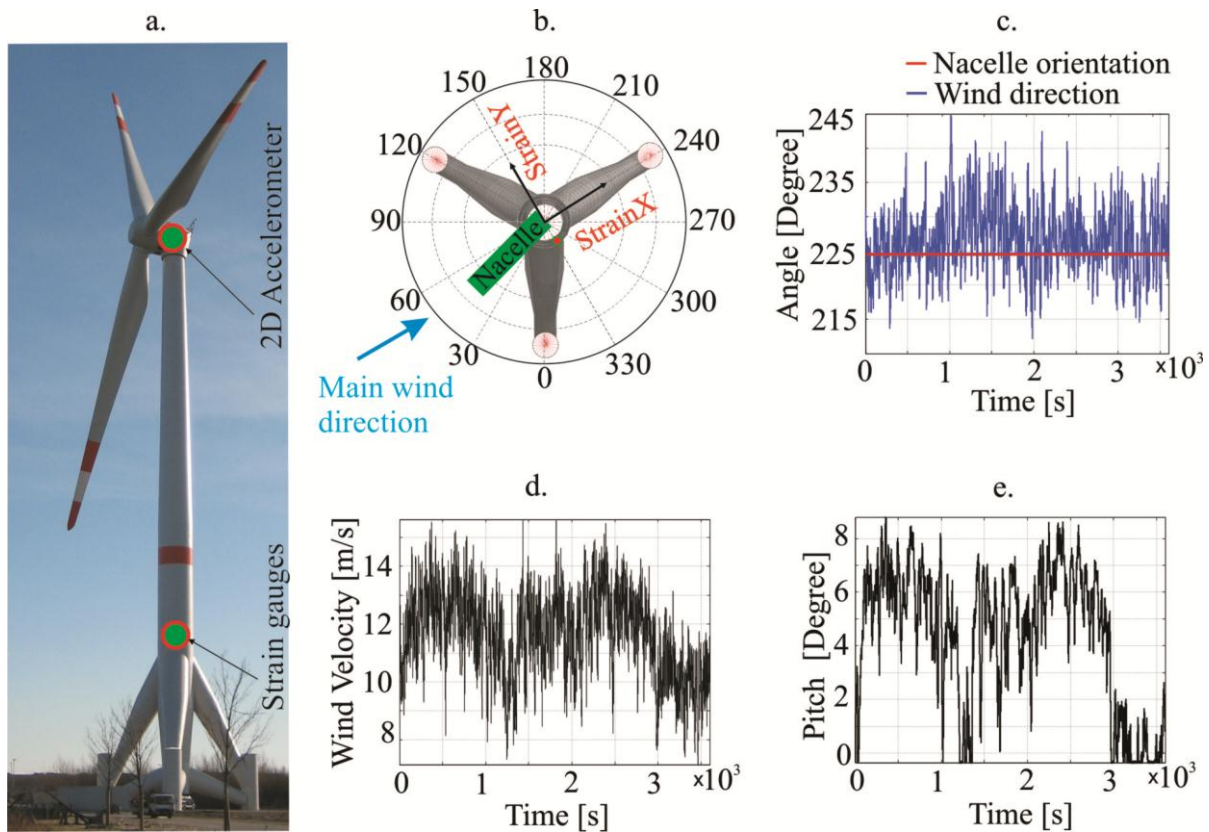
Figure 6.31: Operational state WEA M5000-2 in Bremerhaven: (a) overall structure with schematic sensor positions; (b) and (c) nacelle orientation with respect to the wind together with strain gauges coordinates; (d) and (e) wind velocity and pitch of the rotor blades

The above operational conditions are very close to the ideal ones for the WEP M5000-2, see data sheet [AREVA 2010]: a) the wind direction is almost orthogonal to the rotor area, with a nearly constant wind speed of approximately 12 m/s; b) the blades have a relatively small pitch angle. Such conditions allow using the Betz theory to validate the estimated load. According to Betz, the wind load applied to the rotor area can be calculated as [GASCH and TWELE 2007]:

$$F_{Betz} = \frac{1}{2} c \rho V_{wind}^2 A \tag{6.5}$$

where, c is an aerodynamic thrust coefficient V_{wind} the wind speed, ρ the air density and A the rotor area. The wind is assumed to blow orthogonal to the rotor area. The estimated and Betz forces are depicted in Figure 6.32(c) together with recorded measurements in Figure 6.32(a-b) for a time duration of 25 minutes and the above mentioned operational conditions.

Figure 6.32(c) shows a certain difference between estimated and Betz force especially in the region where the wind velocity is increasing. This is due to the Betz theory as in Equation (6.5), where the Betz force follows the wind velocity behavior for a fixed coefficient c_{air} with no accounting for pitch angles (see for a comparison the wind velocity in Figure 6.31(d) for the time interval 0-1500 seconds; the wind velocity increases and decreases as time evolves).
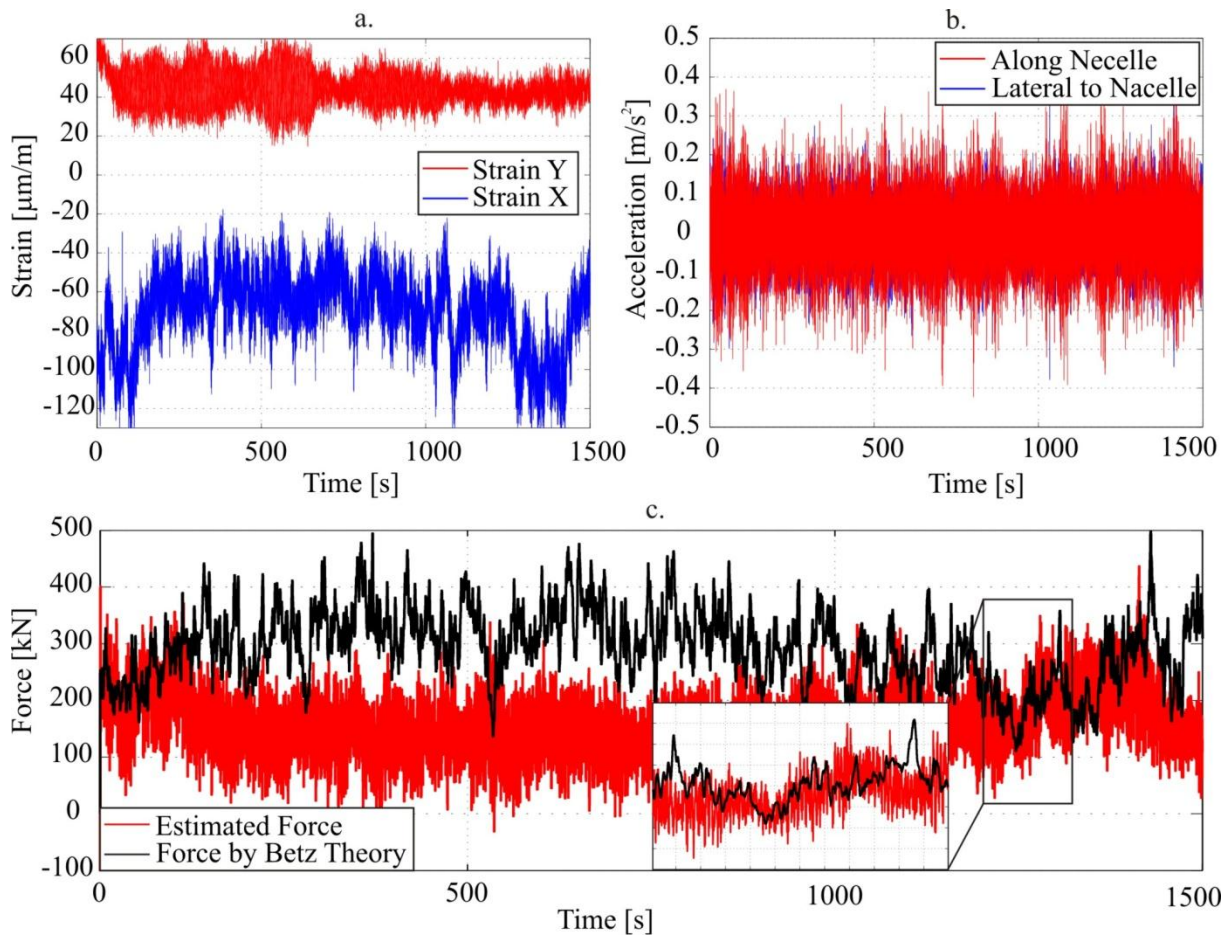
Figure 6.32: Estimated external force for M5000-2

As a result, the Betz force alone cannot be used for the validation; instead, one also needs to take the pitch angle of the rotor blades in consideration. A closer reading of Figure 6.32(c) shows that the estimated force is very close to the Betz force in the regions where the pitch is close to zero (~100 and ~1300 seconds) and decreases as the rotor blades are pitched (see pitch and wind velocity in Figure 6.31(d-e) for the time interval 0-1500 seconds).

A magnification of Figure 6.32(c) demonstrates that the estimated force has slower dynamics similar to the Betz force, but also includes higher frequencies which are obviously the components of all interaction forces between the tower, nacelle and rotor blades. Observations of the estimated load spectrum in Figure 6.33(a) show that the external load lies in a low

frequency range of up to 25 Hz. Moreover, a closer reading of the spectrum in Figure 6.33(b) demonstrates that the stall-effect (blade passage) and its multiples play a very important role in the dynamic excitation of the WEP.

The blade passage frequencies are plotted with orange lines on both plots. The green lines represent the first and the second natural frequencies of the tower which are also present in the estimated load spectra.
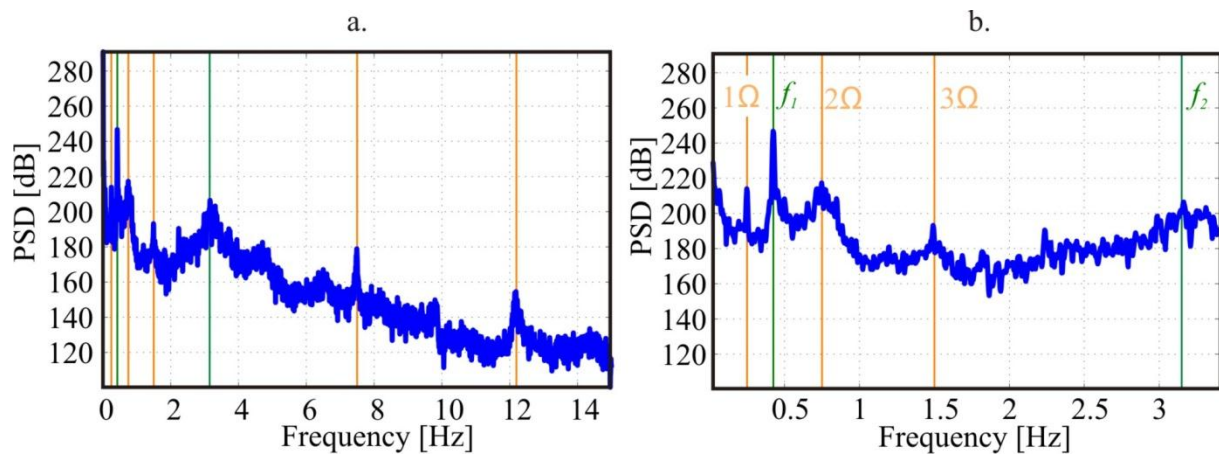
Figure 6.33: Estimated load spectrum [0 - 15] Hz range (left); [0 - 3.5] Hz range (right)

Moreover the spectrum of the wind velocity has a typical logarithmic decay and shown in Figure 6.34. A comparison of the plots in Figure 6.33 and Figure 6.34 reveals the important fact that the load withstood by the WEP tower does not consist solely of the wind load but rather includes loads/forces that result from interactions of other components of the WEP.
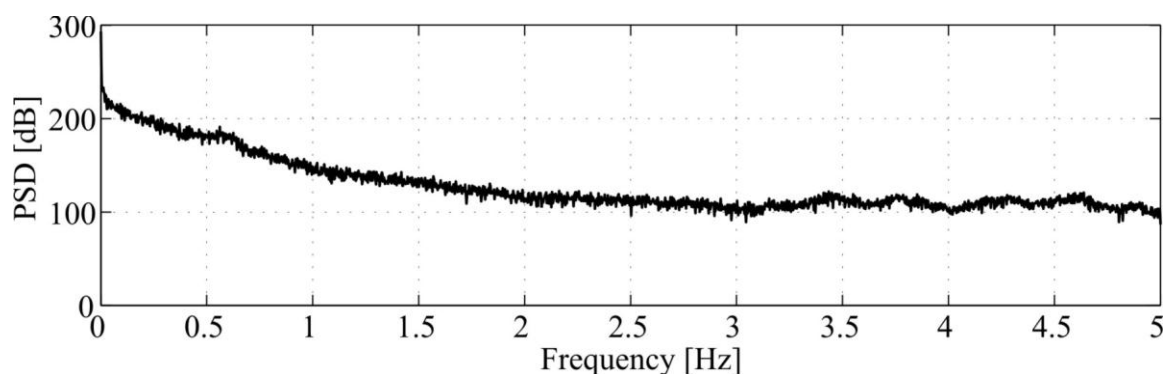
Figure 6.34: Wind velocity spectrum

By means of the estimated force it is possible to calculate shear forces at any location of interest. As an example, the shear forces at the connection of the nacelle and tower for the same operational conditions as in Figure 6.31(c-e) and a time interval of 1500 seconds are

shown in Figure 6.35. An additional important issue associated with the force estimation is its usage in future structural designs.

At the present moment, the most important components of the WEP are designed with the help of commercially available software packages which allow for calculating the wind load and factors in different parameters such as: transients in wind speed, wind direction, and various turbulence spectra. In Figure 6.36, both shear forces at the nacelle tower connection from the Commercial Software Package (CSP) are plotted together with the calculated Betz force for 12.2 m/s wind speed and 19.79% turbulence intensity.
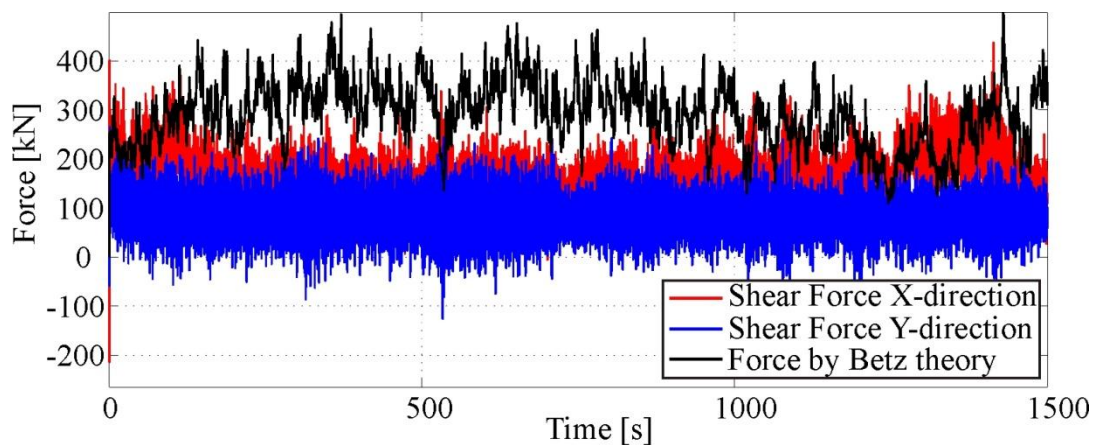
Figure 6.35: Estimated shear forces at the nacelle-tower cross section for 11.8 m/s wind speed and 20.76% turbulence intensity

A comparison of Figure 6.35 and Figure 6.36 shows that the shear forces from CSP are much higher for almost the same operational conditions and do not include all interaction forces of the WEP. The main disagreement between estimated and modeled forces is noticeable in the Y directional shear force; this is due to the different angle of attack of the wind itself, see Figure 6.31(c) and the nacelle orientations.

In the CSP, the nacelle is positioned in the main wind direction which is 240°. This means that the shear force in the X-direction reaches its maximum as shown in Figure 6.31(c), whereas in the case of force estimation the nacelle had only 224.5°. Modeling results might be sufficient for the present design strategy, but this generally leads to structure over sizing at least in the case of the wind load resistance. This might be improved in the future by the records of the estimated dynamic forces from a real, on-field structure. Of course, further reliable usage will still require a validation of the reconstructed forces by means of real, measured shear forces.
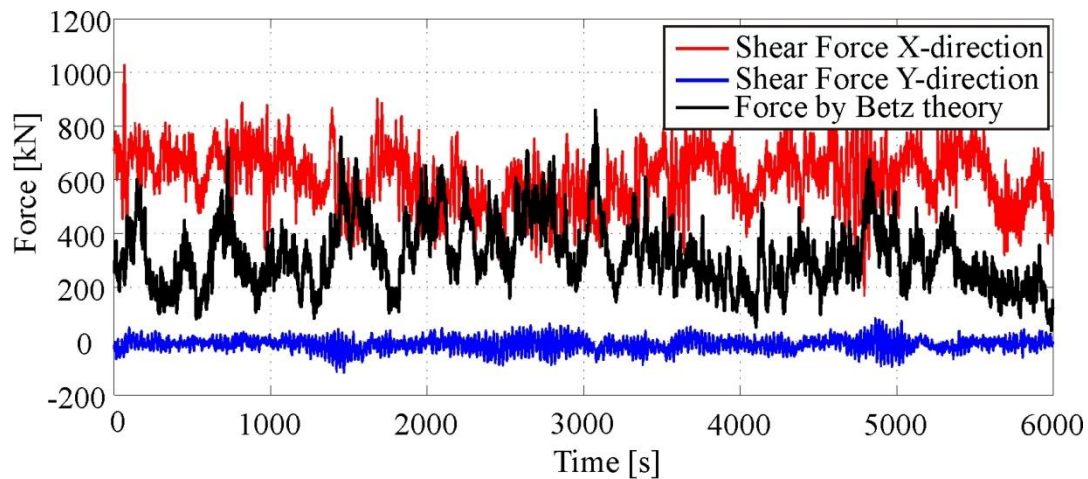
Figure 6.36: Shear forces at the nacelle-tower cross section by GH Bladed at 12.2 m/s wind speed and turbulence intensity of 19.79%

Further investigations of the observer properties should be made together with a validation of the obtained result. Additionally, external moments that play a central role in the life expectancy and fatigue prediction of the tower structure should be estimated and validated in the same way as the external forces. Observations of the estimated load led to a conclusion that the WEP is experiencing a complete bench of forces that are arising throughout the WEP operation and need to be considered for a life expectancy prognosis. Among them are loads from pitching, yaw control, stalling and starting of the rotor.

6.5   NONLINEAR LABORATORY STRUCTURE

A two storey laboratory structure with a non-linear behavior, shown in Figure 6.37(a) and (b) was used to validate the SS&IE performance. The structure in Figure 6.37(a) and (b) is similar to the structure in section 6.2 with a minor modification which makes the overall structure behavior nonlinear. In particular, a stopper element constraining the movement of the lower mass in the positive x direction was added to the supporting frame, as shown in Figure 6.37. The stopper tip was fitted with a "Kistler" quartz load cell of type 9211 to register impacts in order to validate estimated nonlinearity. The nonlinearity was controlled by the distance b between the quartz sensor tip and m_1. The load estimation method was constructed on the basis of the simplified linear mathematical model described in Appendix A. The nonlinear impact effect was taken into the model as an unknown external force which should be estimated together with the load applied from the shaker by the SS&IE algorithm. The data for the observer was acquired in a similar manner as in section 6.2 where the measurements from two accelerometers and two strain gauges were used as inputs to the observer. For structure excitation, a periodic load was generated by means of a shaker in the frequency

range where the difference between the original structure which was connected to the shaker and the mathematical model which was used for the observer design was not large. More details can be found in Chapter 6.2.
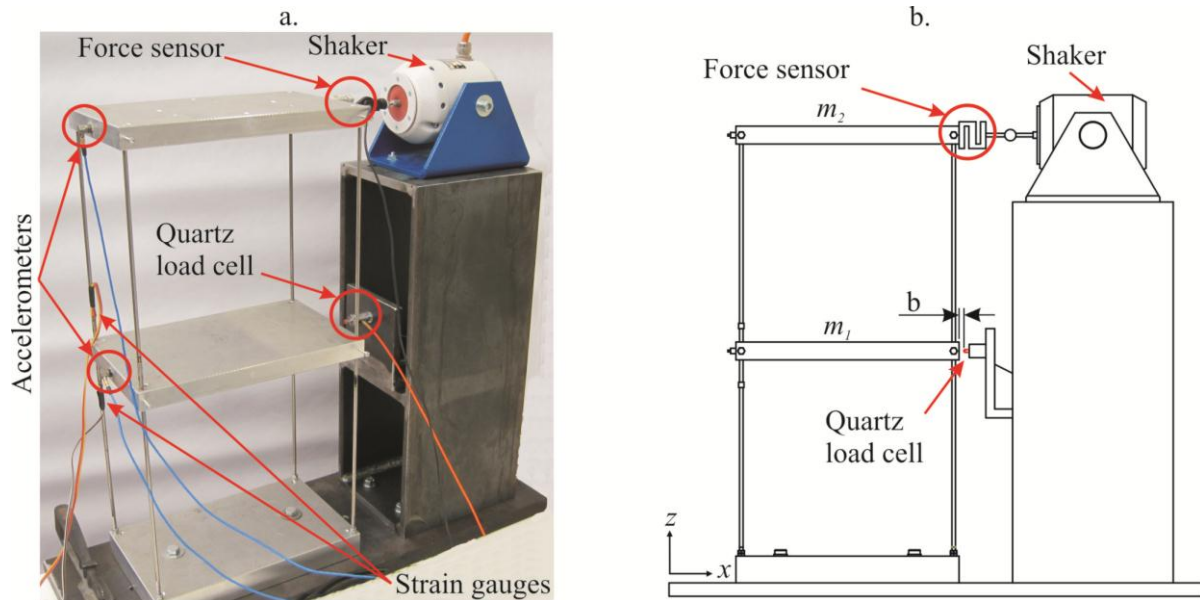
Figure 6.37: (a) A two storey lumped mass nonlinear structure, and (b) side view of same

Figure 6.38 represents an exemplary result of the load reconstruction for a 7 Hz square wave excitation applied to the upper mass m_2. The distance b was held at 2 mm so that the lower mass impacted the holder as it was moving in the positive x direction. Both upper and lower forces were reconstructed with a certain error; see zoomed panels of Figure 6.38. The analysis of the frequency content in the error signal led to the error source, specifically a model simplification which did not take into account the third natural frequency, *i.e.* the longitudinal vibration of the beam legs. The above error occurs only if the impact duration is fast enough to excite the structure up to this frequency range and can be removed easily by the use of a more complete model for the observer design. Figure 6.39 shows SS&IE performance for the impact load type which was applied to the lower mass m_1. The hammer impact was oriented in the positive x direction so that the structure experienced a second impact from the stopper side immediately following the fist impact, see zoomed section in Figure 6.39 for the lower mass where both impacts were captured and estimated well by the SS&IE. The coupling of the shaker introduced a resistive force on the upper mass m_2 which was also estimated by the observer. In contrast to the periodic load which was in the vicinity of first natural frequency (8.2Hz), in the case of the impact an almost complete attenuation of the excited longitudinal beam vibration modes was allowed. As a result, the model error was not as significant as in the case of the periodic load.
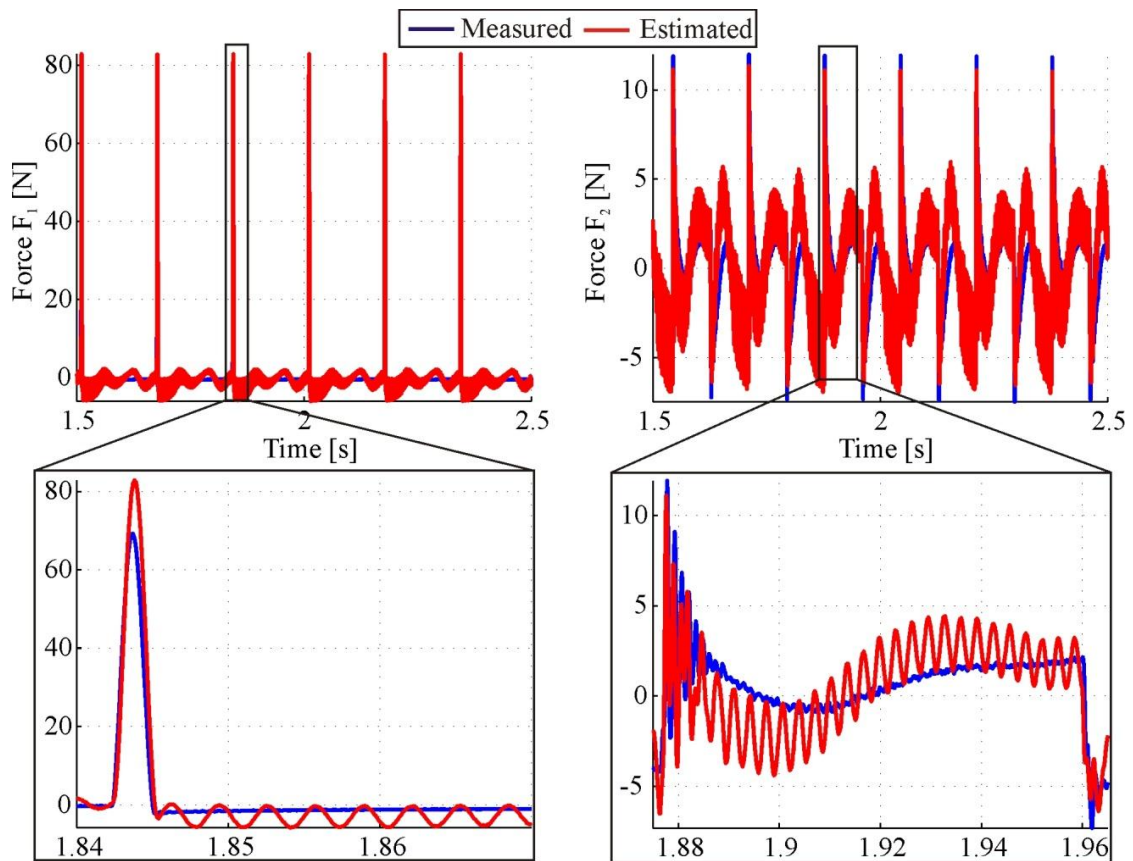
Figure 6.38: Load reconstruction on nonlinear system, square excitation $f_{ex}=7Hz$ on m_2
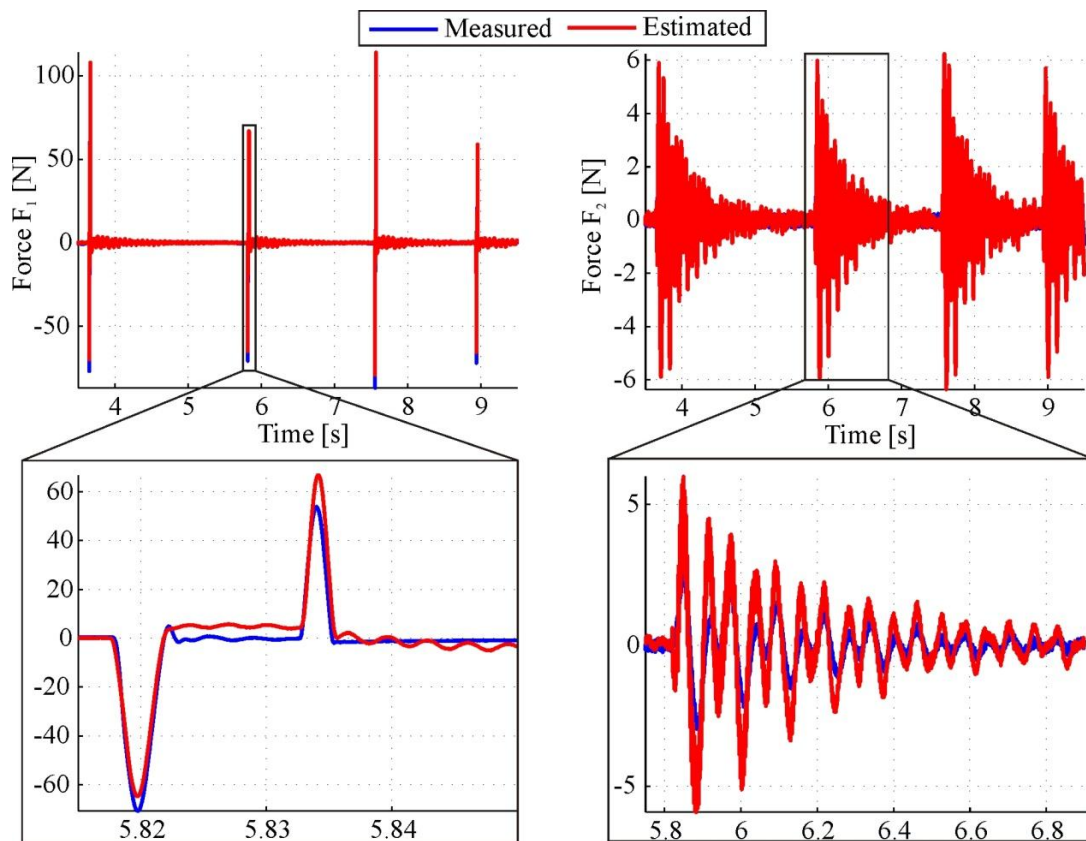
Figure 6.39: Load reconstruction on nonlinear system impact load on m_1

7 Summary, Discussion and Outlook

It is simplicity that makes the uneducated more effective

than the educated when addressing popular audiences.

-Aristotle, Rhetoric

Indirect load reconstruction has been the subject of research for more than three decades. Structural engineers have devoted a great deal of effort to solve this in an efficient way, and the force reconstruction problem is usually solved by using indirect measurement techniques. These techniques include the transformations of related measured quantities such as acceleration, velocity, position or strain. However, these transformations generally lead to the so-called "inverse problem", also known as "deconvolution problem", which is not trivial due to its inherent ill-posedness. Although a number of load estimation methods already exist, most methods are only suited to offline load reconstruction, where the load is reconstructed by means of the recursive optimization procedure with a special treatment of ill-posedness. Therefore, it is the opinion of the present author that they are not applicable for on-field structures where the loads need to be monitored on a permanent basis.

In addition, earlier research efforts attempted to use the estimation methods in an universal fashion without paying attention to the load type, *e.g.* impact time and/or continuous load, which has led to broad palettes of estimation methods. Alternatively, several algorithms can be found in the area of control engineering whereby unknown inputs are estimated with the help of observer-based techniques in order to improve controller performances.

Therefore, the initial goal of the present thesis was first to study and systemize existing algorithms devised by mechanical engineers for the reconstruction of force history and location. The second goal was to determine their respective advantages and merits in solving the inverse problem by comparing simulated and experimental results. Finally possible candidate methods among the other engineering disciplines where identified, that could be applied to overcome the ill-posedness of force history estimation and allow online load reconstruction. The author attempted to incorporate the knowledge of both structural and control disciplines for the purpose of improving the selected algorithms so that transferring the load reconstruction procedure from the laboratory setting to real world applications would be faster.

For this purpose, several modeling possibilities for mechanical structures are presented in Chapter 2. Special attention is paid to the modal model which allows for releasing the sensor placement procedure (from collocated to non-collocated), while simultaneously reducing the model complexity associated with the inverse problem of load estimation. As the analytical modeling of the on-field structure is a tedious procedure, system identification algorithms are considered as an alternative. Since the observers have been adopted by the author from the control engineering field for the purpose of online load estimation, the fundamentals of estimation theory together with those of observer design are presented.

Before qualified estimation methods are presented, an important classification of loads is carried out in Chapter 3. In particular, external loads are classified into three main categories: 1) impact loads; 2) time continuous loads; 3) spatially distributed loads. The classification of loads was an important step because each load type applies special requirements on the load estimation algorithm. For example, an impact load lasts only a short duration of time but can vary in its location, amplitude and duration so that a load estimation procedure has to deal with both location and load history estimation. Conversely, the location of a continuous time load is fixed while its time interval is indefinite.

In Chapter 4 a detailed impact reconstruction procedure is considered. The procedure is divided into two parts: impulse location computation and impulse history reconstruction. To estimate the impulse location a passive sensor technology is used *i.e.* all sensors in the sensor net are in the listening mode and the impact triggers the acquisition of signals. The sensor signals that are recorded following the impact event are used for the information extraction. In particular, the frequency content of the solid wave is extracted with the help of the CWT technique and is used for the estimation of the wave group velocity from the dispersion curve of a specimen. To facilitate the extraction of only the initial wave frequency by the CWT algorithm, acquired signals are truncated and windowed to avoid leakage. Additionally, a reliable automatic onset time picking technique based on the Akaike information criterion (AIC) is used for estimation of the time of arrival. The localization phase is then completed by the location search algorithm which utilizes the extracted wave group velocity and the difference between the wave's arrival times at every specific sensor. A candidate search strategy for the isotropic material is presented in section 4.2.2. This strategy is applicable to a variety of plate type geometries and needs to be modified for anisotropic materials by taking into account the wave velocity profile.

Two most appropriate discrete time methods are suggested by the author for the purpose of impact history reconstruction. The first method is a direct time domain decomposition which was extended by [NORDSTRÖM 2005] by means of a specific sensor time delay to compensate for the rank deficiency which always occurs when the sensors are removed from the impact location. This method works well if certain caveats are taken in consideration. It is important to keep the dimensions of the block Toeplitz matrix to be inverted as small as possible, which in turn implies that recorded signals must optimally capture the impact duration. In addition, a sensor-specific time delay should be chosen in order to guarantee a stable deconvolution. The choice proposed by [NORDSTRÖM 2005] is not connected to any physical quantities and involves a trial and error approach. In the present work, a new sensor specific time delay is introduced which is based on the previous estimated times of arrival. Using the proposed delay ensures a proper rank for the Toeplitz matrix in Equation (4.21) and has a direct connection to wave propagation within the medium.

The second algorithm estimates the impact history by solving the optimal tracking problem, or, more specifically, by finding an optimal control input (impact load) which allows for the tracking of captured measurements. Drawing its origins in control engineering, it is an iterative process having two main loops: a forward loop and a backward loop. The backward loop performs a sequential estimation of appropriate gains which are subsequently used with the model description in the forward loop for the state and input estimation. The estimation quality and speed is controlled by the weighting matrices P, Q and R which play an important role together with the complexity of the mathematical model.

The impact reconstruction procedure is presented for an aluminum plate in Chapter 6.1. Beginning with the estimation of several locations in section 6.1.1, it then continued with the detailed analysis of both impact histories estimation algorithms in section 6.1.2. The impact location was estimated in most of the cases with a maximum error of 10% and with a speed sufficient for online applications (*e.g.* within several seconds). For the purpose of location estimation, a local search algorithm which minimized the error cost function was used for the search procedure that required several runs in order to avoid a local minimum. Therefore, a certain improvement in terms of computation time might be achieved by the utilization of a global minimization algorithm. In addition, the algorithm could not deliver a reasonable location estimation for some impact locations. These areas were labeled as the "insensitive zones" of the sensor configuration set that was used. To avoid such situations in real-world applications, special precautions should be taken beforehand with regard to sensor locations.

In particular, an initial model would be helpful for the purpose of an optimal sensor placement strategy.

The impact history estimation methods are then tested for chosen estimated locations. To ensure a satisfactory impact history estimation by both optimal tracing and direct time deconvolution methods, certain issues should be taken into account. Experimental results show that the length of measured signals that are used for the load estimation should be kept as short as possible in both approaches. Moreover, a proper impact location determination leads to a better estimation of the impact history. Among other factors for obtaining the optimal tracking algorithm, it is recommended to keep the values of weighting matrix $\boldsymbol{R}$ (which is a scalar for the single impact force) in Equations (4.34) - (4.37) as small as possible but larger than zero, as an increase in its values restricts the input variation and simultaneously smoothes the reconstructed impact. Additionally, higher values in weighting matrix $\boldsymbol{Q}$ in Equations (4.34) - (4.37) yield a better estimation but can also lead to instability. Therefore, a trade-off between the estimation closure to a real impact and the solution stability needs to be found by assigning the $\boldsymbol{Q}$ matrix. Direct time deconvolution is not worked if the specific sensor delay was applied. The proposed usage of TOAs for sensor delay delivered always stable and consistent impact history estimations. Nevertheless, the direct time deconvolution required a longer time for the impact estimation in comparison with an optimal tracking filter which required only 0.14 seconds. Therefore, the optimal tracking filter is rather recommended if the impact estimation is to be done near online time mode. An important advantage of the optimal tracking filter is the parallel estimation of state variables which can be used for either control or SHM purposes. Finally, it is important to mention that the model quality and complexity influence impact history estimation. The results of the experiment described in Chapter 6.1 clearly show that the higher model complexity dramatically increases the computational time on the one hand, but a simple model leads to poor load estimation on the other. Therefore, the model should be as simple as possible and should simultaneously cover the highest frequency that the impact can excite.

Continuous time load estimation methods are presented in Chapter 5. At first, the simultaneous state and input estimator (SS&IE) is treated in a very detailed fashion as it has a potential to estimate inputs also in the case of nonlinear systems that can incorporate Lipschitz type[1] and unknown nonlinearity. In particular, a computation of the observer matrices is presented for both linear and nonlinear systems. The SS&IE design implies several conditions to be

---

[1] nonlinear function which satisfy Lipschitz continuity condition

fulfilled. First of all, if both states and inputs need to be estimated, the system under consideration should be observable. This condition can be released to detectable if only inputs are to be estimated. If *Condition 1* in subsection 5.1.2 leads to a construction of extended matrix S such that it is of full column rank, then a simple inversion procedure might be used for the computation of observer matrices T and Q. The full column rank condition also imposes that the number of measurements must be at least equal or greater than the sum of inputs and unknown nonlinear functions. This in its turn makes it obligatory to use sensors that contribute independently to the direct feed trough matrix D such that D has a full column rank, *e.g.* independent acceleration measurements. Consequently, in the case of nodal coordinates the sensors should be collocated with the applied load positions, which is impractical for some real life applications. Therefore, it is preferable to use a modal model for the observer construction since it can release the above collocation condition and assure a stable observer for some load sensor distances. A computation of the observer matrices L and N depends on the systems type. For linear systems a simple pole placement procedure can be used as in [NIU *et al.* 2010], whereas for nonlinear systems a more general LMI approach needs to be applied. Moreover, in the cases of certain linear systems it is possible to improve the load estimation quality by inserting a nonexistent nonlinearity matrix W into the observer design so that a pure numerical improvement of the matrix S will lead to a more robust observer behavior. As shown in section 5.1.4, the SS&IE performance strongly depends on the model and measurement quality; therefore these issues should be dealt carefully if a good estimation is desired.

In sections 5.2 and 5.3, the modified proportional integral observer (MPIO) and Kalman filter with unknown inputs (KF-UI) are presented as additional candidates for continuous load reconstruction in the case of linear systems. Both, of the above demand the system under consideration to be observable. The MPIO is capable of attenuating the measurement noise but still significantly depends on the model quality. Furthermore, as shown in Chapter 5.2.1, the MPIO would fail for the fast changing load, due to its internal structure where the unknown disturbance is assumed to be a piece-wise constant, so that a derivative of unknown forces is present in the error equation. The KF-UI has an immunity to both model and measurement uncertainties. Similarly to SS&IE, the KF-UI requires that a full column rank condition of the direct feed through matrix D is held and the covariance matrices of process and measurement noise are given as *a priori*.

A simple two storey test rig was used in Chapter 6.2 as a benchmark for the SS&IE, the KF-UI and the MPIO. To validate their performance, different load functions were used. In

particular, the impact loads generated by the impulse hammer and the periodic load generated by the shaker, as well as their combination, were applied on either the upper or the lower mass. All the observers were based on the simplified 2DOF model which considered only a planar motion. In addition, the mathematical model was constructed for the free structure without a connection to the shaker. This simplification led to a divergence between model and real structure in the vicinity of resonant frequencies. The load estimation results have given evidence regarding the expected observer's behavior. Above all, the MPIO was not able to estimate the load with high dynamics *e.g.* impulse or high frequency sinusoidal loads; nevertheless, it was capable of delivering a good reconstruction of slowly changing forces. The performance of the SS&IE and the KF-UI was very similar for almost every load type. No particular advantage to the KF-UI as opposed to the SS&IE was noticed for regions of higher order system and model divergence where all three algorithms showed poor estimation quality. Moreover, attempts to increase the immunity of the KF-UI to model uncertainty by means of an increase in process covariance matrix $\boldsymbol{Q}_k$ led to estimator instability. Based on overall results, the SS&IE algorithm was chosen for further analysis as superior to KF-UI and MPIO due to its similar performance to KF-UI in the case of linear systems and its inherent ability to work with nonlinear systems.

A detailed analysis of the SS&IE algorithm was carried out in Chapter 6.3. Here, the continuous distributed models of the structures firstly served as test rigs for numerical simulations.The main objectives of the analysis were:

1. To test the SS&IE algorithm constructed from the modal model which was able to release sensors-load collocation conditions in Equation (5.32) for the direct feed through matrix $\boldsymbol{D}$. For this purpose, an analytical model of a simply supported aluminum beam was used, where the SS&IE was tested for the case when the load and the acceleration sensor were not collocated;

2. To validate the robustness of the algorithm to model variation and noise level changes in both cases *i.e.* collocated and non-collocated accelerometer and force positions. To this end, the SS&IE observer which was based on the FE model of the scaled tripod tower of WEP was tested for different measurement and model uncertainties.

The results of the numerical studies on both test structures proved that the SS&IE algorithm was able to reconstruct an external input in a robust way under model and measurement uncertainties in both the collocated and non-collocated accelerometer and load position instances. Furthermore, the model complexity was dependent only on the range of frequencies that were excited by an external load. In non-collocated cases, the SS&IE could also deliver

acceptable load estimation even if the original system was not observable and special signal filtering was carried out in order to attenuate the noise content of the responses. Finally, the SS&IE algorithm was tested on similar laboratory structures for the quasi-static and wind load reconstruction. The estimation results are presented in subsection 6.3.3, where in both instances the estimated and the measured are very close.

In Chapter 6.4, the SS&IE algorithm was applied on the on-field WEP M5000-2. An updated FE model was used for designing the observer, and two sensor types (two 2-D accelerometers and two strain gauges) were needed. Load estimation was then carried out for the section where the nacelle is connected to the tower. This section was chosen intentionally and includes all possible forces that the tower should subtend (external wind forces, static nacelle orientation, blades dynamics; mass unbalance, etc.). The estimated load was validated with the help of the Betz theory which allowed for computing the wind load applied by the wind on the rotor area of the WEP. The average estimated force was very close to the Betz load as long as the pitch angle was close to zero, but contained higher frequencies which obviously were the components of all interaction forces between the tower, nacelle and rotor blades. A comparison of the estimated load spectra with computed shear forces led to the conclusion that existing commercial software package calculates loads that either exaggerate or do not include overall load dynamics.

At the end of the examples section, a two storey nonlinear system was used as a test rig to assess the ability of the SS&IE algorithm in estimating the load driven by nonlinear effects. For this purpose, the observer was designed on the basis of a simplified linear model, as in Chapter 6.2, and the force produced by the nonlinearity effect (*i.e.* the stopper at lower mass) was considered as an external load. Initially, the structure was excited by a shaker with periodic load. Both upper (shaker) and lower (nonlinearity effect) forces were reconstructed with a certain error. The analysis of the frequency content in the error signal led to the error source, namely a model simplification which did not consider the third natural frequency. *i.e.* the longitudinal vibration of the beam legs. The error occurred only if the impact duration was fast enough to excite the structure up to this frequency range and could be removed easily by the use of a more complete model for observer design. Secondly, the impact load was applied to the lower mass. The hammer impact was followed by a second impact from the stopper side immediately after the first impact. Both impacts were well captured and estimated by the SS&IE. The coupling of the shaker introduced a resistive force on the upper mass which was also estimated by the observer. In contrast to the periodic load which was in the vicinity of the first natural frequency, in the case of the impact an almost complete attenuation of excited

beams flexural modes was allowed. As a result, the model error is not as significant as in the case of the periodic load.

Within the framework of future developments of the load estimation algorithms for on-field applications, the load reconstruction methods presented in this work can be improved upon in several ways. In particular, the impact location search procedure can be optimized and freed of any additional structural knowledge such as dispersion curves. Attempts to increase the immunity to measured and model uncertainty of the SS&IE algorithm could be made in a similar manner as in MPIO by introducing additional integration into an output equation. Additionally, the MPIO could be adjusted for the impact load estimation by a modification of the observer design for the system which included the direct feed through matrix. Finally, the nonlinearity detection ability of SS&IE could be successfully used in SHM for damage detection.

8 REFERENCES

Adams, R. and Doyle, J. F., 2002: *Multiple force identification for complex structures*, Experimental Mechanics (Vol. 42), Nr. 1, pp. 25-36.

Areva, 2010: *M5000 Technical data, Available from*, http://www.areva-wind.com/m5000/technische-daten/.

Bar-Shalom, Y.; Li, X. R. and Kirubarajan, T., 2001: *Estimation with Applications to Tracking and Navigation: Theory Algorithms and Software*, John Wiley & Sons, New York.

Boyd, S.; El Ghaoui, L.; Feron, E. and Balakrishnan, V., 1994: *Linear Matrix Inequalities in Systems and Control Theory*, book, S., Philadelphia.

Carne, T. G.; Bateman, V. I. and Mayes, R. L., 1992: *Force reconstruction using a sum of weighted accelerometers technique*, Proc. of 10th IMAC, San Diego, California, USA, pp. 291-298.

Corless, M. and Tu, J., 1998: *State and input estimation for a class of uncertain systems*, Automatica (Journal of IFAC) archive (Vol. 34), Nr. 6, pp. 754-764.

Crassidis, J. and Junkins, J., 2004: *Optimal Estimation of Dynamic Systems*, Applied Mathematics and Nonlinear Science CRC Press, LONDON.

Deng, S. and Heh, T.-Y., 2006: *The study of structural system dynamic problems by recursive estimation method*, The International Journal of Advanced Manufacturing Technology (Vol. 30), Nr. 3-4, pp. 195-202.

Doyle, J. c. and Stein, G., 1979: *Robustness with Observers*, IEEE Transactions on automatic control (Vol. 24), Nr. 4, pp. 607-611.

Doyle, J. F., 1989: *Determining the contact force during the transverse impact of plates*, Experimental Mechanics (Vol. 29), Nr. 4, pp. 414-419.

Doyle, J. F., 1997: *Wave Propagation in Structures*, Springer, New York, ISBN: 978-0-387-94940-6.

Doyle, J. F., 1999: *Force identification from dynamic response of a biomaterial beam*, Experimental Mechanics (Vol. 33), pp. 64-69.

Doyle, J. F. and Kannal, L. E., 1997: *Combining spectral super-elements, genetic algorithms and massive parallelism for computationally efficient flaw detection in complex structures*, Computational Mechanics (Vol. 20), pp. 67-74.

Doyle, J. F. and Martin, M. T., 1996: *Impact force location in frame structures*, International Journal of Impact Engineering (Vol. 18), Nr. 1, pp. 79-97.

Duan, G. R.; Liu, G. P. and Thompson, S., 2001: *Eigenstructure assignment design for proportional integral observers: continuous-time case*, IEEE Proceedings - Control Theory and Applications (Vol. 148), Nr. 3, pp. 263-267.

Dzhaferov, I., 2009: *Impact Detection, Localization and Reconstruction Based on the Passive Sensing Methodology for Homogeneous Plate, with GUI Development for Future Educational Exposition*, Project Work, Institute of Mechanics and Control Engineering - Mechatronics, University of Siegen, Siegen.

Elliott, K.; Buehrle, R. and James, G., 2005: *Space shuttle transportation loads diagnostics*, Proceedings of the 23rd International Modal Analysis, Orlando, Florida.

Engl, H.; Hanke, M. and Neubauer, A., 2000: *Regularization of Inverse Problems*, Mathematics and its Applications, Kluwer Academic Publishers, Dordrecht.

Gasch, R. and Twele, J., 2007: *Windkraftanlagen*, 5. Ed., Teubner, Wiesbaden, Germany.

Gaul, L. and Hurlebaus, S., 1998: *Identification of the Impact Location on a Plate Using Wavelets*, Mechanical Systems and Signal Processing (Vol. 12), Nr. 6, pp. 783-795.

Gawronski, W. K., 2004: *Advanced structural dynamics and active control of structures*, Springer, New York.

Genaro, G. G. and Rade, D. A., 1998: *Input force identification in time domain*, Proceedings of the 16th International Modal Analysis Conference, pp. 124-129.

Golub, G. H. and Van Loan, C. F., 1996: *Matrix computations* 3. Ed., Johns Hopkins University Press, Baltimore, USA.

Gopalakrishnan, S. and Doyle, J. F., 1994: *Wave propagation in connected waveguides of varying cross-section*, Journal of Sound and Vibration (Vol. 175), Nr. 3, pp. 347-363.

Góral, G.; Zbydoˊn, K. and Uhl, T., 2002: *Intelligent transducers of in-operational loads in construction fatigue monitoring*, Mach. Dyn. Probl (Vol. 2-3), pp. 73-78.

Grosse, C. U. and Ohtsu, M., 2008: *Acoustic Emission Testing*, Springer-Verlag, Berlin Heidelberg.

Ha, Q. P.; Nguyen, A. D. and Trinh, H., 2004: *Simultaneous state and input estimation with application to a two-link robotic system*, Proc. ASCC of the 5th Asian Control Conference, pp. 322-328.

Ha, Q. P. and Trinh, H., 2004: *State and input simultaneous estimation for a class of nonlinear systems*, Automatica (Vol. 40), pp. 1779-1785.

Hansen, P. C., 1998: *Rank-Deficient and Discrete Ill-Posed Problems*, SIAM Mathematical Modeling and Computation, SIAM, Philadelphia.

Hansen, P. C.; Golub, G. H. and O'Leary, D. P., 1999: *Tikhonov regularization and total least squares*, Matrix Analysis Applications, SIAM (Vol. 21), Nr. 1, pp. 185-194.

Hansen, P. C. and O'Leary, D. P., 1993: *The Use of the L-Curve in the Regularization of Discrete Ill-Posed Problems*, SIAM Comput. (Vol. 14), Nr. 6, pp. 1487-1503.

Hensel, E., 1991: *Inverse Theory and Applications for Engineers*, Advance Reference Series, Prentice Hall, New Jersey.

Hensman, J.; Mills, R.; Pierce, S. G.; Worden, K. and Eaton, M., 2010: *Locating acoustic emission sources in complex structures using Gaussian processes*, Mechanical Systems and Signal Processing (Vol. 24), Nr. 1, pp. 211-223.

Herold, C.; Leibfried, T.; Markalous, S. and Quint, I., 2007: *Algorithms for Automated Arrival Time Estimation of Partial Discharge Signals in Power Cables,* International Symposium on High Voltage Engineering, Ljubljana, Slovenia.

Hillary, B. and Ewins, D. J., 1984: *The use of strain gauges in force determination and frequency response function measurements*, Proceeding of 2nd IMAC, Orlando.

Hofmann, B., 1986: *Regularization for Applied Inverse and Ill-posed Problems* Teubner-Texte zur Mathematik, Teubner, Leipzig

Inoue, H.; Harrigan, J. J. and Reid, S. R., 2001: *Review of inverse analysis for indirect measurement of impact force*, Appl. Mech. Rev. (Vol. 54), Nr. 6, pp. 503-524.

Jacquelin, E.; Bennani, A. and Hamelin, P., 2003: *Force reconstruction: analysis and regularization of a deconvolution problem*, Journal of Sound and Vibration (Vol. 265), pp. 81-107.

Jankowski, Ł., 2009: *Off-line identification of dynamic loads*, Structural and Multidisciplinary Optimization (Vol. 37), Nr. 6, pp. 609-623. URL: http://dx.doi.org/10.1007/s00158-008-0249-0

Johannesson, P., 1999: *Rainflow analysis of switching Markov loads*, Institute of Technology, Lund, Denmark.

Juang, J.-N. and Pappa, R. S., 1985: *An Eigensystem Realization Algorithm for Modal Parameters Identification and Model Reduction* Journal of Guidance, Control and Dynamics (Vol. 8), Nr. 5, pp. 620-627.

Kailath, T., 1980: *Linear Systems* Prentice-Hall.

Kalman, R. E. and Bucy, R. S., 1961: *New Results in Linear Filtering and Prediction Theory*, Journal of Basic Engineering, pp. 95-108.

Kammer, D. C. and Steltzner, A. D., 2001: *Structural identification of Mir using inverse system dynamics and Mir/Shuttle docking data*, Journal of Vibration and Acoustics (Vol. 132), Nr. 2, pp. 230-237.

Kautsky, J.; Nichols, N. K. and Van Dooren, P., 1985: *Robust pole assignment in linear state feedback* International Journal of Control (Vol. 41), pp. 1129-1155.

Kishimoto, K.; Inoue, H.; Hamada, M. and Shibuya, T., 1995: *Time frequency analysis of dispersive waves by means of wavelet*, Journal of Applied Mechanics (Vol. 62), Nr. 4, pp. 841-847.

Kraemer, P. and Fritzen, C.-P., 2010: *Aspects of Operational Modal Analysis for Structures of Offshore Wind Energy Plants*, IMAC XXVIII, Jacksonville, Florida, USA.

Krajcin, I. and Söffker, D., 2005: *Diagnosis and control of 3D elastic mechanical structures*, Smart Material Structures, San Diego, CA, USA.

Krishna, K. B. and Pousga, K., 2001: *Disturbance attenuation using Proportional Integral Observer*, International Journal of Systems Science (Vol. 74), Nr. 6, pp. 618-627.

Kurz, J. H.; Grosse, C. U. and Reinhardt, H. W., 2005: *Strategies for reliable automatic onset time picking of acoustic emissions and of ultrasound signals*, Ultrasonics (Vol. 43), Nr. 7, pp. 538-546.

Leissa, A. W., 1969: *Vibration of plates*, NASA SP-160, U. S. Government Printing Offices, Washington, USA

LePage, W. R., 1961: *Complex Variables and the Laplace Transform for Engineers*, McGraw Hill Book Company, New York.

Lewis, F. L., 1986: *Optimal control*, John Wiley & Sons, New York, USA.

Liu, J.-J.; Ma, C.-K.; Kung, I.-K. and Lin, D.-C., 2000: *Input force estimation of a cantilever plate by using a system identification technique*, Computer Methods in Applied Mechanics and Engineering (Vol. 190), Nr. 11-12, pp. 1309-1322.

Ljung, L., 1999: *System Identification Theory for the User*, Thomas, K., Information and System Science, Prentice Hall, London.

Ljung, L., 2008: *Perspectives on System Identification*, IFAC Congress, Seoul. URL: http://www.control.isy.liu.se/~ljung/seoul2dvinew/plenary2.pdf

Lourens, E.; Lombaert, G.; De Roeck, G. and Degrande, G., 2008: *Identification of dynamic axle loads from bridge responses by means of an extended dynamic programming algorithm*, 2nd International Workshop on Civil Structural Health Monitoring, Taormina, Sicily, 59-69.

Lourens, E.; Lombaert, G.; De Roeck, G. and Degrande, G., 2009 *Reconstructing dynamic moving loads using an extended dynamic programming algorithm and eigenvalue reduction*, 2nd International Conference on Computational Methods in Structural Dynamics and Earthquake Engineering, Rhodes.

Luenberger, D. G., 1971: *An introduction to observers*, IEEE Transactions on automatic control (Vol. 16), pp. 596-602.

Ma, C.-K.; Chang, J.-M. and Lin, D.-C., 2003: *Input forces estimation of beam structures by an inverse method*, Journal of Sound and Vibration (Vol. 259), Nr. 2, pp. 387-407.

Ma, C.-K. and Ho, C.-C., 2004: *An inverse method for the estimation of input forces acting on non-linear structural systems*, Journal of Sound and Vibration (Vol. 275), pp. 953-971.

Ma, C.-K. and Lin, D.-C., 2000: *Input forces estimation of a cantilever beam*, Inverse Problems in Engineering (Vol. 00), pp. 1-18.

Meirovitch, L., 1967: *Analytical Methods in Vibration*, Company, T. M., London.

Moon, F. C., 1998: *Applied Dynamics: with Applications to Multibody and Mechatronics Systems*, Wiley, New York.

Nesterov, Y. and Nemirovski, A., 1994: *Interior Point Polynomial Methods in Convex Programming: Theory and Applications*, SIAM, Philadelphia.

Niu, Y.; Klinkov, M. and Fritzen, C. P., 2010: *Online Reconstruction of Concentrated and Continuously Distributed Force using a Robust Observer Technique*, European Workshop on SHM, Sorrento, Italy.

Nordström, L. J. L., 2005: *Input estimation in structural dynamics*, Chalmers University of Technology Sweden, Göteborg, Sweden.

O'reilly, J., 1983: *Observers for linear systems*. (Vol. 170), Mathematics in science and engineering, Academics Press, London.

Ogata, K., 1967: *State Space Analysis of Control Systems*, Instrumentation and Controls, Prentice-Hall, London.

Ogata, K., 1970: *Modern Control Theory*, William, L. E., Instrumentation and Controls, Prentice-Hall, London.

Pan, S.; Su, H.; Wang, H. and Chu, J., 2010: *The study of joint input and state estimation with Kalman filtering*, Transactions of the Institute of Measurement and Control, published online (Vol. 00), Nr. 0, pp. 1-18.

Peeters, B. and De Roeck, G., 1999: *Reference-Based Stochastic Subspace Identification for Output-Only Modal Analysis*, Mechanical Systems and Signal Processing (Vol. 12(6)), pp. 855-878.

Peeters, B. and De Roeck, G., 2001: *Stochastic system identification for operational modal analysis: A Review*, Journal of Dynamic Systems, Measurement and Control (Vol. 123(4)), pp. 659-667.

Rao C. R. and Mitra S. K., 1971: *Generalized inverse of matrices and it is applications*, Jhon Willy & Sons, New York.

Seydel, R. and Chang, F. K., 1994: *Impact identification of stiffened composite panels: I System development*, Smart Material Structures (Vol. 10), pp. 354-369.

Seydel, R. and Chiu, W. K., 2001: *Impact identification of stiffened composite panels: II Implementation studies*, Smart Material Structures (Vol. 10), pp. 370-379.

Shafai, B.; Beale, S.; Niemann, H. H. and Stoustrup, J. L., 1996: *LTR Design of Discrete-Time Proportional-Integral Observers*, IEEE Transactions on automatic control (Vol. 41), Nr. 7, pp. 1056-1062.

Shin, K. and Hammond, J. K., 2008: *Fundamentals of Signal Processing for Sound and Vibration Engineers*, John Wiley & Sons Ltd,, West Sussex, Great Britain

Söffker, D. and Krajcin, I., 2003: *Modified PIO design for robust unknown input estimation*, ASME DETC Conferences, Chicago, Illinois, USA.

Söffker, D.; Yu, T.-J. and Müller, P. C., 1995: *State estimation of dynamical systems with nonlinearities by using Proportional- Integral Observer*, International Journal of System Science (Vol. 26), Nr. 9, pp. 1571-1582.

Steltzner, A. D. and Kammer, D. C., 1999: *Input force estimation using an inverse structural filter*, Proceedings of the 17th International Modal Analysis Conference, pp. 954-960.

Steltzner, A. D. and Kammer, D. C., March 1999: *Input force estimation using an inverse structural filter*, Proceedings of the 17th International Modal Analysis Conference, pp. 954.

Stevens, K., 1987: *Force identification problems - an overview*, Proceedings of SEM, Houston, pp. 838-844.

Strang, G. and Nguyen, T., 1996: *Wavelets and Filter Banks*, Wellesley - Cambridge Press, Wellesley, USA.

Tikhonov, A. N. and Arsenin, V. Y., 1977: *Solutions of Ill-posed Problems*, Scripta Series in Mathematics, Wiley, John & Sons, New York.

Tracy, M. and Chang, F.-K., 1998a: *Identifying Impacts in Composite Plates with Piezoelectric Strain Sensors, Part I: Theory* Journal of Intelligent Material Systems and Structures (Vol. 9), Nr. 11, pp. 920-928.

Tracy, M. and Chang, F.-K., 1998b: *Identifying Impacts in Composite Plates with Piezoelectric Strain Sensors, Part II: Experiment* Journal of Intelligent Material Systems and Structures (Vol. 9), Nr. 11, pp. 929-937.

Trujillo, D. M. and Busby, H. R., 1997: *Practical Inverse Analysis in Engineering*, CRC Press, London.

Tuan, P.-C.; Ji, C.-C.; Fong, L.-W. and Huang, W.-T., 1996: *An input estimation approach to on-line two-dimensional inverse heat conduction problems,* Numerical heat transfer (Vol. 29,3), pp. 345-364.

Uhl, T., 2002: *Identification of loads in mechanical structures-helicopter case study*, Computer Assisted Mechanics and Engineering Sciences, CAMES (Vol. 9), pp. 151-160.

Uhl, T., 2007: *The inverse identification problem and its technical applications*, Archive of Applied Mechanics (Vol. 77), pp. 325-327.

Uhl, T. and Petko, M., 2006: *Load identification with the use of neural networks – design and application*, Mechanical Systems and Signal Processing.

Uhl, T. and Pieczara, J., 2003: *Identification of operational loading forces for mechanical structures*, Arch. Transp. (Vol. 16), Nr. 2, pp. 109-126.

Van Overschee, P. and De Moor, B., 1996: *Subspace Identification for Linear Systems*, Kluwer Academic Publishers, Leuven.

Wang, W., 2004: *Wave Propagation in Composites and Least-squares Damage Localization Technique*, Master Thesis, Aerospace Engineering, North Carolina State University.

Welch, G. and Bishop, G., 2001: *An Introduction to the Kalman Filter*. (Vol. Course 8), SIGGRAPH.

Whiston, G. S., 1984: *Remote impact analysis by use of propagated acceleration signals, I: Theoretical methods*, Journal of Sound and Vibration (Vol. 97), Nr. 1, pp. 35-51.

Wojciechowski, B., 1978: *Analysis and synthesis of proportional-integral observers for single input-output time-invariant continuous systems*, Ph.D Thesis, Technical University of Gliwice, Poland, Gliwice.

Wu, Y. and Du, R., 1996: *Feature extraction and assessment using wavelet packets for monitoring of machining processes*, Mechanical Systems and Signal Processing (Vol. 10), Nr. 1, pp. 29-53.

Zhan, X., 2002: *Matrix Inequalities*. (Vol. 1790), Lecture Notes in Mathematics, Springer-Verlag Heidelberg, ISBN: ISSN 0075-8434.

Zhang, F., 2005: *The Schur Complement and Its Applications* (Vol. 4), Numerical Methods and Algorithms, Springer Verlag, New York, ISBN: ISBN 0-387-24271-6.

APPENDICES

In the following annex all relevant information with regard to test structures and their mathematical models which were used in this thesis are provided.

APPENDIX A: TWO STOREY LABORATORY STRUCTURE PARAMETERS, GEOMETRY AND MODEL

In this section an analytical model for the simplified structure of a two storey laboratory test rig, as shown in Figure A.1, is derived. The test rig was fitted with two kinds of sensors: two accelerometer sensors, and two strain sensors. Accelerometer sensors are mounted on the masses and called accordingly a_1 and a_2, they are used to measure acceleration along the x direction (see Figure A.1). Strain sensors are mounted on one beam, close to the first mass m_1 and denoted by ε_1 and ε_2. Both strain sensors have a half bridge structure in order to compensate for temperature changes and are used to measure strain in the beam. The center positions of these two sensors are given by z_1 and z_2. All geometrical and physical parameters are summarized in Table A.1.
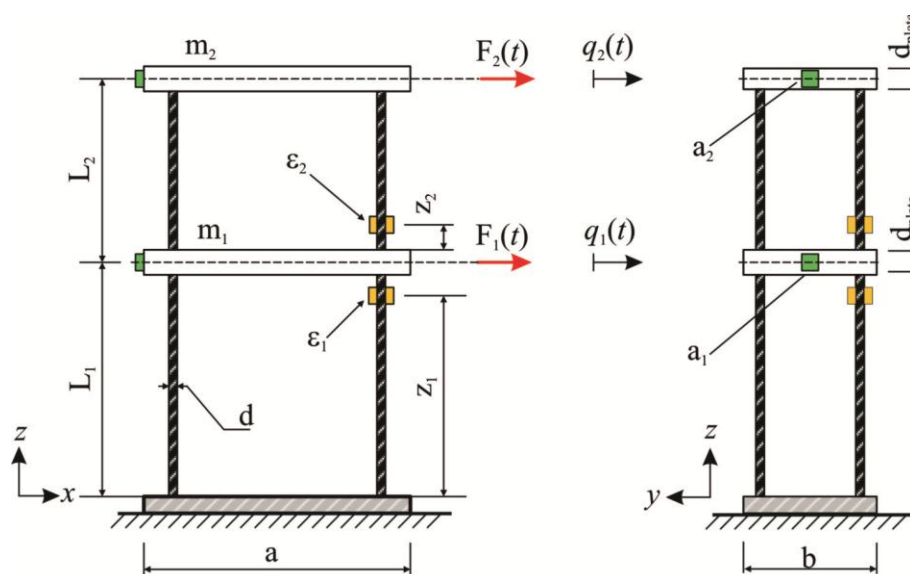
Figure A.1: Original two storey structure with geometrical abbreviation and sensors locations (a_i-accelerometers; ε_i-strain gauges)

Excitations were applied only in the x direction, as shown in Figure A.1, which allowed for using the simplified 2 DOF's structure shown in Figure A.2 for the model construction.
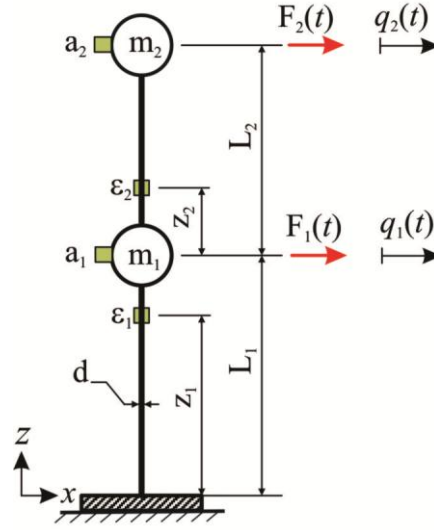
Figure A.2: Simplified 2-DOF's system

In the simplified model (Figure A.2), the plate masses m_1 and m_2 are considered as point masses and the four beams are combined into one beam with stiffness multiplied by a factor of four, and given by the following equations:

$$k_1 = 4 \times 12 \frac{EI}{l_1^3} = 13108[N/m]$$
$$k_2 = 4 \times 12 \frac{EI}{l_2^3} = 11422[N/m]$$

(A.1)

with the assumption that all beams have the same Young's modulus E, area moment of inertia I, and cross section A. It is considered that the beams are subject to the bending only (no longitudinal deformation: $AE = \infty$). The model has two degrees of freedom $q_1(t)$ and $q_2(t)$ along the x axes.

Table A.1: Two storey structure parameters.

L_1	0.213	[m]	z_1	0.2027	[m]
L_2	0.223	[m]	z_2	0.0112	[m]
a	0.3	[m]	m_1	2.1861	[kg]
b	0.2	[m]	m_2	2.1317	[kg]
d_{plate}	0.02	[m]	E	210	[GPa]
d	0.004	[m]	$I = \pi d^4/64$	1.257e^{11}	[m^4]

Using Lagrange's formalism:

$$\frac{d}{dt}\left(\frac{\partial L}{\partial \dot{q}_k}\right) - \frac{\partial L}{\partial q_k} = Q_{k,nc} \tag{A.2}$$

where, L is the Lagrangian function which is constructed as:

$$L = \underbrace{\frac{1}{2}\left(m_1\dot{q}_1^2 + m_2\dot{q}_2^2\right)}_{\text{Kinetic Energy}} - \underbrace{\frac{1}{2}\left(k_1 q_1^2 + k_2(q_2 - q_1)^2\right)}_{\text{Potential Energy}}. \tag{A.3}$$

An equation of motion for the system in Figure A.2 can be constructed analytically with the assumption of proportional nodal damping $\boldsymbol{C}_n = \alpha \boldsymbol{M}_n + \beta \boldsymbol{K}_n$

$$\boldsymbol{M}_n\ddot{\boldsymbol{q}}_n(t) + \boldsymbol{C}_n\dot{\boldsymbol{q}}_n(t) + \boldsymbol{K}_n\boldsymbol{q}_n(t) = \boldsymbol{B}_o\boldsymbol{u}(t) \tag{A.4}$$

where $\boldsymbol{M}_n$, $\boldsymbol{K}_n$ and $\boldsymbol{B}_o$ are the nodal mass, nodal stiffness and the load location (normally filled with ones and zeros) matrices, respectively. The $\boldsymbol{u}(t) = [F_1 \quad F_2]^T$ incorporates two independent external forces and $\boldsymbol{q}_n(t)$ is the nodal generalized coordinates which combines both generalized coordinates as: $\boldsymbol{q}_n = [q_1 \quad q_2]^T$. Expression (A.4) can be transformed into modal coordinates similarly to Equation (2.8) in Chapter 2.1.1 and then into a state space notation according to Equation (2.10) so that the state space representation for the system in modal coordinates is:

$$\dot{x}(t) = \underbrace{\begin{bmatrix} \boldsymbol{0} & \boldsymbol{I} \\ -\boldsymbol{\Omega}^2 & -2\boldsymbol{Z}\boldsymbol{\Omega} \end{bmatrix}}_{A} x(t) + \underbrace{\begin{bmatrix} \boldsymbol{0} \\ \boldsymbol{B}_m \end{bmatrix}}_{B} \boldsymbol{u}(t). \tag{A.5}$$

With the help of a modal analysis procedure, it is possible to obtain circular natural frequencies $\boldsymbol{\Omega}$, modal damping $\boldsymbol{Z}$ and the mode shape $\boldsymbol{\Phi}$ matrices with a high degree of precision. Consequently, that the states transition matrix $\boldsymbol{A}$ is filled directly in and the lower part of the input matrix $\boldsymbol{B}$ is calculated as:

$$\boldsymbol{B}_m = (\boldsymbol{\Phi}^T\boldsymbol{M}_n\boldsymbol{\Phi})^{-1}\boldsymbol{\Phi}^T\boldsymbol{B}_o. \tag{A.6}$$

An output equation which accounts for acceleration is formulated directly from Equation (A.5)

$$\boldsymbol{y}_a(t) = \ddot{\boldsymbol{q}}_n(t) = \boldsymbol{\Phi}\ddot{\boldsymbol{q}}_m(t) = \underbrace{\boldsymbol{\Phi}\begin{bmatrix} -\boldsymbol{\Omega}^2 & -2\boldsymbol{Z}\boldsymbol{\Omega} \end{bmatrix}}_{C_a} x(t) + \underbrace{\boldsymbol{\Phi}\boldsymbol{B}_m}_{D_a}\boldsymbol{u}(t). \tag{A.7}$$

The strain sensors need to be modeled with the help of simple beam theory, which implies the following relation:

$$\varepsilon(z,t) = -\frac{d}{2}\frac{\partial^2 x(z,t)}{\partial z^2},$$ (A.8)

where $x(z,t)$ represents deflection in the x direction at location z, where the strain sensor is positioned. Taking into consideration only the lower part of the specimen, as in Figure A.3(a), which is also representing its free body diagram, see Figure A.3(b), an overall deflection $x(z)$ of the beam for the boundary conditions as in Figure A.3(b), is calculated as:

$$x(z,t) = \frac{F}{6EI}\left(3lz^2 - z^3\right) - \frac{M}{2EI}z^2$$ (A.9)

where, F and M represent the force and moment at the boundary, E is the Young's modulus of elasticity and I is the area moment of inertia.
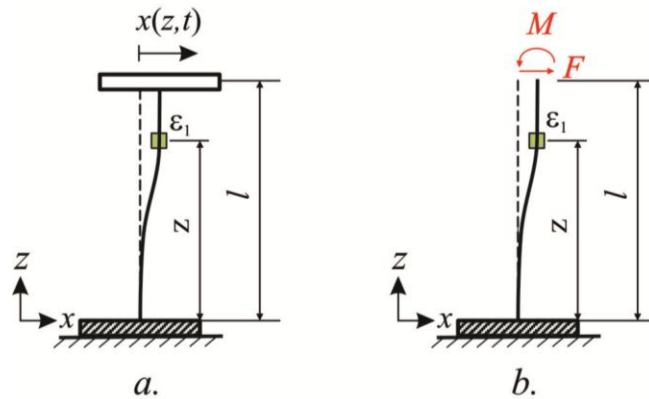
Figure A.3: Beam deflection for the clamped-clamped boundary conditions

In addition, the clamped boundary condition implies

$$\left.\frac{\partial x(z,t)}{\partial z}\right|_{z=l} = \frac{F}{2EI}l^2 - \frac{M}{EI}l = 0,$$ (A.10)

so that the relation between F and M is:

$$M = \frac{Fl}{2}.$$ (A.11)

Inserting this into Equation (A.9) and taking the second derivative leads to:

$$\frac{\partial^2 x(z,t)}{\partial z^2} = \frac{F}{2EI}\left(l - 2z\right).$$ (A.12)

As a consequence, strain in (A.8) is expressed as follows:

$$\varepsilon(z,t) = -\frac{d}{4}\frac{F}{EI}(l-2z). \tag{A.13}$$

There is still a reaction force F in Equation (A.13) which can be related to the generalized displacement x at $z=l$ by inserting (A.11) into Equation (A.9), which in turn produces $F = (12EI/l^3)x(l)$, so that Equation (A.13) would be of following form:

$$\varepsilon(z,t) = \frac{3d(2z-l)}{l^3}x(l). \tag{A.14}$$

Taking into account the relations in Figure A.4 it is possible to summarize both strain measurements into the following output equation:

$$\underbrace{\begin{bmatrix} \varepsilon_1(z_1,t) \\ \varepsilon_2(z_2,t) \end{bmatrix}}_{y_\varepsilon(t)} = \underbrace{\begin{bmatrix} \dfrac{3d(2z_1-l_1)}{l_1^3} & 0 \\ -\dfrac{3d(2z_2-l_2)}{l_2^3} & \dfrac{3d(2z_2-l_2)}{l_2^3} \end{bmatrix}}_{C_\varepsilon} \underbrace{\begin{bmatrix} q_1(t) \\ q_2(t) \end{bmatrix}}_{x(t)}. \tag{A.15}$$

Equation (A.15) together with Equation (A.7) are combined into overall output equation as:

$$y(t) = \begin{bmatrix} y_\varepsilon(t) \\ y_a(t) \end{bmatrix} = \begin{bmatrix} C_\varepsilon \\ C_a \end{bmatrix} x(t) + \begin{bmatrix} 0 \\ D_a \end{bmatrix} u(t) \tag{1.16}$$

Accordingly, Equations (1.16) and (A.5) conclude the state space model of the two storey test rig.
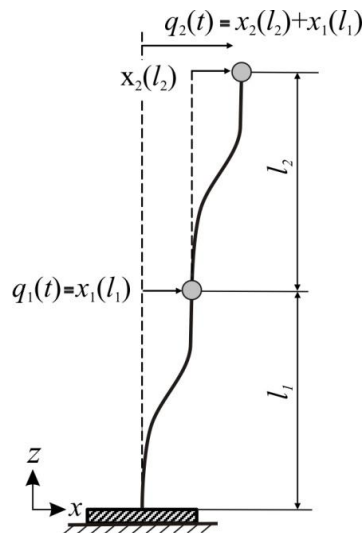
Figure A.4: Connection of generalized coordinates q(t) with beam deflections x(z)

APPENDIX B: SIMPLY SUPPORTED BEAM PARAMETERS, GEOMETRY AND MODEL

In this section, the analytical model for the beam represented in Figure B.1 is derived and transformed into a state space notation. In addition, the output equations for specific sensors are also formulated.
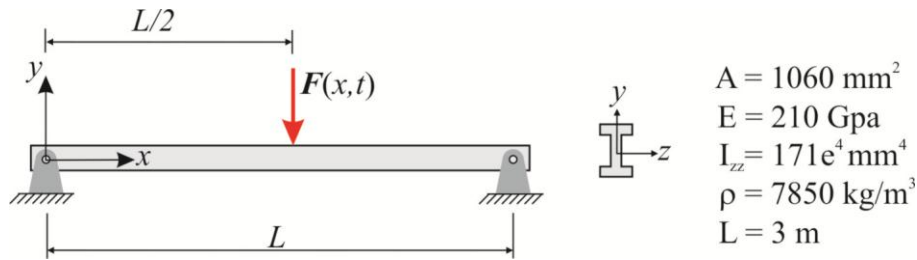
Figure B.1: Uniform hinge-hinge beam

The general Euler-Bernoulli beam theory, which is a simplification of the linear isotropic theory of elasticity, can be used for the modeling of load-carrying beams as in Figure B.1 (up to a certain frequency range). The main governing formulation for the flexural vibration with constant flexural rigidity ($EI = const$) is of the following form [MEIROVITCH 1967]:

$$\frac{\partial^2}{\partial x^2}\left(EI \frac{\partial^2 y(x,t)}{\partial x^2} \right) + \rho A \frac{\partial^2 y(x,t)}{\partial t^2} = F(x,t) \,, \tag{B.1}$$

where $y(x,t)$ is a transverse displacement, $F(x,t)$ is a transverse force, ρ, A, E and I are the density, cross section area, Young's modulus of elasticity and area moment of inertia respectively. Collecting the constant parameters into:

$$\alpha^2 = \frac{EI}{\rho A} \,, \tag{B.2}$$

and assuming that the bending displacement is separated in space and time

$$y(x,t) = W(x)\zeta(t) \,. \tag{B.3}$$

Equation (B.1) is transformed into more compact form:

$$W^{IV}(x)\zeta(t) + \frac{1}{\alpha^2}W(x)\ddot{\zeta}(t) = \frac{F(x,t)}{EI} \,, \tag{B.4}$$

where $W^{IV}(x)$ represents the fourth derivative with respect to spatial orientation x and $\ddot{\zeta}(t)$ represents the second derivative with respect to time t.

Setting free vibration $F(x,t) = 0$, expression (B.4) can be split into the two following characteristic equations:

$$W^{IV}(x) - k^4 W(x) = 0,$$ (B.5)

with $k^4 = \dfrac{\omega^2}{\alpha^2}$ and

$$\ddot{\zeta}(t) + \omega^2 \zeta(t) = 0.$$ (B.6)

Equation (B.5) has a general solution of form:

$$W(x) = C_1 \sin kx + C_2 \cos kx + C_3 \sinh kx + C_4 \cosh kx,$$ (B.7)

where C_1, C_2, C_3 and C_4 are the constants of integration. Solution (B.7) is subject to the boundary conditions of a specific beam structure which describes the way of the beam ends support. For the hinge-hinge beam in Figure B.1 the boundary conditions are defined as:

$$W(0) = W^{II}(0) = W(L) = W^{II}(L) = 0,$$ (B.8)

so that the general solution (B.7) is reduced to the following expression:

$$W(x) = C_1 \sin kL,$$ (B.9)

where the solution of the characteristic equation (B.5) is $k_n L = n\pi$ for $n = 1, 2, \ldots$, with the natural frequency at the nth mode

$$\omega_n = (n\pi)^2 \sqrt{\frac{EI}{mL^4}}.$$ (B.10)

Finally, expression (B.3) for the simply supported beam is presented as follows:

$$y(x,t) = \sum_{n=1}^{\infty} W_n(x)\zeta_n(t) = \sum_{n=1}^{\infty} \left(C_1 \sin \frac{n\pi}{l} x \right) \zeta_n(t).$$ (B.11)

Equation (B.11) and (B.1) serve as a basis for the state-space model, as in Chapter 2.1.2:

$$\dot{x}(t) = Ax(t) + Bu(t).$$ (B.12)

By inserting Equation (B.11) into (B.1) and making use of (B.2) a new form is obtained:

$$\sum_{n=1}^{\infty} \left(\alpha^2 \zeta_n(t) W_n^{IV}(x) + \ddot{\zeta}_n(t) W_n(x) \right) = \frac{F(x,t)}{\rho A}.$$ (B.13)

Using the relation in Equation (B.5) $W_n^{IV}(x) = k_n^4 W_n(x)$ and $\alpha^2 k^4 = \omega^2$ Equation (B.13) is rearranged as follows:

$$\sum_{n=1}^{\infty} \left(\ddot{\zeta}_n(t) + \omega_n^2 \zeta_n(t) \right) W_n(x) = \frac{F(x,t)}{\rho A},$$
(B.14)

multiplying Equation (B.14) by $W_m(x)$ and integrating along beam length L

$$\sum_{n=1}^{\infty} \int_0^L \left(\ddot{\zeta}_n(t) + \omega_n^2 \zeta_n(t) \right) W_n(x) W_m(x)\,dx = \int_0^L \frac{F(x,t)}{\rho A} W_m(x)\,dx,$$
(B.15)

using the orthogonal conditions $\int_0^L W_n(x)W_m(x)dx = 0$, for $n \neq m$ and adding proportional modal damping $2\xi_n \omega_n \dot{\zeta}_n(t)$ the above Equation is transformed into

$$\sum_{n=1}^{\infty} \left[\ddot{\zeta}_n(t) + 2\xi_n \omega_n \dot{\zeta}_n(t) + \omega_n^2 \zeta_n(t) \right] = \frac{1}{\rho A N_A} \int_0^L F(x,t) W_n(x)\,dx,$$
(B.16)

where $N_A = \int_0^L W_n^2(x)dx$. The equation of motion presented in (B.16) can be written in state space form for $n = 1, 2 \ldots, k$ number of modes

$$\dot{x}_{2k \times 1}(t) = \begin{bmatrix} \dot{\zeta}_{k \times 1} \\ \ddot{\zeta}_{k \times 1} \end{bmatrix} = \begin{bmatrix} \mathbf{0}_{k \times k} & \mathbf{I}_{k \times k} \\ -\mathbf{\Omega}_{k \times k} & \left(-2\mathbf{Z}\mathbf{\Omega} \right)_{k \times k} \end{bmatrix} \begin{bmatrix} \zeta_{k \times 1}(t) \\ \dot{\zeta}_{k \times 1}(t) \end{bmatrix} + $$
$$\begin{bmatrix} \mathbf{0}_{k \times m} \\ \left(\frac{1}{\rho A N_A} \left[\int_0^L W_n(x) Q_i(x) dx \right] \right)_{k \times m} \end{bmatrix} \begin{bmatrix} Q_1(t) \\ \vdots \\ Q_m(t) \end{bmatrix}_{m \times 1}$$
(B.17)

where $\mathbf{\Omega}$ and $2\mathbf{Z}\mathbf{\Omega}$ are matrices which combine the natural frequencies and modal damping for k number of modes. The external force function $F(x,t)$ is separated in time and space $F_i(x,t) = Q_i(x)Q_i(t)$. In addition the space allocation $Q_i(x)$ is carried out with the help of Dirac's delta function as in Equation (3.4)

$$Q_i(x) = F_i \delta(x - a_i),$$
(B.18)

where $i = 1, 2, \ldots, m$ is the number of inputs. Using the property of Dirac's delta function $\int_{-\infty}^{\infty} f(x)\delta(x-a)dx = f(a)$ it is possible to simplify the input matrix $\mathbf{B}$ in Equation (B.17), *i.e.* for the hinge-hinge beam

$$\int_0^L \left(W_n(x)Q_i(x) \right) dx = \int_0^L \left(C_1 \sin(k_n x) F_i \delta(x-a_i) \right) dx = C_1 F_i \sin(k_n a_i), \tag{B.19}$$

which is a constant value for a certain force location and certain mode shape. Construction of the output equation

$$y(t) = Cx(t) + Du(t) \tag{B.20}$$

depends on the measurement type.

The output equations for acceleration and strain measurements are constructed as follows:

ACCELERATION MEASUREMENT

The acceleration can be expressed with the help of the Equation (B.3) as second derivative of the bending displacement

$$\ddot{y}(x,t) = \sum_{n=1}^{k} W_n(x)\ddot{\zeta}_n(t). \tag{B.21}$$

So that Equation (B.16) with $F_i(x,t) = Q_i(x)Q_i(t)$ can be transformed for the nth mode

$$\ddot{\zeta}_n(t) = -\omega_n^2 \zeta_n(t) - 2\xi_n \omega_n \dot{\zeta}(t) + \left[\underbrace{\frac{1}{\rho A N_A} \left(\int_0^L Q_i(x) W_n(x) dx \right)}_{q_{in}} \right] Q_i(t). \tag{B.22}$$

Substituting (B.22) into expression (B.21) leads to output equations for r sensors of a form:

$$\begin{bmatrix} \ddot{y}_1(x_{r1},t) \\ \vdots \\ \ddot{y}_r(x_{rr},t) \end{bmatrix} = \begin{bmatrix} -\omega_1^2 W_1(x_{r1}) & \cdots & -\omega_k^2 W_k(x_{r1}) \\ \vdots & \ddots & \vdots \\ -\omega_1^2 W_1(x_{rr}) & \cdots & -\omega_k^2 W_k(x_{rr}) \end{bmatrix} \begin{bmatrix} \zeta_1(t) \\ \vdots \\ \zeta_k(t) \end{bmatrix} +$$
$$\begin{bmatrix} -2\xi_1\omega_1 W_1(x_{r1}) & \cdots & -2\xi_k\omega_k W_k(x_{r1}) \\ \vdots & \ddots & \vdots \\ -2\xi_1\omega_1 W_1(x_{rr}) & \cdots & -2\xi_k\omega_k W_k(x_{rr}) \end{bmatrix} \begin{bmatrix} \dot{\zeta}_1(t) \\ \vdots \\ \dot{\zeta}_k(t) \end{bmatrix} + \tag{B.23}$$
$$\begin{bmatrix} q_{11} W_1(x_{r1}) & \cdots & q_{k1} W_k(x_{r1}) \\ \vdots & \ddots & \vdots \\ q_{1m} W_1(x_{rr}) & \cdots & q_{km} W_k(x_{rr}) \end{bmatrix} \begin{bmatrix} Q_1(t) \\ \vdots \\ Q_m(t) \end{bmatrix},$$

where x_{ri} represents the ith location along the beam and q_{ij} symbolizes the input influence for the jth particular allocated input on the ith mode shape. The two first elements on the right hand side of Equation (B.23) can be combined into a C matrix while the last one is associated with the D matrix.

The strain along the beam can be calculated according to:

$$\varepsilon(x,t) = -\frac{d}{2}\frac{\partial^2 y(x,t)}{\partial x^2}$$

(B.24)

with d being the thickness along the y axis, see Figure B.1. Similarly to the acceleration in Equation (B.3), the strain is represented as:

$$\varepsilon(x,t) = -\frac{d}{2}\frac{\partial^2 y(x,t)}{\partial x^2} = -\frac{d}{2}\sum_{n=1}^{k}W_n^{II}(x)\zeta_n(t),$$

(B.25)

where W_n^{II} is the second partial derivative of the nth mode with respect to x, so the output equation for the r strains along the beam has the following form:

$$\begin{bmatrix} \varepsilon(x_{r1},t) \\ \vdots \\ \varepsilon(x_{rr},t) \end{bmatrix} = -\frac{d}{2}\underbrace{\begin{bmatrix} W_1^{II}(x_{r1}) & \cdots & W_k^{II}(x_{r1}) \\ \vdots & \ddots & \vdots \\ W_1^{II}(x_{rr}) & \cdots & W_k^{II}(x_{rr}) \end{bmatrix}}_{W_{xx}}\begin{bmatrix} \zeta_1(t) \\ \vdots \\ \zeta_k(t) \end{bmatrix}.$$

(B.26)

Finally, expression (B.26) is transformed into state space output equation

$$y(t) = [W_{xx} \quad 0]\begin{bmatrix} \zeta(t) \\ \dot{\zeta}(t) \end{bmatrix},$$

(B.27)

where $\zeta(t)$ and $\dot{\zeta}(t)$ combine the model displacements and modal velocities respectively.

APPENDIX C: ALUMINUM PLATE STRUCTURE PARAMETERS, GEOMETRY AND MODEL

In this section, a mathematical model of a thin, rectangular, simply supported from all sides aluminum plate measuring 0.5m by 0.4m with the following parameters: h = 3mm, E = 72GPa, ρ = 2800kg/m^3 and the Poisson ratio v = 0.3, is provided, see Figure C.1. The plate has been instrumented with 8 strain gauges s_1 to s_8 located as in Figure C.1 and excited with impact-type load $F(x, y, t)$ which can change its position along the plate structure.
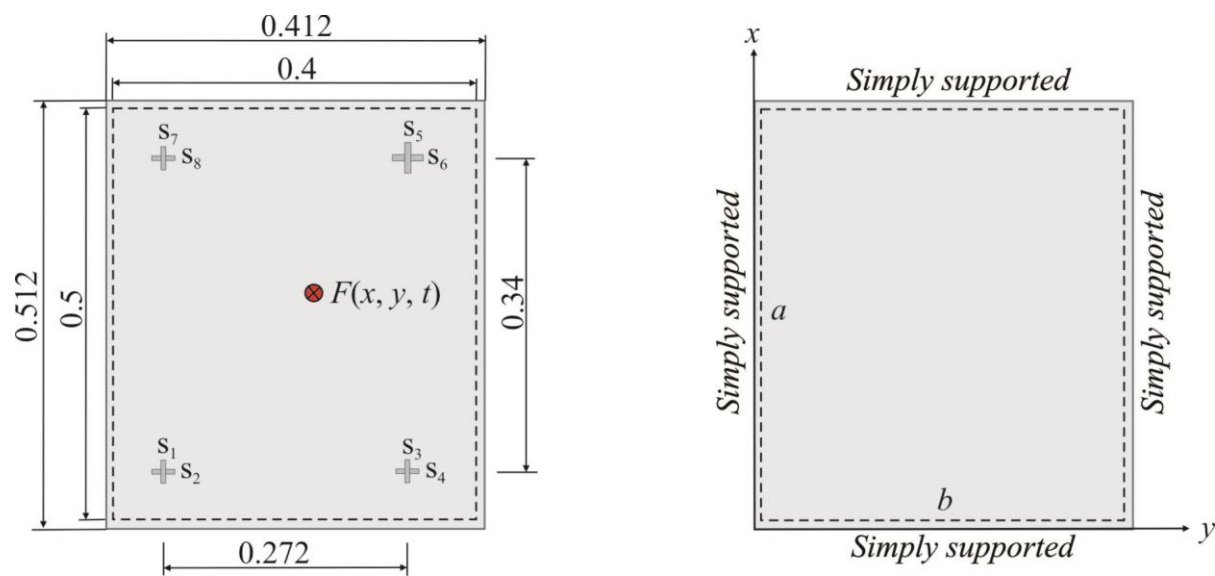
Figure C.1: Aluminum plate simply supported from all sides and fitted with 8 strain sensors

An elementary plate theory provided a basis for model derivation. Extending the Euler-Bernoulli beam expression in two dimensions, the classical differential equation of motion for the transverse displacement $w(x, y, t)$ of a plate with uniform thickness is obtained as follows [LEISSA 1969]:

$$D\nabla^4 w(x,y,t) + \rho h \frac{\partial^2 w(x,y,t)}{\partial t^2} = F(x,y,t), \tag{C.1}$$

where D represents the flexural rigidity of the plate and is defined as:

$$D = \frac{Eh^3}{12(1-v^2)}. \tag{C.2}$$

In Equations (C.1) and (C.2) E, h, v and ρ are the Young's modulus of elasticity, plate thickness, Poisson's ratio, mass density per unit area of the plate and time, respectively. The

$\nabla^4 = \nabla^2 \nabla^2$ where ∇^4 is the Laplace operator in the rectangular coordinates of the second power, also known as *biharmonic operator*:

$$\nabla^4 = \left(\frac{\partial^2}{\partial x^2} + \frac{\partial^2}{\partial y^2} \right)^2 \qquad \text{(C.3)}$$

and $F(x, y, t)$ represents the external load per a unit area. Applying an approach of variable separation, as in Appendix B, for two spatial variables x and y and one time variable t the general solution of the transverse displacement $w(x, y, t)$ for the free vibration is expressed in the following form:

$$w(x, y, t) = W(x, y)\zeta(t), \qquad \text{(C.4)}$$

where $\zeta(t) = \cos \omega t$ is similar to the Euler-Bernoulli beam and $W(x, y)$ is only a function of the position coordinates. Inserting expression (C.4) into Equation (C.1) yields

$$(\nabla^4 - k^4)W(x, y) = 0, \qquad \text{(C.5)}$$

where k is a parameter of convenience defined as:

$$k^4 = \frac{\rho h \omega^2}{D} . \qquad \text{(C.6)}$$

The general solution of transverse displacement $W(x, y)$ of the rectangular plate is obtained by assuming Fourier series in one of the variables, for example x

$$W(x, y) = \sum_{m=1}^{\infty} Y_m(y) \sin \alpha x + \sum_{m=0}^{\infty} Y_m^*(y) \cos \alpha x, \qquad \text{(C.7)}$$

and substituting it into Equation (C.5) [LEISSA 1969]:

$$
\begin{aligned}
W(x, y) = &\sum_{m=1}^{\infty} \left(\begin{array}{l} \left(A_m \sin \sqrt{k^2 - \alpha^2}\, y + B_m \cos \sqrt{k^2 - \alpha^2}\, y + C_m \sinh \sqrt{k^2 + \alpha^2}\, y + \right. \\ \left. D_m \cosh \sqrt{k^2 + \alpha^2}\, y \right) \sin \alpha x \end{array} \right) + \\
&\sum_{m=1}^{\infty} \left(\begin{array}{l} \left(A_m^* \sin \sqrt{k^2 - \alpha^2}\, y + B_m^* \cos \sqrt{k^2 - \alpha^2}\, y + C_m^* \sinh \sqrt{k^2 + \alpha^2}\, y + \right. \\ \left. D_m^* \cosh \sqrt{k^2 + \alpha^2}\, y \right) \cos \alpha x \end{array} \right)
\end{aligned}
\qquad \text{(C.8)}
$$

where A_m, B_m, C_m, D_m and $A_m^*, B_m^*, C_m^*, D_m^*$ are arbitrary coefficients determining the mode shape that are obtained from the boundary conditions. For the plate simply supported from all edges, which is the simplest case for rectangular plates, the boundary conditions are

$$w(x,y)=0 \text{ and } M_x = -D\left(\frac{\partial^2 w(x,y)}{\partial x^2} + v\frac{\partial^2 w(x,y)}{\partial y^2}\right)=0 \quad (\text{for } x=0,a)$$

$$w(x,y)=0 \text{ and } M_y = -D\left(\frac{\partial^2 w(x,y)}{\partial y^2} + v\frac{\partial^2 w(x,y)}{\partial x^2}\right)=0 \quad (\text{for } y=0,b)$$

(C.9)

applying such conditions to a general expression (C.8) leads to solution:

$$W_{mn}(x,y) = A_{mn}\sin\left(\frac{m\pi x}{a}\right)\sin\left(\frac{m\pi y}{b}\right),$$

(C.10)

where A_{mn} is an amplitude coefficient that depends on the initial conditions of the problem $m=1,2,\ldots,k$ and $n=1,2,\ldots,k$ are integers. The frequencies are then obtained by substituting Equation (C.10) into Equation (C.5)

$$\omega = \sqrt{\frac{D}{\rho h}\left(\left(\frac{m\pi}{a}\right)^2 + \left(\frac{n\pi}{b}\right)^2\right)}.$$

(C.11)

Finally, the expression (C.4) can be represented as follows

$$w(x,y,t) = \sum_{m,n}^{k}\left\{A_{mn}\sin\left(\frac{m\pi x}{a}\right)\sin\left(\frac{m\pi y}{b}\right)\right\}\xi(t).$$

(C.12)

The external force function $F(x,y,t)$ is separated in time and space $F(x,t)=Q(x,y)Q(t)$. In addition, for the concentrated force at location (x0, y0) the space allocation $Q(x_0,y_0)$ is carried out with the help of Dirac's delta function as in Equation (3.4)

$$Q(x,y) = \delta(x-x_0)\delta(y-y_0).$$

(C.13)

Using orthogonal conditions and proceeding in a similar manner as in Appendix B, initial Equation (C.1) with external forces can be represented as a combination of uncoupled single degree of freedom oscillators:

$$\ddot{\xi}_{mn}(t) + \omega_{mn}^2\xi_{mn}(t) = Q(t)\frac{4}{ab}\frac{1}{\rho h}\sin\left(\frac{m\pi x_0}{a}\right)\sin\left(\frac{m\pi y_0}{b}\right).$$

(C.14)

Adding proportional damping Equation (C.14) can be used directly for the state space system assembly as in Appendix B, Equation (B.17).

Finally, for the construction of the output equation for the strain measurements the following equations are valid:

$$\varepsilon_{xx}(x,y,z,t) = -z\frac{\partial^2 w(x,y,t)}{\partial x^2} \qquad \varepsilon_{yy}(x,y,z,t) = -z\frac{\partial^2 w(x,y,t)}{\partial y^2} . \qquad \text{(C.15)}$$

Using again the variable separation principle (C.4) in (C.15) the output equation for the r strain sensors in x direction would be:

$$\begin{bmatrix} \varepsilon(x_{r1x},t) \\ \vdots \\ \varepsilon(x_{rrx},t) \end{bmatrix} = -\frac{h}{2}\underbrace{\begin{bmatrix} W_1^{II}(x_{r1}) & \cdots & W_k^{II}(x_{r1}) \\ \vdots & \ddots & \vdots \\ W_1^{II}(x_{rr}) & \cdots & W_k^{II}(x_{rr}) \end{bmatrix}}_{W_{xx}}\begin{bmatrix} \zeta_1(t) \\ \vdots \\ \zeta_k(t) \end{bmatrix}, \qquad \text{(C.16)}$$

the output equation in the y direction is obtained by replacing x with y in Equation (C.16). Finally, expression (C.16) is transformed into a state space output equation for both x and y

$$y(t) = \begin{bmatrix} W_{xx} & 0 \\ W_{yy} & 0 \end{bmatrix}\begin{bmatrix} \zeta(t) \\ \dot{\zeta}(t) \end{bmatrix}, \qquad \text{(C.17)}$$

where $\zeta(t)$ and $\dot{\zeta}(t)$ combine the modal displacements and modal velocities, respectively.